Distributed fiber optic strain sensing in pavements

Kontinuierliche Dehnungsmessung mit Glasfasern in Strassen

Détection en continu des déformations dans les chaussées à l'aide de fiber optique

ETH Zürich, Institut für Geotechnik
Alexander Puzrin, Prof. Dr.
Carlo Rabaiotti, Prof. Dr.
Dominik Hauswirth, Dr.
Frank Fischli, MSc ETH
Danai Tsirantonaki, MSc ETH

Marmota Engineering AG
Michael Iten, Dr.

Brugg Kabel AG
Massimo Facchini, Dr.
Etienne Friedrich, Dr.

Schweizerische Eidgenossenschaft
Confédération suisse
Confederazione Svizzera
Confederaziun svizra

Distributed fiber optic strain sensing in pavements

Kontinuierliche Dehnungsmessung mit Glasfasern in Strassen

Détection en continu des déformations dans les chaussées à l'aide de fiber optique

ETH Zürich, Institut für Geotechnik
Alexander Puzrin, Prof. Dr.
Carlo Rabaiotti, Prof. Dr.
Dominik Hauswirth, Dr.
Frank Fischli, MSc ETH
Danai Tsirantonaki, MSc ETH

Marmota Engineering AG
Michael Iten, Dr.

Brugg Kabel AG
Massimo Facchini, Dr.
Etienne Friedrich, Dr.

Imprint

Forschungsstelle und Projektteam
Projektleitung
Alexander M. Puzrin, Prof. Dr.

Mitglieder
Carlo Rabaiotti, Prof. Dr.
Dominik Hauswirth, Dr.
Frank Fischli, MSc ETH
Danai Tsirantonaki MSc ETH
Michael Iten, Dr.
Massimo Facchini, Dr.
Etienne Friedrich, Dr.

Federführende Fachkommission
Fachkommission 4: Bau- & Geotechnik

Begleitkommission
Präsident
Martin Stolz, Prof.

Mitglieder
Christiane Raab, Prof. Dr.
Armando Casanova, dipl. Bauing. ETH
Hans-Peter Beyeler, dipl. Bauing. HTL

Antragsteller
Schweizerischer Verband der Strassen- und Verkehrsfachleute (VSS)

Bezugsquelle
Das Dokument kann kostenlos von http://www.mobilityplatform.ch heruntergeladen werden.

Table of Contents

Zusammenfassung

Die vorliegende Forschungsarbeit hatte zum Ziel, das Potential von in Asphaltschichten eingebauten und verteilt messenden faseroptischen Sensoren zum Zweck der Charakterisierung des Tragverhaltens von Strassen unter Verkehrslasten zu untersuchen. Um dieses Ziel zu erreichen, wurden in einem ersten Schritt robuste Glasfaserkabel im Labor getestet, um deren Eignung für die raue Umgebung der Asphaltschichten zu prüfen. In einem zweiten Schritt wurden verschiedene Einbauverfahren für das faseroptische Kabel auf zwei Testgeländen mit Asphaltschichten getestet. Nach der erfolgreichen Installation der verteilt messenden Glasfasersensoren auf dem Testgelände wurden über mehr als 2.5 Jahre erfolgreich Messungen durchgeführt. Die unübertroffene grosse Datenmenge an hochaufgelösten Dehnungen, welche entlang dieser Sensoren aufgezeichnet werden kann, wurde abschliessend benutzt, um die Messdaten mit einer numerischen Modellierung der Asphaltschichten unter Last zu verbinden. In Verbindung mit der numerischen Modellierung hat die Anwendung von verteilt messenden faseroptischen Sensoren ein grosses Potential zur Untersuchung des Tragverhaltens von neuem Belagsmaterial oder der Kalibration neuartiger Bemessungsmethoden. Dies darum, weil die Technologie die Quantifizierung des Dehnungsfeldes erlaubt, welches in der Asphaltschicht vorhanden ist. Weiter könnten verteilt messende Glasfasersensoren eventuell in Zukunft auch als zusätzliches Werkzeug für die Beurteilung des Zustandes der Strassen benutzt werden.

Aufbau des vorliegenden Berichts

Der Aufbau des vorliegenden Berichtes folgt mehrheitlich den verschiedenen Forschungsaufgaben, welche im Rahmen dieses Forschungsprojektes durchgeführt wurden. Nach einer kurzen Einführung in die Thematik in Kapitel 1 werden in Kapitel 2 verschiedene, in diesem Projekt verwendete, verteilt messende faseroptische Sensortechnologien eingeführt. Die Resultate der Laborversuche sind anschliessend in Kapitel 3 festgehalten, während ein Beschrieb der verschiedenen angewandten Installationsmethoden der Sensoren in Kapitel 4 zu finden ist. Die Messresultate der beiden Versuchsstandorte, eine innerstädtische Strasse in Zürich und ein Flugzeugstandplatz am Flughafen Zürich, werden in Kapitel 5 und 6 gezeigt. Die Ergebnisse einer anschliessend durchgeführten numerischen Modellierung der Feldversuche sind in Kapitel 7 bis 9 zusammengefasst. Der Bericht wird in Kapitel 10 mit einer Schlussfolgerung und weiteren Empfehlungen abgeschlossen. Zusätzliche Informationen zu den numerischen Resultaten der Modellierung sind im Anhang zu finden.

Vorschau über die gezeigten Forschungsergebnisse

Betrachtet man die Struktur dieses Forschungsprojektes, so können drei Gruppen von Hauptaufgaben identifiziert werden: das Testen der Sensorkabel im Labor und ihr Einbau in die Asphaltschichten im Feld, die Messung mit den neuartigen Sensoren an den Versuchsstandorten und abschliessend die Resultate der numerischen Modellierung der Feldversuche mittels Finite-Elemente-Methode (FE). Eine kurze Vorschau auf die wichtigsten Resultate dieser drei Aufgaben wird in den folgenden Abschnitten gezeigt, direkt nach einer kurzen Beschreibung der verwendeten faseroptischen Messtechnologie.

Verteilt messende faseroptische Messtechnologie

Verteilt messende faseroptische Sensoren ermöglichen die kontinuierliche Messung von Grössen wie Temperatur oder Dehnung entlang eines faseroptischen Kabels. Dazu wird von einem Messgerät Licht durch eine herkömmliche single mode Glasfaser gesendet. Im Gegensatz zu anderen eher diskontinuierlichen faseroptischen Messtechnologien wie z.B. Fiber Bragg Grating, sind die verteilt messenden Sensoren nicht nur an vordefinierten Orten, wo z.B. ein Gitter eingeschrieben ist, empfindlich auf externe Messgrössen sondern auf der gesamten Faserlänge. In Kombination mit einer hohen räumlichen Auflösung der Messgrössen kann somit ein leistungsfähiges Werkzeug zum

Analysieren und Überwachen von Tragstrukturen gebildet werden, welches die Erfassung einer einzigartigen Datenmenge innerhalb der Struktur ermöglicht. Heutzutage sind verschiedene verteilt messende faseroptische Technologien kommerziell erhältlich. Im vorliegenden Projekt wurden Technologien verwendet, welche auf der Rayleigh und Brillouin Streuung in Glasfasern beruhen.

Laborversuchsresultate und Installationsprozedur

Für einen Sensor, dessen Messprinzip auf den intrinsischen Eigenschaften einer dünnen zerbrechlichen Glasfaser beruht, repräsentiert der Asphalt eine relativ raue Umgebung. Obwohl die in diesem Forschungsprojekt verwendeten verschiedenen faseroptischen Kabel, produziert von Brugg Kabel AG (jetzt Solifos AG), im Prinzip entwickelt wurden, um unter rauen Bedingungen zu bestehen, gab es für diese konkrete Anwendung trotzdem Klärungsbedarf betreffend die hohen Temperaturen während des Einbaus und den grossen Querdruck nahe der Strassenoberfläche, welcher während des Baus und des Betriebs der Strasse auf die Kabel wirkt. Diese Bedenken wurden in diesem Forschungsprojekt mittels Laborversuchen untersucht.

Auch wenn man mit Laborversuchen bestätigen kann, dass die verwendeten Kabelversionen für Anwendungen in Belägen geeignet sind, müssen feldtaugliche Installationsmethoden definiert werden, welche sicherstellen, dass der Prozess des Kabeleinbaus den Bau der Strasse nicht behindert und dass die Kabel in einem vordefinierten Layout auf den Schichten fixiert werden können. Die Angemessenheit solcher verschiedener Installationsmethoden wurde im Zuge der Planung und Ausführung der beiden Sensortestfelder „Hohlstrasse" und „Flughafen Zürich" getestet.

Laborversuche

Temperatur

Dünne Asphaltschichten sollten vor dem verdichten mit Walzen eine Mindesttemperatur von ca. 120 – 150°C aufweisen. Für die spezifischen in diesem Projekt verwendeten faseroptischen Sensorkabel existierten von früheren Installationen leider keine Erfahrungswerte für diesen Temperaturbereich. Bezüglich der wichtigsten Sensoreigenschaft, der Umwandlung der gemessenen Frequenzverschiebung in eine Dehnung, gab es Bedenken, ob die vorübergehend hohe Temperatur möglicherweise die Eigenschaften der Kabel verändern könnte. Um das Verhalten der Kabel in diesem Temperaturumfeld zu untersuchen, wurde folgender Testplan verwendet:

- Messung der Dehnungsantwort eines definierten Kabelabschnittes auf eine äussere Verlängerung in einem Versuchsstand
- Diesen Kabelabschnittes Temperaturen von 140°C aussetzen und dabei Messungen durchführen
- Erneute Messung der Dehnungsantwort des definierten Kabelabschnittes auf eine äussere Verlängerung im Versuchsstand

Durch den Vergleich des Kabelverhaltens vor und nach der Temperaturexposition konnte gefolgert werden, dass kein signifikant nachteiliger Einfluss des für Walzasphalt üblichen Temperaturbereichs besteht. Wie zu erwarten war, induzierte der Kunststoffkabelmantel auf dem freien unbehinderten Kabelabschnitt eine nichtlineare Kennlinie während der Temperaturexposition. Dies muss aber für die vorliegende Anwendung nicht unbedingt von Nachteil sein. Ausserdem wurde bei einigen Kabelversionen während des Erhitzens eine sehr heterogene Reaktion auf die Temperatureinwirkung beobachtet. Diese Heterogenität erfordert weitere Untersuchungen und kann in Anwendungen ausserhalb des Rahmens dieser Studie zu zusätzlichen Schwierigkeiten führen z. B. dann wenn thermische Auswirkungen in der Frequenzverschiebung kompensiert werden müssen.

Querdruck

Während hohe Temperaturen in den Asphaltschichten nur vorübergehend während des Belagseinbaus auftreten, treten hohe Querdrücke während des Belagseinbaus und, in

oberflächennahen Schichten, auch während der Betriebsdauer durch Schwerverkehr auf. Da faseroptische Sensoren sensitiv auf Dehnungen sowie Änderungen der Temperatur und des hydrostatischen Druckes (schwach) sind, wurde die Reaktion der verwendeten Kabeltypen mit einem einfachen Druckversuch mit hydrostatischen Drücken von bis zu 1MPa mit getestet. Die Sensitivität gegenüber hydrostatischem Druck war jedoch, in dem für dieses Projekt relevanten Bereich, eher klein. Daher wurde entschieden, den Beitrag des hydrostatischen Druckes näherungsweise zu vernachlässigen.

Installationsmethoden im Feld

Obwohl die verwendeten Kabel für eine eher raue Umgebung ausgelegt sind, können die Installation der Kabel und der Bau der Strasse zu möglichen Schäden an den Kabeln führen. Zwei grundlegende Konzepte wurden beim Einbau der Kabel verfolgt: Die Installation auf einer Oberfläche mit verschiedenen Fixierungsmethoden und einer manuellen Abdeckung des Sensorkabels mit einer kleinen Menge Feinmischgut sowie die Installation in Nuten im Belag, welche anschliessend mit einer Vergussmasse rückverfüllt wurden.

Die Evaluation der verschiedenen Einbauprozeduren der faseroptischen Kabel zeigte, dass verschiedenen Kabelversionen für den vorgesehenen Zweck genügend mechanische Robustheit bieten. Sogar die am wenigsten robuste Kabelversion überstand die Installation ohne Schaden und zeigte gute Resultate während des gesamten Forschungsprojektes. Im Allgemeinen wurden gute Erfahrungen mit einer Installationsart gemacht, bei welcher die Sensorkabel mit einer dünnen Schicht feines Asphaltmischgutes überdeckt wurden, bevor die Kabel vom Einbaufertiger überfahren wurden. Als Alternative hat sich auch die Installation der Kabel in einer Nut bewährt, welche mit einem Bewehrungsstab während des Walzens des Asphalts geformt wurde.

Messresultate von den Versuchsstandorten

Zwei verschiedene Standorte wurden mit verteilt messenden Glasfasersensoren instrumentiert: eine innerstädtische Strasse in Zürich („Hohlstrasse") und ein Standplatz am Flughafen Zürich. An beiden Standorten wurden faseroptische Sensoren in verschiedenen Tiefen im Asphalt eingebettet und während die Oberfläche mit verschiedenen Fahr- oder Flugzeugen belastet wurde, wurden damit Dehnungen gemessen. Diese Versuche wurden in verschiedenen Jahreszeiten wiederholt, um den Effekt des temperaturabhängigen Tragverhaltens von Asphalt abzubilden. Die gemessene Dehnungsverteilung zeigte eine starke räumliche Variabilität mit lokal hohen räumlichen Dehnungsgradienten, dies insbesondere nahe an der Strassenoberfläche. Diese räumlich enge Variation des Dehnungsfeldes im Asphalt ist ein starkes Argument für die Verwendung dieses Dehnungssensortyps, da die Dehnungen kontinuierlich mit hoher räumlicher Auflösung entlang des Kabels gemessen werden können, während klassische Dehnungssensoren nur isolierte Punktmessungen zulassen. Mehr als $1500\mu\varepsilon$ wurden in der Strasse als Maximum während des Sommers in 4cm Tiefe direkt unter einem Lastwagenrad gemessen, während die maximale Dehnung am Flughafenstandplatz in etwa das Doppelte betrug, obwohl dort der Test zu Herbstbeginn und nicht im Hochsommer durchgeführt wurde. Wie erwartet, konnte eine starke Abhängigkeit dieser maximalen Dehnung unter Last von der Temperatur des Asphalts beobachtet werden. Die Änderung der Temperatur über die Jahreszeiten beeinflusste jedoch nicht nur die Grösse der Dehnung sondern auch ihre Verteilung.

Testfeld Hohlstrasse

Testfeld und Aufbau

Das Testfeld Hohlstrasse repräsentiert eine städtische Strasse unter hohem Verkehrsaufkommen und mit einer Buslinie. Die Hohlstrasse besteht aus drei Asphaltschichten, welche insgesamt 22cm stark sind und auf einem ungebundenen Gemisch für den Strassenbau ruhen. Zum Zweck der Messung von Dehnungen wurden zuunterst bei den Asphaltschichten in 22cm Tiefe, wie auch auf der Binderschicht in 4cm Tiefe, faseroptische Kabel eingebaut. Die Kabel wurden in der Form von kurzen Schlaufen von rund 10m Länge eingebaut, mit parallelen Geraden quer oder längs zur

Verkehrsrichtung. Eine rund 70m lange Schleife wurde in der Form eines Gitters mit Gitterabstand von 0.5m eingebaut. Die Zugänglichkeit zu den Kabelenden, welche mit dem Messgerät verbunden werden müssen, wurde durch kleine Schächte in dem benachbarten Gehsteig gewährleistet. Die Installation funktionierte durch die gesamte Projektdauer einwandfrei, nur einige kleinere Schäden, aufgrund der gewählten Kabelführung bei dem Eintritt in den Zugangsschacht, konnten beobachtet werden

In diesem Projekt wurden die verteilt messenden faseroptischen Sensoren in erster Linie benutzt, um die Dehnungsverteilung in Belägen unter kurzzeitig ruhender wie auch sich bewegender Verkehrslast zu messen. Um den Strassenbelag zu belasten, wurden ein Lastwagen und ein Auto als Testfahrzeuge benutzt. Während das Auto Achslasten von etwas mehr als 12kN auf die Strassenoberfläche brachte, applizierte die Vorderachse des Lastwagens (einfach bereift) rund 50kN und die Hinterachse (doppelt bereift) rund 100kN auf den Strassenbelag. Die Tests, in welchen die Dehnung im Strassenbelag unter unterschiedlicher Belastung und Geschwindigkeiten des darüberfahrenden Fahrzeugs gemessen wurde, wurden in verschiedenen Jahreszeiten durchgeführt, um den Einfluss der Temperatur auf die Dehnungsverteilung im Belag zu studieren. Solche Versuche wurden während des Tages innerhalb des üblichen Verkehrsflusses aber nicht während den Hauptverkehrszeiten durchgeführt. Um den Verkehrsfluss nicht übermässig zu stören, war es nicht möglich, die statische Last länger als für einige Sekunden aufzubringen. Um in der Lage zu sein, statische Lasten auch für einige Minuten aufzubringen, wurde während einer Nacht eine Spur gesperrt und Dehnungsmessungen mit ruhenden Lasten sowie Messungen betreffend die Setzungsmulde des Belages durchgeführt.

Da die Temperatur die Steifigkeit der Asphaltschichten stark beeinflusst, wurden während den Tests die Temperaturen periodisch gemessen. Die Temperaturen wurden an der Strassenoberfläche und in drei weiteren Tiefen mit Nadelthermometern und Pt100 Elementen gemessen. In diesem Testfeld wurden verschiedenen Kernbohrungen durchgeführt, um eine numerische Simulation mit möglichst realistischen Steifigkeitsparametern zu ermöglichen. Die Proben, welche aus diesen Kernbohrungen entnommen worden sind, wurden an der EMPA untersucht.

Erste kontinuierliche Dehnungsmessungen zeigten im Bereich direkt um den Reifen, dass die Dehnungsverteilung im Belag räumlich stark variiert. Um in der Lage zu sein, diese stark variierende Dehnungsverteilung räumlich genügend aufzulösen, wurden hauptsächlich die Messgeräte benutzt, welche auf der Rayleigh Rückstreuung basieren. Diejenigen Geräte, welche auf diesem Messprinzip beruhen und für dieses Forschungsprojekt verfügbar waren, ermöglichten eine deutlich feiner räumliche Auflösung der Dehnungen entlang des Sensorkabels als diejenigen spezifischen Messgeräte basierend auf der Brillouin Rückstreuung, welche für dieses Projekt verfügbar waren. Innerhalb des vorliegenden Projektes wurden mittlere Dehnungen oft über eine räumliche Distanz im Bereich von 10mm oder weniger errechnet und in einem Abstand im Bereich von oft rund 5mm oder weniger entlang der Faser ausgegeben.

Messresultate

Um eine Vergleichbarkeit der Messresultate von verschiedenen Testserien zu erlauben, wurden die Dehnungsmessungen beim Testfeld Hohlstrasse oft in sehr ähnlicher Weise durchgeführt. Zwischen der Installation im November 2015 und März 2018 wurden rund 10 Testserien durchgeführt. Nicht alle dieser Testserien bestanden aus dem gleichen Testprogramm, üblicherweise wurden aber Dehnungsmessungen auf der Binderschicht durchgeführt, mit der Hinter- und Vorderachse des Lastwagens als kurzzeitig ruhende Last. In Ergänzung zu diesen Messungen wurden von Zeit zu Zeit Messungen mit dem Sensor auf der Unterseite der Asphaltschichten oder unter Verwendung des Autos durchgeführt, Letzteres um kleinere Lasten auf den Belag aufzubringen zu können. Die Referenzmessung, zu welcher die Dehnung unter Last gemessen wurde, wurde üblicherweise einige Sekunden vor Aufbringen der Last aufgezeichnet. Sobald die Messung unter Last beendet war (oft rund 10s bis 15s nachdem die Last aufgebracht wurde), wurde eine dritte Messung unmittelbar nach Entfernung der Last gestartet. Diese dritte Messung wurde durchgeführt, um die Viskosität und somit das zeitabhängige

Verhalten des Belags zu erfassen. Solche statische Messungen wurden oft durch dynamische Messungen begleitet, in welchen die Testfahrzeuge (Auto, Lastwagen) den Sensor mit unterschiedlichen Geschwindigkeiten überquerten, während zeitgleich die Dehnungen mit hoher zeitlicher Auflösung ausgegeben wurden.

Der Effekt der abnehmenden Asphaltsteifigkeit mit zunehmender Temperatur war, wie erwartet, auch in den gemessenen Dehnungsverteilungen klar ersichtlich. Gesamthaft resultierte ein Verhältnis von rund 50 der gemessenen maximalen Dehnungen einer Testserie an einem heissen Sommertag einerseits und an einem kalten Wintertag andererseits. Dies obwohl die Wintermessung während des Tages und nicht während einer kalten Winternacht durchgeführt wurde. Es ist daher zu erwarten, dass das Verhältnis der wirklich auftretenden Dehnungsmaxima noch grösser als das gemessene ist.

Der Belag direkt unter dem Reifen, welcher kurzzeitiger statischer Belastung unterworfen wurde, zeigte expansive Dehnungen in 4cm wie auch in 22cm Tiefe. Die gemessene Dehnung war aber, im Speziellen an heissen Sommertagen, im oberen Sensorkabel deutlich grösser als im unteren und erreichte Grössen von bis zu $1500\mu\varepsilon$. Während die Dehnung in der oberen Schicht das Vorzeichen unmittelbar neben dem Reifenumfang wechselt und zur kontraktiven Dehnung wurde, trat der Vorzeichenwechsel auf der Unterseite der Asphaltschichten weiter entfernt auf. Wenn der Belag mit einem einzelnen Reifen belastet wurde, erschien nur eine expansive Dehnungsspitze in den Messungen, während zwei expansive Dehnungsspitzen bei einer Belastung mit einem Doppelreifen sichtbar wurden. Interessanterweise waren diese beiden Dehnungsspitzen auch in einer Tiefe von 22cm, auf der Unterseite der Asphaltschichten, immer noch klar ersichtlich. Verglichen mit den Resultaten aufgezeichnet während eines heissen Sommertages, wo die expansive Dehnungsspitze unterhalb des Reifens die Dehnungsverteilung dominierte, war diese Dehnungsspitze während kalten Wintertagen kaum mehr dominierend, verglichen mit den benachbarten kontraktiven Dehnungen.

Neben den Tests mit Dehnungsmessungen unter kurzzeitig ruhenden Fahrzeugen, wurden in einer Sommernacht auch noch ergänzende Tests mit längerer Lasteinwirkungsdauer durchgeführt. Während dieser Nacht erlaubten die Behörden die Sperrung einer Fahrspur für den Verkehr während einige Stunden. Daher war es möglich, Lasten auf die instrumentierte Fläche aufzubringen, welche zumindest für einige Minuten ruhen konnten. Dies ermöglichte die Untersuchung des viskosen Verhaltens der Asphaltschichten an diesem spezifischen Versuchsstandort. Zusätzlich zu den Dehnungsmessungen wurden dabei auch Setzungsmessungen auf der Strassenoberfläche mit einem Messgerät namens „ETH Delta" durchgeführt. Dies um zusätzliche unabhängige Messgrössen, neben den Dehnungen in den Asphaltschichten, zu erlangen.

Zusätzlich zu den oben diskutierten Messungen zum kurzfristigen Verhalten des Strassenbelags unter statischer Last, wurden kontinuierliche Dehnungsmessungen mit hoher räumlicher Auflösung und mit Messraten von 100Hz durchgeführt. Verschiedene Testfahrzeuge traversierten den im Asphalt eingebetteten Sensor mit Geschwindigkeiten zwischen 5km/h und 50km/h, um den Effekt einer dynamischen Belastung, welche dem Verkehr entspricht, auf die Strasse zu untersuchen. Erwartungsgemäss reduzierte sich gesamthaft die Dehnung mit zunehmender Fahrzeuggeschwindigkeit aufgrund der viskosen Belagseigenschaften. Der Effekt der überproportionalen Reduktion der expansiven Dehnungsspitze in kalten Temperaturen intensivierte sich in Kombination mit hohen Fahrzeuggeschwindigkeiten. Dieser Umstand führte zur Situation, dass in kalten Bedingungen bei hohen Fahrzeuggeschwindigkeiten gar keine expansiven Dehnungen mehr in den Asphaltschichten in 4cm Tiefe gemessen wurden und die Dehnung durchwegs kontraktiv blieb, auch direkt unter dem Reifen. Zusätzlich zu der detaillierten Einsicht in das Verhalten der Asphaltschichten unter dynamischer Verkehrslast erlaubten die Messresultate die Fahrrichtung und –position wie auch die Fahrzeuggeschwindigkeit und die Anzahl Achsen und Räder zu erfassen. Die aktuellen Grenzen der Testanwendung zur Detektion von dynamischen Lasten lagen bei Überfahrten von leichten Fahrzeugen in kalten Wintertemperaturen bei hohen Geschwindigkeiten. In diesen Bedingungen wurden die Dehnungen sehr klein und es wurde schwierig, die

Dehnungsänderung ohne weitere Datenauswertungstechniken im Rauschen zu erkennen. Es muss jedoch erwähnt werden, dass die Messungen in einer normalen Asphaltbetonschicht mit 22cm Dicke stattgefunden haben, welche für schweren Verkehr bemessen war. Falls nötig, könte dieser Umstand durch die Anwendung weiterer Massnahmen verbessert werden.

Testfeld Flughafen Zürich

Testfeld und Aufbau

Im Gegensatz zu dem Versuchsstandort Hohlstrasse, welcher hauptsächlich durch dynamische Verkehrsbelastung mit vielen Lastwechseln beansprucht wird, repräsentiert der Versuchsstandort am Flughafen Zürich einen Flugzeugstandplatz, welcher eine kleine Anzahl Lastwechsel aber dafür hohe Verweildauern der Last mit sich bringt. Trotz diesem Umstand wurde dieses Testfeld ebenfalls in Asphalt und nicht Beton ausgeführt, weil die Planung nur eine zeitlich begrenzte Nutzung vorsah. Der Aufbau besteht aus einer ersten 4cm starken und einer zweiten 9.5cm dicken Asphaltschicht, ruhend auf einem hydraulisch gebundenen Gemisch mit 53cm Gesamtstärke.

Die Verlegeanordnung der faseroptischen Installation wurde eher grossformatig ausgeführt. Dies im Sinne, dass die Kabelschlaufen am Standplatz eine Gesamtlänge von rund 140m aufwiesen. Die Installation bestand aus zwei fast 30m langen parallelen Kabelabschnitten mit einem Abstand von 6m. Die verbleibende Kabellänge wurde eigentlich nur dazu benutzt, um die Kabelenden zum nächsten Elektroschacht zu führen, welcher den Zugang mit den Messgeräten zu den Kabeln ermöglichte. Wie in der Hohlstrasse, so wurden auch am Flughafen verschiedene Sensorkabeltypen in 4cm Tiefe und an der Unterseite der Asphaltschicht eingebaut, was hier in 13.5cm Tiefe lag. Der Einbau der Kabel wurde im Juli 2015 zeitgleich mit dem Bau des Standplatzes durchgeführt.

Unerwartete Schwierigkeiten traten an diesem Versuchsstandorten während der ersten Messungen infolge der Überlänge der Sensorschlaufe auf. Als diese Schwierigkeiten aber mit einem adaptierten Messvorgang überwunden werden konnten, funktionierte die Installation während der gesamten Dauer des Forschungsprojektes reibungslos.

Messresultate

Mit den im Flugzeugstandplatz eingebauten faseroptischen Sensoren wurden Messungen an einem kalten Wintertag und an zwei warmen Herbsttagen ausgeführt. Dabei wurden Flugzeuge des Typs A330-300 und A340-300 zu Belastungszwecken benutzt. Statische Messungen wurden durchgeführt, nachdem ein Flugzeugtraktor das Flugzeug in die zuvor definierten Positionen geschoben hatte. Verteilte faseroptische Messungen wurden an rund 5 bis 6 verschiedenen Positionen in Bezug zum Sensorstandort durchgeführt.

Obwohl die Gesamtdicke der der Asphaltschichten eher klein ist und sie zudem auf einem hydraulisch gebundenen Gemisch ruhen, war die Abhängigkeit der gemessenen Dehnungen von der Temperatur auch bei diesem Aufbau sehr gross. Dieser Umstand zeigte sich in den grossen expansiven Dehnungsspitzen von über $3000\mu\varepsilon$ welche direkt unter dem Reifen an einem warmen Herbsttag gemessen werden konnten. Am kalten Wintertag blieb diese Dehnung auch direkt unterhalb des Reifens in 4cm Tiefe kontraktiv und erreichten nur in 13.5cm Tiefe eine expansive Form. Auch wenn die Asphaltschichten auf einem hydraulisch gebundenen Gemisch ruhen, die Einflusszone des Flugzeugfahrwerks blieb eher klein und das Fahrwerk generierte ein eher schmales und lokalisiertes Dehnungsfeld in den Asphaltschichten.

Numerische Modellierung der Feldversuche

Motivation
Die Einbettung verteilter faseroptischer Sensoren in die Fahrbahn ermöglichte einen detaillierten Einblick in das strukturelle Verhalten von Asphaltschichten unter

Verkehrslasten. Auf den ersten Blick bestätigen die Dehnungsmessungen, was zumindest qualitativ zu erwarten war: Höhere Lasten erzeugen höhere Dehnungen; die Dehnungen nehmen mit steigender Temperatur für dieselbe Belastung zu; schnelle Fahrzeugüberfahrten erzeugen geringere Beanspruchungen als langsame Überfahrten. Es wurden jedoch auch Effekte gemessen, die schwieriger zu erklären sind, sowohl in qualitativer als auch in quantitativer Weise. Darüber hinaus basiert die Abschätzung von Dehnungen für eine bestimmte Temperatur, Last und Fahrzeuggeschwindigkeit nur mit Hilfe der numerischen Modellierung auf zahlreichen Annahmen, weshalb sie ohne den Abgleich mit Messdaten schwierig zutreffend anzuwenden ist.

Auf der anderen Seite steht eine grosse Menge von Dehnungsdaten aus verteilten faseroptischen Sensoren für verschiedene Randbedingungen wie Temperatur, Last Grösse und Fahrzeuggeschwindigkeiten zur Verfügung. Dies ermöglicht wiederum die Auswahl und Kalibrierung geeigneter Materialmodelle, Randbedingungen und Modellierungstechniken aufgrund der Messdaten, die nicht im Labor sondern unter realen Feldbedingungen gesammelt wurden. Dies wird möglicherweise immer wichtiger, wenn der mechanistische Entwurfsansatz bei der Gestaltung von Strassen weiter verbreitet wird oder neue Materialien zur Anwendung kommen, über welche nicht genügend empirisches Wissen verfügbar ist. Aus diesem Grund wurden die zuvor diskutierten Feldversuche durch eine numerische Modellierung ergänzt. Dies erlaubt das Wissen über die Angemessenheit von Materialmodellen, Randbedingungen und Modellierungstechniken zu vertiefen.

Numerische Modellierung der Feldversuche in der Hohlstrasse

Damit die Auswahl von näherungsweise zutreffenden Modellen, Materialparameter und Randbedingungen für die Modellierung der Feldversuche möglichst klein wird, wurden viele unabhängige Messdaten gesammelt. Proben aus Kernbohrungen wurden in den Labors der EMPA untersucht, um den Bereich der Steifigkeit bei unterschiedlichen Temperaturen und Frequenzen zu bestimmen. Neben Dehnungen wurden auch Temperaturen und, in einem Test, die Setzungsmulde unter der Last mit der Hilfe des „ETH Delta" Gerätes aufgezeichnet.

Modellierung der Setzungsmulde mit ETH Delta Tests

Die Messung der Setzungsmulde mit dem ETH Delta Gerät wurde für eine vorläufige Rückrechnung der Materialparameter des Untergrunds mit einem dreidimensionalen Finite Elemente Modell (FE, Software Abaqus) verwendet. Das Modell besteht aus einer 4cm starken Deckschicht, 9cm Binderschicht, 9cm Tragschicht auf ungebundener Fundationsschicht und Untergrund. Der Asphaltbeton wurde mit Hilfe eines linearen viskoelastischen Modells modelliert und der Untergrund wurde als lineares elastisches Material eingeführt. Zwischen der Tragschicht und dem Untergrund wurde ein Interface mit Reibung implementiert.

Es konnte gezeigt werden, dass die mit dem ETH Delta Gerät gemessene Setzungsmulde hauptsächlich durch die Steifigkeitsparameter des Untergrunds beeinflusst wird und wenig empfindlich auf die Änderung der Parameter der Asphaltschichten reagiert. Nur die Setzungen in unmittelbarer Nähe des Reifens, wo das Gerät aber nicht misst, werden durch das viskose Verhalten des Asphaltbetons bestimmt. Für die Rückrechnung der Eigenschaften des Untergrunds war die Asphaltbetonsteifigkeit mit Hilfe der faseroptischen Dehnungsmessungen bestimmt worden. Auf diese Weise konnte eine gute Übereinstimmung zwischen Messungen und Modellergebnissen erhalten werden, und die Parameter des Untergrunds konnten bestimmt werden. Abweichungen wurden im unter Kontraktion stehenden Bereich bemerkt, möglicherweise aufgrund der spannungsabhängigen Steifigkeit des Asphaltbetons, deren Einfluss in dieser Analyse vernachlässigt wurde.

FE-Modelle

Für die Modellierung der Feldversuche in der Hohlstrasse Zürich wurden zwei FE-Modelle verwendet. Das erste ist ein einfaches axialsymmetrisches Modell, mit welchem

der Einfluss verschiedener Modellparameter auf effiziente Weise untersucht werden konnte. Der Hauptvorteil des axialsymmetrischen Modells besteht darin, dass es aus einer viel geringeren Anzahl von Elementen besteht und damit die Verwendung eines feineren Netzes bei weitaus geringerem Rechenaufwand ermöglicht. Mit Hilfe dieser vorläufigen Sensitivitätsanalyse konnten die Wahl des geeigneten Materialmodells, die Kalibrierung der Materialparameter sowie die angemessene Modellierung der Kontaktspannung deutlich beschleunigt werden. Das zweite FE-Modell ist ein dreidimensionales Modell mit einer Symmetrieebene, welches eine realistischere Modellierung der stehenden und bewegenden Verkehrslast, Einzel- und Doppelreifen sowie ihrer gegenseitigen Beeinflussung ermöglicht.

Die Abmessungen der Kontaktfläche der Reifen auf der Fahrbahn wurden zuerst im Feld gemessen und danach, zusammen mit der bekannten Achslast, ins Modell eingeführt. Die Kontaktspannung auf der Fahrbahn wurde daher mit Hilfe dieser beiden Parameter und unter der Annahme einer konstanten und einer konvexen Spannungsverteilung bestimmt. Über konvexe Kontaktspannungsverteilungen für Reifen mit hohem Innendruck bei zeitglich niedrigen Achslasten, wie dies bei den in den Feldversuchen eingesetzten Lastwagen der Fall war, wird auch in der Literatur berichtet. Die Belastungsabfolge für die statischen Testreihen wurden mit einem geostatischen Phase modelliert, gefolgt von einer 15s langen Belastungs- und einer 15s langen Entlastungsphase, um die durchschnittliche Zeit für eine Messung zu berücksichtigen.

Die sich bewegende Last wurde mit Hilfe eines Unterprogramms in Abaqus modelliert. Obwohl dieses vereinfachte Verfahren keine vollständige dynamische Analyse darstellt, konnte das viskose Verhalten des Asphaltbelags unter der Belastung eines Lastwagens (fünf Achsen), welcher sich mit unterschiedlichen Geschwindigkeiten bewegt, ziemlich gut angenähert werden. Die unterschiedlichen Geschwindigkeiten wurden berücksichtigt, indem die Position des Lastwagens mit jedem Zeitschritt geändert wurde. Sowohl die gewählten Zeitschritte als auch das viskoelastische Materialmodell für den Asphaltbeton wurden optimiert, damit eine ausreichende Genauigkeit erzielt wird.

Materialmodelle

Materialmodelle zum Verhalten von Asphaltbeton wurden in der Literatur umfassend untersucht. Viskoelastizität bei niedrigen Temperaturen und Viskoplastizität bei hohen Temperaturen, konstitutive Modelle unter Berücksichtigung von Ermüdung, Viskoelastizität und chemischer Heilung, Spannungsgeschichte und Geschwindigkeitsabhängigkeit werden in der Literatur beschrieben. In der vorliegenden Analyse wurde der Asphaltbeton einfacher modelliert, die Modellierung der Viskoelastizität kam unter Verwendung der in Abaqus eingebetteten Prony series-Erweiterung zustande. Die Prony series-Koeffizienten, welche die zeitliche Abhängigkeit der Steifigkeit bestimmen, wurden für alle Testreihen einzeln definiert, während der Langzeit-Steifigkeitsmodul und die Poissonzahl mit der Temperatur variiert wurden. Weder die Schädigung noch das viskoplastische Verhalten wurde modelliert, aber die Eigenschaften des Asphalts wurden in Anlehnung an die Proben aus den Kernbohrungen gewählt.

Der Untergrund wurde als linear elastisches Material mit den Parametern aus der Messung der Setzungsmulde modelliert. Die spannungsabhängige Steifigkeit des Untergrundes wurde teilweise ebenfalls angewendet. Darüber hinaus wurde das irreversible Verhalten des Untergrundes mit Plastizitätsmodellen nach Drucker-Prager und nicht-assoziiertem Fliessgesetz untersucht.

Kalibrierung

Für die Kalibrierung des konstitutiven Modells der Asphaltschichten wurden die Ergebnisse des speziellen Feldversuches verwendet, welcher während einer der Nacht auf einem gesperrten Fahrstreifen durchgeführt wurde (mit Betonblöcke als Belastung). Während diesen Versuchen wurde die Entwicklung der Dehnungen über die Zeit unter einem Betonblock gemessen, dies für eine Belastungs- und Entlastungsdauer von mehreren Minuten. Somit wurde eine Kalibrierung der Prony-Serienkoeffizienten des

viskoelastischen Modells ermöglicht, allerdings für eine Belastungsdauer von mehr als 15s. Für eine kürzere Belastungsdauer (z.B. für die dynamischen Feldversuche) konnten aus diesen Versuchen allerdings keine Informationen gewonnen werden. Für spezifische Versuchsbedingungen (hohe Temperatur) konnten zudem nicht reversible Dehnungen im Versuch beobachtet werden, die durch das rein viskoelastische Modell nicht reproduziert werden konnten.

Vor dem Modellieren des Feldversuchs im dreidimensionalen Modell wurden die temperaturabhängigen Parameter für jede Testreihe am effizienten axialsymmetrischen Modell kalibriert. Bei kalten bis warmen Temperaturen (zwischen etwa 1°C und 25°C) ergaben sich unter der Berücksichtigung des viskoelastischen Materialverhaltens für den Asphalt in Kombination mit dem linearen elastischen Untergrund befriedigende Ergebnisse. Die Langzeitsteifigkeit des Asphalts stimmt bei jedem Versuch gut mit der zur Asphalttemperatur gehörenden Steifigkeit überein und der Steifigkeitsmodul des Untergrunds entspricht dem Wiederbelastungsmodul eines Untergrunds von guter Qualität. Bei einer Testreihe, durchgeführt bei sehr warmen Asphalttemperaturen (um 40°C), wurden jedoch Schwierigkeiten festgestellt, das gemessene Verhalten mit diesem relativ einfachen Modell abzubilden. Die Einführung von spannungsabhängiger Asphaltbetonsteifigkeit (insbesondere Steifigkeitsreduktion unter Zugspannungen) könnte die Ergebnisse möglicherweise verbessern.

Simulation der statischen Versuche

Die statischen Feldversuche wurden unter Verwendung obig beschriebener Kalibration am dreidimensionalen FE-Modell simuliert. Die senkrecht zur Fahrtrichtung gemessene Dehnungsverteilung wurde mit den Resultaten des FE-Modells in der Tiefe von 4cm und 22cm sowie für Einzel- und Doppelreifen vergleichen, dies am Ende der Belastungs- und Entlastungsdauer. An der Unterseite der Asphaltschichten (22cm Tiefe), konnten die Ergebnisse des Feldversuches mit der numerischen Simulation nahezu zur vollständigen Übereinstimmung gebracht werden. Die Abbildung der gemessenen Dehnungsverteilung auf der Binderschicht (4cm Tiefe) mit dem FE-Modell erwies sich als schwieriger, was möglicherweise auf kleine Mängel im Asphaltbeton, höhere Temperaturschwankungen oder auf eine imperfekte Modellierung des Kontaktdrucks zurückzuführen ist. Letzteres kann, so nahe an der Lastangriffsfläche, die Resultate lokal sicherlich auch beeinflussen.

Im Allgemeinen konnten die Ergebnisse des Feldversuches recht gut mittels numerischer Simulation abgebildet werden und ähnliche Beobachtungen, wie im Feld festgestellt, konnten auch bei der Simulation gemacht werden. Beim Versuch, die Dehnungsverteilung bei hohen Temperaturen zu simulieren, traten jedoch Schwierigkeiten auf, welche bereits bei der Anwendung des axialsymmetrischen Modells festgestellt werden konnten. Die Grösse der Dehnung am Ende der Entlastungsphase wurde durch das FE-Modell durchwegs unterschätzt, da der Asphalt als rein viskoelastisches Material modelliert wurde, welches keine irreversiblen Dehnung des Asphaltbetons reproduzieren kann. Kleinere Abweichungen der Simulation von der Messungen können ihren Ursprung aber auch in kleinen Abweichungen der Länge der Belastungsphase der unterschiedlichen Versuche haben, im Gegensatz zu der immer exakt gleich langen Belastungs- und Entlastungphase im Modell. Aufgrund der Wechselwirkung zwischen benachbarten Reifen wurden, insbesondere bei kalten Temperaturen und Doppelreifen, asymmetrische Dehnungsverteilungen im Feld gemessen, welche mit dem FE-Modell ebenfalls abgebildet werden konnten.

Simulation der dynamischen Versuche

Mit Hilfe des dreidimensionalen Modells und der für jeden Test gewählten Materialparametern wurden die durch die Überfahrt des Fahrzeugs induzierten, sich bewegenden Lasten, numerisch simuliert. Schnappschüsse der räumlichen Dehnungsverteilung in einer Tiefe von 4cm zeigen aufgrund der Lastwagenbelastung nicht einen sofortigen Abfall der Dehnungen, sondern einen zeitlich verzögerten, welcher als Resultat dazu führt, dass sich die Dehnungen unter den nachfolgende Achsen akkumulieren. Die Umhüllende der Dehnungsentwicklung mit der Zeit zeigt ein ähnliches Muster für die FE-Simulation und den Feldversuch. Die zeitliche Abfolge der Pulse von

kontraktiven und expansiven Dehnungen führt zu einer schrittweisen Erhöhung der Dehnungen, insbesondere bei niedrigen Geschwindigkeiten. Gemäss dem FE-Modell treten die maximalen expansiven und kontraktiven Dehnungen immer unter der dritten und der fünften Achse auf, bedingt durch das Gewicht der Achsen und die Kumulierung von Dehnungen aufgrund der viskoelastischen Natur von Asphaltbeton. Die verbleibende Dehnung nach der Überfahrt der letzten Achse, wie sie im Versuch gemessen wurde, kann jedoch nicht abgebildet werden, da der Asphaltbeton nur als viskoelastisches Material modelliert wurde. Die Dehnungsgrössen aufgrund der sich bewegenden Lasten sind erwartungsgemäss niedriger als diejenigen aufgrund der statischen Belastung. Je höher die Geschwindigkeit ist, desto kleiner sind die Dehnungen für die gleichen Temperaturbedingungen.

Numerische Modellierung der Feldversuche am Flughafen Zürich

Für die Simulation der Feldversuche am Flughafen Zürich wurde ein dreidimensionales FE-Modell mit zwei Symmetrieebenen verwendet. Der Strassenaufbau wurde mit den folgenden Schichten modelliert: 4cm Deckschicht, 9.5cm Asphalttragschicht und eine Schicht von 53cm hydraulische gebundenem Gemisch auf dem Untergrund. Eine vereinfachte Analyse mit linear elastischen Materialien (sowohl für den Asphalt als auch für den Untergrund) wurde durchgeführt. Die Kontaktspannung zwischen dem Reifen und dem Untergrund wurde als konstant modelliert. Das Model war in der Lage, die Dehnungsverteilung an der Unterseite der Asphalttragschicht zu reproduzieren. Bei dem Versuch, die Messungen in 4cm Tiefe mit diesem stark vereinfachten Modell abzubilden, sind aber grössere Schwierigkeiten aufgetreten.

Diskussion und Schlussfolgerungen

Verteilt messende faseroptische Sensoren ermöglichen eine kontinuierliche Dehnungsmessung entlang einer optischen Faser mit hoher Ortsauflösung und, abhängig von der verwendeten Messtechnik und Sensorlänge, mit Aufzeichnungsraten von bis zu 100Hz. Im vorliegenden Projekt haben sie sich als leistungsfähiges Werkzeug erwiesen, um das Verhalten des Asphaltbelags in Strassen, unter statischen und dynamischen Belastungen des Verkehrs, zu charakterisieren.

Die verwendeten Glasfaserkabel waren ausreichend robust, um auf realen Strassenbaustellen in Verbindung mit den untersuchten Installationsverfahren eingesetzt zu werden. Die zeitweise hohe thermische Belastung der Kabel während des Strassenbaus zeigte, für den vorliegenden Zweck, keine wesentliche nachteilige Auswirkung. Die beobachtete räumlich heterogene Reaktion der Kabel während der thermischen Einwirkung kann jedoch, bei anderen Anwendungen als der hier gezeigten, zu Schwierigkeiten führen. Die in Asphalt eingebetteten faseroptischen Sensoren waren während der gesamten Projektdauer funktionsfähig. Beschädigungen der Sensoren traten nur innerhalb des Zugriffsschachtes aufgrund einer nicht idealen Kabelführung auf, die durch einfache Massnahmen in möglichen weiteren Projekten behoben werden kann.

Dehnungen konnten im Strassenbelag unter verschiedenen statischen und dynamischen Verkehrslasten, resultierend von verschiedenen Testfahrzeugen, kontinuierlich gemessen werden. Dies gab interessante Einblicke in das viskose und temperaturabhängige Verhalten von Asphaltbeton in verschiedenen Jahreszeiten während der Lebensdauer von realen Strassenbauten. Darüber hinaus konnten durch verteilte Dehnungsmessungen bei hohen Aufzeichnungsraten Fahrtrichtung, Position und Geschwindigkeit sowie die Anzahl der Achsen und Reifen des über den Sensor fahrenden Fahrzeugs detektiert werden. Eine verlässliche Schätzung der Achslast würde jedoch eine weiter gehende Betrachtung von Parametern der unmittelbaren Umgebung und zusätzlichen Anstrengungen bei der numerischen Simulation erfordern.

Die Ergänzung der Messungen im Strassenbelag mit numerischer Modellierung und mit Materialparametern von Kernbohrungen erlaubte eine detaillierte Simulation der Feldversuche und somit ein verbessertes Verständnis des Verhaltens von Fahrbahnen unter Verkehrslasten. Es konnte gezeigt werden, dass die statischen und dynamischen Testergebnisse unter kalten und warmen Bedingungen mit einfachen viskoelastischen Modellen in groben Zügen abgebildet werden können. Um eine verbesserte Abbildung zu

erreichen und auch die unter sehr warmen Bedingungen gemessenen Ergebnisse zu studieren, sind weitere Anstrengungen zur Modellierung des konstitutiven Verhaltens von Asphalt erforderlich, wobei Modelle verwendet werden sollten, die z. B. Plastizität, spannungsabhängige Steifigkeit und weitere Auswirkungen umfassen.

Als Thema für weitere Untersuchungen zur numerischen Modellierung der Feldversuche wird vorgeschlagen, dass für Asphaltbeton ein Materialmodell implementiert wird, welches nicht-reversibles Verhalten und spannungsabhängige Steifigkeit betrachtet. In Bezug auf die geeignete Wahl des Sensorkabels wird vorgeschlagen, das Verhalten der verschiedenen Kabel in ähnlichen Bedingungen aufgrund ihrer gemessenen Dehnungsverteilung zu vergleichen. Es kann möglich sein, dass die robusten Kabelversionen, die aus vielen Mantelschichten bestehen, dem Dehnungsfeld im Asphalt nicht so genau zu folgen vermögen wie Kabel mit geringerem Schutzniveau. Schliesslich könnte die langfristige Fortführung der Feldversuche in Kombination mit der Implementierung eines Schadensparameters im FE-Modell zu einer wegweisenden zerstörungsfreien Bewertungsmethode für Asphaltbetonbeläge führen.

Résumé

Ce projet de recherche avait pour but d'investiguer le potentiel des capteurs en fibre optique insérés dans des couches de revêtement bitumineux afin de caractériser le comportement des routes sous l'effet des charges du trafic. Dans ce but, différentes versions de robustes câbles de fibre optique ont été testées, d'abord en laboratoire, pour savoir s'ils étaient adéquats pour le rude environnement des revêtements bitumineux. Dans un deuxième temps, différentes procédures d'insertion des câbles de fibre optique dans un revêtement bitumineux ont été testées sur deux sites de test. Après l'implémentation de capteurs de fibre optique couronnée de succès dans les deux sites d'essai, les mesures avec ces capteurs ont été poursuivies pendant plus de 2.5 années. La grande quantité de données de mesures des tensions, sans précédents, qui peut être récoltée avec ce type de capteurs, a été utilisée pour comparer les résultats des mesures avec la modélisation numérique des revêtements testés. L'application des capteurs en fibre optique distribués a, avec la modélisation numérique, un potentiel élevé pour l'investigation du comportement de nouveaux matériaux de revêtement des routes ou pour la validation de nouvelles méthodes de dimensionnement, puisqu'elle permet de quantifier le champ des tensions présent dans le revêtement sous une charge de trafic soit statique que dynamique. De plus, des mesures de tension distribuées peuvent aussi être utilisées éventuellement dans le futur comme outil additionnel pour l'évaluation de la santé structurale des routes

Structure du rapport

La structure de ce rapport suit simplement les différentes tâches des recherches entreprises dans ce projet. Après une brève introduction sur le sujet étudié dans le chapitre 1, dans le chapitre 2 sont présentées les différentes technologies de capteurs en fibres optiques distribués et les outils utilisés dans ce projet de recherché. Dans le chapitre 3 sont résumés les résultats des essais en laboratoire avec les fibres optiques, alors que les différentes méthodes d'installation des capteurs en fibre optique distribués sont présentées et évalués dans le chapitre 4. Dans les chapitre 5 et 6 sont décrits les résultats des mesures obtenues sur les deux champs d'essai avec les capteurs en fibre optique, une route urbaine à Zurich et une place de parc pour avion à l'aéroport de Zurich. Les résultats de la modélisation numérique de ces champs d'essai sont reportés dans les chapitres de 7 à 9. Enfin, le chapitre 10 termine le rapport avec les conclusions et les recommandations. Des informations supplémentaires concernant les champs de tension et de déformation calculés sont présentées en annexe.

Aperçu de la recherche

Concernant la structure du projet de recherche, trois tâches principales peuvent être identifiées: Les essais en laboratoire sur les câbles et leur introduction dans le revêtement bitumineux in situ, les résultats des mesures effectuées dans les deux sites test "Hohlstrasse" et "Zurich Airport" en utilisant ces classes de nouveaux capteurs, et enfin la modélisation numérique de ces essais test en utilisant des modèles à éléments finis. Un bref aperçu des principaux résultats dans ces trois domaines est présenté dans les paragraphes suivants, tout de suite après une brève description de la technique de mesure par fibre optique distribuée utilisée.

Techniques de mesure par fibre optique distribuée utilisées

Les capteurs de fibre optique distribués permettent la mesure en continu de grandeurs telles que déformation ou température le long d'un câble de fibre optique par la transmission de lumière à travers une fibre de silice type en mode singulier. En opposition à des techniques de mesure par fibre optique plutôt discontinues comme p. ex. un réseau de Bragg (FBG), les techniques de mesure distribuées ne sont pas seulement sensibles à ces grandeurs à mesurer externes dans une position fixe prédéfinie où se trouve le réseau, mais utilisent la longueur totale de la fibre comme élément de mesure. Par conséquent, en combinaison avec une haute résolution spatiale

des grandeurs à mesurer, un outil puissant pour l'analyse et le contrôle des structures peut être formé qui permet le recueil d'une quantité unique de données à l'intérieur de la structure instrumentée. A présent, divers types de techniques de mesure par fibre optique distribuée sont disponible dans le commerce. Dans ce projet, des techniques basées sur des phénomènes de diffusion dans les fibres de silice selon Rayleigh et Brillouin ont été utilisées.

Les résultats des essais au laboratoire et les méthodes de mise en place des essais in situ

L'asphalte représente un environnement rude pour des capteurs dont le principe de mesure est basé sur les propriétés intrinsèques de vulnérables fibres minces de silice. Néanmoins, les différentes fibres optiques utilisées dans ce projet de recherche, fabriquées par le partenaire de la recherche Brugg Kabel AG (maintenant Solifos AG), ont été conçues pour résister dans ce rude environnement. Cependant, quelques éclaircissements supplémentaires ont été nécessaires sur l'effet de la haute température pendant la construction des routes et sur les tensions transversales élevées agissant sur les câbles près de la surface pendant la construction et l'utilisation finale de la route. Ces inquiétudes ont été investiguées dans ce projet par le biais d'essais en laboratoire.

Même s'il est possible de vérifier l'aptitude du câble choisi pour l'utilisation dans des revêtements routiers par des essais en laboratoire, des méthodes d'essais in situ doivent être définies qui puissent garantir que le processus d'intégration n'engendre aucun conflit avec le processus de construction routière et que les câbles peut être intégré dans une disposition prédéfinie dans les différentes couches. L'adéquation de telles méthodes de mise en place in situ a été testée pendant la planification et l'implémentation des deux champs d'essais instrumentés "Hohlstrasse" et "Zurich Airport".

Essais en laboratoire

Température

Des couches minces d'asphaltes devraient avoir des températures minimums autour de 120-150°C avant le compactage par rouleaux. Pour les câbles de mesure spécifiques de fibre optique utilisés dans ce projet, malheureusement il n'y avait pas d'indications d'usage préalable pour cette fourchette de températures. Quant à la propriété la plus importante de ce capteur, la conversion du décalage de fréquence mesuré à déformation, il y avait un souci que la température temporairement élevée pourrait modifier les propriétés du câble. Pour pouvoir investiguer le comportement des câbles à de telles températures, le plan d'essai suivant a été adopté

- Mesurer la réponse en déformation, d'une section de câble définie, à une élongation externe dans un banc d'essai de déformation
- Exposer cette section de câble temporairement aux températures autour de 140°C pendant les mesures
- Mesurer de nouveau la réponse en déformation d'une section de câble définie à une élongation externe dans un banc d'essai de déformation

En comparant le comportement du câble dans le banc d'essai de déformation avant et après l'échauffement, on pourrait conclure qu'aucun effet significatif négatif de la température dans la fourchette pertinente pour la construction routière en asphalte a été observé. Comme prévu, la gaine plastique du câble a induit une réponse non linéaire sur la section du câble libre pendant l'exposition à la température. Cependant pour cette application ça ne représente aucun inconvénient. En outre, pour quelques types de câbles, une réponse très hétérogène à la température appliquée a été observée pendant l'échauffement du câble. Cette hétérogénéité pourrait créer des difficultés supplémentaires dans des applications hors de la portée de cette étude, p. es. lors d'un besoin de compensation des effets thermaux sur le décalage de fréquence, et requiert plus d'études.

Pression transversale

Tandis que de hautes températures sont atteintes dans les couches d'asphaltes seulement pendant la construction routière, des pressions transversales importantes sont présentes pendant la construction routière aussi bien que pendant le temps de fonctionnement du capteur dans les couches d'asphaltes près de la surface en cas de fort trafic. Puisque les capteurs de fibre optique distribués sont sensibles à la déformation, à la température ainsi que légèrement à la pression hydrostatique, la réponse des types de câbles utilisés a été testée simplement dans une chambre de pression par l'application de pressions hydrostatiques jusqu'à 1MPa. La sensibilité à la pression hydrostatique dans la fourchette pertinente pour ce projet a été plutôt petite. Pour cette raison il a été décidé de négliger la contribution de la pression hydrostatique dans ce projet.

Les méthodes de mise en place des essais in situ

Bien que les câbles utilisés aient été projetés pour un environnement plutôt rude, la mise en place des câbles et la construction routière mènent à des difficultés supplémentaires concernant des dégâts possibles aux câbles. Deux approches principales ont été adoptées concernant la mise en place des câbles in situ sur une surface par des méthodes de fixation diverses y compris un recouvrement du capteur avec une petite quantité de matériau bitumineux fin posé à la main et la mise en place dans des entailles remplies par la suite par une pâte à joint.

L'évaluation des différentes procédures de mise en place des câbles de fibre optique a montré que les versions des câbles utilisées fournissent une robustesse mécanique suffisante pour le but prévu. Même la version de câble la plus vulnérable a survécu à la mise en place sans dégâts et s'est bien comportée par la suite pendant tout le projet de recherche. En général, le fait de couvrir les câbles des capteurs par une fine couche de matériau bitumineux avant le passage sur le capteur par le rouleau ou de placer les câbles dans des entailles crées avec une barre d'armature pendant le compactage de l'asphalte chaud, s'est avéré très positif.

Résultats des mesures sur les sites test

Deux différents sites d'essai ont été instrumentés avec les capteurs de fibre optique répartis: une route urbaine à Zurich ("Hohlstrasse") et une place de parc pour avions à l'aéroport de Zurich. Sur les deux sites ont été insérés des capteurs de fibre optique répartis à différents niveaux dans le revêtement bitumineux et les réponses du revêtement ont été mesurées pendant le chargement avec différents types de véhicules ou d'avions. Ces tests ont été répétés sur les deux sites en différentes saisons de façon à comprendre le comportement du revêtement à différentes températures. La mesure des tensions dans le revêtement a montré une grande variabilité avec des gradients élevés dans l'espace, en particuliers à de faibles profondeurs près de la surface. Cette rapide variation du champs des tensions dans le revêtement s'est révélée comme une forte argumentation pour ce type de capteurs puisque les tensions peuvent être mesurées en continu avec une résolution spatiale le long du câble, chose possible uniquement pour des points de mesure isolés en utilisant des câbles classiques. Plus de $1500\mu\varepsilon$ ont été mesurés directement sous une roue, à 4cm de profondeur, pendant l'été, alors que la tension maximale à l'aéroport était de deux fois cette ampleur, malgré le test ait été effectué au début de l'automne et non pendant l'été. Comme attendu, une forte dépendance de l'amplitude des tensions a été observée par rapport à la température du revêtement. Cependant, non seulement l'amplitude mais aussi la forme de la distribution des tensions varie avec les saisons.

Site test Hohlstrasse

Champs d'essai et installation

Le site test "Hohlstrasse" à Zurich représente une route urbaine soumise à un grand volume de trafic y compris une ligne de bus. Le revêtement de la Hohlstrasse comporte trois couches d'asphalte, pour une épaisseur totale de 22cm, au-dessus d'une grave non traitée pour la construction routière. Des câbles de fibre optique avec le but de mesurer des déformations ont été intégrés au fond des couches d'asphalte à une profondeur de

22cm ainsi qu'à la surface de la couche de liaison à une profondeur de 4 cm. Les câbles ont été installés en boucles courtes d'approximativement 10m di longueur avec des lignes parallèles transversales ou longitudinales par rapport à la direction du trafic. Une boucle de longueur d'environ 70m a été installée en forme de réseau avec un espacement de la grille de 0.5m. Les bouts des câbles étaient accessibles pour la connexion à l'appareil de mesure par le biais de petits puits dans le trottoir adjacent. L'installation a fonctionné parfaitement pendant la durée entière du projet. Seuls quelques dommages mineurs ont été observés à l'emplacement où le câble du capteur entre dans le puits d'accès.

Les capteurs de fibre optique distribués ont été utilisés dans le cadre de ce projet pour quantifier la distribution de la déformation dans la chaussée sous des charges statiques de court-terme ainsi que sous des charges du trafic en mouvement. Pour appliquer cette charge à la chaussée, un camion et une voiture ont été utilisés comme véhicules test. Tandis que la voiture a apporté une charge d'essieu d'un peu plus de 12kN à la surface de la chaussée, l'essieu devant du camion (pneu simple) a appliqué approximativement 50kN et l'essieu derrière (pneu double) a appliqué à peu près 100kN à la chaussée. De tels essais, avec la mesure des déformations sous des charges différentes d'essieux et pour des vitesses diverses du véhicule test, ont été effectués dans des différentes saisons afin d'étudier l'effet de la température sur la distribution de la déformation à l'intérieur de la chaussée. Ces essais ont eu lieu pendant la journée avec un flux de circulation usuel mais pas de pointe. Par conséquent, il n'a pas été possible d'appliquer la charge statique pendant plus que quelques secondes pour ne pas trop déranger la circulation. Pour pouvoir appliquer des charges pendant des durées plus longues, p. es. quelques minutes, une voie de la route a été fermée au trafic pendant la nuit et des mesures de déformations ont été effectuées avec les charges statiques ainsi que des mesures additionnelles concernant la déflexion de la chaussée.

Puisque la température influence fortement la raideur des couches d'asphalte, les températures pendant les essais ont été mesurés périodiquement. Les températures ont été mesurées à la surface de la chaussée et à trois profondeurs supplémentaires par des thermomètres à aiguille et des éléments Pt100. Pour permettre une simulation numérique des essais avec des paramètres de raideur réalistes, plusieurs forages ont été effectués sur ce site test. Les échantillons prélevés de ces carottes ont été analysés à l'EMPA.

Les mesures initiales de déformation ont indiqué une haute variabilité spatiale des déformations à l'intérieur de la chaussée, surtout autour de la position du pneu. Pour pouvoir résoudre correctement la distribution des déformations présente dans la chaussée, des mesures ont été effectuées en utilisant principalement les dispositifs basés sur la rétrodiffusion de Rayleigh. Les dispositifs utilisant cette technologie et disponibles dans le cadre de ce projet de recherche ont permis une résolution spatiale des déformations le long du câble du capteur nettement plus fine que les dispositifs de mesure basés sur Brillouin disponibles pour ce projet. Dans le cadre du présent projet, une déformation moyenne a généralement été calculée sur une distance spatiale de 10mm et exportée tous les 5mm le long de la fibre.

Résultats des mesures

Les mesures de déformation sur le site test de Hohlstrasse ont été souvent conduit d'une manière semblable de façon à permettre une comparaison entre les différents séries d'essais qui ont été effectuées à des températures différentes. Entre la mise en place en novembre 2015 et mars 2018, plus ou moins 10 séries d'essais ont été conduits. Ils n'étaient pas tous identiques, mais en général des mesures de déformation à la surface de la couche de liaison ont été effectuées en utilisant les essieux devant et derrière du camion pour la charge statique à court-terme. De temps en temps, ces mesures ont été complétées avec des mesures provenant du capteur mis en place au fond des couches d'asphalte ou en utilisant la voiture pour pouvoir appliquer des charges plus petites à la chaussée. La mesure de référence, utilisée pour calculer le changement de déformation sous charge, a été en général prise seulement quelque secondes avant l'application de la charge. Une fois que la mesure sous charge était finie (souvent autour de 10sec à 15sec après l'application de la charge), une troisième mesure était effectuée immédiatement

après que la charge ait été enlevée de la chaussée. La troisième mesure a été effectuée pour pouvoir saisir la réponse de déformation différée dûe au comportement visqueux de l'asphalte. En général, de telles mesures statiques étaient accompagnées de mesures dynamiques, avec les véhicules test qui passaient sur le capteur à des vitesses différentes pendant que les déformations ont été indiquées du capteur à un taux d'acquisition élevé.

Comme prévu, l'effet d'une diminution de raideur de l'asphalte avec une augmentation de la température a aussi été observé dans les distributions de déformation mesurées. Le rapport global de la grandeur de la déformation maximale mesurée dans une série d'essais d'un jour chaud d'été, d'un coté, et d'un jour froid d'hiver, de l'autre, était autour de 50 et ceci malgré que la mesure hivernale ait été effectuée pendant la journée, et non pendant une nuit froide hivernale. Par conséquent, le vrai rapport entre les déformations extrêmes présentes dans la chaussée sous la même charge axiale est probablement encore plus élevé que celui enregistré.

La chaussée directement au-dessous du pneu qui a subi un chargement statique de courte durée a montré des déformations expansives à une profondeur de 4 cm aussi bien qu'à 22cm. Cependant, en particulier pendant les journées chaudes estives, l'ampleur de la déformation mesurée dans le câble du capteur supérieur était sensiblement plus grande que la déformation en dessous et a atteint des valeurs jusqu'à environ $1500\mu\varepsilon$. Tandis que la déformation dans la couche supérieur a changé de signe pour devenir une déformation contractive juste à côté du pneu, au fond de la couche d'asphalte le changement de signe s'est avéré plus loin. Quand la chaussée a été chargée par un seul pneu, un seul pic de déformation expansive a été observé dans les mesures tandis que deux pics de déformation expansive se sont montrés quand un pneu double chargeait l'asphalte. Curieusement, ces deux pics étaient aussi clairement visibles au fond des couches d'asphalte à une profondeur de 22cm. En comparaison avec les résultats obtenus pendant les journées chaudes estives, où le pic de déformation expansive régissaient la distribution de la déformation, ce pic de déformation était beaucoup moins marqué dans les mesures effectuées pendant les journées froides hivernales par rapport aux déformations contractives adjacentes.

En plus de ces essais, dans lesquels les déformations ont été mesurées sous des véhicules test soit par chargement statique de courte durée soit en mouvement, des essais supplémentaires ont été effectués pour une série particulière pendant une nuit d'été. Pendant cette nuit, les autorités ont permis la fermeture au trafic d'une voie pendant plusieurs heures et par conséquent la chaussée a pu être soumise aux charges statiques pendant plusieurs minutes dans la zone instrumentée. Ceci a permis l'étude du comportement visqueux des couches d'asphalte pour ce site spécifique. En plus des mesures de déformation, des mesures de tassement à la surface de la chaussée ont été effectuées avec un appareil dénommé "ETH Delta" pour obtenir des mesures additionnelles indépendantes en plus des déformations à l'intérieur des couches d'asphaltes.

En plus du comportement de la chaussée mesuré sous chargement statique de courte durée, comme discuté ci-dessus, les déformations ont aussi été mesurées en continu et avec une résolution élevée le long du câble avec des vitesses d'acquisition de 100Hz. Des véhicules test différents ont passés au-dessus du capteur intégré à des vitesses comprises entre 5km/h et 50km/h afin de pouvoir étudier l'effet d'un chargement dynamique dû au trafic sur la chaussée. Comme prévu, à cause des propriétés visqueuses de l'asphalte, l'ordre de grandeur global de la déformation a diminué avec une augmentation de la vitesse du véhicule. L'effet de la réduction disproportionnée du pic expansif de déformation dans les régimes de basses températures a été intensifié en combinaison avec des vitesses élevées des véhicules. Cette circonstance a mené à la situation, dans les conditions froides et à vitesse élevée, qu'aucun pic expansif de déformation a été mesuré dans la couche d'asphalte à une profondeur de 4cm et la déformation est aussi restée contractive directement sous le pneu. En outre de l'aperçu détaillé du comportement de la chaussée sous charge dynamique de trafic, les résultats du capteur installé ont permis de déterminer la direction du mouvement et la position ainsi que la vitesse du véhicule et le nombre d'essieux et de pneus. Les limites actuelles

de l'installation testée se sont avérées d'être la détection de charges dynamiques qui proviennent des véhicules légers comme des voitures à vitesse élevée dans les conditions froides hivernales. Les déformations sont devenues très petites dans ces conditions et il était difficile de différencier le changement de déformation mesuré du niveau du bruit sans appliquer plus de techniques traitements des données. Cependant il faudrait mentionner que ces mesures ont été effectuées dans une chaussée projetée pour des conditions de fort trafic et que les couches d'asphalte avaient une épaisseur totale de 22cm, menant à de petites déformations dans les conditions discutées ci-dessus. Avec l'application de mesures supplémentaires, la situation pourrait être améliorée dans ces conditions, si nécessaire.

Site test Zurich Airport
Champs d'essai et installation

Contrairement au site test de Hohlstrasse qui est sujet principalement à des charges de trafic dynamiques qui provoquent un grand nombre de cycles de charge, le site test à l'aéroport de Zurich représente un stand d'avions, caractérisé par un petit nombre de cycles de charge mais de longes périodes d'application de la charge. Néanmoins ce site test a aussi été construit en asphalte, non pas en béton, à cause de l'utilisation temporaire prévue de ce stand d'avions. Le dimensionnement prévoit une première couche d'asphalte de 4cm puis une seconde couche de 9.5cm sur un mélange traité au liant hydraulique de 53cm d'épaisseur totale.

La disposition de l'installation du capteur de fibre optique était plutôt large dans le sens que les boucles de câbles utilisées à l'aéroport avait une longueur un peu supérieur à 140m. La disposition prévoyait deux sections parallèles de câble de presque 30m de longueur avec un espacement de 6m. La longueur supplémentaire a été utilisée en fait pour diriger les bouts du câble vers le prochain puits de conduite électrique, pour garantir l'accès aux câbles des capteurs à l'appareil de mesure. Comme sur le site test Hohlstrasse, différents câbles de fibre optique ont été aussi intégrés à une profondeur de 4cm et au fond des couches d'asphalte, dans ce cas à une profondeur de 13.5cm. L'intégration du capteur de fibre optique a eu lieu en juillet 2015 pendant la construction des stands d'avions.

Des difficultés inattendues se sont produites lors des premières mesures à cause de la longueur excessive des boucles de capteurs. Malgré celà, une fois que les difficultés ont été surmontées par le biais d'un plan modifié de mesures, l'installation a fonctionnée à la perfection pendant toute la durée du projet de recherche.

Résultats de mesure

Les mesures par les capteurs de fibre optique intégrés dans le stand d'avions ont été effectuées pendant une journée froide d'hiver et deux journées tempérées d'automne avec des avions type A330-300 et A340-300. Les mesures statiques ont été effectuées après le déplacement de l'avion par un tracteur d'aérodrome dans la position prédéfinie. Les mesures de fibre optique distribuées ont été collectées dans approximativement 5 à 6 positions d'avions différentes par rapport à l'emplacement du capteur.

Malgré l'épaisseur totale réduite des couches d'asphalte et en outre le fait qu'ils reposent sur un mélange traité au liant hydraulique, la dépendance de la déformation mesurée par rapport à la température était aussi dans le cas de ce projet très grande. Cette situation a produit des pics de déformation expansive mesurables d'à peu près $3000\mu\varepsilon$ directement en-dessous du pneu pendant la journée tempérée d'automne. Pendant la journée froide hivernale ces déformations sont restées contractives à une profondeur de 4cm et atteint seulement à une profondeur de 13.5cm une forme expansive. Même si les couches d'asphalte se trouvaient sur un mélange traité au liant hydraulique, la zone d'influence des avions semblait être plutôt petite et l'avion engendrait un champ de déformations plutôt étroit et localisé dans les couches d'asphalte.

Modélisation numérique des essais in situ

Motivation

L'intégration des capteurs de fibre optique distribués dans la chaussée a permis un aperçu détaillé du comportement structurel des couches d'asphalte sujettes à des charges de trafic. A première vue, la tendance générale des mesures de déformation confirme les attentes au moins qualitativement: des charges plus grandes produisent des déformations plus grandes, les déformations mesurées pour le même ordre de grandeur de charge augmentent en fonction de la température, les passages rapides des véhicules produisent des déformations plus petites que les passages lents. Cependant, il y avait aussi des effets mesurés qui sont plus difficiles à expliquer directement et en se limitant à une interprétation qualitative, pas quantitative. De plus, l'évaluation des déformations pour des conditions de température, de charge et de véhicule données seulement sur la base d'une modélisation numérique sans mesures réelles est une tâche difficile qui requiert de nombreuses hypothèses.

De l'autre coté, il y a une grande quantité de données de déformation recueillies avec des capteurs en fibre optique distribués pour de conditions aux limites diverses telles que température, ordre de grandeur de charge et vitesses des véhicules. Ces données peuvent aider dans le choix et la calibration des modèles constitutifs adéquats, conditions aux limites et techniques de modélisations basées sur ces données de mesure qui ne proviennent pas du laboratoire mais des conditions in situ réelles. Ceci pourrait devenir de plus en plus important si l'approche mécanistique prend de l'ampleur ou de nouveaux matériaux avec peu de connaissances empiriques sont utilisés dans le dimensionnement des chaussées. Pour cette raison, les tâches de recherche expérimentales discutées ci-dessus ont été complétées par une modélisation numérique des essais in situ pour approfondir les connaissances autour de la pertinence des modèles, les conditions aux limites et les techniques de modélisation.

Modélisation numérique des essais in situ à Hohlstrasse

Afin de limiter la fourchette possible de modèles, paramètres de matériaux et conditions aux limites qui pourraient reproduire les mesures convenablement, beaucoup de données de mesure indépendantes ont été rassemblées. Des échantillons des carottages ont été analysés dans les laboratoires d'EMPA afin d'obtenir grossièrement la fourchette des raideurs à des températures et des fréquences différentes. En outre, en plus des mesures de déformation distribuées, les températures ont aussi été mesurées et, dans un essai, des données de tassement sous charge ont été obtenues avec l'appareil ETH-Delta.

Modélisation de la cuvette de tassement en utilisant les essais ETH Delta

Les données de tassement spatial mesuré obtenues par l'appareil ETH-Delta ont été utilisées pour une analyse inverse préliminaire des paramètres du matériaux du sol de fondation avec un modèle trois dimensionnel par éléments finis avec le logiciel Abaqus. Le modèle comporte une couche de roulement de 4cm, une couche de liaison de 9cm, une couche de base d'asphalte de 9cm sur une couche de base granulaire puis le sol de fondation. L'asphalte a été modélisé en utilisant un modèle linéaire viscoélastique et le sol de fondation avec un matériau linéaire élastique. Une interface pour simuler le frottement a été placée entre la couche de base d'asphalte et le sol de fondation.

Il a pu été démontré que la cuvette de déflection mesurée par l'appareil ETH-Delta est principalement influencée par les paramètres de raideur du sol de fondation et elle est plutôt insensible aux paramètres des couches d'asphalte. Seulement le tassement, près du pneu où l'appareil ne mesure pas, est influencé par le comportement visqueux de l'asphalte. Pour le calcul inverse des propriétés du sol de fondation, la raideur de l'asphalte a été déterminée à l'aide des mesures de déformation fibre optique. En faisant cela, un bon accord entre les mesures et les résultats du modèle ont pu être obtenus et les paramètres du sol de fondation ont pu être déterminés. Des déviations ont été remarquées dans la région en contraction, peut-être à cause de la raideur de l'asphalte

qui dépend de la tension mais qui n'a pas été inclue dans cette analyse. Modèles par éléments finis

Deux modèles par éléments finis ont été utilisés pour la modélisation des essais à Hohlstrasse à Zurich. Le premier est un modèle simple, axisymétrique, qui a été utilisé pour étudier l'influence de différents paramètres sur le modèle d'une façon efficace. L'avantage principal du modèle axisymétrique est le nombre réduit d'éléments qui permet d'utiliser un réseau plus fin à un coût de calcul réduit. A l'aide de cette analyse préliminaire de sensibilité, le choix du matériau approprié et la calibration des paramètres du matériau ainsi que la modélisation appropriée de la pression de contact ont été sensiblement accélérée. Le deuxième modèle par éléments finis est un modèle trois dimensionnel avec un plan de symétrie, qui permet une modélisation plus réaliste du trafic stationnaire et en mouvement, des pneus simples et doubles aussi bien que leur interférence mutuelle.

La surface de contact des pneus avec la chaussée a été mesurée d'abord in situ et introduite dans le modèle par la suite avec la charge d'essieux connue. La pression de contact sur la chaussée modélisée a été donc déterminée à l'aide de ces deux paramètres et avec l'hypothèse d'une répartition de tension à la fois constante et convexe. Effectivement, la supposition d'une répartition de tension constante et convexe a été citée dans la littérature pour de hautes pressions de gonflages avec des charges basses d'essieux, comme pour des camions qui ont été utilisé dans les essais in situ. Les pas de chargement pour la série d'essais statiques ont été modélisés avec un pas géostatique suivi d'un chargement pendant 15sec et un long pas de décharge de 15sec, ainsi correspondant au temps moyen nécessaire pour effectuer une mesure.

La charge en mouvement a été modélisée à l'aide d'une sous-routine Abaqus. Bien que cette procédure simplifiée ne reflète pas une analyse complète dynamique, le comportement visqueux de la chaussée en asphalte sous la charge d'un camion (cinq essieux), avec des vitesses différentes, a pu être approximé assez bien. Les différentes vitesses ont été considérées par un changement de position du camion avec chaque incrément de temps. Tous les deux, les incréments de temps choisis ainsi que le modèle de matériau viscoélastique pour l'asphalte, ont été optimisés de façon à obtenir une précision suffisante.

Modèles de matériaux

Les modèles de matériaux qui décrivent le comportement de l'asphalte ont été rigoureusement étudiés dans la littérature. La viscoélasticité à basses températures et la viscoplasticité à températures élevées, les modèles constitutifs avec fatigue, la viscoélasticité et réparation chimique, l'histoire tensionnelle et le taux de dépendance peuvent tous être trouvés dans la littérature. Dans l'analyse présente, l'asphalte a été modélisé d'une façon moins sophistiquée, la viscoélasticité dépendante du temps a été modélisée en utilisant les séries d'expansion de Prony contenues dans Abaqus. Les coefficients de série Prony, qui déterminent la dépendance du temps de la raideur, ont été définis d'une façon individuellement pour toutes les séries d'essais, tandis que le module de raideur à long-terme et le coefficient de Poisson ont été variés avec la température. Aucun dégât ou comportement viscoplastique n'a été modélisé mais les propriétés de l'asphalte ont été choisies en fonction des échantillons des carottages.

Le sol de fondation a été modélisé par un matériau linéaire élastique avec les paramètres qui ressortaient des mesures de la cuvette de tassement. Une raideur dépendante de la tension dans le sol de fondation a aussi été appliquée partiellement. De plus, le comportement irréversible du sol de fondation a été étudié par des modèles de plasticité selon Drucker-Prager et une loi de flux non-associée.

Calibration

Pour la calibration du modèle constitutif des couches d'asphalte, les résultats de la série spéciale d'essais in situ qui a été effectuée pendant la nuit sur une voie fermée ont été utilisés (avec des blocs de béton pour le chargement). Pendant ces essais, le

développement des déformations dans le temps a été mesuré sous un bloc en béton pour un chargement et un déchargement d'une durée de quelques minutes. Une calibration des coefficients de la série de Prony pour le modèle viscoélastique a donc été possible, mais pour une durée de chargement de plus de 15sec. Pour des durées de chargement plus brèves (p. ex. pour les essais in situ dynamiques) aucune information n'a pu être obtenue de ces essais. Il était aussi évident que pour les conditions spécifiques d'essai (haute température), une conformité non-réversible a été observée pendant l'essai, une situation qui ne peut pas être reproduite par le modèle purement viscoélastique.

Avant de passer à la modélisation de l'essai in situ avec le modèle trois dimensionnel, les paramètres qui dépendent de la température ont été calibrés pour chaque essai utilisant le modèle axisymétrique efficace. A des températures de froides à tempérées (entre 1°C et 25°C), le comportement du matériau viscoélastique pour l'asphalte en combinaison avec le sol de fondation linéaire élastique a donné des résultats satisfaisants. La raideur à long-terme de l'asphalte montre une bonne correspondance avec la raideur appartenance de la température de l'asphalte dans chaque essai et le module du sol de fondation correspond au module de rechargement d'un sol de fondation de bonne qualité Cependant, des difficultés de mettre en correspondance le comportement mesuré pour ce modèle plutôt simple ont été observés pour une série de test menée avec des températures d'asphalte relativement chaudes (autour de 40°C). L'introduction d'une raideur d'asphalte qui dépend de la pression (surtout une diminution de raideur sous tension) pourrait donner des résultats légèrement meilleurs.

Simulation des essais statiques

En utilisant les paramètres choisis selon la calibration décrite ci-dessus, les essais statiques in situ ont été simulés par le modèle trois dimensionnel. La répartition des déformations mesurées perpendiculairement à la direction du mouvement a été comparée avec les résultats du modèle d'éléments finis aux profondeurs de 4cm et de 22cm, pour des pneus simples et doubles et à la fin du pas de chargement et de déchargement. Au fond des couches d'asphalte (profondeur de 22cm), les résultats des essais in situ auraient pu être mis presque parfaitement en correspondance avec la simulation numérique. La reproduction de la répartition des déformations mesurées à la surface de la couche di liaison (profondeur de 4cm) était plus difficile, peut-être à cause de petites imperfections dans l'asphalte, de variations de température potentiellement plus élevées ou à cause d'imperfections dans la modélisation de la répartition de la pression de contact dans le modèle par éléments finis, qui pourrait en plus influencer les résultats près de l'endroit de l'application de la charge.

Les résultats des essais in situ pourraient généralement être mis en correspondance avec la simulation numérique et d'observations semblables aux résultats des essais in situ pourraient être faites. Cependant, comme déjà mentionné pendant l'application du modèle simple axisymétrique, des difficultés majeures se sont avérées pendant la tentative d'obtenir les répartitions des déformations mesurées avec des températures élevées. L'ordre de grandeur des déformations à la fin du pas de déchargement a été systématiquement sous-estimé par le modèle des éléments finis, puisque l'asphalte a été modélisé avec un matériau purement viscoélastique, incapable de reproduire la conformité de l'asphalte. De petites déviations des résultats pourraient être dues à de petites fluctuations de la durée des mesures des essais in situ opposés à la durée fixe des pas de chargement et de déchargement dans le modèle. Enfin, de petites asymétries dans les répartitions des déformations à cause de l'interaction entre les pneus proches, présentes dans les résultats de mesure, pourraient être reproduites par le modèle trois dimensionnel, surtout pour des températures plus basses et pour des pneus doubles.

Simulation des essais dynamiques

En utilisant le modèle trois dimensionnel et l'ensemble des paramètres de matériau choisis pour chaque essai, les charges en mouvement, induites par le passage du véhicule d'essai, ont été simulées numériquement. Des instantanées photographiques de la répartition spatiale des déformations à une profondeur de 4cm montrent que la

répartition des déformations due au camion ne se dispersent pas instantanément mais graduellement et par conséquent les déformations formées par des essieux subséquent accumulent. L'enveloppe des déformations en fonction du temps montre une tendance semblable pour la simulation par éléments finis et l'essai in situ. La séquence des pulsations des déformations contractives et expansives en fonction du temps donne comme résultat une augmentation pas à pas des déformations, surtout remarquée pour de faibles vitesses. Selon le modèle par éléments finis, la déformation pic expansive et contractive semble apparaître toujours sous le troisième et le cinquième essieu, respectivement, comme résultat du poids des essieux en combinaison avec l'accumulation de déformations due à la nature viscoélastique de l'asphalte. Cependant, contrairement aux mesures expérimentales in situ, la déformation résiduelle après le dernier essieu n'arrive pas à être reproduite, car l'asphalte a été modélisé avec un matériau viscoélastique. Les ordres de grandeurs des déformations dues aux charges en mouvement sont, comme prévus, plus bas que ceux dus au chargement statique. Plus élevé est la vitesse du camion, plus bas sont les ordres de grandeurs des déformations pour les mêmes conditions thermique.

Modélisation des essais à l'aéroport de Zurich
Pour la simulation des essais in situ à l'aéroport de Zurich, un modèle d'éléments finis trois dimensionnel avec deux plans de symétrie a été choisi. La structure de la chaussée a été modélisée par les couches suivantes: une couche de roulement de 4cm, une couche de base d'asphalte de 9.5cm et une couche mélange traité au liant hydraulique de 53cm sur le terrain de fondation. Une analyse simplifiée avec des matériaux linéaires élastiques (asphalte et le sol de fondation) a été effectuée. La pression de contact entre le pneu et le sol a été modélisée par une constante. Le modèle a pu reproduire la répartition des déformations en bas de la couche traitée au ciment mais des difficultés ont surgies pour comparer les mesures avec ce modèle simple près de la surface à une profondeur de 4cm.

Discussion et conclusions
Les capteurs de fibre optiques distribués permettent une mesure de déformation continue le long d'une fibre optique avec une résolution spatiale élevée et, selon la technique de mesure appliquée et la longueur du capteur, avec des vitesses d'acquisition allant jusqu'à 100Hz. Dans ce projet, ils ont démontré être un outil puissant pour la caractérisation du comportement de la chaussée pour des routes sous charges statiques et dynamiques provenant du trafic.

Les câbles de fibre optique appliqués ont fournis une robustesse mécanique suffisante pour des routes actuelles en combinaison avec des procédures de mise en place évaluées. Pour le présent but, aussi l'exposition thermique élevée temporaire des câbles pendant la construction de la route n'a pas montré d'effets néfastes significatifs. Cependant, la réponse homogène observée pendant l'exposition thermique pourrait causer des difficultés dans des applications différentes de la présente. Les capteurs de fibre optique intégrés dans l'asphalte ont fonctionné pendant toute la durée du projet. Quelques dégâts aux capteurs se sont produits seulement à l'intérieur du puits d'accès à cause d'une orientation non optimale des câbles qui pourrait être améliorée par quelques simples mesures de mitigation dans des projets potentiels futurs.

Les déformations ont pu être mesurées d'une façon continue dans les chaussées sous différentes charges statiques et dynamiques provenant des véhicules test. Ceci a fourni d'intéressants aperçus du comportement dépendant de la viscosité et de la température de l'asphalte dans des routes réelles pendant leur durée de vie opérationnelle et dans des saisons différentes. En outre, il a été possible de détecter la direction du mouvement, la position et la vitesse ainsi que le nombre d'essieux et de pneus du véhicule qui passait au-dessus du capteur à l'aide des mesures de déformations distribuées à des vitesses d'acquisition élevées. Cependant, une estimation fiable des charges d'essieu nécessiterait une considération plus approfondie des paramètres environnementaux et les efforts supplémentaires des simulations numériques.

La combinaison des mesures dans les chaussées avec la modélisation numérique en conjonction avec les paramètres des matériaux obtenus par les carottages, ont permis une simulation détaillée des essais in situ et, par conséquent, une compréhension plus approfondie du comportement des chaussées sous charges de trafic. Il a pu être démontré que les résultats obtenus des essais statiques et dynamiques dans des conditions froides et tempérées correspondaient en général en utilisant des modèles viscoélastiques simples. Des efforts supplémentaires quant à la modélisation du comportement constitutif de l'asphalte seraient nécessaires pour permettre une meilleure correspondance des modèles et aussi d'étudier les résultats mesurés dans des conditions très chaudes, en utilisant des modèles avec p. ex. de la plasticité, de la raideur dépendante de la tension et encore d'autres effets.

Comme sujet de recherches futures pour la modélisation des essais in situ, il est proposé d'utiliser un modèle de matériau pour l'asphalte qui prend un compte certains effets tels qu'une conformité non-réversible et une dépendance de la raideur. Concernant le choix approprié du câble du capteur, il est suggéré de comparer les prestations de différents câbles dans des conditions similaires par rapport à leur distribution de déformation mesurée. Il se peut que des versions de câbles plus robustes qui comporte plus de couches de gaines ne suivent pas le champ de déformations présente dans l'asphalte aussi bien que les câbles avec un niveau de protection mineur. Enfin, la suite à long-terme des essais in situ en combinaison avec l'introduction d'un paramètre de dégât dans le modèle par éléments finis pourrait mener à une méthode non destructive pionnière pour l'évaluation des chaussées en asphalte.

Summary

The present research project aimed to investigate the potential of asphalt-embedded distributed fiber optic sensors for the purpose of characterizing the behavior of roads under traffic loads. Towards this goal, robust fiber optic cable versions were tested, in a first step in the laboratory, in order to figure out, whether they were suitable for the harsh environment present in asphalt. In a second step, different embedment procedures of the fiber optic cables were tried out on two test sites with an asphalt pavement. After the successful implementation of distributed fiber optic sensors on the test sites, measurements were conducted with these sensors in a time window of more than 2.5 years. The unprecedented amount of highly resolved strain data, which can be gathered with this class of sensors, was finally used in order to connect the measurement results with numerical modelling of the pavements under test. The application of the distributed fiber optic sensors has, in conjunction with numerical modelling, a high potential for the purpose of investigating the behavior of new pavement material or the adequateness of new design methods, since it allows quantifying the strain field present in the pavement under static as well as dynamic traffic load. Furthermore, distributed strain measurements may also be used in future as an additional tool for the assessment of the structural health of roads.

Structure of the present report

The structure of the present report follows merely the different research tasks carried out within this project. After a brief introduction into the subject under study in chapter 1, the different distributed fiber optic sensor technologies and devices applied in this research project are introduced in chapter 2. The test results from the laboratory experiments with the fiber optic cable are summarized in chapter 3, whereas the different installation methods of the distributed fiber optic sensors are presented and assessed in chapter 4. The measurement results gathered on the two field test sites with the fiber optic sensors, an urban road in Zurich and an aircraft stand on Zurich airport are shown in chapter 5 and 6. The results of the numerical modelling of these field tests are provided in chapter 7 to 9. Finally the report closes with conclusions and recommendations in chapter 10. Additional information about the calculated stress and strain fields is presented in the Appendix.

Preview over the presented research

Regarding the structure of the research project, three groups of main tasks can be identified: The testing of the cables in the laboratory ant their implementation into asphalt in the field, the measurement results gathered on the field test sites "Hohlstrasse" and "Zurich airport" using this class of novel sensors and, finally, the numerical modelling of this field tests (Hohlstrasse & Zurich airport) applying finite element method. A short preview over the main findings in these three groups is provided in the following sections, directly after a short description of the applied distributed fiber optic measurement technique.

Applied distributed fiber optic measurement techniques

Distributed fiber optic sensors allow for continuously measuring quantities as strain or temperatures along a fiber optic cable by sending light through a standard single mode silica fiber. In contrast to rather discontinuous fiber optic measurement techniques as e.g. fiber Bragg grating, distributed measurement techniques are not only sensitive to these external measurands in a predefined fixed position where the grating is located but use the whole length of the fiber as the sensing element. Hence, in combination with a high spatial resolution of the measurands, a powerful tool for analyzing and monitoring structures can be formed, which enables for gathering a unique amount of data within the instrumented structure. Different distributed fiber optic measurement techniques are nowadays commercially available. Within the present project, techniques were used which are based on Rayleigh and Brillouin scattering phenomena in silica fibers.

Laboratory test results and field installation methods

Asphalt represents a relatively harsh environment for a sensor whose measurement principle is based on the intrinsic properties of a thin vulnerable silica fiber. However, the different fiber optic cables applied in this research project, manufactured by the project partner Brugg Kabel AG (now Solifos AG), were in principle designed to withstand harsh environment. Nevertheless, some further clarification was required concerning the effect of the high temperature during road construction and the large transverse stress acting on the cables close to road surface during construction and operation of the road. These concerns were investigated within this project by means of laboratory tests.

Even though one can proof with laboratory experiments that the applied cable version are suitable for the application in pavements, field installation methods need to be defined, which ensure that the embedment process causes no conflicts with the road construction process and that the cables can be set in a predefined layout on the different layers. The adequateness of such different field installation methods was tested in the course of the planning and the implementation of the two sensor test fields "Hohlstrasse" and "Zurich Airport".

Laboratory tests

Temperature

Thin asphalt layers should have minimum temperatures of around 120 – 150°C before they are compacted with rollers. For the specific fiber optic sensor cables used in this project, unfortunately no experience from prior application was available for this temperature range. Regarding the most important sensor property, the conversion of measured frequency shift to strain, a concern was that the temporarily high temperature may affect the properties of the cable. In order to investigate the behavior of the cables under such temperatures, the following test plan was used.

- Measuring the strain response of a defined cable section to external elongation in a strain test bed
- Exposing this cable section temporarily to temperatures of around 140°C while taking measurements
- Measuring again the strain response of the defined cable section to external elongation in the strain test bed

By comparing the cable behavior in the strain test bed before and after heating, it could be concluded, that no significant disadvantageous effect of temperatures in the relevant range for asphalt road construction could be observed. As could be expected, the plastic cable sheath induced on the free unconstrained cable section a nonlinear response during the temperature exposure, which, however, represents for the present application not a drawback. In addition, for some cable types, a very heterogeneous response on the applied temperature was observed during heating of the cable. This heterogeneity may create additional difficulties in applications out of the scope of this study, e.g. when thermal effects on the frequency shift need to be compensated and requires further investigation.

Transversal pressure

Whereas high temperatures occur in the asphalt layers only temporarily during road construction, significant transversal pressure is present during road construction as well as during operating time of the sensor in asphalt layers close to the road surface under heavy traffic. Since distributed fiber optic sensors are sensitive to strain, temperature as well as hydrostatic stress (weakly), the response of the applied cable types was tested in a simple way in a pressure chamber applying hydrostatic pressures of up to 1MPa. The sensitivity to hydrostatic pressure in the range relevant for the present project was rather small. Hence it was decided to neglect the contribution of hydrostatic pressure in this project.

Field installation methods

Although the applied cables were designed for rather harsh environment, the installation of the cables and the construction of the road lead to additional difficulties regarding possible damage of the cables. Two principal approaches were followed concerning the installation of the cables in the field: installation on a surface using different fixation methods including a manual covering of the sensor with a small amount of fine asphalt material and installation in notches which were backfilled afterwards using a jointing compound.

The evaluation of the different installation procedures of the fiber optic cables showed that the applied cable versions provide sufficient mechanical robustness for the foreseen purpose. Even the most vulnerable cable version survived the installation without damage and performed well afterwards during the whole research project. In general, good experience was made with covering the sensor cables with a thin layer of fine asphalt material before the paver traversed the sensors or, alternatively, embedding the cables in notches, created with a rebar during rolling of the hot asphalt.

Measurement results from the test sites

Two different test sites were instrumented with distributed fiber optic sensors: an urban road in Zurich ("Hohlstrasse") and an airfield stand at Zurich airport. On both test sites, distributed fiber optic sensors were embedded in different depth into the asphalt and the strain response of the pavement was measured while the surface was loaded by means of different vehicles or aircrafts. These tests were repeated on both test sites in different seasons in order to capture the temperature dependent behavior of the pavement. The measured strain distribution in the pavements showed a strong spatial variability of strains with high spatial strain gradients, in particular in shallow depths close to surface. This fast spatial variation of the strain field present in asphalt turned out to be a strong argument for this type of strain sensors, since the strains can be measured continuously with high spatial resolution along the cable, whereas classical sensors allow only for isolated point measurements. More than $1500\mu\varepsilon$ were measured directly under the tire in 4cm depth in the road during summer, whereas the maximum strain magnitudes at the airfield stand were around twice this magnitude, even though the test was carried out in beginning of autumn and not in summer. As expected, a large dependency of this strain magnitude on temperatures of the asphalt was observed. However, not only the magnitude, but also the shape of the strain distribution changed with the season.

Test site Hohlstrasse

Test site and setup

The test site Hohlstrasse in Zurich represents an urban road under a large traffic volume including a bus line. The Hohlstrasse consists of three asphalt layers, in total 22cm thick, which are resting on an unbound granular mixture for road construction. Fiber optic cables for the purpose of strain sensing were embedded at the bottom of the asphalt layers in 22cm depth as well as on the top of the binder course in 4cm depth. The cables were installed as short loops of around 10m length with parallel lines transversal or longitudinal to the traffic direction. An around 70m long loop was embedded in the form of a mesh with a grid spacing of 0.5m. The cable ends were made accessible for the connection to the measurement device by means of small shafts in the adjacent sidewalk. The installation worked perfectly during the whole project duration, only some minor damages owing to the chosen cable guidance were observed at the position where the sensor cable enters the access shaft.

Distributed fiber optic sensors were used within this project primarily in order to quantify the strain distribution in the pavement under short term resting loads as well as moving traffic loads. In order to apply this load to the pavement, a truck and a car were used as test vehicles. Whereas the car brought an axle load of slightly more than 12kN to the road surface, the front axle of the truck (single tire) applied approximately 50kN and the rear axle (double tire) applied around 100kN to the pavement. Such tests, where strains were measured under different axle loads and at different velocities of the traversing test

vehicle, were carried out in different season in order to study the effect of temperature on the strain distribution within the pavement. These tests were carried out during daytime within the usual traffic flow but not during the rush hours. Hence, it was not possible to apply the static load longer than for a few seconds in order to not disturb the traffic flow too much. In order to be able to apply loads not only for seconds but also over several minutes, one lane of the road was closed in a special test series for traffic during the night and strain measurements were conducted using resting loads as well as additional measurements concerning the deflection of the pavement were carried out.

Since temperature is affecting the stiffness of the asphalt layers strongly, temperatures during the tests were measured periodically. The temperatures were measured at the road surface and in three further depths using needle thermometers and Pt100 elements. In order to enable a numerical simulation of the tests using realistic stiffness parameters, several core drillings were made at this test site. The samples taken from these cores were analyzed at EMPA.

First continuous strain measurements indicated a high spatial variability of strains within the pavement in particular around the position of the tire. In order to be able to resolve the strain distribution present in the pavement properly, measurements were conducted using mainly the devices based on Rayleigh backscattering. The devices using this technology and being available in the framework of this research project, allowed for a clearly finer spatial resolution of the strains along the sensor cable than the particular Brillouin based sensing devices available for this project. Within the present project, an average strain was often computed over a spatial distance of 10mm or less and exported often every 5mm or less along the fiber.

Measurement results

The strain measurements at the test site Hohlstrasse were conducted often in a similar manner in order to allow for comparability between the different tests series carried out at various temperatures. Between installation in November 2015 and March 2018 around 10 test series were conducted. Not all of them consisted of the identical test program but usually strain measurements on top of the binder course, using the rear and front axle of the truck as a short term static load, were carried out. From time to time, these measurements were complemented with measurements using the sensor installed at the bottom of the asphalt layers or using the car in order to apply smaller loads to the pavement. The reference measurement, to which the strain change under load was measured, was taken usually only a few seconds before the load was applied. Once the measurement under load was completed (often around 10s to 15s after the load was applied), a third measurement was launched immediately after the load was removed from the pavement. This third measurement was carried out in order to capture the delayed strain response owing to viscous behavior of the asphalt. Usually such static measurements were accompanied by dynamic measurements, in which the test vehicles (car, truck) were traversing the sensor at different velocities while the strains were read out from the sensor at a high acquisition rate.

As expected, the effect of decreasing asphalt stiffness with increasing temperature was also reflected in the measured strain distributions. The overall ratio of the maximum strain magnitude measured in a test series during a hot summer day on one hand and a cold winter day on the other hand was around 50 and this although the winter measurement was carried out during daytime and not during a cold winter night. Hence the true ratio of the extreme strains present in the road under the same axle load is likely to be even higher than the recorded one.

The pavement directly under the tire, which was subjected to short term static loading, showed expansive strains in 4cm as well as 22cm depth. However, in particular during hot summer days, the strain magnitude measured in the upper sensor cable was clearly larger than the strain at the bottom and reached magnitudes of up to around 1500$\mu\varepsilon$. Whereas the strain in the upper layer changed its sign and turned into contractive strain right beside the perimeter of the tire, at the bottom of the asphalt layer, the sign change occurred farther away. When the pavement was loaded by a single tire, only one

expansive strain peak was visible in the measurements, whereas two expansive strain peaks became visible when a twin tire was applying load to the asphalt. Interestingly this two strain peaks where still clearly visible also at the bottom of the asphalt layers in 22cm depth. Compared to the results gathered during hot summer days, where the expansive strain peak under the tire was dominating the strain distribution, in measurements recorded during cold winter days this strain peak became less dominant compared to the adjacent contractive strains.

Beside of these tests, where strains under short term resting vehicles were measured, also complementary tests were carried out in one special test series during a summer night. During this night, authorities allowed for closing one lane of the road for traffic for a few hours and hence, the pavement could be subjected to loads resting for several minutes on the instrumented area. This allowed for investigating the viscous behavior of asphalt layers on this specific test site. In addition to strain measurements also settlement measurements on the road surface were carried out, using an instrument called "ETH Delta" in order to gather additional independent measurands beside of strains within the asphalt layers.

In addition to the measured behavior of the pavement under short term static loading, as discussed above, strains were also measured continuously and highly resolved along the cable with acquisition rates of 100Hz. Different test vehicles traversed the embedded sensor at velocities between 5km/h and 50km/h, in order to be able to investigate the effect of dynamic loading, originating from the traffic, to the road. As expected, owing to the viscous properties of asphalt, the overall strain magnitude decreased with increasing vehicle velocity. The effect of the disproportional reduction of the expansive strain peak in cold temperature regimes intensified in combination with high vehicle velocities. This circumstance lead to the situation that in cold conditions at high velocities no expansive strain peak was measured at all in the asphalt layer in 4cm depth and the strain remained throughout contractive, also directly under the tire. In addition to the detailed insight into the pavement behavior under dynamic traffic load, the results of the installed sensor allowed for capturing the driving direction and position as well as the vehicle velocity and the number of axles and tires. The current limits of the tested setup were found to be the detection of dynamic loads originating from light vehicles as cars with high velocities in cold winter conditions. The strains became very small in this conditions and it was difficult to distinguish the measured strain change from the noise level without applying further data processing techniques. However, it should be mentioned that these measurements were conducted in a road designed for strong heavy traffic and the asphalt layers were in total 22cm thick, leading to small strains in the conditions discussed above. By applying additional measures, the situation could also be further improved in these conditions, if required.

Test site Zurich airport
Test site and setup

In contrast to the test site in Hohlstrasse, which is subjected mainly to dynamic traffic loads inducing a large number of load cycles, the test site at Zurich airport represents an aircraft stand, characterized by a small number of load cycles but long resting times of the load. Nevertheless, also this test site was built from asphalt and not concrete owing to the provisional intended usage of this aircraft stand. The design consists of a 4cm and a second 9.5cm thick asphalt layer which is resting on a hydraulically bound granular mixture, having a total thickness of 53cm.

The layout of the fiber optic sensor installation was rather large-sized in the sense that the cable loops used at the aircraft stand had a length of slightly more than 140m. The layout consisted of two almost 30m long parallel cable sections with a 6m spacing. The remaining cable length was actually used in order to guide the cable ends to the next electro shaft, which was used to enable access to the sensor cables with the measurement devices. As on the test site Hohlstrasse, also on Zurich airport different fiber optic cables were embedded in 4cm depth and at the bottom of the asphalt layers,

which was here in 13.5cm depth. The embedment of the fiber optic sensor took place in July 2015 and was carried out while the aircraft stands were constructed.

Unexpected difficulties occurred during the first measurements owing to the overlength of the sensor loops. However, once the difficulties have been overcome using an adapted measurements scheme, the installation worked perfectly throughout the whole duration of this research project.

Measurement results

Measurements using the fiber optic sensors embedded in the aircraft stand were carried out on a cold winter day and on two warm autumn days using an A330-300 and an A340-300 aircraft type. Static measurements were carried out after the aircraft was moved by an airfield tractor into the predefined position. Distributed fiber optic measurements were gathered in around 5 to 6 different aircraft positions with respect to the sensor location.

Although the total thickness of the asphalt layers is rather small and, furthermore, they are resting on a hydraulically bound granular mixture, the dependency of the measured strain on temperature was also in the case of the present design very large. This circumstance lead to measureable expansive strain peaks directly under the tire of up to around $3000\mu\varepsilon$ during a warm autumn day. During the cold winter day, these strains remained contractive in 4cm depth and reached only in 13.5cm depth an expansive form. Even though the asphalt layers are resting on a hydraulically bound granular mixture, the influence zone of the aircraft gear appeared to be rather small and the aircraft gear generated a rather narrow and localized strain field present in the asphalt layers.

Numerical modelling of the field tests

Motivation
The embedment of distributed fiber optic sensors within the pavement enabled for a detailed insight into the structural behavior of asphalt layers subjected to traffic loads. At a first glance, the general trend of the strain measurements is confirming what could be expected at least qualitatively: larger loads generate larger strains; strains measured under the same load magnitude increase with increasing temperatures; fast vehicles passages generate smaller strains than slow vehicle passages. However, there were also effects measured, which are more difficult to explain directly and this already only in a qualitative, let alone in a quantitative manner. In addition, the estimation of strains for a given temperature, load and vehicle velocity only with the help of numerical modelling techniques without being able to use measurement data is a difficult task, based on numerous assumptions.

On the other hand, there is a large amount of strain data gathered with distributed fiber optic sensors available for different boundary conditions as temperature, load magnitude and vehicle velocities. This in turn enables choosing and calibrating adequate constitutive models, boundary conditions and modelling techniques on the basis of the measurement data, gathered not in the laboratory, but under real field conditions. This may become increasingly important if in the design of roads the mechanistic design approach becomes more widespread or new materials are applied, on which not sufficient empiric knowledge is available. For this reason, the experimental research tasks discussed before were completed by numerical modelling of the field tests in order to deepen the knowledge about appropriateness of constitutive models, boundary conditions and modeling techniques.

Numerical modelling of the field tests in Hohlstrasse
In order to keep the possible range of models, material parameters and boundary conditions, which can reproduce the measurements adequately, as small as possible, many independent measurement data were gathered. Samples from core drillings were analyzed in the laboratories of EMPA in order to roughly obtain the range of stiffness at different temperatures and frequencies. Furthermore, beside distributed strain

measurements also temperatures were measured and, in one test, settlement data under the load was measured using the ETH Delta device as well.

Modelling the settlement trough using ETH Delta tests

The spatial settlement measurement data obtained with the ETH Delta device were used for a preliminary inverse analysis of the subgrade material parameters with a three dimensional finite element model using the software Abaqus. The model consists of a 4cm wearing course, 9cm binder course, 9cm asphalt base course on top of a granular base course and the subgrade. The asphalt concrete was modelled with the help of a linear viscoelastic model and the subgrade was introduced as a linear elastic material. Between the asphalt base course and the subgrade, a frictional interface was implemented.

It could be shown that the settlement trough measured with the ETH Delta device is majorly influenced by the stiffness parameters of the subgrade, and is rather insensitive to the parameters of the asphalt layers. Only the settlement in the close proximity of the tire, where the device is not measuring, is governed by the viscous behavior of the asphalt concrete. For the inverse calculation of the subgrade properties, the asphalt concrete stiffness was determined with the help of the fiber optic strain measurements. By doing so, a good agreement between measurements and model results could be obtained and the subgrade parameters could be determined. Deviations were noticed in the region under contraction, possibly due to the stress dependent stiffness of the asphalt concrete, which was neglected in this analysis.

Finite element models

Two finite element models were used for the modelling of the tests in Hohlstrasse Zurich. The first one is a simple axisymmetric model, which was used to investigate in an efficient way roughly the influence of different parameters of the models. The main advantage of the axisymmetric model is that it consists of a much lower number of elements, rendering thus feasible the use of a finer mesh at much lower computational cost. With the help of this preliminary sensitivity analysis, the choice of the suitable material model and the calibration of the material parameters, as well as the appropriate modelling of the contact pressure were significantly speeded up. The second finite element model is a three dimensional model with one plane of symmetry, enabling a more realistic modelling of resting and moving traffic load, single and twin tires as well as their mutual interference.

The contact surface size of the tires on the pavement was first measured in the field and afterwards introduced into the model together with the known axle load. The modelled contact pressure on the pavement was therefore determined with the help of these two parameters and under the assumption of both a constant and a convex stress distribution. Indeed, the assumption of a convex contact stress distribution is reported in literature for high inflation pressures with low axle loads, as in the case of the trucks used in the field experiments. The loading steps for the static test series were modelled with a geostatic step followed by a 15s long loading and a 15s long unloading step, to account for the average time required for a measurement.

The moving load was modelled with the help of an Abaqus subroutine. Although this simplified procedure does not reflect a full dynamic analysis, the viscous behavior of the asphalt pavement under the loading of a truck (five axles), moving with different velocities, could be approximated quite well. The different velocities were considered by changing the position of the truck with each time increment. Both, the chosen time increments as well as the viscoelastic material model for the asphalt concrete, were optimized in order to obtain sufficient accuracy.

Material models

Material models describing the behavior of asphalt concrete have been thoroughly investigated in literature. Viscoelasticity in low temperatures and viscoplasticity in high

temperature, constitutive models considering fatigue, viscoelasticity and chemical healing, stress history and rate dependency can be found in the literature. In the present analysis, the asphalt concrete was modelled in a less sophisticated way, time domain viscoelasticity was modelled using the Prony series expansion embedded in Abaqus. The Prony series coefficients, which determine the time dependency of the stiffness, were defined individually for all the test series, whereas the long-term stiffness modulus and Poisson's ratio were varied with the temperature. No damage or viscoplastic behavior was modelled but the properties of asphalt were chosen in dependence on the samples from the core drillings.

The subgrade was modelled as linear elastic material using the parameters from the settlement trough measurement. Stress dependent stiffness of the subgrade was also partially also applied. Moreover, the irreversible behavior of the subgrade was studied with plasticity models according to Drucker-Prager and non-associative flow rule.

Calibration

For the calibration of the constitutive model of the asphalt layers, the results of the special field test series carried out during the night on a closed lane were used (using concrete blocks for the purpose of loading). During these tests, the development of strains with time was measured under a concrete block for a loading and unloading duration of several minutes. A calibration of the Prony series coefficients of the viscoelastic model was thus enabled, though for a loading duration of more than 15s. For shorter loading time durations (e.g. for the dynamic field tests) no information could be gained from these tests. It was also evident that for the specific test conditions (high temperature), non-reversible compliance was noticed in the test, which cannot be reproduced by the purely viscoelastic model.

Before modelling the field test on the three-dimensional model, the temperature dependent parameters were calibrated for each test series in the efficient axisymmetric model. In cold to warm asphalt temperatures (between around 1°C and 25°C), the viscoelastic material behavior for the asphalt in combination with linear elastic subgrade gave satisfying results. The long-term stiffness of the asphalt is in good agreement at each test with the stiffness belonging to the asphalt temperature and the subgrade modulus corresponds to the reloading modulus of a good quality subgrade. However, difficulties to match the measured behavior with this rather simple model were observed for one test series conducted in very warm asphalt temperatures (around 40°C). The introduction of pressure dependent asphalt concrete stiffness (especially stiffness reduction under tension) might give slightly better results.

Simulation of static tests

Using the parameters chosen according to the calibration described above, the static field tests were simulated with the three dimensional finite element model. The strain distribution measured perpendicular to the driving direction was compared with the results of the finite element model at both 4cm and 22cm depth, for single and twin tires and at the end of the loading and the unloading step. At the bottom of the asphalt layers (22cm depth), the field test results could be almost perfectly matched by the numerical simulation. The reproduction of the measured strain distribution on top of the binder course (4cm depth) was more difficult, which might be a result of small imperfections in the asphalt concrete, potentially higher temperature variations or due to imperfections in modelling of the contact pressure distribution in the finite element model, which may additionally influence the results so closely to the position of load application.

The field test results could be matched in general quite well using the numerical simulation and similar observations to the field test results could be made. However, as already observed during the application of the simple axisymmetric model, larger difficulties occurred during the attempt to obtain the measured strain distributions in very warm temperature. The strain magnitude at the end of the unloading step was consistently underestimated by the finite element model, as the asphalt concrete was modelled as a purely viscoelastic material, unable to reproduce the non-reversible

compliance of the asphalt concrete. Small deviations at the results could also be due to small fluctuations of the duration of the field test measurements in contrast to the fixed duration of the loading and unloading steps in the model. Finally, small asymmetries in the strain distributions due to the interaction of the neighboring tires, as present in the measurement results, could also be reproduced by the three-dimensional model, especially for lower temperatures and for the twin tires.

Simulation of dynamic tests

By using the three dimensional model and the chosen set of material parameters for each test, the moving loads, induced by the test vehicle passage, were simulated numerically. Snapshots of the spatial strain distribution at 4cm depth show that the strain distribution caused by the truck does not fade instantly, but gradually, and as a result, the strains caused by subsequent axles accumulate. The strain envelope with the time shows a similar pattern for both the finite element simulation and the field test. The sequence of pulses of contractive and expansive strains with the time results in a stepwise increase of the strains, especially noticed for low velocities. According to the finite element model, the peak expansive and contractive strain appear consistently underneath the third and the fifth axles respectively, as a result of the weight of the axles in combination with the accumulation of strains due to the viscoelastic nature of asphalt concrete. However, unlike the field experiment measurements, the residual strain after the last axle fails to be reproduced, as the asphalt concrete was modelled as a viscoelastic material. The strain magnitudes due to the moving loads are, as expected, lower than those due to the static loading. The higher is the truck velocity, the lower are the strain magnitudes for the same thermal conditions.

Numerical modelling of tests in Zurich airport
For the simulation of the field tests at Zurich airport, a three dimensional finite element model with two planes of symmetry was used. The pavement structure was modelled using the following layers: 4cm wearing course, 9.5cm asphalt base layer course and 53cm of hydraulically bound granular mixture on the top of subgrade. A simplified analysis with linear elastic materials (both asphalt and subgrade) was conducted. The contact stress between the tire and the subgrade was modelled as constant. The model was able to reproduce the strain distribution at the bottom of the binder course, larger difficulties to match measurements with this simple model occurred close to surface in 4cm depth.

Discussion and Conclusions
Distributed fiber optic sensors allow for a continuous strain measurement along an optical fiber with high spatial resolution and, depending on the applied measurement technique and sensor length, with acquisition rates of up to 100Hz. In the present project they proved to be a powerful tool in order to characterize the behavior of the pavement in roads under static and dynamic loading originating from the traffic.

The applied fiber optic cables provided sufficient mechanical robustness on real road construction sites in conjunction with the evaluated installation procedures. For the present purpose, also the high temporarily thermal exposure of the cables during road construction did not show a significant detrimental effect. However, the observed heterogeneous response during thermal exposure may cause difficulties in applications different from the present one. The fiber optic sensors embedded in asphalt were functioning over the whole project duration. Some damage of the sensors occurred only within the access shaft owing to a non-ideal cable guidance, which could be improved by simple mitigation measures in potential further projects.

Strains could be measured in a continuous manner in the pavements under various static and dynamic traffic loads originating from different test vehicles. This gave interesting insights into the viscous and temperature dependent behavior of asphalt in real roads during their operational lifetime in different seasons. Furthermore, by means of distributed strain measurements at high acquisition rates, it was possible to detect driving direction,

position and velocity as well as the number of axles and tires of the vehicle traversing the sensor. However, a reliable estimate of the axle loads would require a deeper consideration of environmental parameters and additional efforts using numerical simulations.

The supplementation of the measurements in the pavements with numerical modelling in conjunction with material parameters obtained from core drillings, enabled for a detailed simulation of the field tests and hence, for a deepened understanding of the behavior of pavements under traffic loads. It could be shown that the static and dynamic test results obtained in cold to warm conditions could be matched along general lines, using simple viscoelastic models. In order to achieve a better fit of the models and to study also the results measured in very warm conditions, further efforts on the modelling of the constitutive behavior of asphalt would be required, using models including e.g. plasticity, stress dependent stiffness and further effects.

As a topic for further research concerning the numerical modelling of the field tests, it is proposed that a material model is implemented for asphalt concrete, which considers effects, as non-reversible compliance and stiffness dependency. Concerning the appropriate choice of the sensor cable, it is suggested to compare the performance of the different cables in similar conditions with respect to their measured strain distribution. It may be possible, that the robust cable versions, consisting of many sheath layers, may not follow the strain field present in asphalt as close as cables with a smaller protection level. Finally, the long-term continuation of the field tests in combination with the implementation of a damage parameter in the finite element model could lead to a pioneering non-destructive evaluation method for asphalt concrete pavements.

1 Introduction

1.1 Goals

The mechanical properties of pavement layers are determined by many factors, among which the material composition, the mixing process and the compaction method. While in service, the effects of traffic and of the environment tend to deteriorate the road structure.

The main goal of this research is to develop a sensor methodology, based on the latest fiber optics technology, which is able to detect the condition and deterioration mechanism of a road pavement. Through analysis of the experimental data it is the possible to quantify and follow the evolution of the mechanical properties of the single layers.

Assessing the layers properties and their evolution with time allows 1) improving performance prediction, 2) evaluating the construction phase in order to develop better equipment, material and specifications, and 3) monitoring structural health to manage maintenance operations.

1.2 Methods

Conventional non-destructive road testing techniques are very limited in assessing the material pavement properties. These instrumentations usually measure surface deflection of road pavement under a load (i.e. Falling Weight Deflectometer), and not the real mechanical deformation of the single layers. This can only be interpreted through inverse analysis of the deflection data. This method provides only indirect information, often of difficult interpretation. Aim of the this research is to give a practical tool to directly assess the structural properties and the health of the different layers of a road using an innovative technology based on fiber optics that provides reliable and fast direct measurement of strains within the pavement itself. The newly developed system of road + fiber optics will also act as a smart mean to detect type and speed of the loading.

The measuring system is validated by laboratory and field testing. Additionally the results are extensively interpreted by means of advanced finite element modelling.

1.3 State of the art

The use of fiber optics as sensing system for structural health monitoring is rapidly growing, thanks to their many qualities: optical fiber sensors are immune to electromagnetic fields, chemically and biologically inert, small and lightweight; they can withstand high temperatures; the signal can be transported for kilometers. Examples of civil engineering structures where fiber optics sensing is integrated are bridges, dams, tunnels, piles, power plants and so on (see, e.g., [1]). Fiber optic sensors used for strain monitoring in civil engineering face two important challenges: on one hand, they need a good mechanical contact between the fiber sensor and the structure (or soil) to solidly follow the movements, while on the other hand they must be protected from mechanical damage.

The fiber optic sensor techniques already applied in civil engineering are [1]:

- Fabry-Perot interferometric strain and temperature sensors - point sensing, i.e. similar to a strain gauge.
- Fiber Bragg Grating (FBG) strain and temperature sensors - point sensing; up to 16 points can be measured with a single fiber.
- SOFO system - long gauge point sensing
- Microbending sensors - quasi-distributed sensing
- Brillouin distributed strain (and temperature) sensors - distributed sensing.

The latest development in distributed fiber optics sensing is represented by SWI measuring technology (Swept wavelength interferometry, e.g. [2], [3]), which currently allows the finest measuring resolution (5mm).

Brillouin distributed strain and SWI sensing uses optical fibers, which play both the role of linear sensing elements and that of transmission lines to convey the optical information to the processing unit at the fiber end. Differently from localized (point) fiber optic sensing (like the more renowned FBG sensing and Fabry-Perot interferometry), in which each sensor can measure only at one or few points, this technique is able to measure a physical parameter along the whole length of the fiber optic sensing cable, as each point along the fiber can separately and selectively sense the strain, providing simultaneously the linear distribution of the quantity along the entire fiber length up to many km. Distributed fiber optics sensing represents a further evolution of the concept of sensor integration, and a huge step in the sensing techniques.

Applications of fiber optics sensors in road structures have been few so far, and they have involved mainly point sensors used as strain gauges. Among these is Monitor Optics Systems Ltd., who used FBG sensors to monitor the pavement of a highway subjected to mining-induced subsidence effects [6]. Bueche et al. [4], from EPFL, found good comparison between point measurements made using FBG-based sensors and strain gauges embedded in a pavement facility and subjected to loads. Opsens, in collaboration with Laval University (Canada) [5], designed a gauge made out of a cylindrical polymeric body holding Fabry-Perot interferometric fiber optic strain sensors, which can be attached directly to the wall of a core hole cut in the pavement. A similar system was used by Doré & Duplain [7] to measure spring-thaw related strains. Also Loizos et al. [8] used Fabry-Perot sensors embedded in polymeric bodies to characterize cold in-place recycled pavements made of foamed asphalt against fatigue failure.

One of the first examples of distributed sensing applied to a road (although not strain sensing) comes from Imacho et al. [9], [10], who embedded distributed temperature sensing cables 2 km long in an existing road to detect temperature changes and ice formation; results were successful. Temperature sensing cables differ from strain sensing cables in that they are loose-buffered, i.e. the fiber inside the cable is loose. This makes the manufacturing and the embedment of the cable much easier, and the cable itself less prone to breakage.

In the last years several applications of fiber optics distributed sensing in pavements have been developed. Chapelau et al. [11], [12] have successfully implemented fiber optics cables for measuring strains and cracks in asphalt pavements. The cables were installed in the hot asphalt during building of the pavement. They adopted SWI measuring technology in pavements built in the IFSTTAR accelerated pavement testing Facility in Nantes (Fr.).

Similar experiences were obtained by Liu et al [15], as well as Xiang & Wang [13], [14] with BOTDA / R technology. Zhou et al [16] used FBG sensors in an attempt to depict the strains of a highway pavement in three dimensions due to static loading.

Udd et al [17]have also monitored with the FBG sensors a asphalt and concrete highway pavement and seen potential on vehicle classification, axle counting, weigh in motion and traffic signal activation. Weigh in motion with the help of FO sensors has also been investigated by Cosentino et al. as an alternative to piezoelectric sensors [18] and Malla et al [19].

2 Measurement technology and sensing cables

Abstract

The strains within the asphalt layers were measured using distributed fiber optic sensing technology. It has an essential advantage that continuous measurements along an optical fiber and thus a sensing cable are possible with spatial resolutions as low as 1cm. In addition distributed dynamic measurements with up to 250Hz sampling rate over very short distances can be obtained. This chapter gives a brief introduction into distributed fiber optic sensing and highlights in particular the two utilized sensing technologies in the present project (Rayleigh and Brillouin backscattering). Further information on the sensing technologies can be found e.g. in [20], [21], [22] and [44]. The specifications of the distributed sensors installed in the asphalt are provided in section 2.2.

2.1 Distributed fiber-optic sensing

The distributed fiber optic sensing makes use of a standard optical single mode fiber (SMF) through which light emitted from a laser source is guided (c.f. Fig. 1). According to Snell's law, the travelling light is trapped inside the core of the fiber due to a higher refractive index (n) of the core with respect to the cladding. Optical fibers are made of fused silica and usually have a refractive index around 1.5 (c.f. [20]).

Coating, d = 250μm
Cladding, d = 125μm, n_2
Core, d = 8-9μm, $n_1 > n_2$
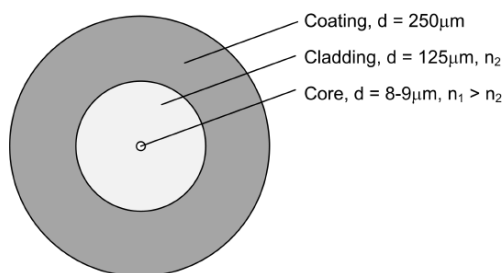
Fig. 1 *Cross-section of a single mode fiber (SMF) after [22]*

As the emitted light pulse travels along the fiber, a small fraction is spontaneously backscattered due to the interaction with the fiber medium. Several backscattering phenomena occur simultaneously and can be divided into Rayleigh, Brillouin and Raman scattering. Fig. 2 schematically shows the different backscattering phenomena with respect to the incident wavelength λ_0. Generally said, an external change in strain or temperature results in a frequency shift or a change of intensity of the anti-stokes and/or stokes components of this scattering.

Anti-Stokes components   Stokes components

Rayleigh

Brillouin   Brillouin

Raman   Raman

λ_0 *Wavelength*
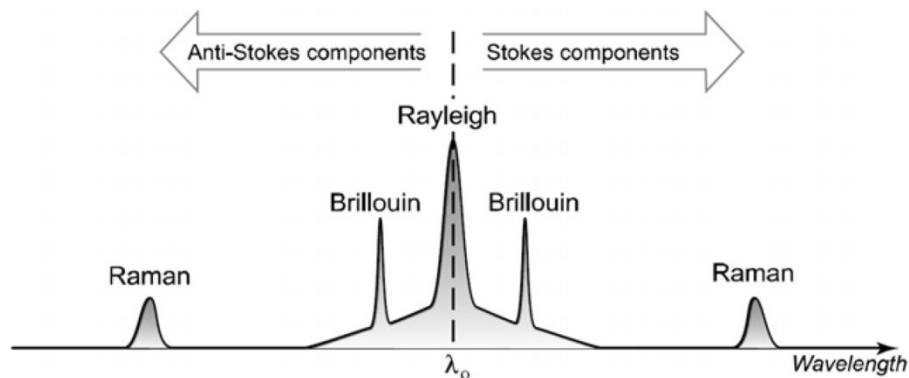
Fig. 2 *Spectrum of the spontaneously backscattered light in an optical fiber [23]*

By measuring the time between the launch of the pulse and the detection of the backscattered light, the location of the occurring backscattering can be calculated. The distance x is dependent on the velocity of light in vacuum c, the refractive index of the fiber core n and the time between the launch of the pulse and its detection Δt:

$$x_i = \frac{c \cdot \Delta t}{2 \cdot n}$$

As the Brillouin and Rayleigh backscatter is sensitive to both, external strain, and temperature, the temperature effects in a strain sensor need to be taken into account and compensated for. Therefore, a parallel temperature sensor that only captures the thermal effects is required, especially for long term measurements. In the present project, the temperature compensation was not required for a single test, as the time period was very short and thus temperature changes were minor. For comparisons between two tests or campaigns however, temperature effects would have to be taken into account.

The different available sensing technologies based on the different scattering phenomena have their own characteristics in terms of maximum sensor length, spatial resolution, sampling interval and accuracy. The sampling interval represents the sensor spacing along the fiber, whereas the spatial resolution can be visualized as the gauge length of each individual sensor. Further details on the involved measurement technologies are described in the following chapters. Fig. 3 gives an overview of the used measurement devices in this project.

1: DITEST STA-202 (Brillouin)
2: OBR 4600 (Rayleigh static)
3: ODISI-B (Rayleigh dynamic)
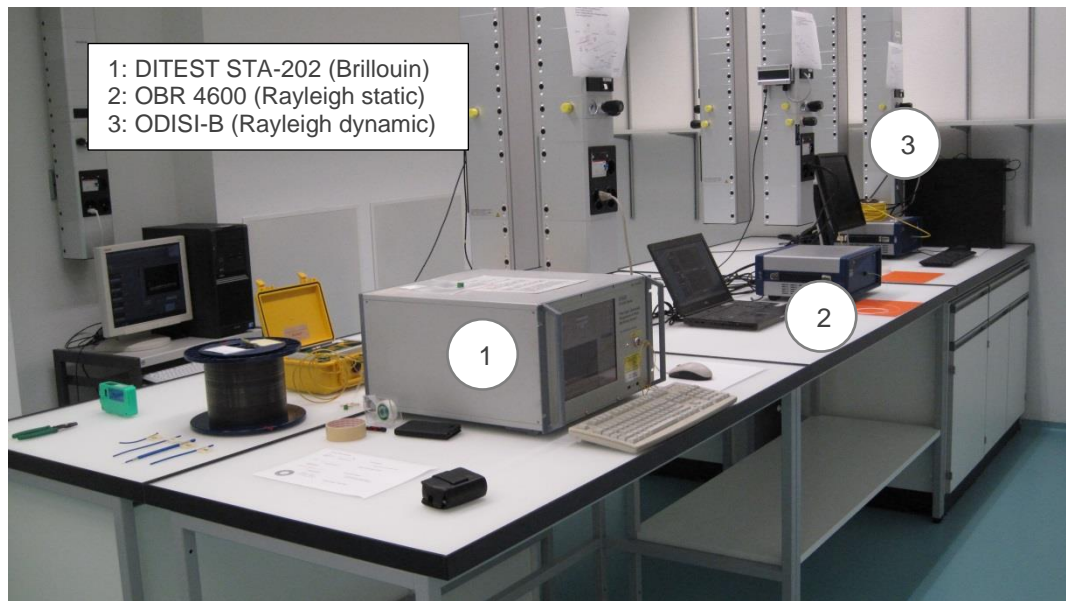
Fig. 3 *Involved measurement devices set up in laboratory*

2.1.1 Brillouin backscattering and sensing

The incident light pulse within the fiber interacts with thermally excited acoustic waves and the backscattered portion of light experiences a frequency shift owing to the Doppler Effect. This frequency shift ν_B is dependent on the acoustic wave velocity V_A, the refractive index n of the fiber material and the vacuum wavelength of the initial light λ (c.f. [24], [25], [26]).

$$\nu_B = \frac{2\,n \cdot V_A}{\lambda}$$

The acoustic wave velocity V_A is primarily dominated by the density ρ and the Young's Modulus E of the fiber material at a specific location. These local variations are caused by external strain or temperature changes and thus the fiber can be used as a distributed

strain and temperature sensor (e.g. [27]). The Brillouin frequency shift for an unstrained fiber is around 11GHz. The measured frequency shift as a function of the external strain and temperature can be denoted as follows (after [25] and [27]):

$$\Delta\nu = C_\varepsilon \Delta\varepsilon + C_T \Delta T$$

The Brillouin Optical Time Domain Analysis (BOTDA), which was used as sensing technology in the present project, makes use of stimulated Brillouin scattering effects. This can be achieved by sending a continuous wave optical signal from the other end of the fiber. Hence, access to both ends of the fiber, i.e. a loop is required. This stimulation leads to an amplification of the signal and a better scattering efficiency (c.f. [25], [28]). A typical Brillouin sensing setup is shown in Fig. 4. The BOTDA sensing technology allows for long sensor length (several kilometers) with a minimal spatial resolution of 0.5 – 1.0m.

The used measurement device is of type DITEST STA-202, manufactured by Omnisens SA in Switzerland. The devices allow a maximum distance range of up to 30km combined with a minimal spatial resolution of 1m and a sampling interval of 0.1m. The measurement resolution is stated as $2\mu\varepsilon$ or 0.1°C respectively, whereas the accuracy, depending on the distance range, is around $10\mu\varepsilon$ or 0.5°C at its best [29].
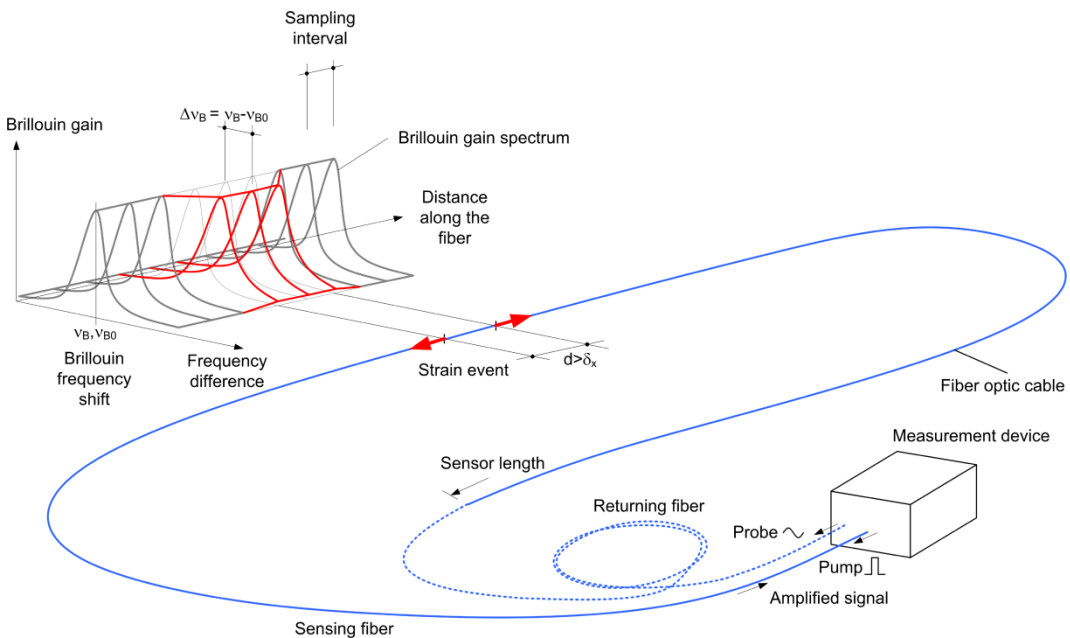
Fig. 4 *Schematic principle of Brillouin Optical Time Domain Analysis (BOTDA) after [22], [31] and [32]*

2.1.2 Rayleigh backscattering

The Rayleigh backscattering occurs due to small random variations in the density and the refractive index, originating from manufacturing imperfections, along the fiber. A tunable laser, connected to the fiber, sweeps over a certain wavelength range within a short time. The signal of the backscattered light has a pattern which is different and unique for each fiber, as it depends on random fluctuations of the fiber properties originating from the manufacturing process. It can be seen as a sort of fingerprint of the attached sensor ([3], [30]). A cross correlation of this specific pattern between two measurements allows for determining a frequency shift $\Delta\nu_s$, which is again linear dependent on temperature and strain. Therefore, such a setup can serve as a distributed sensor (e.g. [2]).

In the current project, the Swept Wavelength Interferometry (SWI), which is based on the Rayleigh scattering, was used. This principle can be used for both, static and dynamic, measurements and requires only access to one end of the fiber. The technology generally allows shorter sensor length as compared to the Brillouin technologies but in

turn offers a significantly better spatial resolution in the sub-centimeter range. A typical Rayleigh/SWI measurement setup is shown in Fig. 5.

The static measurement device is an OBR 4600 (Fig. 6), manufactured by Luna Inc. in the USA. A static measurement in the current project denotes a measurement which last several seconds, depending on the exact instrument configuration. It can cover a maximum sensor length of 70m with a spatial resolution below 1cm at the same time. The sensing resolution is reported as 1$\mu\epsilon$ or 0.1°C respectively, the accuracies as 25me and 3°C (c.f. [33]).
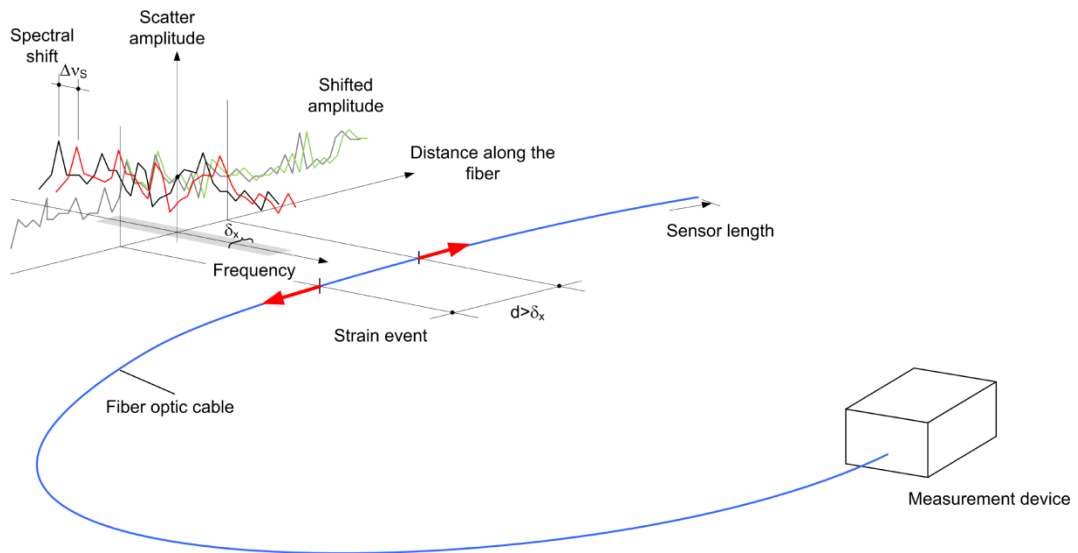
Fig. 5 *Schematic principle of swept wavelength interferometry (SWI) after [22] and [35]*

For the dynamic measurement, the ODiSI B instrument, also manufactured by Luna Inc. was used. Compared to the OBR 4600 it allows measurements at a sampling rate of 250Hz but only over a maximum length 2m or 100Hz over a maximum length of 10m and 50Hz over a maximum length of 20m. The spatial resolution can be as good as 0.13cm. The repeatability is stated as 5$\mu\epsilon$ and 0.4°C (c.f. [34]).
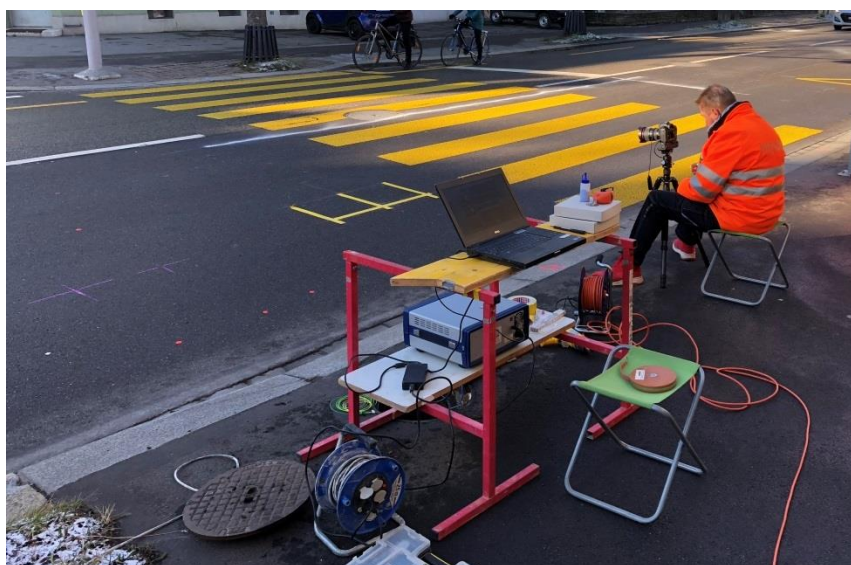
Fig. 6 *OBR 4600 in usage during a field test (Hohlstrasse Zurich)*

2.1.3 Discussion

Each involved measurement technology or device has its own advantages and disadvantages, where no technology is able to combine the best properties. BOTDA is able to measure kilometer long sensing length, whereas SWI is limited to 70 m or 20m. The spatial resolution on the other hand is shorter for SWI, which was a great advantage in the current project. Another main difference is the sensing setup; BOTDA requires access to both ends of the fiber and therefore a loop, for SWI, access to one end of the fiber is sufficient.

For monitoring projects involving moving traffic the measurement time is yet another important factor. A static SWI measurement only takes a few seconds or can even be dynamically acquired at up to 250Hz, where in turn a BOTDA measurement requires several minutes.

A single BOTDA measurement already contains useful information (e.g. approximate strain or temperature level) as the absolute Brillouin frequency is measured. For the SWI technology, on the other hand, two measurements are required to give a statement about strain or temperature changes.

In case of an unrepairable fiber break within the instrumented section, the SWI technology is in advantage, as the sensor until the failure location can still be measured while with BOTDA, the loop is damaged and thus a measurement is not possible anymore. If the fiber can be repaired, the BOTDA technology is however more robust, as the measurements can be continued and compared to earlier measurements, even though the sensing length might be shifted. A repaired SWI sensor on the other hand can usually not be correlated to earlier measurements without further modifications, as the unique fingerprint of the cable changes at the repaired location and is shifted afterwards.

The linear strain and temperature coefficients were experimentally determined for the used cables and the different technologies and can be found in chapter 3.

2.2 Distributed sensing cables

A bare optical fiber can be packaged and protected in such a way that it can be embedded directly into asphalt or other materials (c.f. [36]) without damage during instrumentation, construction and product lifetime. This protected fiber then serves as a distributed sensing cable. Several applications and commercial projects have already been carried out using these types of sensors (e.g. [37]). The optical fiber not only serves as a distributed sensor, but it can as well be used as a signal transport cable, which is a great advantage in terms of cable routing.

2.2.1 Strain sensing cables

For strain sensing applications, it needs to be assured that any externally applied strain on the outer layer is directly transferred down to the sensing fiber without large slippage. Therefore, the cross-section of a strain sensing cable needs to be designed in such a way that the individual protection layers have a good bond between them. In the present project, three different strain cables were installed and tested. They are all manufactured by Brugg Kabel AG (now Solifos AG) in Switzerland and mainly differ in terms of fiber protection and longitudinal stiffness. An overview of the strain and temperature cables is presented in Fig. 7.
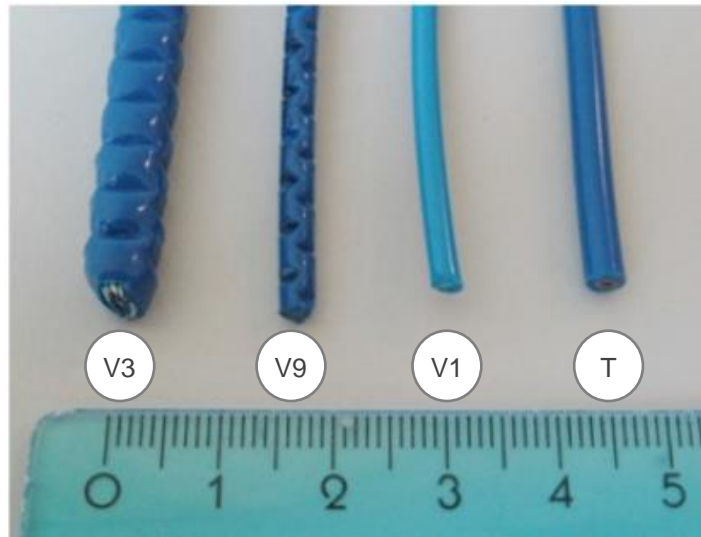
Fig. 7 *Strain (V3-V1) and temperature (T) sensing cables used in the project*

The V1 cable (Fig. 8) is a light, non-metallic and thus sensitive but delicate sensing cable. The fiber is protected by an EPR layer. It is the least protected cable and it was unsure whether it would withstand the harsh conditions during the paving of the asphalt.
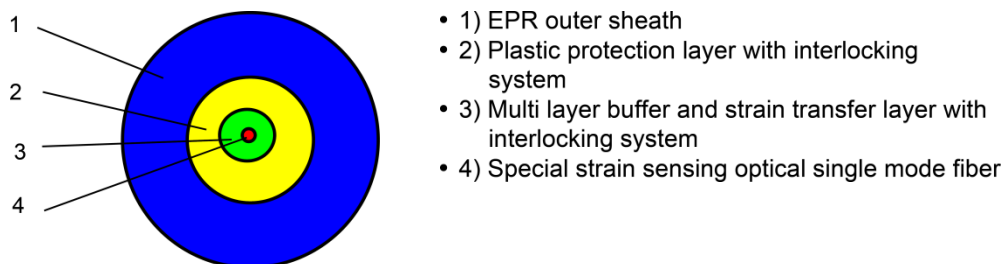

- 1) EPR outer sheath
- 2) Plastic protection layer with interlocking system
- 3) Multi layer buffer and strain transfer layer with interlocking system
- 4) Special strain sensing optical single mode fiber

Fig. 8 *Schematic cross-section of the V3 cable after Product Datasheet Brugg [38]*

The V9 is a more robust sensor (Fig. 9) where the fiber is directly coated by and glued to a steel tube, followed by a structured outer PA layer.

- 1) PA outer sheath, with structured surface with interlocking system
- 2) Metal tube SS316L for protection and hermetic seal
- 3) Multi layer buffer and strain transfer layer with interlocking system
- 4) Special strain sensing optical single mode fiber
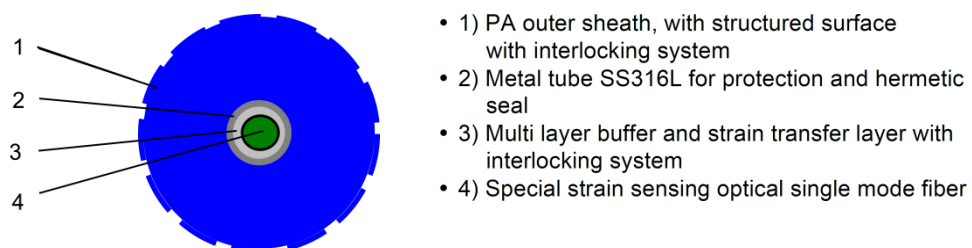
Fig. 9 *Schematic cross-section of the V9 cable after Product Datasheet Brugg [39]*

The V3 cable (Fig. 10) is built on the basis of the V9 cable but has an additional protection layer consisting of steel wires with a lay angle surrounding the inner steel tube, followed by a structured outer PA layer.

- 1) PA outer sheath, with structured surface
- 2) Special grade galvanized steel armoring
- 3) Plastic protection layer with interlocking system
- 4) Metal tube SS316L for protection and hermetic seal
- 5) Multi layer buffer and strain transfer layer with interlocking system
- 6) Special strain optical single mode fiber
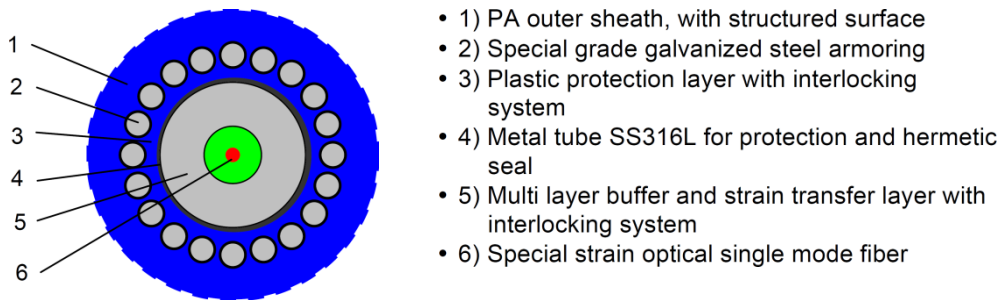
Fig. 10 Schematic cross-section of the V3 cable after Product Datasheet Brugg [40]

The used strain sensing cables differ mainly in terms of mechanical but also slightly in the optical properties. Tab. 1 gives an overview of the properties for the three strain cables.

Tab. 1 Mechanical and optical properties of the used sensing cables [38] [39] [40]

	V1	V9	V3
Strain range [$\mu\varepsilon$]	10'000	10'000	10'000
Diameter [mm]	2.8	3.2	7.2
Long. Stiffness EA (up to 2000$\mu\varepsilon$) [kN] [22]	Approx. 3	59	520
Weight (kg/km)	5.9	10.5	75
Min. bending radius (mm)	56	64	144
Crush resistance (N/cm)	150	250	500
Central Brillouin Frequency (GHz)	10.5	10.6	10.6
Attenuation @ 1550 nm (dB/km)	< 0.5	< 0.5	< 0.5

2.2.2 Temperature sensing cables

In contrast to a strain sensing cable, the fiber in a temperature sensing cable shall be free of any external strain and only deform due to thermal effects. Thus, the fiber is usually loosely embedded inside a steel tube with a certain overlength. The used temperature cable consists of a steel tube embedding the fibers, surrounded by steel wires with a lay angle and followed by a PA outer layer. It is also manufactured by Brugg Kabel AG (Solifos AG) and accommodates 4 SMF (c.f. Fig. 11). An overview of the mechanical and optical properties can be found in Tab. 2.

- 1) PA outer sheath
- 2) Stainless steel wires, 316L
- 3) Stainless steel loose tube, 316L
- 4) Bend insensitive optical fibers with dual layer acrylate coating for increased micro bending performance
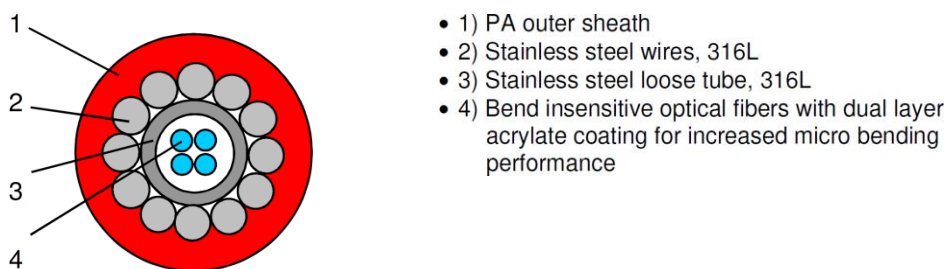
Fig. 11 Schematic cross-section of the temperature cable after Product Datasheet Brugg [41]

Tab. 2 Mechanical and optical properties of the temperature cable [41]

Temp. range (°C)	No. of fibers	Diameter (mm)	Weight (kg/km)	Min. bending radius (mm)	Attenuation @ 1550 nm (dB/km)
-40 … +85	4	3.8	26	76	< 0.25

3   Laboratory tests

Abstract

The present chapter contains the results of the laboratory tests conducted on the fiber optic cables which were foreseen for the application in field tests. In a first test, the effects of high temperatures, as present in the asphalt during construction on the sensor behavior were investigated. The effects of large transverse stress on the sensor, which are present during the lifetime of the sensor close to road surface, were quantified in a second test using a pressure cell.

3.1   Introduction and purpose

The main issue of interest was the impact of the relatively high temperatures during the pouring of the asphalt layers. Depending on the type of bitumen and the thickness of the layer, the asphalt must have a minimum temperature of 120 – 150°C (thickness < 50mm) right before the compaction with rollers [42]. One concern was, whether the sensing cables can physically withstand the temperatures or if they would get damaged. The other consideration was whether the temporarily applied high temperatures would change the strain characteristic of the sensors. In order to test the cable behavior under high temperatures, the cables were placed in an oven and heated up to a maximum of 138°C (c.f. section 3.3). For the investigation of possible changes in the strain characteristics, the strain calibration was determined before and after the heating in the oven in a strain test (c.f. section 3.2 and 3.4).

Another important aspect is the mechanical robustness of the sensing cables to be able to withstand the harsh environment during construction of asphalt layers using a paver and the subsequent compaction by rollers. As it is difficult to reproduce realistic installation conditions in the laboratory, it was decided to directly test all types of cables outside in the course of the real field installations. Different methods for prestraining and protecting the sensing cables were developed and applied. The concern was to prevent single sharp edged granules contained in the asphalt from being impressed in the cable, and the cable from sticking on the paver wheel and getting pulled away and thus damaged. Therefore the cables were either covered with a thin layer of finer asphalt or embedded in a jointing compound before the passing of heavy machinery. Further details are outlined in chapter 4.

All sensors survived the installation process in the asphalt and hence the used prototype sensors in combination with the applied installation methods are appropriate. It was therefore concluded that the available, proven sensing cables are sufficient for the purpose and no further prototypes need to be developed. The focus of the project could consequently be shifted to the field applications.

The radial or lateral pressure on the sensor cable can reach relatively high pressures of up to 1000kPa right under the position of the applied load (wheels). This pressure possibly has an influence on the strain measurements in the sensing cables: there might be a mechanical influence or a fiber-optic effect of the radial or lateral pressure on the measurements. Therefore a first basic test was conducted to get estimate the order of magnitude of a possible influence (c.f. section 3.5). This type of laboratory tests was not originally foreseen in the scope of this research project but was discovered as a possible influence without knowing its extent. Therefore the testing should be regarded as preliminary results with the purpose of roughly estimating the influence of the radial or lateral pressure on strain measurements.

The current chapter describes the different laboratory testing that was carried out in terms of test setup and testing procedure and presents the obtained results. Furthermore, the test results are discussed and further information, such as calibration coefficients, that can be gained are described in detail.

3.2 Strain calibration before heating

3.2.1 Calibration setup and procedure

The strain calibration was performed in a specially designed straining device, in which strain can be applied on the cable stepwise and in a controlled manner (c.f. Fig. 12). The stepwise elongation of the cable to be tested can be applied by a precise step motor at one end of the reference frame and the resulting strain can be calculated using the initial length. A maximum strain of $1000\mu\varepsilon$ was applied in 8 steps of 100 or $200\mu\varepsilon$ each (c.f. Tab. 3 below). The strain calibration was done for both involved measurement technologies, Brillouin and Rayleigh backscattering.

Step motor, load cell, displacement measurement

2.1 m
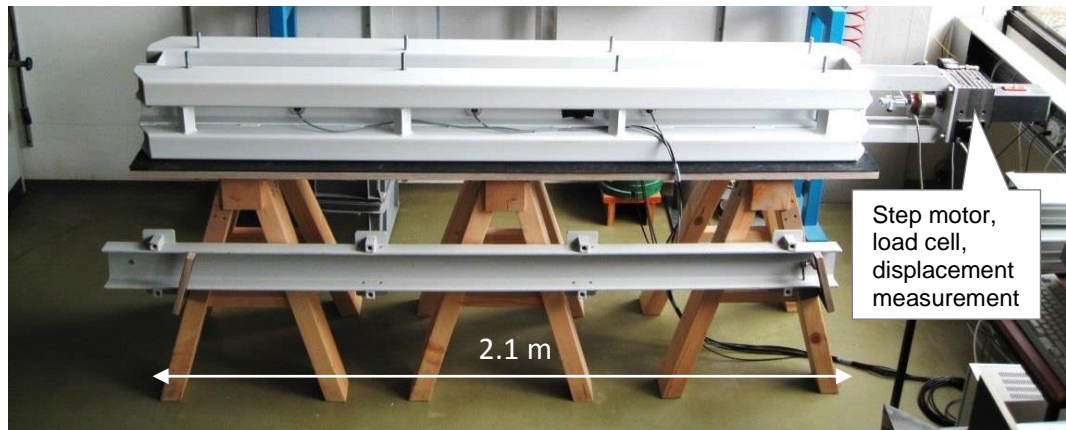
Fig. 12 Pulling device for strain calibration of the cables

Tab. 3 Test program for the strain calibration

Step	0	1	2	3	4	5	6	7
Nominal strain [$\mu\varepsilon$]	0	100	200	300	400	600	800	1000

3.2.2 Measurement results

The following diagrams (Fig. 13 - Fig. 15) show the measured frequency / spectral shift over the elongated section of approx. 2.1 m length for each load step. Measurements were taken with both technologies in each load step for the exact same applied strain. Note that positive strain ($+\Delta\varepsilon$) will result in a positive Brillouin frequency shift ($+\Delta\nu_B$) but in a negative Rayleigh spectral shift ($-\Delta\nu_S$).

3.2.3 Calibration parameters

In a subsequent step, the constant section of the strain level (sections a-b in Fig. 13) can be plotted against the externally applied strain. As the relation between the measured frequency or spectral shift respectively and the externally applied strain is almost linear over the tested range, the strain calibration coefficient can be obtained by fitting a linear regression curve on the data points (c.f. Fig. 16 - Fig. 18).
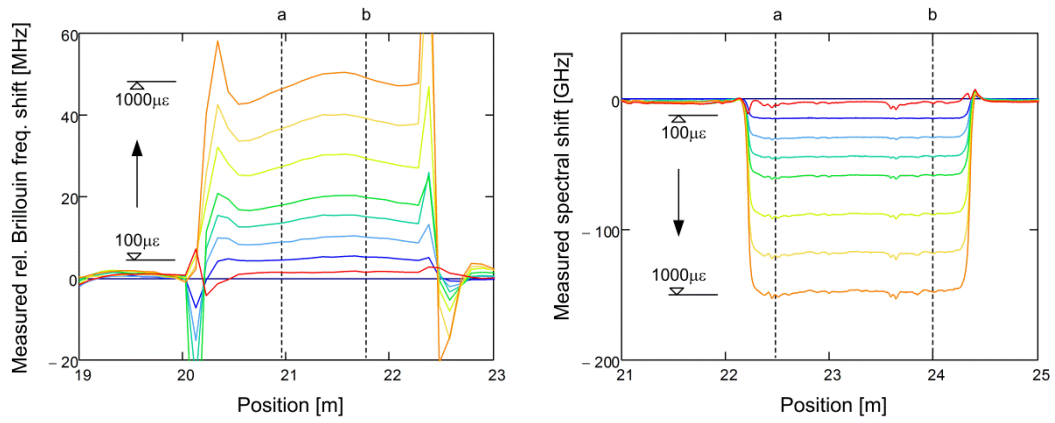
Fig. 13 *Measured frequency shift for each elongation step for the Brillouin (left) and the Rayleigh (right) backscattering of the V9 cable*
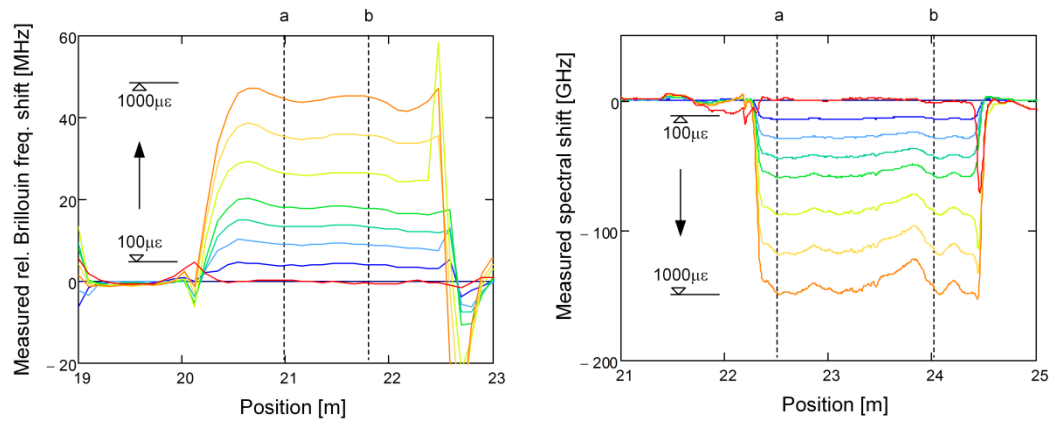
Fig. 14 *Measured frequency shift for each elongation step for the Brillouin (left) and the Rayleigh (right) backscattering of the V3 cable*
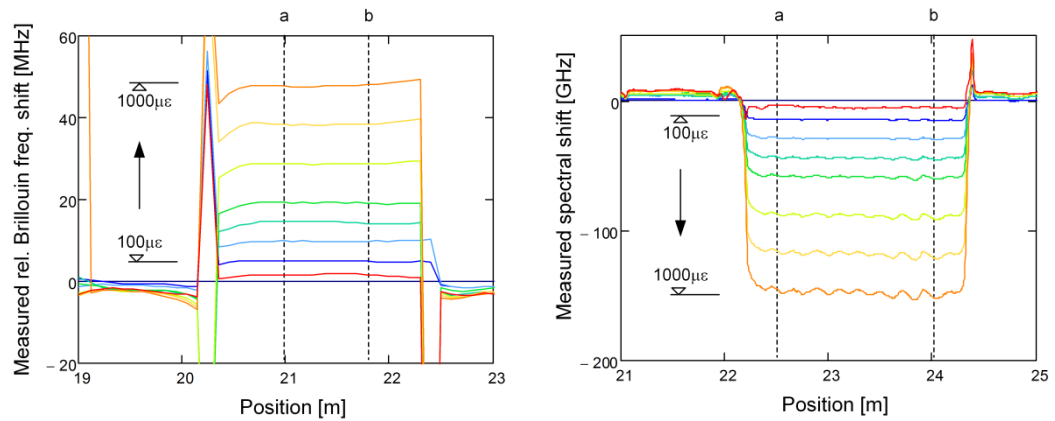
Fig. 15 *Measured frequency shift for each elongation step for the Brillouin (left) and the Rayleigh (right) backscattering of the V1 cable*
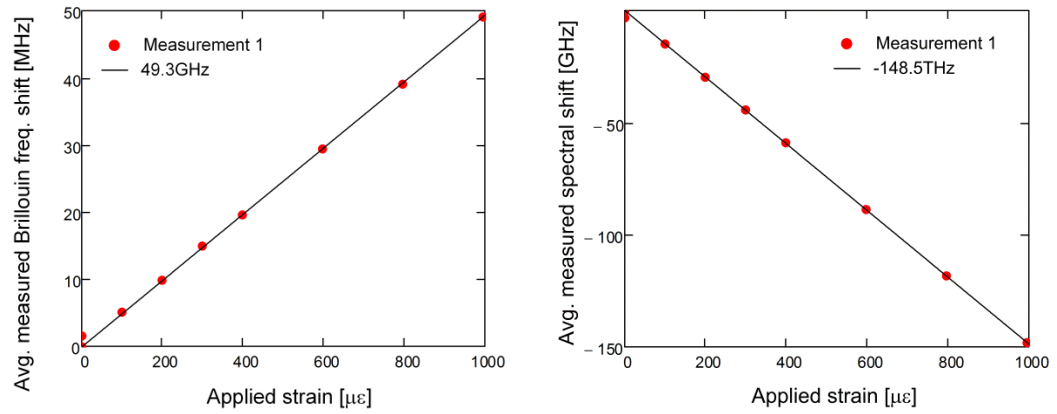
Fig. 16 *Measured frequency or spectral shift against externally applied strain and linear regression for the Brillouin (left) and Rayleigh (right) technology of the V9 cable*
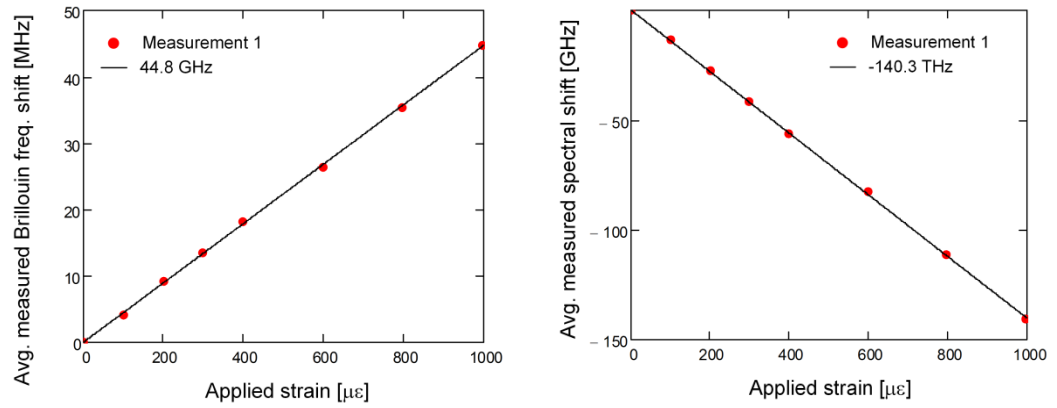
Fig. 17 *Measured frequency or spectral shift against externally applied strain and linear regression for the Brillouin (left) and Rayleigh (right) technology of the V3 cable*
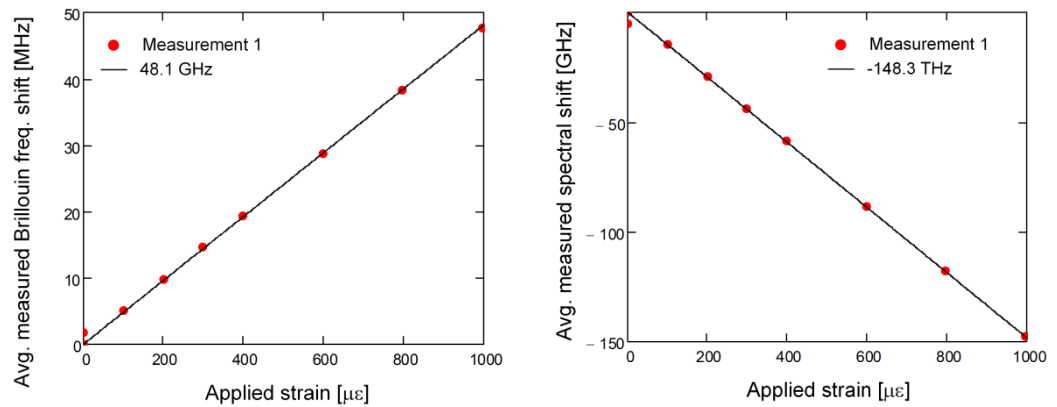
Fig. 18 *Measured frequency or spectral shift against externally applied strain and linear regression for the Brillouin (left) and Rayleigh (right) technology of the V1 cable*

3.3   Temperature calibration

Even though the cables are designed for operating temperatures 'only' up to 85°C according to the manufacturer, it was decided to use them in asphalt where temperatures of up to around 150°C can arise temporarily during paving. Thus it is vital to know if the cables can withstand such temperatures and if so, would the characteristics of the cables change in any aspect.

3.3.1   Testing setup and procedure

All used strain and temperature sensing cables were tested in an oven regarding their behavior under thermal loading (Fig. 19). However, the main purpose of this test was not the investigation of the behavior under temperature. The motivation for this test was only to figure out, whether the high temperatures during paving damage or change significantly the characteristics of the cables. All sensing cables were connected together in series and were coiled up to fit in the heating chamber of the oven. The setup was subsequently heated up stepwise from room temperature up to a maximum temperature of 138°C and was subsequently let cool down to room temperature again (c.f. Tab. 4). As before, measurements using both involved sensing technologies (Brillouin and Rayleigh backscattering) were performed.

Note that during temperature exposure of an unconstrained "free" cable frequency shifts will be measured owing to a pure thermal effect of temperature on the fiber and, in addition, owing to thermal expansion of the cable, which induces longitudinal strain. In a theoretically completely constrained cable, which cannot experience thermal expansion, only frequency shifts owing to a pure thermal effect of temperature on the fiber would be measured. As a test, one section of 30cm length was prestrained against a frame made of Invar which has a very low coefficient of thermal expansion. This section was implemented to attempt to see initially the separate influences of the thermal expansion and thus induced strain in the cable and the pure thermal effect occurring within the fiber. Of course, as soon as the thermals expansion of the cable exceeds prestraining, it cannot be separated anymore.

Fig. 19: *Setup for testing the thermal behavior of the sensing cables*

Tab. 4 Test program for the thermal loading of the sensor cables

Heating phase						Cool down phase	
22°C	39°C	59°C	78°C	99°C	138°C	84°C	21°C

3.3.2 Measurement results

A typical set of results (V9 cable) for the heating phase (Fig. 20) and for the whole testing cycle (Fig. 21) is shown below. For the remaining cables, only the diagram containing the whole cycle is shown to be able to identify the irreversible spectral/frequency shifts (black line) after the cooling down of the cables (Fig. 22 - Fig. 28). For the Brillouin backscattering, positive changes in temperature ($+\Delta T$) result in a positive Brillouin frequency shift ($+\Delta\nu_B$), whereas a negative spectral frequency shift ($-\Delta\nu_S$) occurs for the Rayleigh backscattering.
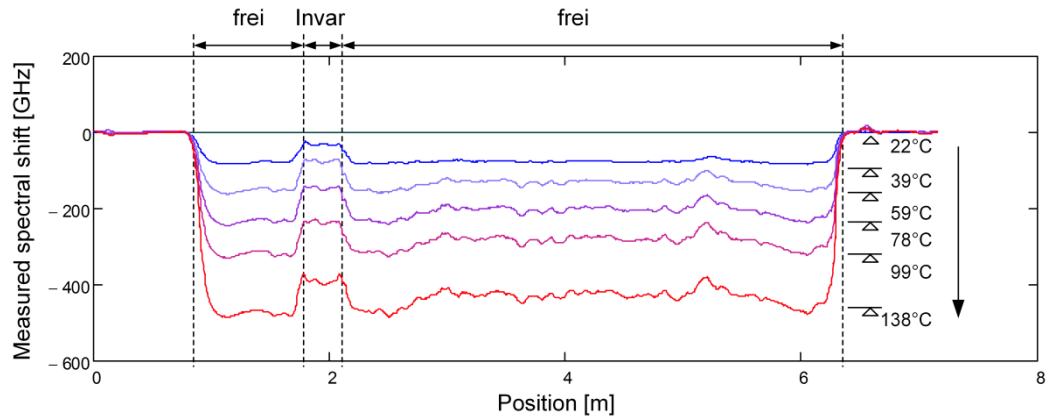
Fig. 20 Measured spectral shift in the V9 cable during heating using Rayleigh backscattering based sensing technology
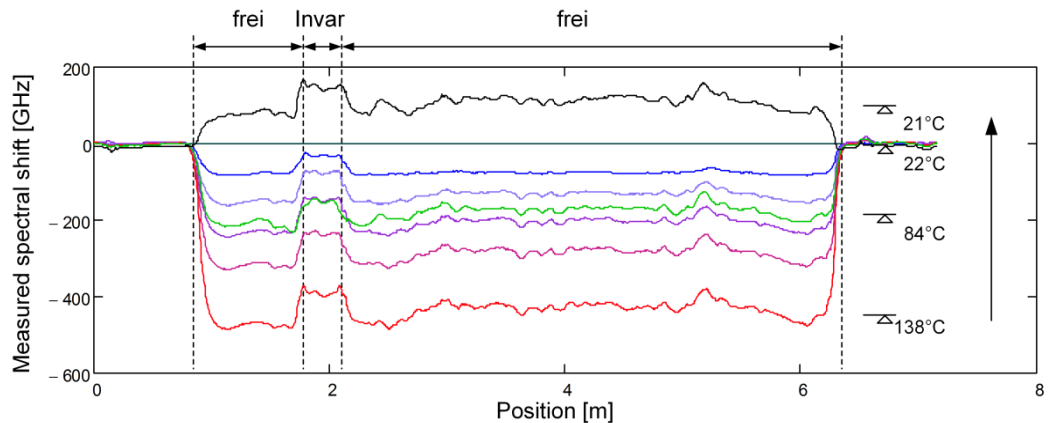
Fig. 21 Measured spectral shift in the V9 cable over the whole testing cycle using Rayleigh backscattering based sensing technology
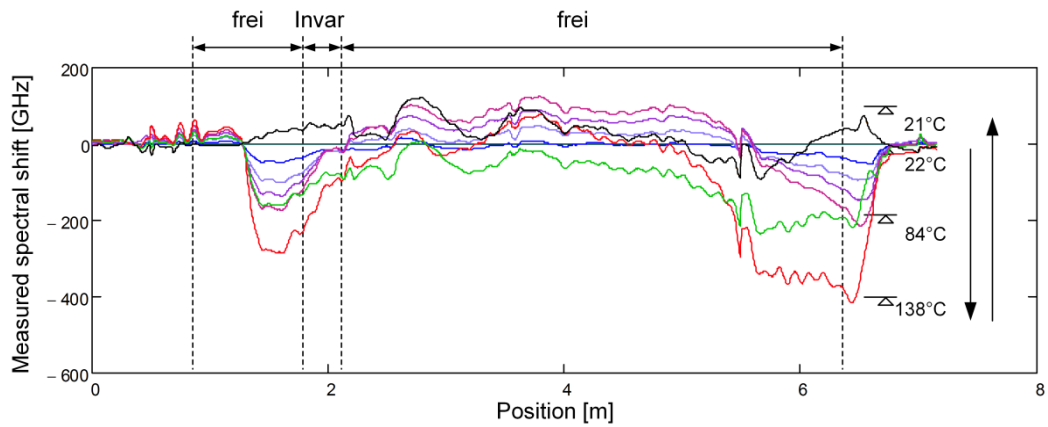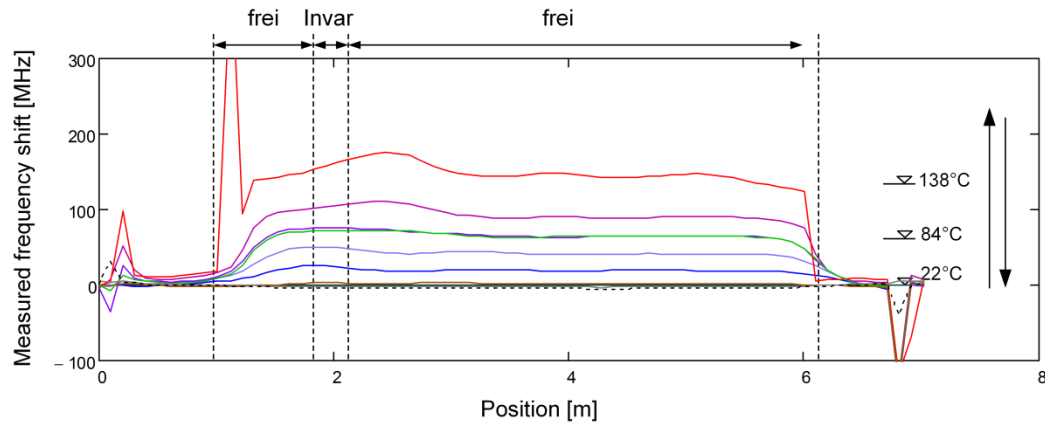
Fig. 22 *Measured spectral shift in the V3 cable over the whole testing cycle using Rayleigh backscattering based sensing technology*
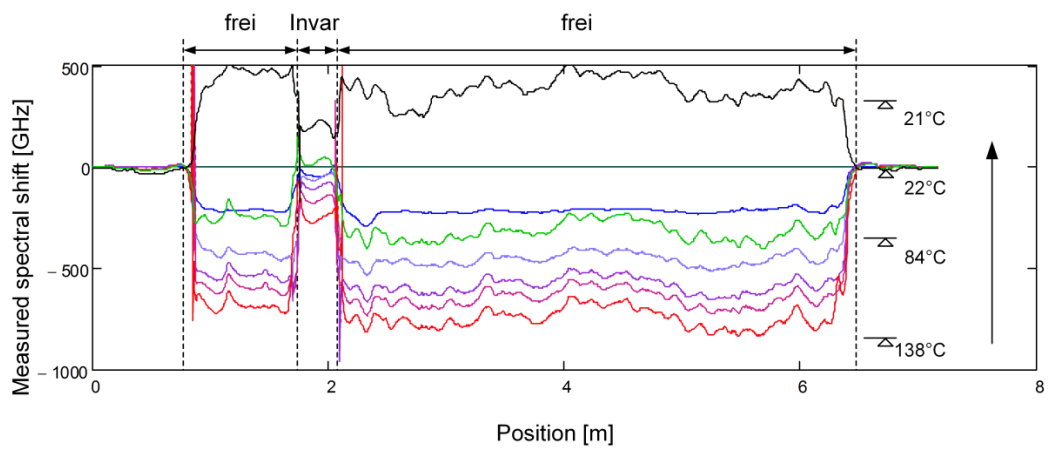
Fig. 23 *Measured spectral shift in the V1 cable over the whole testing cycle using Rayleigh backscattering based sensing technology*
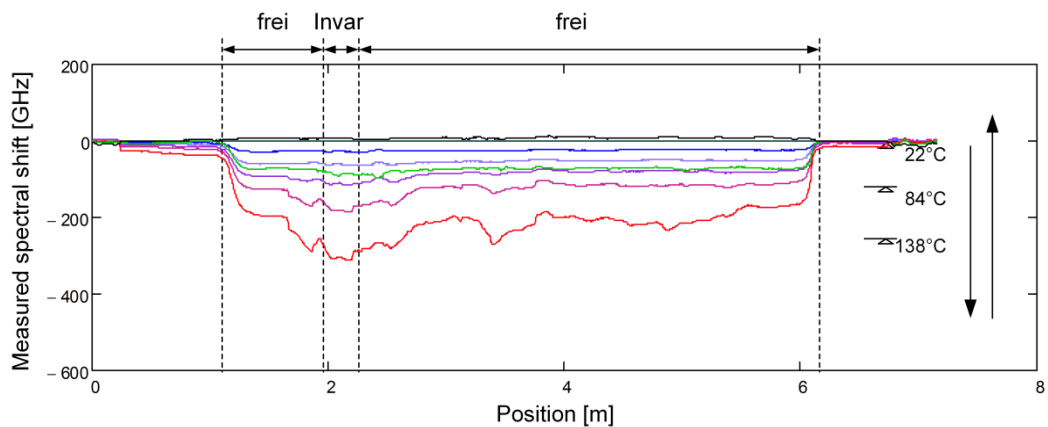
Fig. 24 *Measured spectral shift in the temperature cable over the whole testing cycle using Rayleigh backscattering based sensing technology*

The following diagrams (Fig. 25 - Fig. 28) show the measured Brillouin frequency shift for the same set of cables.
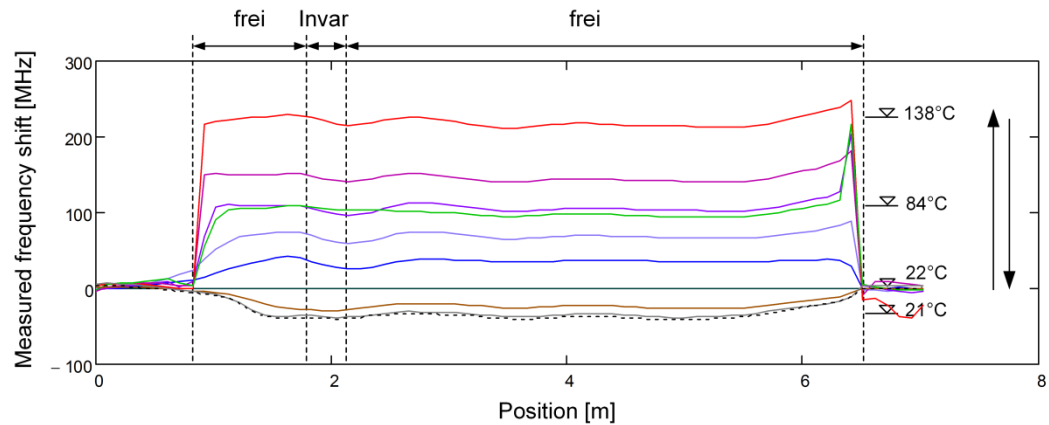
Fig. 25 *Measured spectral shift in the V9 cable over the whole testing cycle using Brillouin backscattering based sensing technology*
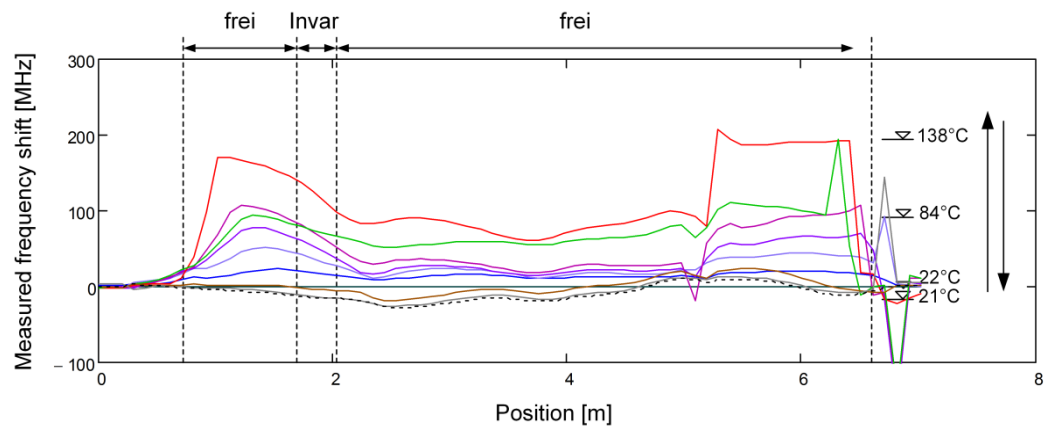
Fig. 26 *Measured spectral shift in the V9 cable over the whole testing cycle using Brillouin backscattering based sensing technology*
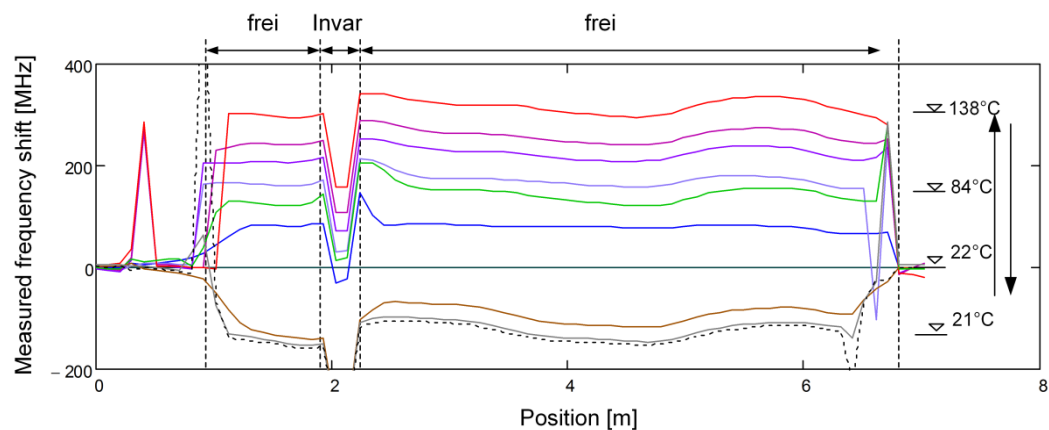
Fig. 27 *Measured spectral shift in the V1 cable over the whole testing cycle using Brillouin backscattering based sensing technology*

***Fig. 28** Measured spectral shift in the temperature cable over the whole testing cycle using Brillouin backscattering based sensing technology*

3.3.3 Average frequency shifts

The measured frequency shift shows for some cables a strongly heterogeneous response along the cable, which may potentially be caused by the non-homogenous thermal expansion of the cable layers. In order to assess the average behavior, the measured frequency / spectral shift between 2.5 and 5.0m (free cable section) along the cable was averaged and plotted against the externally applied temperature difference ΔT (c.f. Fig. 29).
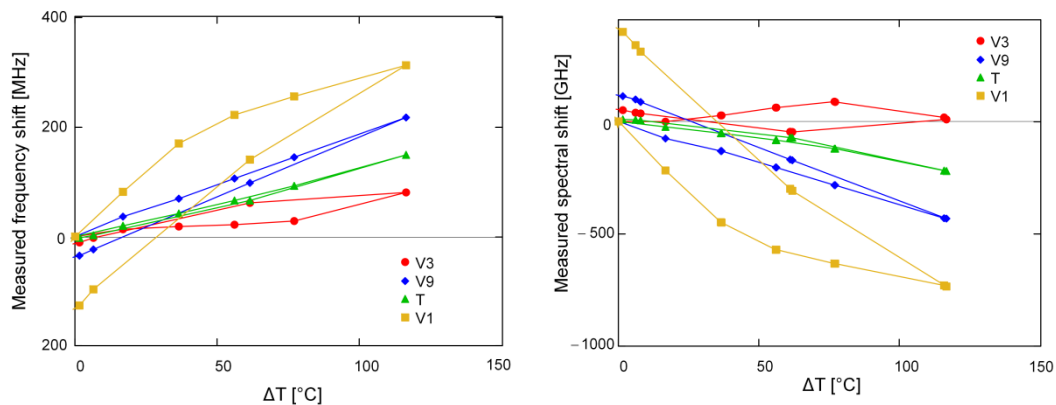
***Fig. 29** Measured frequency shift plotted against the externally applied temperature for all involved cables and the Brillouin (left) and the Rayleigh (right) technology*

The "free" strain cables mostly show a non-linear and a different behavior for the heating and cool down phase. This might be caused by the specific behavior of the cable sheath materials. It often results in an irreversible frequency shift. Therefore, a meaningful definition of a constant C'_T (unconstrained cable) is not possible for the strain cables. In particular the temperature response of the unconstrained V3 cable is difficult to interpret. A similar behavior can be observed for the strain cables in the section that was prestrained against the Invar frame (c.f. Fig. 30), since the prestraining is lost at a very early stage owing to thermal expansion of the cable. Note that the cables are designed for temperatures only up to 85°C according to the manufacturer.
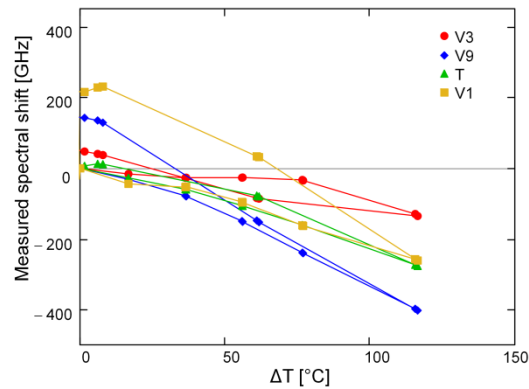
Fig. 30 *Measured frequency shift plotted against the externally applied temperature for all involved cables and the Rayleigh (right) technology in the prestrained section*

The temperature cable shows a more linear behavior, especially for lower temperatures. Here, a thermal coefficient C'_T may be calculated (c.f. Tab. 5 and Fig. 31). One however has to keep in mind that the test setup with non-constrained temperature cables does not reflect fully the circumstances in the field, where the cable is constrained due to the asphalt. This is even more pronounced for the strain sensor cables V1, V3 and V9. The coefficients in Tab. 5 are only informative for this project.

Tab. 5 Thermal coefficients for the temperature cable (free section)

$C'_{T, Brillouin, loose}$	$C'_{T, Rayleigh, loose}$
1.17 MHz / °C	- 1.48 GHz / °C
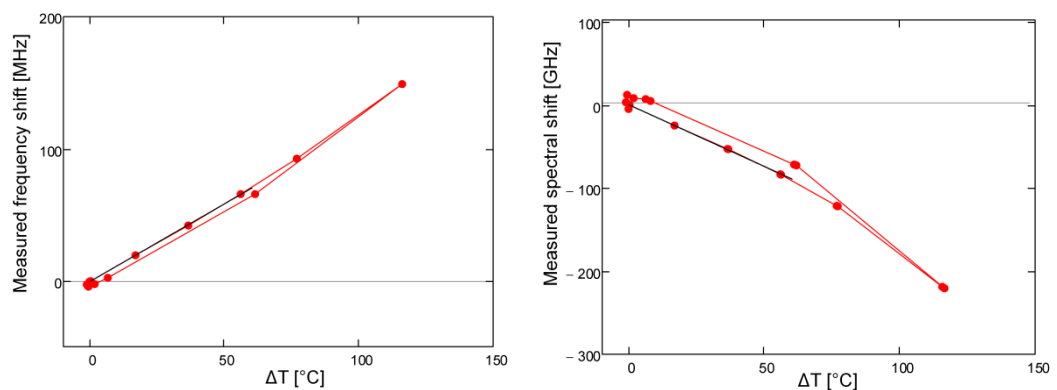
Fig. 31: *Measured frequency or spectral shift against externally applied temperature change and linear regression for the Brillouin (left) and Rayleigh (right) technology of the temperature cable*

3.3.4 Discussion

It can be stated that all tested cables can withstand temperatures of almost 140°C for one hour or more without notable damage. Bearing in mind that the cables are placed on a colder surface and are only partially exposed to the hot asphalt, this cables survive the temperatures occurring during the paving.

The cables have very different behaviors under thermal loading as can be seen in Fig. 20 to Fig. 28. The Temperature cable shows below 85°C (foreseen temperature range according to the manufacturer) probably the most homogeneous response, beyond this temperature some heterogeneity is recorded, which can be caused partially by the test

setup (imperfect temperature field) but is more likely to be caused by the cable sheath layers itself. Similar heterogeneity can be observed for the V1 and V9 cable. For the non-metal cable V1, the averaged frequency shift is observed to be strongly non-linear with temperature (Fig. 30).The V3 cable in general has a strongly non-uniform frequency / spectral shift distribution along the fiber and shows contrary frequency / spectral responses along the cable with increasing temperatures. This irregular behavior might originate from the spirally wound steel wires in the cross-section of the cable.

The section which was prestrained against the Invar frame shows a smaller change in frequency or spectral shift in comparison with the loose section for the strain cables. For the temperature cable, no such effect can be observed in the Invar section (loose tube). In a first phase of heating, the thermal expansion only diminishes the prestraining and no elongation is applied on the fiber and only the pure thermal effect on frequency shift is measured. In a second phase, after the prestrain is lost, the same frequency or spectral shift as in the loose section can be observed. The measurements in the Invar section thus allow theoretically for a determination of the pure thermal frequency shift that is occurring within the fiber, without the additional effect of thermal expansion of the cable sheath. However, the setup is working clearly better for a temperature decrease after prestraining than for a temperature increase after prestraining.

As mentioned above, an irreversible frequency/spectral shift remain in some cables after cooling them down to room temperature again. The irreversible part is negative for the Brillouin frequency shift and positive for the Rayleigh spectral shift. For the Rayleigh backscattering, a positive frequency shift ($-\Delta\nu_S$) is induced either through a negative change in temperature or negative change in strain (shortening of the cable). For the Brillouin technology signs are opposite. As the temperature difference is almost zero, the induced frequency shift must be caused by a permanent shortening of the cable due to the applied high temperatures. This is presumably also caused by the characteristics of the plastic material that is used for the coating of the cables. Using the previously obtained strain coefficients, the irreversible frequency / spectral shift can be converted into a strain. Tab. 6 gives an overview of the irreversible strain in each cable after the heating in the loose section of the cables for the two technologies. The irreversible strains correspond well between the two technologies for all cables except the V3 cable.

Tab. 6 Irreversible strain after heating for each cable and technology

Technology	V3	V9	T	V1
Brillouin	-292με	-786με	-4με	-2850με
Rayleigh	-368με	-798με	12με	-2837με

The temperature behavior of the cables is very complex and a full understanding of it could not be elaborated in the course of this work. It remains unclear if the irreversible and non-linear behavior is a recurring phenomenon or if the linearity might be improved in second heating of the cables. This and many other aspects need to be further investigated to get a better understanding of the temperature behavior of the embedded cables. As the duration of a real field test in this project was short, no temperature compensation or correction was required and thus the limited understanding of the temperature behavior can be accepted for the evaluation of the current testing. For other applications, out of the scope of this study, where simultaneously strain and temperature changes occur and the host material is rather soft, the thermal behavior needs to be investigated further.

3.4 Strain calibration after heating

The same strain calibration procedure in the pulling device (as described in section 3.2.1 above) was carried out again after heating up the cables. This was to simulate the process of embedding the cables in hot asphalt and thus to discover possible changes in the strain behavior of the cables after their installation.

3.4.1 Measurement results

The following diagrams (Fig. 32 - Fig. 34) show the measured frequency/spectral shift over the elongated section of approx. 2.1m length for each load step as above. The plots show two curves for each load step, one representing the measurement before and one after the heating of the cables.
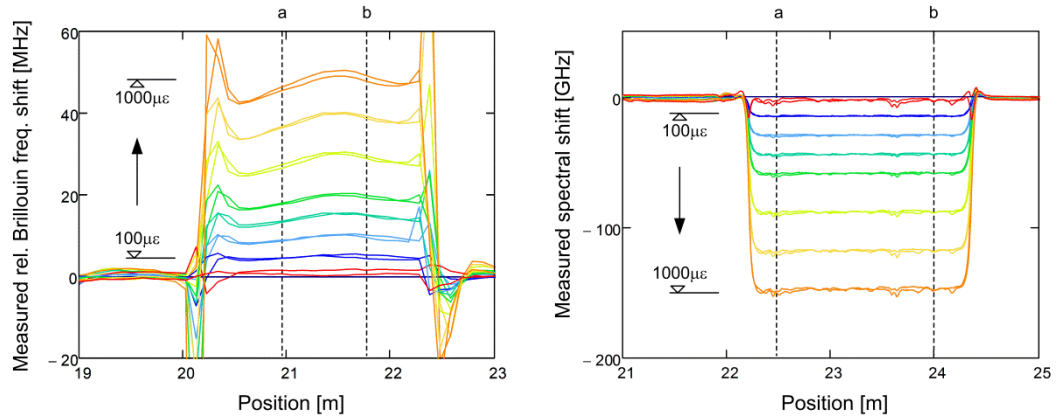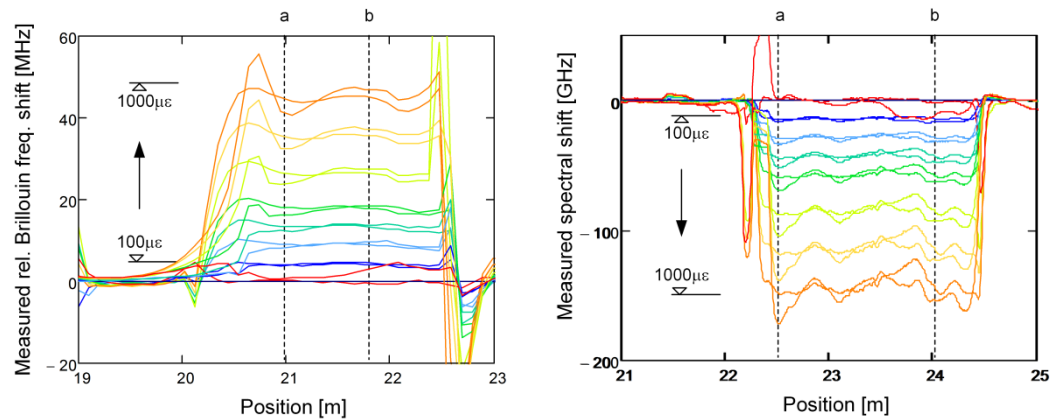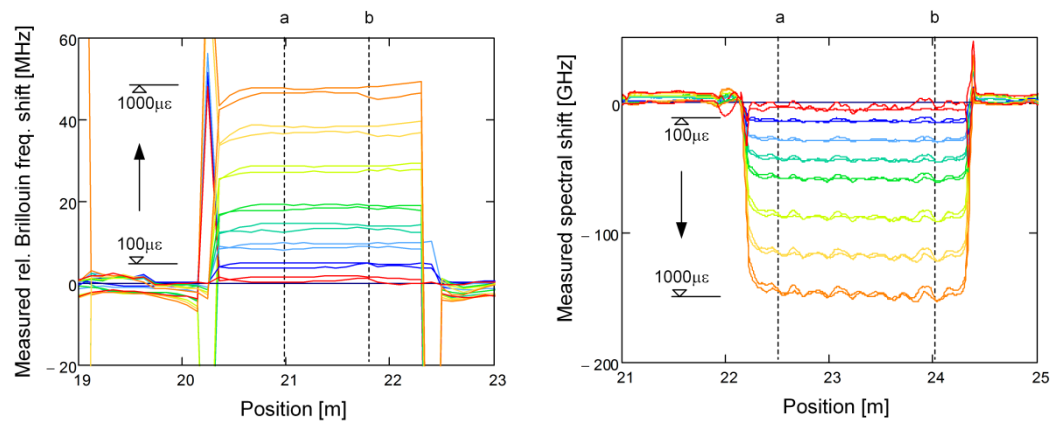

Fig. 32 *Measured frequency shift before and after heating for each elongation step for the Brillouin (left) and the Rayleigh (right) backscattering of the V9 cable*

Fig. 33 *Measured frequency shift before and after heating for each elongation step for the Brillouin (left) and the Rayleigh (right) backscattering of the V3 cable*

Fig. 34 *Measured frequency shift before and after heating for each elongation step for the Brillouin (left) and the Rayleigh (right) backscattering of the V1 cable*

3.4.2 Calibration parameters

The constant strain section (section a-b in Fig. 32) for both calibration tests can again be plotted against the externally applied strain. This allows for a direct comparison of the strain behavior of the cables before and after the heating of them (c.f. Fig. 35 - Fig. 37).
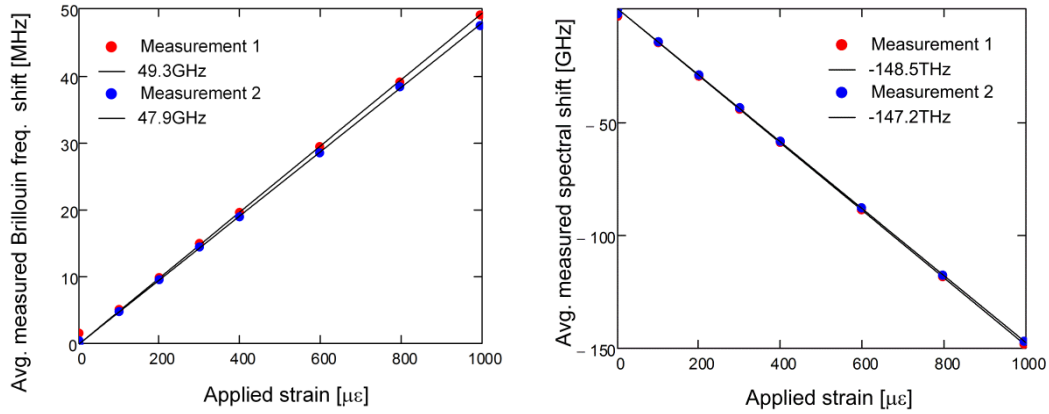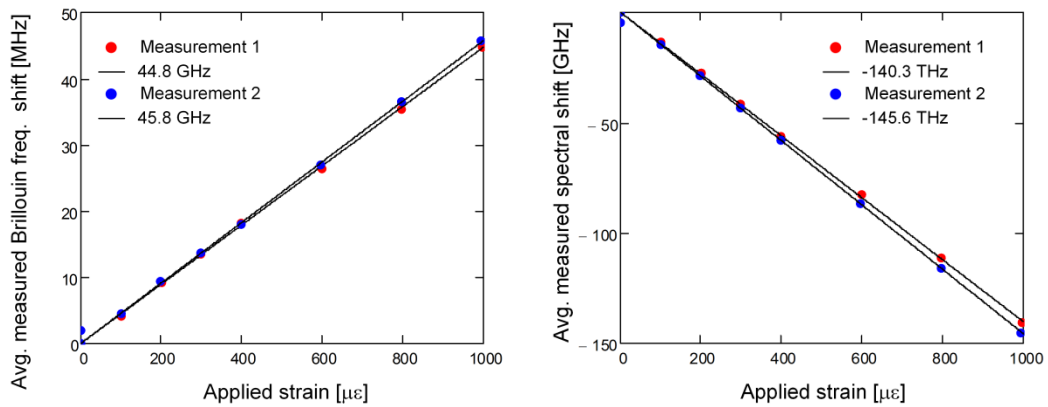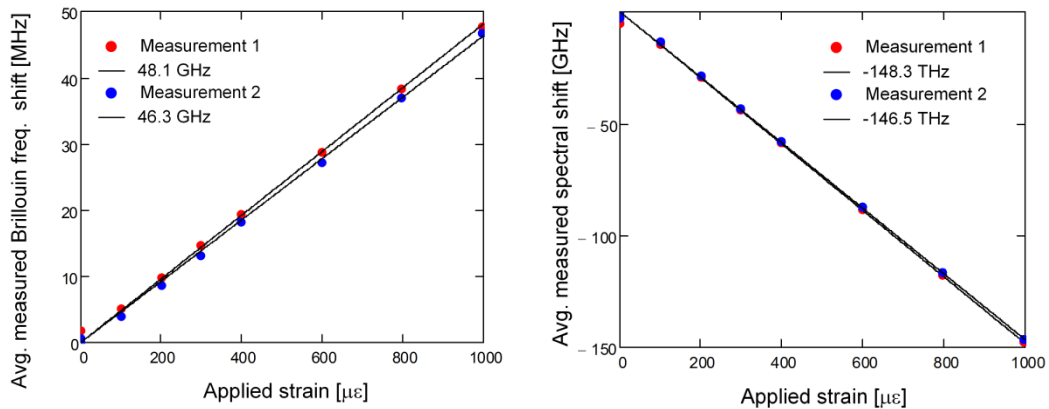

Fig. 35 *Measured frequency or spectral shift against externally applied strain and linear regression for the Brillouin (left) and Rayleigh (right) technology of the V9 cable*

Fig. 36 *Measured frequency or spectral shift against externally applied strain and linear regression for the Brillouin (left) and Rayleigh (right) technology of the V3 cable*

Fig. 37 *Measured frequency or spectral shift against externally applied strain and linear regression for the Brillouin (left) and Rayleigh (right) technology of the V1 cable*

The following Tab. 7 and Tab. 8 show an overview of all strain calibration factors for both technologies before and after heating.

Tab. 7 Strain coefficient before and after heating for the Brillouin backscattering

	V3	V9	V1
Strain coefficient before heating (GHz)	44.8	49.3	48.1
Strain coefficient after heating (GHz)	45.8	47.9	46.3

Tab. 8 Strain coefficient before and after heating for the Rayleigh backscattering

	V3	V9	V1
Strain coefficient before heating (THz)	-140.3	-148.5	-148.3
Strain coefficient after heating (THz)	-145.6	-147.2	-146.5

3.4.3 Discussion

The fitted strain coefficients C_ε correlate well when comparing before and after heating for the V9 and V1 cable. For the Brillouin technology, the deviation is around 3 %, whereas for the Rayleigh it is generally around 1% or less (for details see Tab. 9). The correlation for the V3 cable is unusual, especially the high deviation for the Rayleigh technology, c.f. below. The Brillouin technology shows mostly higher deviations compared to the Rayleigh technology which reflects the measurement repeatability of the two measurement systems.

Tab. 9 Relative deviation of the strain coefficient before and after heating

Technology	V9	V3	V1
Brillouin	-2.8 %	2.2 %	-3.7 %
Rayleigh	-0.8%	3.8 %	-1.2 %

The V3 cable shows a rather unexpected behavior, as the deviation for the Rayleigh measurements is unusually high, whereas the deviation for the Brillouin measurements is rather small. Additionally the signs are opposite comparing with the V9 and V1 cable. This could be caused by internal slippage or a slight slack of the cable at the beginning of the tensile test before heating (Meaning that potentially the observed deviation might not be caused by the heating of the cable but by two not fully corresponding tensile tests (slight initial slack)). Further measurements would be required in order to understand this small deviation to the full extent, which would maybe also require an adaption of the test setup, since the difference is rather small (measurement precision of the externally applied strain).

The deviations between the two tests before and after the heating seem therefore mainly to occur due to minor variances in testing conditions and slight internal slippage in the cable. It is assumed that the slippage around the cable fixation only occurs due to the large strain gradients that are applied at this location. The slacking as disadvantageous testing condition and such high strain gradients do not normally develop in the field. In addition, other factors, such as the measurement precision during the testing, also influence the deviation.

Therefore it can be concluded, that the strain behavior does not change significantly due to the heating of the cables and the obtained strain coefficients can be applied for strain determination in the field tests. Moreover the coefficients before and after heating are known and can be adjusted situational.

3.5 Hydrostatic pressure

Local contact pressures (typically under a tire) and therefore the load in the asphalt and on the sensing cable can rise to high levels. It can reach slightly more than 1000kPa under a tire of an airplane or more than 600kPa under a truck wheel. The possible influence of this radial or lateral pressure on the measurements in the strain sensing cables was investigated in a hydrostatic pressure tests. Such a test is easier to conduct and easier to interpret than for example a more realistic lateral pressure element test with applied lateral pressure. Furthermore, the influence in a hydrostatic pressure test is presumably higher than in a lateral pressure element test.

3.5.1 Testing setup

The pressure chamber of a triaxial test apparatus was used to apply pressures of up to 1000kPa on the sample sensing cables. Several samples of different sensing cables with a length of 2m were tested (c.f. Tab. 10). All cable samples to be tested were connected together using loose tube connecting cables of 1m length to clearly separate the individual sample. The chain was fixed on a supporting structure in an oval shape and placed in the pressure chamber (c.f. Fig. 38). The chamber was subsequently completely filled with deaerated water to allow for a quick and proper application of the pressure on the sensing cables.

Tab. 10 Cable samples tested under hydrostatic pressure

Identification	Cable Type	Manufacturer	Diameter	Stiffness (up to 2000$\mu\varepsilon$)
V1	Strain	Brugg Kabel AG	2.8mm	Approx. EA = 3kN
V3	Strain	Brugg Kabel AG	7.2mm	EA = 520 kN
V9	Strain	Brugg Kabel AG	3.2mm	EA = 59 kN
Vollader	Strain	Brugg Kabel AG	0.9mm	n.a.
T	Temperature	Brugg Kabel AG	3.2mm	n.a.
Bare Fiber	Strain	Brugg Kabel AG	0.25mm	n.a.
Loose Tube	Temp	Huber & Suhner AG	0.9mm	n.a

During testing, the pressure was increased stepwise up to 1000kPa as detailed in Tab. 11. Measurements using both involved sensing technologies (Brillouin and Rayleigh backscattering) were performed to get a complete set of data. A first test was conducted straight after filling the pressure chamber. Thereafter, the setup was left in water for a month and subsequently another test was performed. This procedure was chosen to investigate possible effects or influence of differently saturated cable coatings.

Tab. 11 Load steps during hydrostatic pressure test

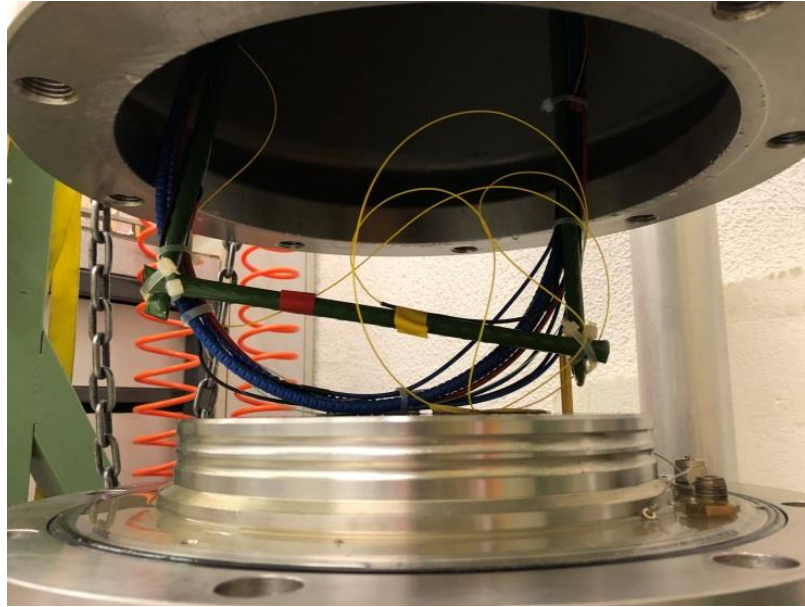| Step	0	1	2	3	4	5	6	7	8	9	10	11
Pressure (kPa)	0	50	100	200	300	400	500	600	700	800	900	999

Fig. 38 *Cable samples during placement in pressure chamber*

3.5.2   Results

For better comprehension, the measured frequency/spectral shift was averaged over the length of the cable sample and converted to an equivalent strain change. This does not mean that the shift was necessarily caused by a mechanical strain. The shift may also originate from a pressure dependent effect that was initiated in the fiber. A clear distinction between the two effects cannot be made on the basis of these measurements. The results for the two different technologies can be found in Fig. 39 and Fig. 40.

Fig. 39 *Equivalent strain difference due to hydrostatic pressure for the Rayleigh technology*

Strain change under hydrostatic pressure (Brillouin backscattering)

Fig. 40 *Equivalent strain difference due to hydrostatic pressure for the Brillouin technology*

As no significant difference between the test conducted right after the filling of the pressure chamber and one month later was revealed, only one set of results is presented here.

The results of the Brillouin technology measurements show a more fluctuating behavior compared to the measurements with the Rayleigh technology. This presumably originates from the higher spatial resolution of 1m and the lower repeatability of the Brillouin technology.

3.5.3 Discussion

The cables reveal a linear dependency between the applied hydrostatic pressure and the measured frequency/spectral shift or a calculated equivalent strain. This dependency appears clearer in the Rayleigh measurements, but can also be observed for some cables using the Brillouin technology. It is notable that the frequency/spectral shift response is positive for some cables while it's negative for others.

The induced frequency / spectral shift is very small and varies in terms of strain between +10 and -40$\mu\varepsilon$ for a pressure difference of 1000kPa. The comparison between the two involved technologies shows a similar tendency, especially for the V3, V9, Vollader and the H&S loose tube cables, however the magnitude can significantly vary.

The interpretation of the measurement results or the extraction of a pressure dependent effect at these pressure levels is difficult due to several reasons:

- The frequency / spectral shift could be induced by a combination of a pressure dependent effect occurring within the fiber or by a longitudinal, mechanical strain that is induced trough transverse elongation due to the hydrostatic pressure. These two components cannot be separated unambiguously.
- Frequency/spectral shifts may be positive or negative. This is not straightforward to explain and might indicate a combined influence of the above mentioned effects.

As the measured influence for the maximum pressure is relatively small, it was decided that the hydrostatic / lateral pressure does not have to be taken into account as a significant influence for the current project. As a comparison, a few degrees change in temperature would have the same influence on the cables. It is however suggested that the aspect is followed further to be able to definitely exclude or quantify the influence of the lateral pressure on the measured spectral / frequency shift (see section 3.6).

3.6 Lateral pressure element test

The testing of an asphalt element with an embedded sensing cable by applying a lateral pressure on the cable would be a continuative and more realistic test for investigating the effects of lateral pressure.

It is assumed that the effectively acting pressure on the cable in a lateral pressure element test is smaller than in a hydrostatic pressure test (c.f. section 3.5). For this reason and due to time constraints no testing under lateral pressure was carried out in the course of this project. Ideas of how such a test could be designed are available as picture in Fig. 41.
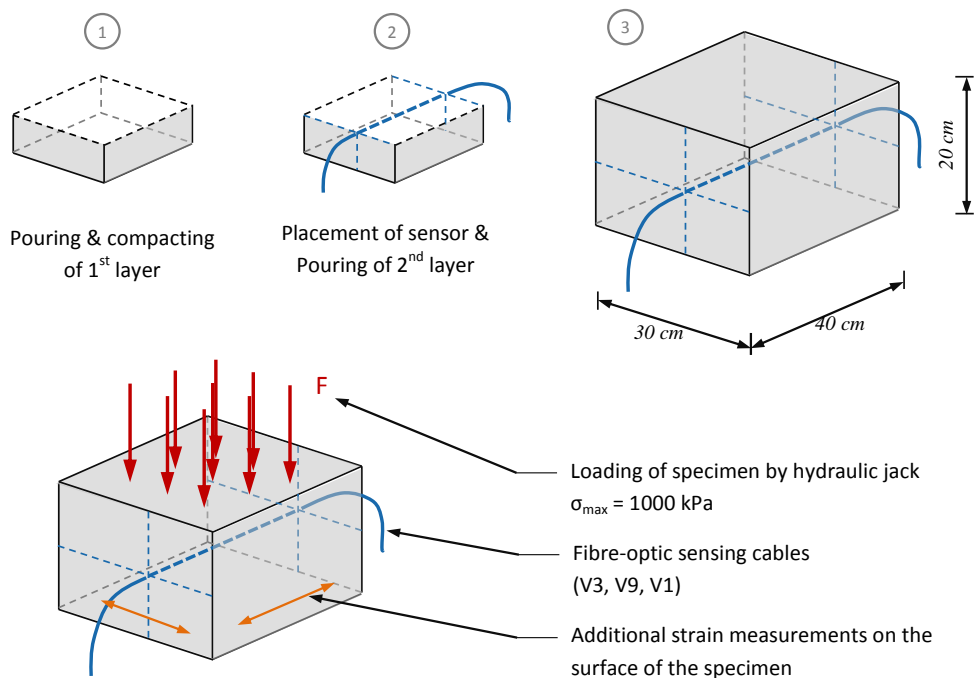
Fig. 41 Preliminary design of a lateral pressure element test

For a concluding assessment, either such a test needs to be carried out or the above assumption, that the influence in a lateral pressure test is smaller than in a hydrostatic test, should be verified.

3.7   Discussion

The most important and fundamental conclusion out of the laboratory testing is that all tested sensing cables are suitable for field installations in the very harsh environment while paving the new asphalt layers. This includes the influences of mechanical impacts and the influence of the high temperatures during the paving.

No significant changes in the strain behavior were observed before and after the exposure to the high temperatures during paving (except the not fully understood small deviation of the V3 cable). This is a reassuring outcome in regard to the strain sensing. Furthermore the strain calibration coefficients are known before and after the exposure to heat.

The temperature sensitivity showed, dependent on the cable, a more or less strong non-homogeneous and non-linear behavior, especially above 85°C (which is the maximum temperature for application according to the manufacturer). It is in general difficult to interpret or to extract temperature coefficients out of it. In particular the strongly non-homogeneous response along the V3 cable might cause in other applications where simultaneous strain and temperature changes occur in rather soft host materials, create difficulties in data interpretation. However, for the present project, no temperature compensation was required and therefore this behavior was not affecting the measurements.

In addition, the high lateral pressure of up to 1000kPa that can occur under a tire of an airplane or a truck was investigated as the potential influence on the strain measurements was unknown. As a first approximation, a hydrostatic pressure test was carried out on several sensing cables. The results showed a minor influence and therefore it was decided that the lateral pressure does not have to be taken into account for the assessment of the measurement results. For a closing reassurance, a lateral element test should be conducted.

4 Field installation methods

Abstract

Asphalt is a rather harsh environment for the fiber optic sensors. Hence, the installation of the fiber optic cables represents an important task for the successful instrumentation of a road. Furthermore, the embedment of the sensors should be kept simple, in order not to create too many additional difficulties in the road construction process. The different methods of cable installation in this research project are summarized and assessed in the present chapter.

4.1 Requirements

The proper installation of the cables is a very important aspect with regards to the functionality of the complete sensing system. The method must fulfil a number of requirements and properties, as listed below:

- Firstly, and most important, the sensing cables have to survive the harsh conditions during the installation and must be protected well enough against the heavy mechanical loads of the passing asphalt paver. This also includes the high temperatures of up to around 150 °C that can arise in the asphalt.
- It must be possible to prestrain the sensors, so that a defined strain state can be achieved for the measurements.
- Furthermore, the placement of the sensing cables must allow a good bonding between the sensing cable and the surrounding material layer.
- Reproducibility and reliability: the technique shall be repeatable in a reliable and good quality for long-term installations.
- The procedure needs to be as rapid as possible, as the time frame for the instrumentation on site is usually short.

Different methods for the sensor protection, the prestraining of the sensor and bonding techniques can be applied, depending on the substrate layer and the afore chosen method of prestraining.

4.2 Prestraining methods

The prestraining is usually performed over one or several individual sections to achieve an as homogeneous prestrain as possible.

4.2.1 Cable clamps with screws

The fixation of the cable for prestraining is achieved by the friction between the cable and the substrate layer that is generated by the clamp which is screwed against the asphalt (c.f. Fig. 42). The clamps are specially designed to match the cable diameter in order to apply an adequate pressure to guarantee the required friction while not damaging the cable or disturbing the optical properties at the clamping location. It is a straightforward and reliable fixation procedure and the preferred technique to fix cables on bituminous or stabilized layers if the screw grips. The best screw type has to be determined depending on the mixture that is used for the installation. Screws are however not suitable for use in granular soil.

4.2.2 Cable clamps with corrugated steel nails

In principle, this method is identical to the above described method, only that nails are used to press the clamp on the substrate instead of screws. In general, this method is slightly less controllable and reliable compared to screwing the clamps on the substrate layer. However on certain bituminous layers on which the screws do not have enough

grip, the fixation using steel nails can be a valuable alternative. The lower anchorage performance of the nails can lead to cases where not enough friction can be mobilized through the pressure of the clamp to fix the cable. In such cases it can be necessary to additionally attach the cable at the clamp to prevent slippage of the cable under it. The use of corrugated steel nails is also suitable for bituminous layers but not for granular soil.

4.2.3   Cable clamps with peg

In granular and non-stabilized soil layers, screws or nails usually do not provide enough support nor is the screwing or hammering possible. Therefore, longer nails or pegs are required which at least offer a horizontal anchorage. The fixation of the cable through friction against horizontal movements is normally not possible. Hence a pair of clamps that fully encloses the cable is needed to achieve a prestraining of the cable (Fig. 42). This method is the only possible method for fixation in granular soils but not applicable on bonded layers.

Fig. 42 Prestraining of sensors (left); fixation of cable clamps using screws (top right); fixation of sensing cable using a pair of clamps and a peg (bottom right) at Zurich Airport test site

4.2.4   Clamping wedges

In situations where a channel or another type of cavity was formed in the asphalt, the cable can be prestrained using wedges to fix within the cavity. This method can also be combined with previous methods if required. This technique is suitable for finer bituminous layers in which a cavity can easily be imprinted, e.g. by pressing rebars into the warm asphalt. It however requires careful in advance planning and access to the warm substrate asphalt layer in order to create the necessary cavities.

4.3 Methods of sensor protection

The asphalt paver passing over the sensors after instrumentation (Fig. 43 and Fig. 46) induces a heavy impact on the sensors placed on the substrate layer. On the one hand, the cables might stick to the wheels of the paver and might be teared off. On the other hand, larger granular particles in the asphalt could get pressed on the sensor cable and damage it.

4.3.1 Covering of sensors with fine asphalt

A simple method and required for all prestraining methods where sensor cables are placed on existing layers, is to cover them with a first layer of finer asphalt before the passing of the paver (Fig. 43 and Fig. 45).

Fig. 43 *Covering of the sensors with fine asphalt at Zurich Airport (left); asphalt paver passing over the covered sensing cables (right) at Hohlstrasse test site*

4.3.2 Jointing compound

In this method, a cavity is pressed into the substrate layer in the location of the cable (Fig. 44 left). The sensing cable is subsequently placed and prestrained within the cavity (Fig. 44 right). Once the sensor is in the correct position, the cavity is filled with a liquid mixed-in-place jointing compound that infills the previously created cavity around the sensing cable and serves as a protection.
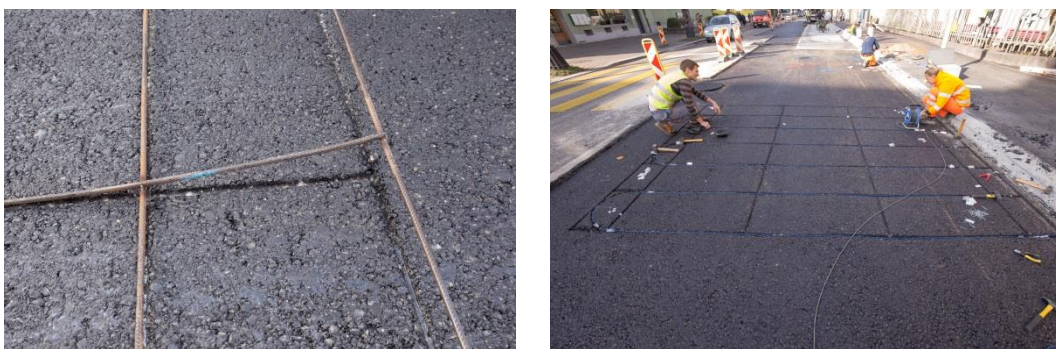
Fig. 44 *Creation of a cavity for embedment of the sensing cable in the freshly paved substrate layer (left); placement of the sensing cable in the asphalt cavity (right) at Hohlstrasse test site*

4.4　Sensor bonding techniques

The last aspect of the installation is to create a good bonding between the sensor and the embedded asphalt layer to assure that strains in the asphalt can be measured accurately and with minimal slippage. In contrary to fixing the cable at distinct locations for the prestraining, the bonding requires to be guaranteed and equally good along the whole sensor length. Only this makes it possible to also have highly spatial resolved measurements along the sensor.

4.4.1　Fine asphalt

For the installation methods where the cables are placed on top of existing layers and the cables are anyway covered with finer asphalt, this layer establishes the bonding between the sensing cables and the surrounding layer. The finer asphalt of course has a different stiffness and strength compared to the 'normal' asphalt and forms a small anomaly as well as an additional contact surface. Despite that, it is assumed that the influences of the finer asphalt are minor and an adequate bonding and strain transfer can be accomplished.

Fig. 45 Covering of the sensors with fine asphalt (left and top right); small compactor passing over the covered sensing cables (right) at Zurich Airport test site

Fig. 46 *Paver passing over the sensor (left); wheel of a paver with gravel sticking on it (top right) and passing of a heavy compactor over the asphalt layer and the sensors (bottom right) at Zurich Airport test site*

4.4.2   Jointing compound

The liquid jointing compound mass (Fig. 44) is ideally suitable for creating a good bonding connection. It develops very similar mechanical properties as paved asphalt during the curing phase and in the end forms an almost homogeneous structure with the substrate layer. As with the fine asphalt, the jointing compound also forms an anomaly within the substrate layer but the properties in terms of stiffness and strength are regarded as equal to the asphalt for this application.

4.5   Discussion and recommendations

There is not one ideal method that fulfils all requirements in terms of sensor prestraining and protection as well as in terms of the bonding characteristics. It rather depends much on the substrate layer and its properties, which method of prestraining is the most suitable (c.f. Tab. 12).

For granular and non-stabilized layers (e.g. foundation) there's basically only one feasible solution available: the fixation of the cable using clamps that are fixed with pegs in the soil.

Tab. 12 Comparison of different prestraining methods

Screws	Nails	Cable clamps with peg	Jointing compound
Foundation layer / base layer	Foundation layer / base layer	Foundation layer only (non-stabilized)	Base layer only
+ suitable for bituminous or stabilized layers + better fixation than nails if screw grips - coverage with fine asphalt layer required	+ suitable for bituminous layers where screws do not work - coverage with fine asphalt layer required	+ only possible solution for granular soil - coverage with fine asphalt layer required	+ very good compound with surrounding layer - no coverage with fine asphalt layer required - more laborious preparation and planning

In the authors' opinion, the jointing compound is the favorable method for all bituminous layers. It offers a very good compound between the cable and the surrounding layer over the whole cable length and forms a mostly homogeneous structure with its surrounding. At the same time, the sensors are already covered and protected against the paver. This combination seems to allow for measuring the most accurate and realistic strains.

There might be cases where the jointing compound method is not applicable, e.g. where access to the freshly paved and warm substrate layer is not possible or for very coarse asphalt layers. In this case the fixation using screwed clamps is preferable over the nailed clamps.

As an additional prestraining method, for granular layers or thicker asphalt layers, soil anchors might be considered (c.f. [46]).

4.6   Measurements during installation

In order to monitor the sensor performance and the prestraining of the sensor, regular measurements were taken before, during and after the installation process. The following diagrams show selected measurements of the sensing cables that were installed in a grid in the field installation at Hohlstrasse test site in Zurich (c.f. chapter 5).

Tab. 13 Measurements taken before, during and after installation

Event / Description	Measurements taken
After commissioning of cables	E-0
After prestraining and fixation	E-1
During covering with fine asphalt	U-1 to U-3
Passing of the paver	F-1 to F-6
Passing of the compactor	WK-1 to WK-7 and WG-1 to WG-4

4.6.1 Prestraining during installation

As seen before, it is vital to have the sensing cables prestrained for achieving good quality measurements. This especially applies when measuring compressive strains. In the current project, it was the goal to prestrain the sensors to $500\mu\varepsilon$ which corresponds to 0.05%. The measured strain difference between the assembling of the sensors in the lab and after prestraining can be gathered from Fig. 47. It can be seen that the prestraining target could be achieved well for all the sensors.
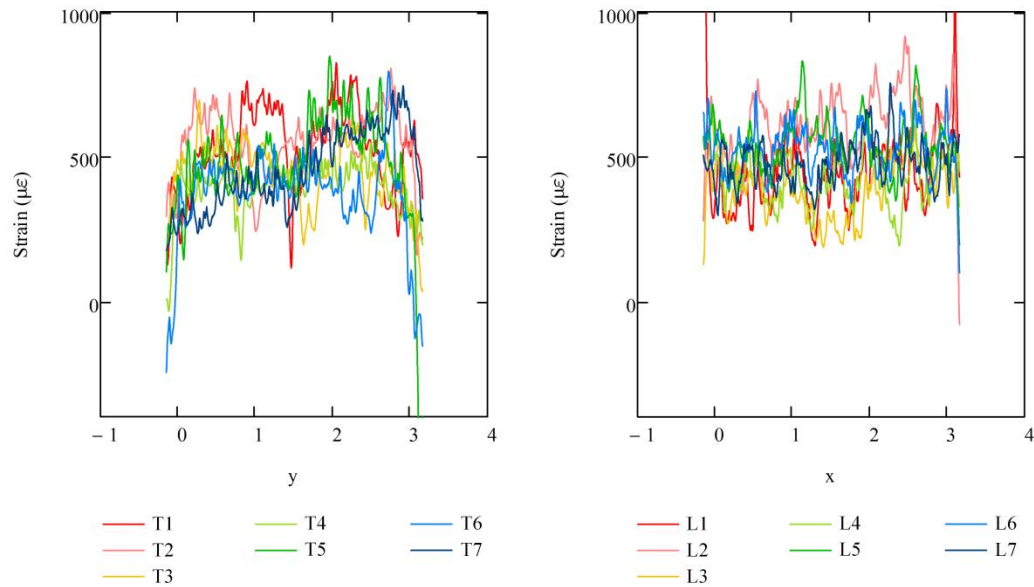
Fig. 47 *Strain in the sensing cables after prestraining for the transversal sensors (left) and the longitudinal sensors (right)*

4.6.2 Covering with fine asphalt

The coverage of the sensors with fine asphalt heats up the sensing cables. As the asphalt is still soft, the sensing cables will elongate due to the temperature increase. During the cool down of the asphalt, it gains more and more stiffness and strength and thus the shortening of the cables during cooling is constrained. This effect causes an additional prestraining on the sensor (c.f. Fig. 48).

An increase in temperature also causes an apparent increase in strain. This amount presumably measured in the transversal sensors, as they are already fully embedded in grooves and are constrained against thermal expansion. Therefore, the effectively induced additional prestraining is the difference between the equivalent strain in the longitudinal and the transversal sensors.
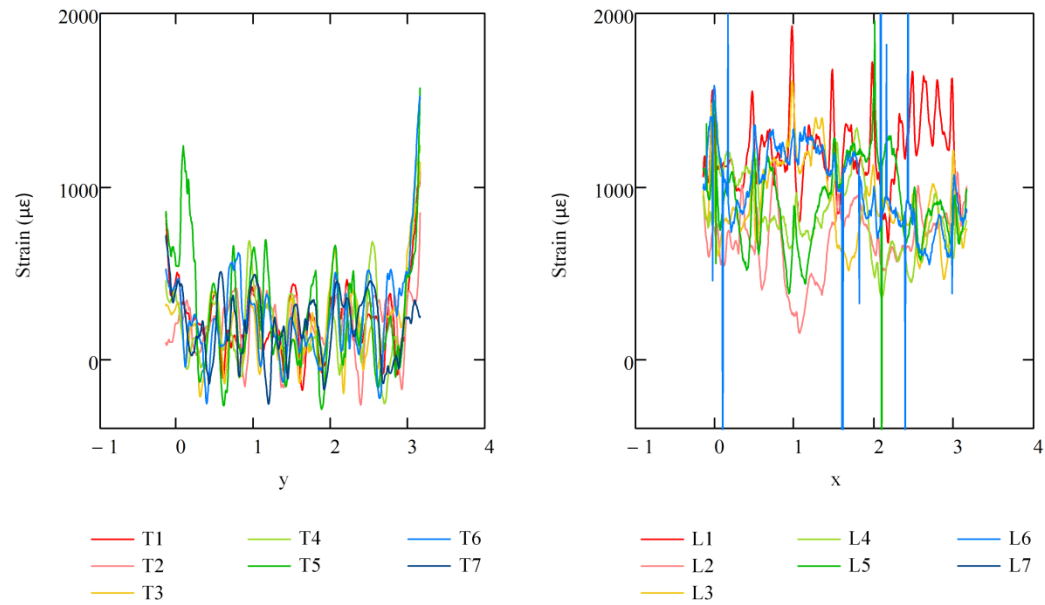
Fig. 48 *Equivalent strain in the sensing cables due to covering with fine asphalt for the transversal sensors (left) and the longitudinal sensors (right)*

4.6.3 Behavior during paving and passing of the roller

The measurements during the passing of the paver and the compacter clearly reveal the heavy impacts and the harsh environments during the installation of the cables (c.f. Fig. 49 and Fig. 50). This specially applies to the longitudinal sensors in the upper layer (diagrams on the right), where the correlation of the measurements was not possible anymore. Also for transversal sensor high, possibly permanent strains are induced. After all, all sensing cables still survived the installation and were fully functional.
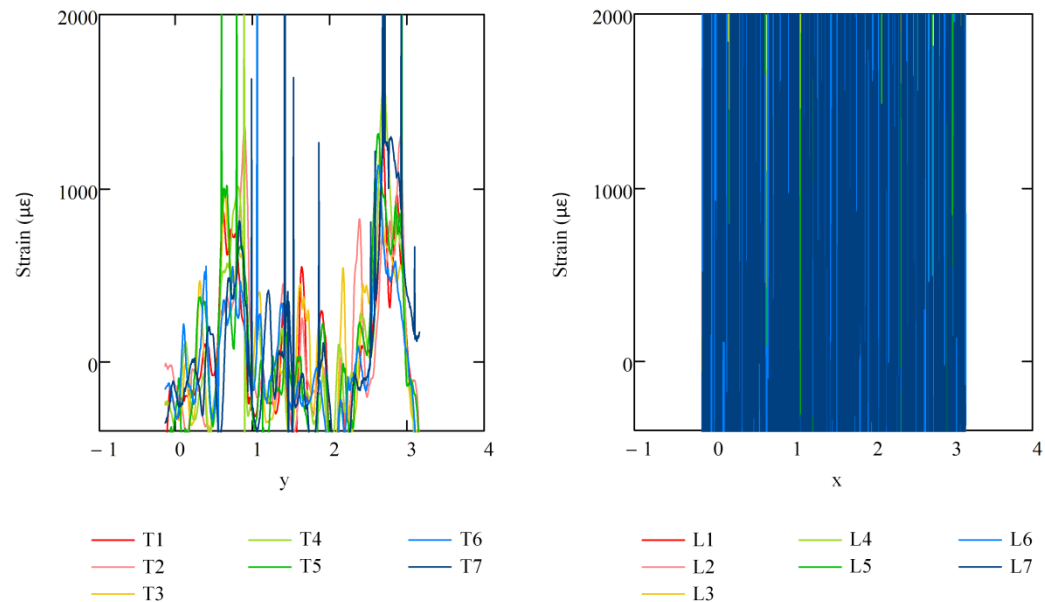
Fig. 49: *Strain in the sensing cables due the passing of the paver for the transversal sensors (left) and the longitudinal sensors, where the correlation was not possible (right)*
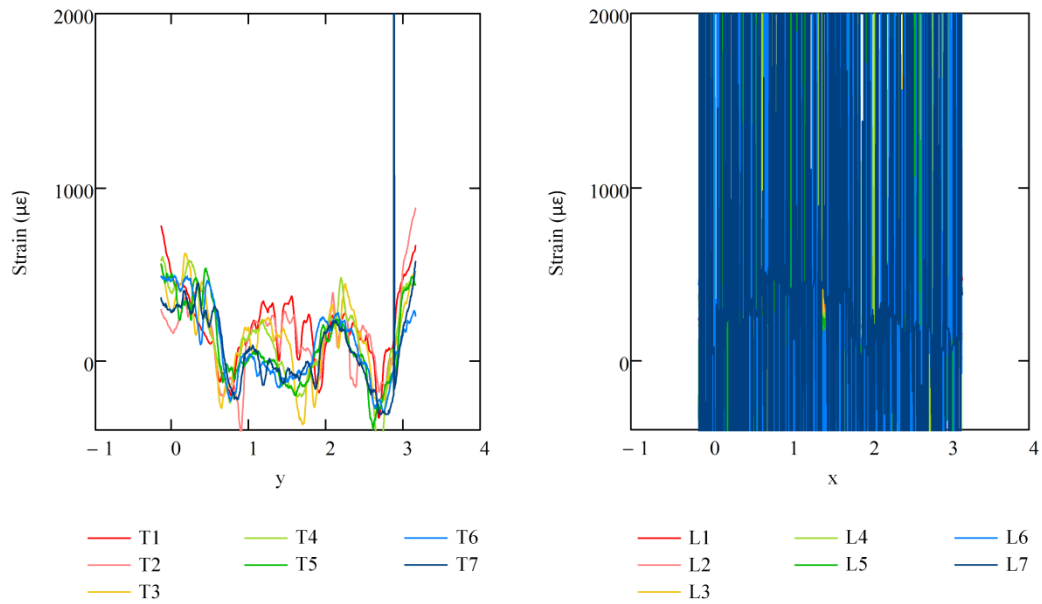
Fig. 50 *Strain in the sensing cables due the passing of the compactor for the transversal sensors (left) and the longitudinal sensors, where the correlation was not possible (right)*

4.7 Discussion

The most important outcome is that all sensing cables survived the installation process in the harsh installation environment due to mechanical impacts and high temperatures. Some sensors that were installed for dynamic measurements, however, got later during the project inoperable because of damages at the sensor ends or the connectors in the shaft but not along the embedded section. Due to the limited sensor length of the dynamic measurements, these ends had to be designed very shortly and thus it was not always possible to repair them (c.f. Fig. 51).

Fig. 51: *Cable shaft at Hohlstrasse test site with short cable ends*

The choice of the appropriate fixation method is a very important and challenging task. There is no ideal method that fulfils all the requirements to the best and the chosen method strongly depends on the substrate layer. For the purpose of the present research project the methods discussed before were sufficient. However, for an application involving larger cable lengths, more efficient, reliable and standardized methods could be elaborated.

The properties of the fine asphalt that was used as a first cover of the sensors are notably different to those of the coarser grained asphalt around. This presumably distorts the strain measurements but in the authors opinion this influence is not significant. Furthermore, not covering the sensors with fine asphalt is a useful alternative, as this increases the vulnerability of the sensors drastically and may endanger the whole instrumentation.

5   Test field Hohlstrasse, Zurich

Abstract

The current chapter comprises the measurement results from the road-embedded distributed fiber optic strain sensors in the test field „Hohlstrasse" in Zurich. After a short introduction showing the sensor layout, the strains measured along these sensors for different static loading with a car and a truck are revealed. In addition, this chapter contains also the dynamically measured strain distributions while the same vehicles drove with different velocities over the embedded strain sensors. The static and the dynamic test were repeated in different seasons under varied ambient temperature which allows for discussing the effect of temperature on the measured strains and on the behavior of the road under load. The chapter closes with conclusions about the measured behavior of the asphalt road.

5.1   Measurement setup

5.1.1   Site conditions

In autumn 2015, the VBZ Bus stop „SBB Reparaturwerkstätte"in "Hohlstrasse" in Zurich was renewed. In the course of this renewal, a concrete plate was built underneath the bus stop. The required adjustment works around this 25m long concrete plate allowed for using an approximately 10m long and 4m wide area in front of the concrete plate as a test field for this research project (Fig. 52). Owing to the bus stop nearby, the buses run usually already close to the roadside. The new pavement design beside of the bus stop lead to a solution with a base course consisting of 60cm recycled concrete material (Fig. 53). On top of that, a 9cm thick asphalt base course (AC T 22H) followed by another 9cm thick binder course (AC B 22H) was built-in. For the wearing course on top another 4cm of asphalt were used (AC 11H). The whole asphalt layer is 22cm thick. Core drillings (some results are shown in chapter 8), on which later on laboratory tests were conducted at EMPA [60], showed that there was some variation in the thickness of each layer, but in average the total layer thickness corresponded quite well with the cross section shown in Fig. 53. The process of fiber optic cable configuration and installation is described in detail in the foregoing chapter 4. The present chapter comprises the most important measurement results which were obtained with the distributed fiber optic sensors in the test field Hohlstrasse. Note that the test field "Hohlstrasse" represents not an ideal test field situation: Measurements were only allowed outside of the main traffic times and the road was usually under traffic while measurements were carried out. Only for the static measurements the traffic flow was interrupted on one lane for less than a minute. However, on the other hand the non-ideal test field Hohlstrasse proves that the sensors not only work under test conditions but also under real conditions. This holds in particular for the installation process under usual construction site conditions and shows that the sensors work also under permanent loading from the traffic over years.

5.1.2   Test project description

The test project in the test field Hohlstrasse consisted of different test series which were carried out within a time window of around 2.5 years after installation of the distributed fiber optic sensors in the road. In total ten test series were conducted in Hohlstrasse up to spring 2018. Some of them were carried out only for the purpose of checking and optimizing the performance of the fiber sensors or in order to compare the fiber optic measurements to other already established tests as the "ETH Delta" test. Distributed fiber optic sensors were installed at different depth within the asphalt pavement and different test vehicles (truck 1, truck 2 and a car) were used to apply load on the road and to measure strains with distributed fiber optic sensors. A part of the test, which is called hereinafter "static" tests shows the strain response of the road under a short term static load, whereas the second part of the test, the "dynamic" tests, show the pavement response during the transit of the test vehicles with different velocities. Since the

pavement response is strongly dependent on the environmental conditions (here mainly the effect of temperature was investigated), the test series were conducted at different temperatures (seasons) in order to characterize the behavior over a whole circle of the year. Each test series, conducted within one day, consisted itself of various tests, e.g. a static test with the rear axle of truck 1 on a sensor in 22cm depth, a dynamic test with a certain velocity of the car using a sensor which is in 4cm depth etc.). By doing so, a large database has accumulated of which the most important tests are shown in the present chapter.
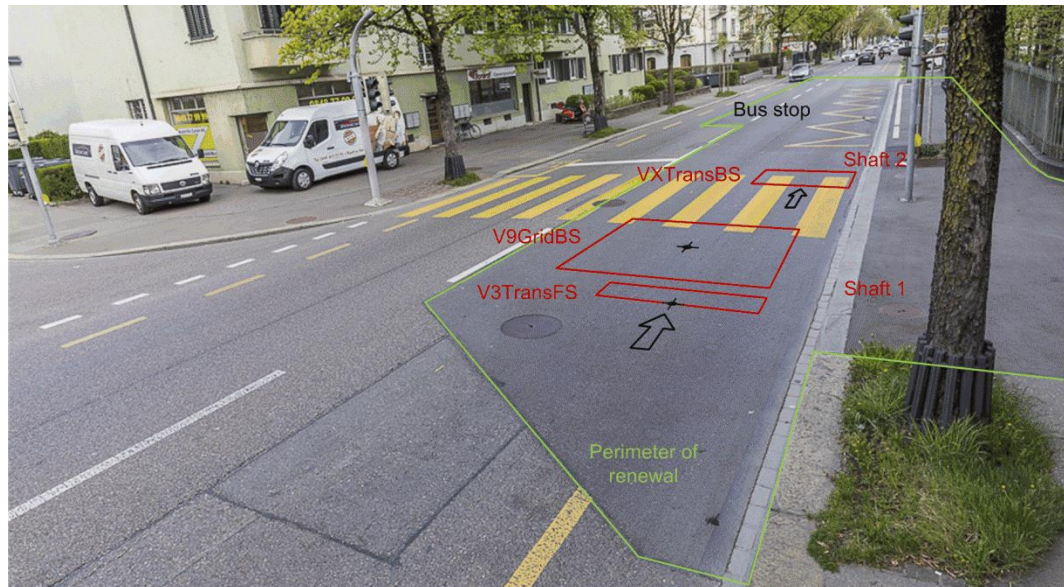
Fig. 52 *Test site Hohlstrasse (from west)*

5.1.3 Distributed fiber optic sensor layout

An overview of the installed fiber optic sensors is provided in Tab. 14. Two fiber optic sensors, „V3TransFS"and „TFS", were installed at the grade of the base course (see Fig. 53, dashed lines). On the grade of the binder course, six further fiber optic sensors were installed. These fiber optic sensors are formed by different type of cables, which have different mechanical properties (see chapter 2). In particular on the grade of the binder course around shaft 2, different fiber optic cables were installed for the reason of redundancy and comparison. All sensors having a name starting with "V" are tight buffered cables. The sensor names starting with "T" are loose tube cables which were foreseen to measure temperature changes within the asphalt layers. However, the measurement results of the latter mentioned sensors are not part of the present report. The distance between the parallel parts of all strain sensing cables is 0.5m, except for the V9LongBS, which has a slightly smaller inner distance. In order to achieve a maximum temporal readout resolution of 100Hz, the sensor lengths of all sensors for dynamic measurements had to be smaller than 10m. Although the mainly applied distributed fiber optic strain sensing technology SWI does not require a closed cable loop for the measurements, both cable ends were made accessible and guided in a loop configuration to an access shaft. This procedure limited of course the perimeter of the area which can be monitored, on the other hand, it provides higher redundancy and options in case of configuration problems at the cable ends. Hence, the cable loops close to shaft 2 were only foreseen to capture one side of the vehicle since they could not cover the whole width of a traffic lane. The foreseen technology for the static measurements limited the length of the cable loop to around 70m, which lead to the grid layout shown in Fig. 53 consisting of 7 transverse (1 to 7) and 7 longitudinal (A to G) sensor sections, forming a squared pattern 3 by 3m with spacing of 0.5m.

Plan view

Section s – s (scaled)

Fig. 53 Layout of fiber optic cables in the test field Hohlstrasse, Zurich
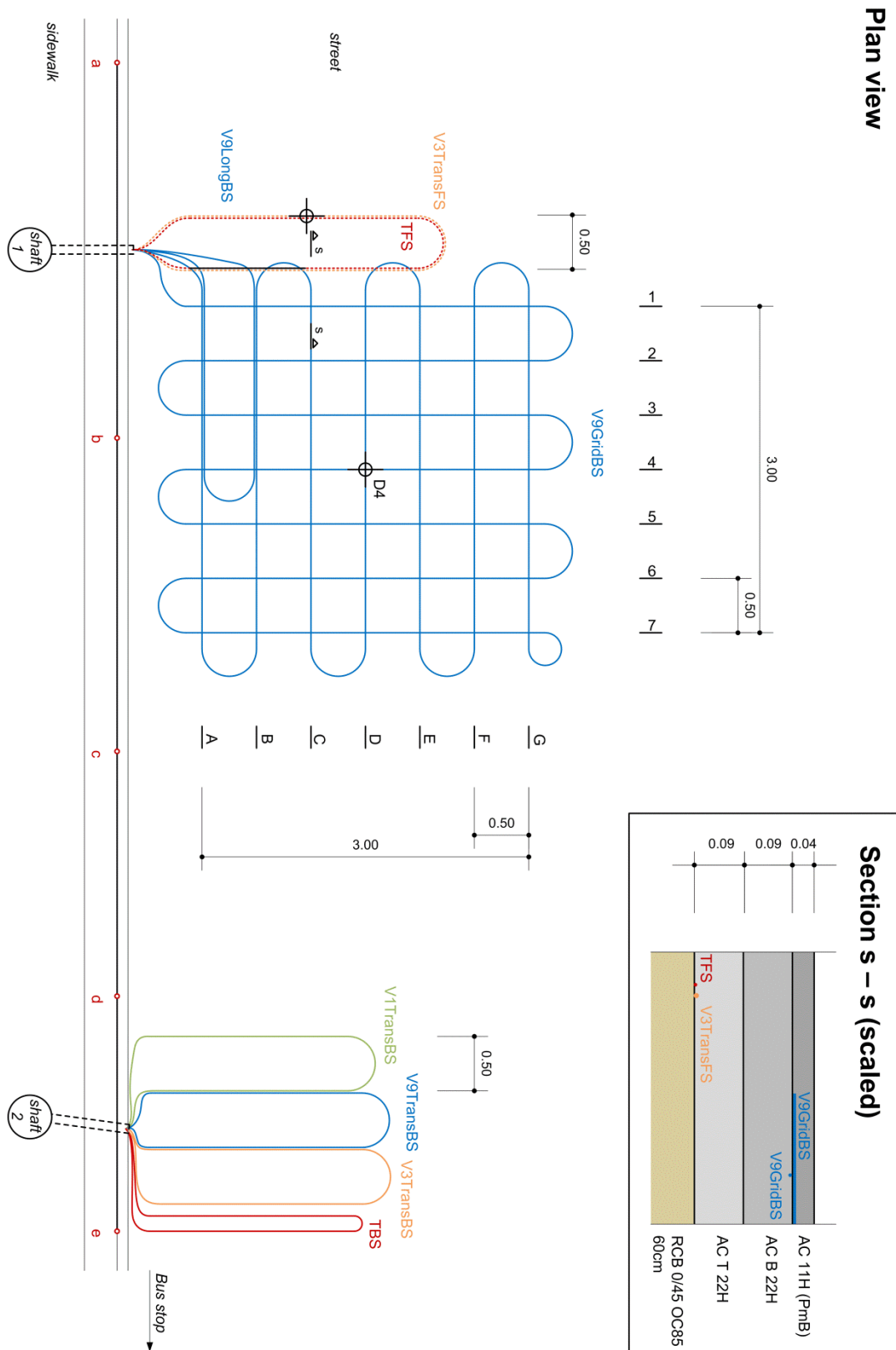
Tab. 14 Sensor installation in the test field Hohlstrasse

Sensor name	Cable	Depth	Length	Foreseen measurement purpose
V3TransFS	V3	22cm	Around 10m	Static & dynamic strain measurements at the bottom of the asphalt layers
TFS	T	22cm	Around 10m	Temperature change measurements at the bottom of the asphalt layers (loose tube cable)
V9LongBS	V9	4cm	Around 10m	Dynamic strain measurements close to the road surface in parallel to the driving direction
V9GridBS	V9	4cm	Around 70m	Static strain measurements close to the road surface in longitudinal and transversal direction at different spacing from the load
V1TransBS	V1	4cm	Around 10m	Dynamic strain measurements close to the road surface transversal to the driving direction in loop configuration (soft, vulnerable cable)
V9TransBS	V9	4cm	Around 10m	Dynamic strain measurements close to the road surface transversal to the driving direction in loop configuration (stiff, robust cable)
V3TransBS	V3	4cm	Around 10m	Dynamic strain measurements close to the road surface transversal to the driving direction in loop configuration (very stiff, very robust cable)
TBS	T	4cm	Around 10m	Temperature change measurements close to the road surface within the asphalt layers (loose tube cable)

5.1.4 Distributed fiber optic measurement devices

A more detailed description of the fiber optic measurement technologies applied within this project is shown in chapter 2. At the test field Hohlstrasse mainly the SWI technology was applied, however, in the beginning of this project also some measurements with BOTDA were carried out (mainly for the purpose of potential long term measurements and temperature changes). The SWI technology, based on Rayleigh scattering along the silica fiber, was applied in the form of two commercially available measurement devices from the company Luna Inc. The specific devices used were an OBR 4600 for the static measurements and an ODiSI B device for the dynamic measurements.

Distributed fiber optic measurements are usually characterized by a spatial resolution (or gauge length) and a sampling interval (or sensor spacing). Whereas the first is, in simple words, a measure for the length of the spatially smallest detectable strain event, the latter denotes the spacing between two points on which the strain is computed. For the test field Hohlstrasse and for static measurements, usually a gauge length of 10mm and a sensor spacing of 5mm were applied (oversampling). For one specific test series 20mm and 10mm had to be chosen (mentioned later). Note that a static measurement using the OBR 4600 device, with the chosen set of measurement parameter for this project, took around 10s time. Hence, if the strain present in asphalt changes its magnitude during this measurement time slightly e.g. owing to viscous effects under static load, it is expected and assumed within the present study, that the measured strain represents a sort of averaged strain present in the asphalt within this time window. For the dynamic measurements, using the ODiSI B device, a gauge length of 5mm and a sensor spacing of 2.5mm were chosen. Dynamic measurements were carried out with an acquisition rate of 100Hz and hence, much faster than the static measurements, but limited to 10m sensor length.

5.1.5 Temperature measurements

The general behavior of the asphalt material (in particular its stiffness) is strongly dependent on the temperature. In addition, the response of the base layer below the asphalt courses changes with freezing pore water. Hence, knowing the current temperature in asphalt while performing the tests is important and it is the key parameter for the application of realistic parameters in numerical models. For this purpose, holes of different depth were drilled into asphalt (Fig. 54) and two Pt100 elements (T_2 and T_4) as

well as a needle thermometer were used (T_1 and T_3) in order to determine periodically during the measurements the temperature within the asphalt.

In principle, the temperature changes could have also been measured using the embedded fiber optic loose tube cable. However, owing to the tight measurement schedule it was decided to measure temperatures conventionally.
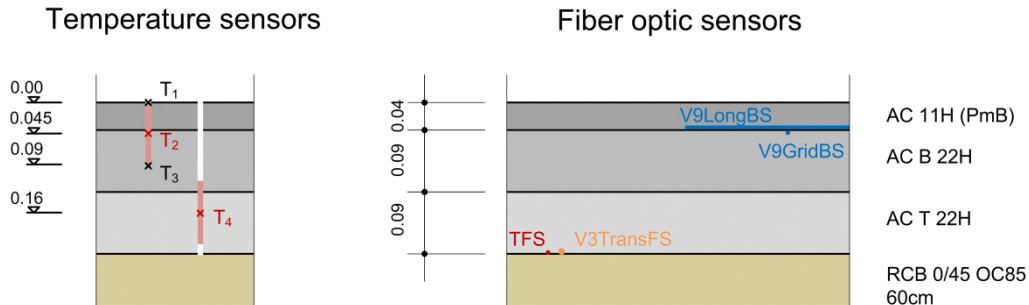
Fig. 54 *Temperature sensors and position of the fiber optic sensors*

5.1.6 Test vehicles

Different vehicles were used in order to apply a defined load to the pavement. With exception of the calibration test with ETH Delta, which was a special test in order to compare the fiber optic results to the deflection measurements with ETH Delta (see section 5.2.4), a truck (truck 1, 40t in total, 5 axles) and a car (car, 2.4t in total, 2 axles) were used (Tab. 15).

Tab. 15 Used test vehicles

Vehicle	Axles	Test axle load (nominal)	Tests
Truck 1, Volvo FM 480	5	Rear axle : 100kN, double tire 315/80/R22.5 Front axle 50kN, single tire 315/80/R22.5	All tests except calibration test with ETH Delta
Truck 2, Scania 124G 420	3	Front axle 90kN, single tire 385/65R/22.5	Calibration test with ETH Delta
Car, Toyota Landcruiser	2	Front axle 12.5kN, single tire 265/65/R17	All tests except calibration test with ETH Delta

The axle loads reported for truck 1 in Tab. 15 are nominal axle loads. Owing to the slightly different loading of the truck from measurement campaign to measurement campaign, the axle load slightly varied around this nominal load (within +-10%). The true axle load for each test series is reported in the corresponding figure. However, the load of the front axle could not be measured in all test series and had to be assumed in some test series as the average from the other tests (indicated with *). The footprint of each vehicle is shown in Fig. 55, where the grey rectangles mark the approximated contact area between road and tire. For truck 2 only the front axle was relevant for the test.

Truck 1: Volvo FM 480
Tires: 315/80R22.5
Total weight: 40t

rear axle 10t   front axle 5t

1.37   1.40   2.00   2.00

6.77

Truck 2: Scania 124G 420
Tires: 385/65R22.5

Rear axles not relevant
for the test

front axle 9.2t

3.90

Car: Toyota Landcruiser
Tires: 265/65R17
Total weight: 2.4t

rear axle 1.1t   front axle 1.3t

2.82

Fig. 55 *Footprints of the test vehicles with nominal loads*

5.1.7   Test procedure

A test series on Hohlstrasse usually comprised static and dynamic measurements and required, including installation and deinstallation, around 8 hours. Before the measurements were started, the position of the sensors underneath the road surface was marked with adhesive tape or chalk spray in order to be able to assess the correct positioning of the vehicle. Measurements were carried out on different sensors within a time window of approximately 4 to 5 hours during which the temperatures were periodically measured. The measurement device was connected via access shaft to the distributed fiber optic sensor. Afterwards the vehicles were driving loops in the vicinity of the test field while measurements were conducted. Around every 5 to 7 minutes the vehicle was passing the sensor.

Static measurements

For the purpose of static measurements, the truck was stopped a few meters in front of the sensor. A first reference measurement was carried out within around 10 seconds using the OBR 4600 device while the sensor was free of traffic. Afterwards the truck drove slowly onto the sensor, stopped in the foreseen position and a further measurement (lasting also around 10s) was carried out. By the time the truck has left the sensor, one (usually) or two (exceptional) further measurements were carried out while the road was free of traffic. After usually less than 60s, the road was again free for the traffic. The strain can then be computed as the difference between the reference measurement and the measurements under load and after unloading. No compensation for temperature effects was applied, because in this short time no significant temperature change is expected and hence, the full frequency shift measured was converted to strain. Since the positioning of the truck on the sensor was not ideal straightaway and care had to be taken that not another heavy vehicle passed the sensor slowly right before the test truck (viscous strains), several loops were necessary in order to have a measurement with good boundary conditions.

Dynamic measurements

A slightly modified procedure was used for the dynamic tests. The test vehicle was driving in each loop with predetermined velocity over the fiber optic sensor in asphalt and did not stop as it was the case during static measurements. The measurement sequence (usually 4 to 10 seconds corresponding to 400 to 1000 individual measurements) was started with the ODiSI B device when the test vehicle was close to the sensor. Before the test vehicle was driving over the sensor, the road was kept free for a few seconds and care was taken that not a heavy vehicle was passing over the sensor directly in front of the test vehicle. In some tests, the decrease of strains (viscosity) after the vehicle passed the sensor was additionally measured over a few further seconds. The nominal velocities of the test were chosen to 5, 10, 15 and 30km/h. In some test series also 50km/h was tested.

Calibration measurements using ETH Delta device and concrete blocks

The calibration test with ETH Delta device and concrete blocks, which was carried out in June 2017, was a special test. This test was carried out during the night between the latest and the earliest bus arrival. Owing to that, one lane of the road could be temporarily closed and the traffic was running in a one-lane mode. The ETH Delta device measures the pavement deflection on a reference line on the surface of the road beside the wheel. If the distance of the wheel to this reference line is continuously changed, a settlement trough can be reconstructed using this device (see also [45]). In the tests carried out for this research project, the reference line was chosen right above a fiber optic sensor and for the same test not only deflection but also strains were measured in order to gain more information for an inverse analysis of the problem. In a second sort of test during this night, load was applied by concrete blocks using a crane instead of the usual load application by a vehicle rolling on the sensor. This allowed achieving a radial symmetric loading scheme, whereas the loading scheme of the vehicle always includes viscous effects, visible in the zones which were traversed by the wheels before the vehicle stopped on the sensor. Furthermore, load could be applied during the night not only for seconds but also for several minutes.

5.1.8   Test series overview

The vehicles and sensors used during the 10 test series are collocated in Tab. 16. In order to characterize roughly the temperature conditions, the approximate average of temperature T_3 during the whole test is listed in the table. Whereas test series No. 2, 4 to 6, and 8 to 10 were normal tests, No. 1 was a test series right after the emplacement of the hot asphalt when a roller drove over it. No. 3 was a test series used for optimization of the performance of the dynamic measurements, where randomly arriving buses were used for the loading the pavement. Finally test series No. 7 was the calibration test using

ETH Delta device and concrete blocks as mentioned in the section above. Static tests can be recognized in Tab. 16 by the remark on the axle (rear, front) which was used in order to apply load. Although it is in general not sufficient to characterize the asphalt temperature simply by the single value T_3 (90mm depth), this average temperature information can be used in order to rank qualitatively the thermal conditions. Regarding Tab. 16, there is data available for the front and rear axle of truck 1 but also for the car which is covering the temperature range from 5°C to 32°C. The same temperature range was reached with the dynamic sensors V1TransBS for the truck and the car.

Tab. 16 Test series overview

Test series	Date	Temperature T3 (mean)	V9GridBS (static)	V3TransFS (static & dynamic)	VXTransBS and / or V9BSLong (dynamic)
1	13.11.2015	Hot, placing conditions	Roller		
2	17.2.2016	cold	Rear axle truck 1		
3	17.6.2016	warm			Bus (sensor performance optimization)
4	22.6.2016	warm			Truck 1
5	8.8.2016	38°C	Rear axle truck 1, front axle truck 1, front axle car	Truck 1, car	Truck 1, car
6	27.2.2017	16°C	Rear axle truck 1, front axle truck 1, front axle car	Truck 1	Truck 1
7	20.6.2017	34°C	Truck 2, concrete blocks (calibration)		
8	16.10.2017	23°C	Rear axle truck 1, front axle truck 1	Rear axle truck 1, front axle truck 1	Truck 1
9	02.02.2018	5°C	Rear axle truck 1, front axle truck 1, front axle car	Rear axle truck 1, front axle truck 1, front axle car	Truck 1, car
10	13.2.2018	3°C	Rear axle truck 1, front axle truck 1	Rear axle truck 1, front axle truck 1	

5.2　Static Measurements

5.2.1　Introduction

As shown in Tab. 16, many static measurements were carried out and not all could be included in this report. However, in the present section, some selected tests from different test series originating from three test vehicles are shown. These measurements were carried out using the OBR 4600 device requiring a measurement duration of around 10s. Hence the strains shown in this section are assumed to represent a sort of averaged strains occurring in this time window in asphalt (viscous effects in asphalt). Before presenting these measurement results, some further boundary conditions of the test will be discussed. Fig. 56 to Fig. 58 show the tire position for truck 1 (rear and front axle) and the car (front axle) during conduction of static measurements on point D4 using sensor V9GridBS in 4cm depth. Fig. 59 shows the location of the tires of truck 1 (only rear axle illustrated) during measurements with sensor V3TransFS in 22cm depth. In order to illustrate the measurement results of sensor V9GridBS, the grid was subdivided in sensor lines 1 to 7 (transverse, y-direction) and A to G (longitudinal, x-direction). The measured strains are shown only along these sensor lines. As Fig. 56 indicates, also other wheels of the truck than the right rear axle wheels are on the grid and the effects of the other wheels (e.g. close to G4, G7, D7) should become visible although they do not stand exactly above the cable. Furthermore it is important to note that between the reference measurement and the measurement when the pavement is under static load, the axles of the test vehicles traversed already some of the sensor lines. This situation is pronounced the most in tests with the rear axle in warm conditions when the creep strains of the traverse of axles No. I to IV are still visible in all sensor lines. In order to milden this effect, tests with the front axle were conducted (Fig. 57 and Fig. 58), where first of all only one axle traversed the sensor and second only half of the sensor lines (lines 1 to 3). Naturally the situation is reversed in the unloading measurement when the vehicle has left. In order to avoid this situation completely, tests were conducted where concrete blocks instead of vehicles (section 5.2.4) were used. In order to illustrate the measurements along the sensor V3TransFS, the loop was divided into sensor line A and B (Fig. 59).
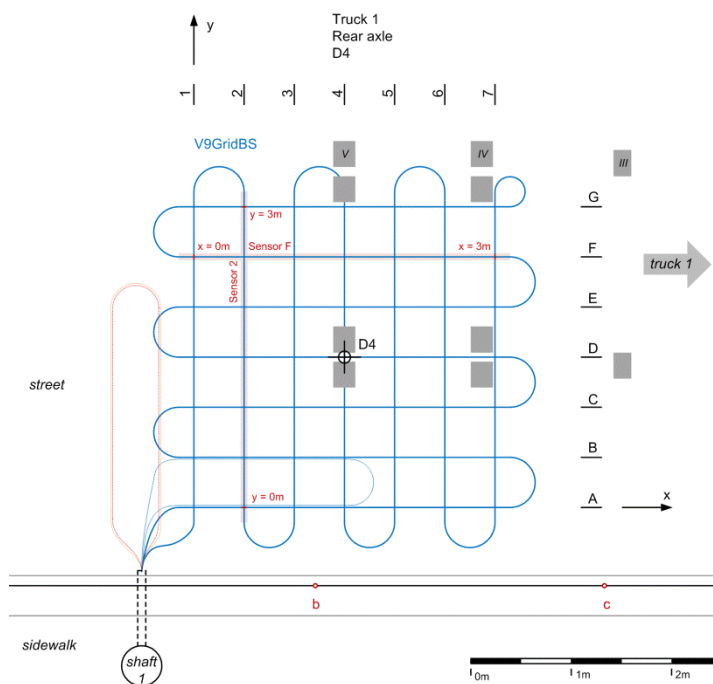
Fig. 56 *Footprint of truck 1 in tests using the rear axle with sensor V9GridBS*
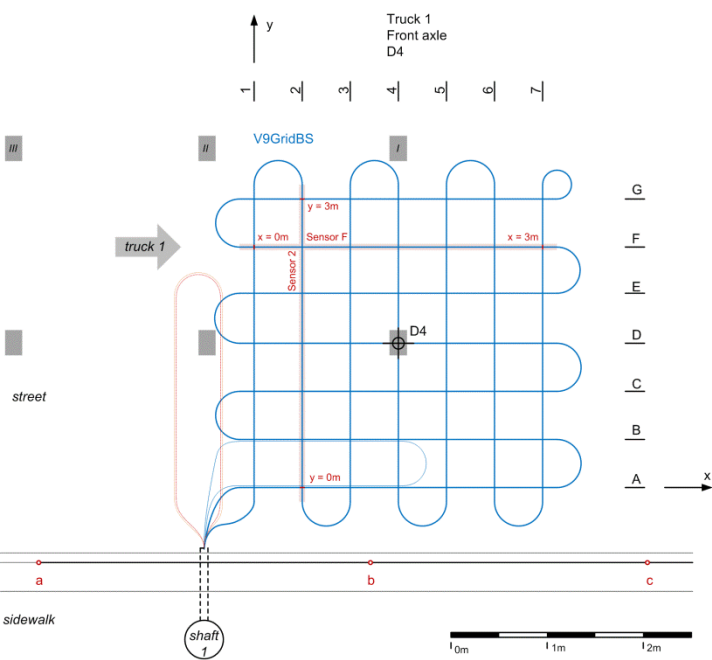
Fig. 57 *Footprint of truck 1 in tests using the front axle with sensor V9GridBS*
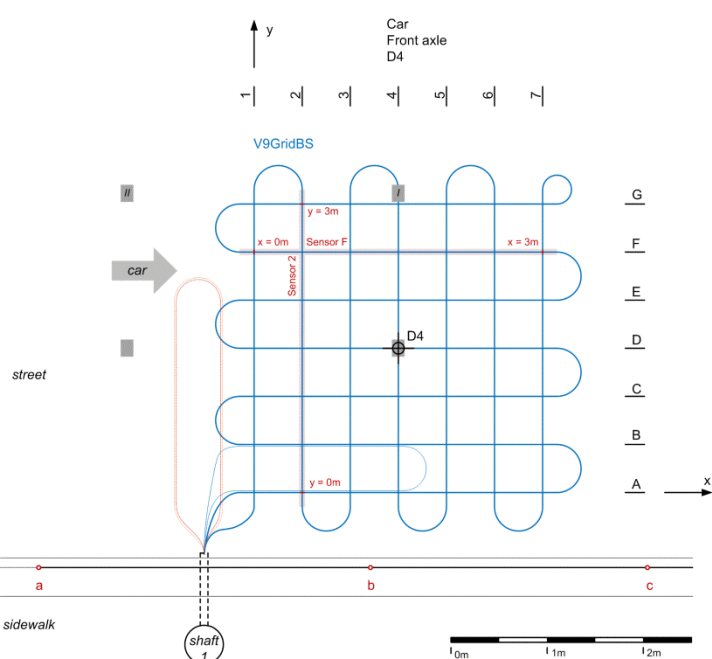
Fig. 58 *Footprint of the car in tests using the front axle with sensor V9GridBS*
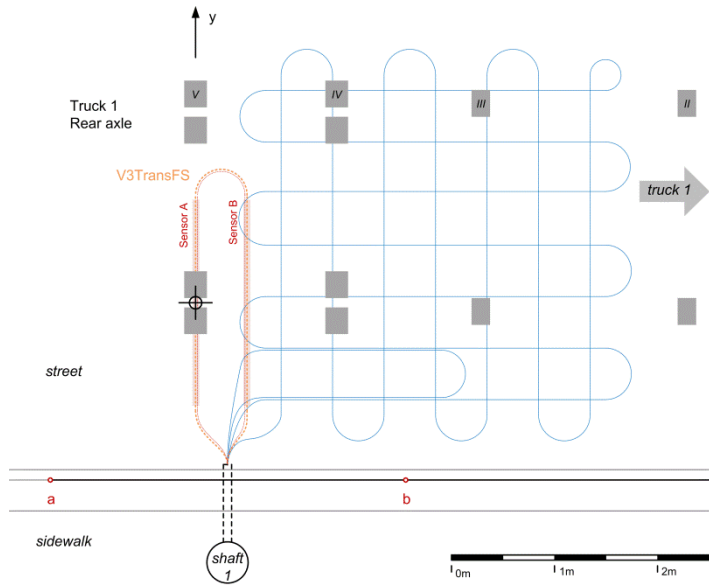
Fig. 59 *Footprint of truck 1 in tests using the rear axle with sensor V3TransFS*

5.2.2 Measurements in 4cm depth using the sensor V9GridBS

A large number of measurements was conducted with sensor V9GridBS, involving different vehicles and temperature condition. The subsequent figures show some selected test results from this sensor involving the rear and the front axle of truck 1 as well as the front axle of the car in three different seasonal conditions.

Measurements in winter

Fig. 60 to Fig. 62 show the strains in longitudinal as well as transverse direction gathered with the sensor V9GridBS in 4cm depth during February 2 in 2018 for the rear axle of truck1, the front axle of truck 1 and the front axle of the car. The measurements were carried out when the sensor was under load. The measurement results obtained immediately after unloading are shown later in this report. The positioning of the sensor sections 1 to 7, A to G as well as of the load is shown in Fig. 56 to Fig. 58. The twin tires on the right hand side of the rear axle (axle No. V) are positioned on the point D4. However, as Fig. 56 to Fig. 58 indicate, also the twin tires on the left side of axle No. 5 and the twin tires on both sides of axle No. IV are positioned close to the boundary of the grid. This circumstance is also reflected in the strain measurement data shown in Fig. 60, where it can be clearly seen, that the load is not only present in point D4, but also close to the points G4, G7 and D7. However, since the footprint of truck 1 does not match with the 0.5m spacing of the grid, the other tires are not directly above the cable as in point D4, which is reflected in smaller strains, since the spatial strain gradient close to the load (4cm depth), is rather high. Note that the fact that also strains are measured on the sensor section 1 and 2 does not imply that the measureable zone of load influence reaches from point D4 to sensor 1 or 2. The strains measured in section 1 and 2 are creep strains owing to the viscous nature of asphalt and the fact that the axles No. I to V traversed this two sensors before the rear axle stopped above point D4. In tests involving the front axle of truck 1 this is not the case (Fig. 61): Creep strains can be observed on the sensor section 2 and 3 but not along section 5, 6 and 7, because the front axle stopped above sensor section 4. Finally, in Fig. 62 the strains measured under the front axle of the car are shown, which are clearly smaller than those caused by the truck, since the axle load is significantly smaller. The maximum strain (expansive strain, positive) is reached under the front axle and is below $100\mu\varepsilon$, whereas the minimum strain (largest contractive strain, negative) is slightly lower.
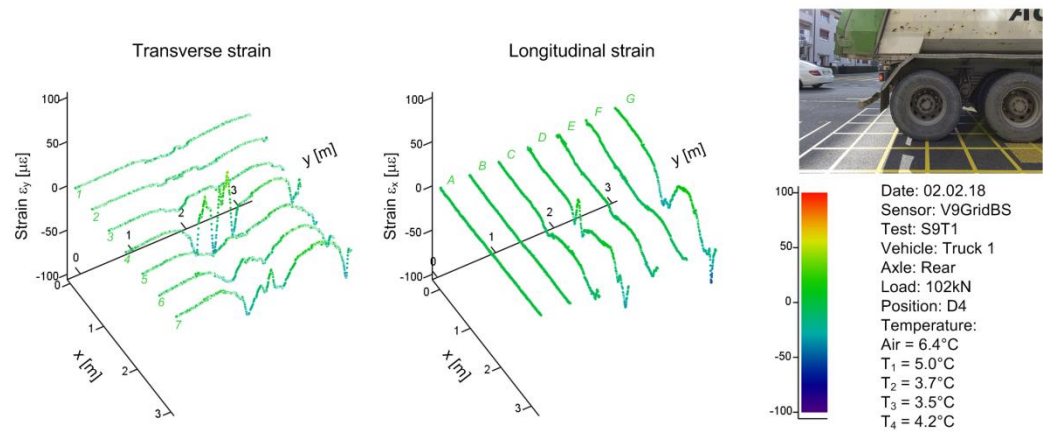
Fig. 60 *Strain measurement under the rear axle of truck 1, winter*
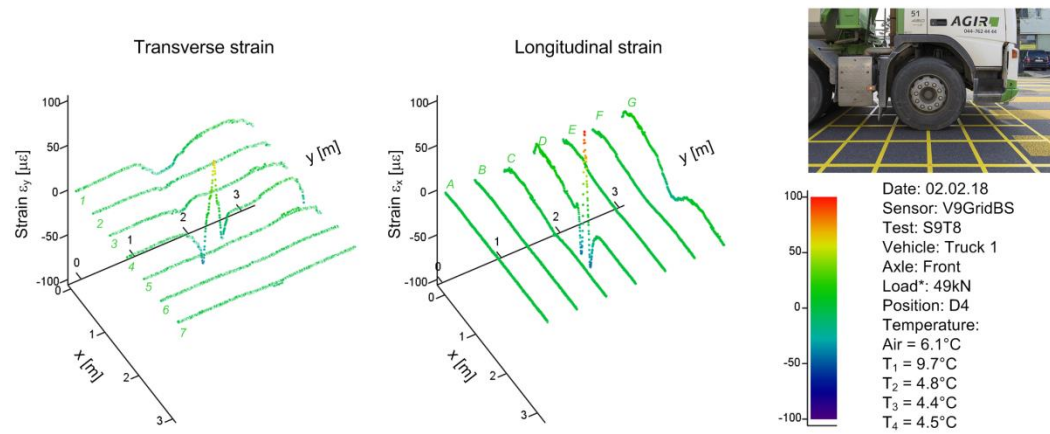
Fig. 61 *Strain measurement under the front axle of truck 1, winter*
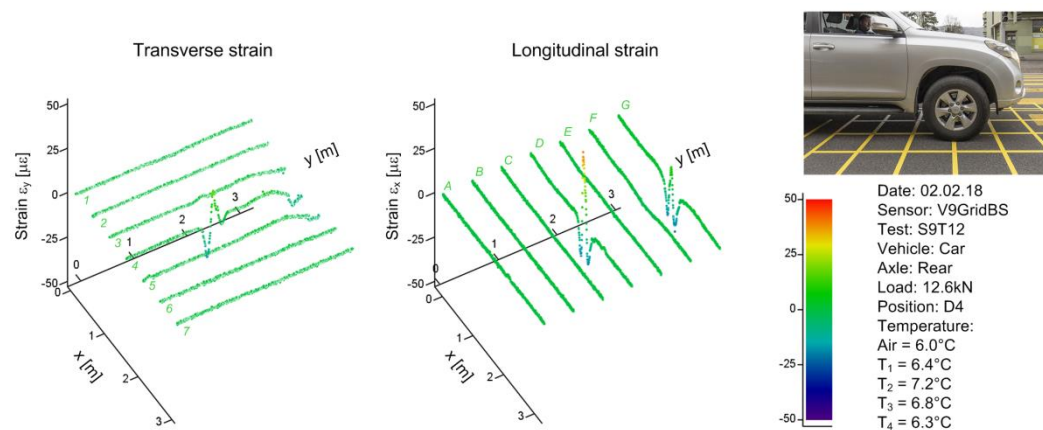
Fig. 62 *Strain measurement under the front axle of the car, winter*

Considering the shape of the measured strain distribution, it becomes obvious, that exactly under the tire in 4cm depth expansive strains can be measured. Contractive strains occur close beside the tire. The twin tire of the rear axle causes therefore in transverse direction a double strain peak, whereas a single tire (front axle) causes only a single strain peak. In longitudinal direction also the twin tires cause only one strain peak. Interestingly the strain under the rear axle has a comparable magnitude although it brings twice the load as the front axle to the pavement. However, the load under the rear axle is also distributed to four tires, whereas the load of the front axle is only split to two tires. The maximum strain magnitude under the front axle of the car is clearly smaller, however, not proportional to the applied load if compared to the results from the front axle of truck 1. This might be the case because these tests were conducted later at this day, when the relevant temperatures in asphalt (T_2 to T_4) were slightly higher and the stiffness of the asphalt already smaller. Note that the load of the front axle of truck 1 could not be measured in all test series. Where the value of the load is labelled with * it was estimated as the average from the other test series.

Measurements in autumn

Fig. 63 and Fig. 64 show the measured strain distribution under the rear and front axle of truck 1 in warmer conditions than in winter. Whereas the average temperature of T_2 and T_3 in Test series 9 in winter was around 5 to 7°C, it was around 24 to 27°C during test series 8 in autumn. Correspondingly also the strain magnitude under comparable loading increased clearly, owing to the temperature dependent stiffness of asphalt. The maximum expansive strain increased to 300 to 500$\mu\varepsilon$ whereas the maximum contractive strain was always around 200 to 300$\mu\varepsilon$ (absolute value). Furthermore, also the creep strains from the axles which were traversing the sensors prior to the measurement, become clearly more visible.

Measurements in summer

Fig. 65 to Fig. 67 show the strains measured during August 8, 2016 in very warm conditions. The average temperature of T_2 and T_3 during test series 5 in summer was around 40°C. Consequently, the strain magnitudes reached values of around 1200 to 1600$\mu\varepsilon$ under the tire (expansion) and around 400 to 600$\mu\varepsilon$ beside the tire (contraction) of truck 1. Directly under the tire of the car, strains as high as 600$\mu\varepsilon$ were observed. Interestingly these strain magnitudes accumulated already a few seconds after the load was positioned (measurement time of around 10s) and represent therefore not values reached only under a long loading time.

Measurements after unloading the pavement

The asphalt layer shows a delayed response owing to the viscous nature of asphalt. Hence, as discussed above, creep strains from the axles which crossed the sensor can be seen in the previously discussed figures. In order to elaborate this behavior more in depth, after each measurement under the static load of the rear or the front axle, a further measurement was carried out, once the truck left the sensor. Fig. 68 to Fig. 70 show the transverse strain ε_y measured under the load of rear axle of truck 1 (denoted "pavement under load") and a few seconds (measurement time of around 10s) after the rear axle has left the sensor (denoted "pavement unloaded"). Note that sensor sections 1 to 3 were crossed by 5 axles before the measurement "pavement under load" was conducted, whereas no further axle crossed the these sensor sections until the measurement "pavement unloaded" was carried out. On the other hand, sensor sections 5 to 6 were crossed by 4 axles before "pavement under load" was conducted (sensor section 7 by 3 axles), whereas only 1 further axle crossed these sensor sections until the measurement "pavement unloaded" was carried out. The further decrease of strain with time owing to creep becomes clearly visible in sensor section 1 to 3. The time difference between these two measurements "pavement under load" and "pavement unloaded" is 25s (summer), 33s (autumn) and 20s (winter). The time difference between these specific measurements in autumn was unusual high. Typically the time difference ranges often from 15s to 25s.
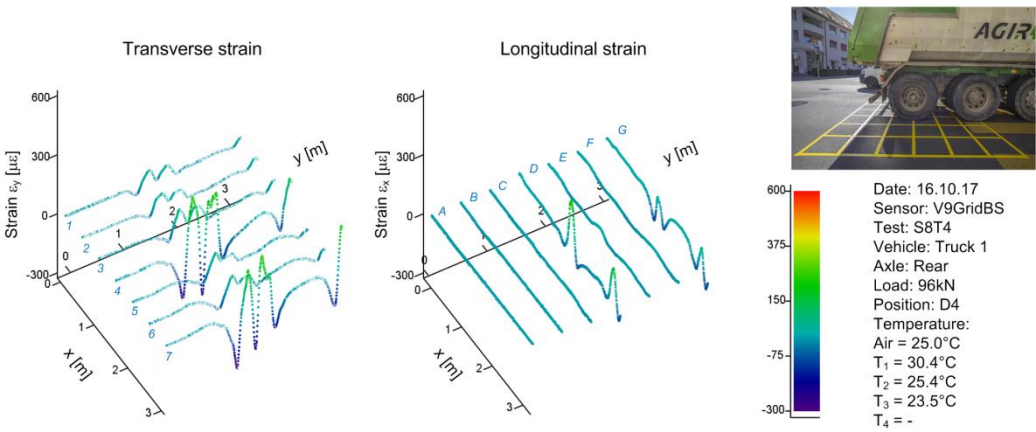
Fig. 63 *Strain measurement under the rear axle of truck 1, autumn*
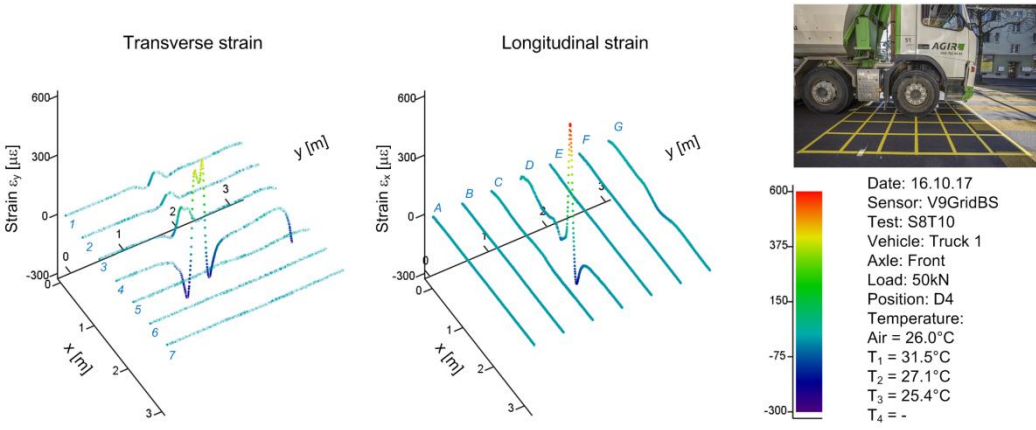
Fig. 64 *Strain measurement under the front axle of truck 1, autumn*
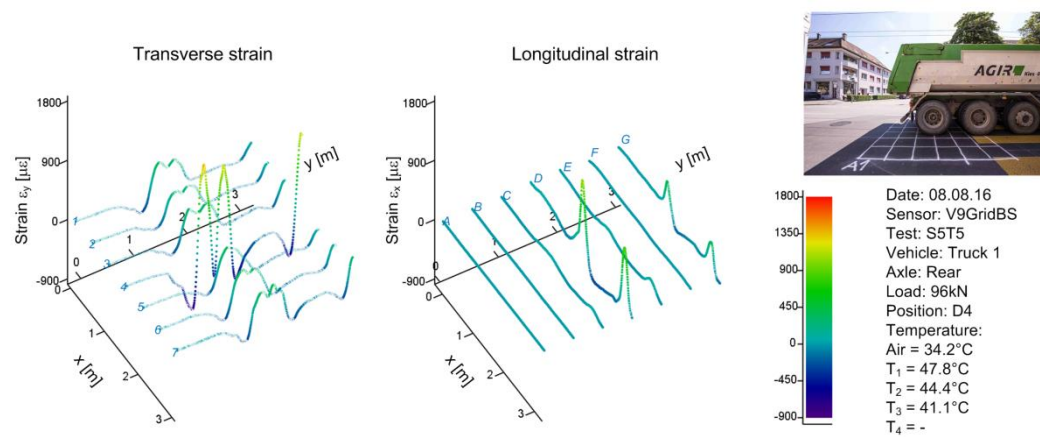
Fig. 65 *Strain measurement under the rear axle of truck 1, summer*
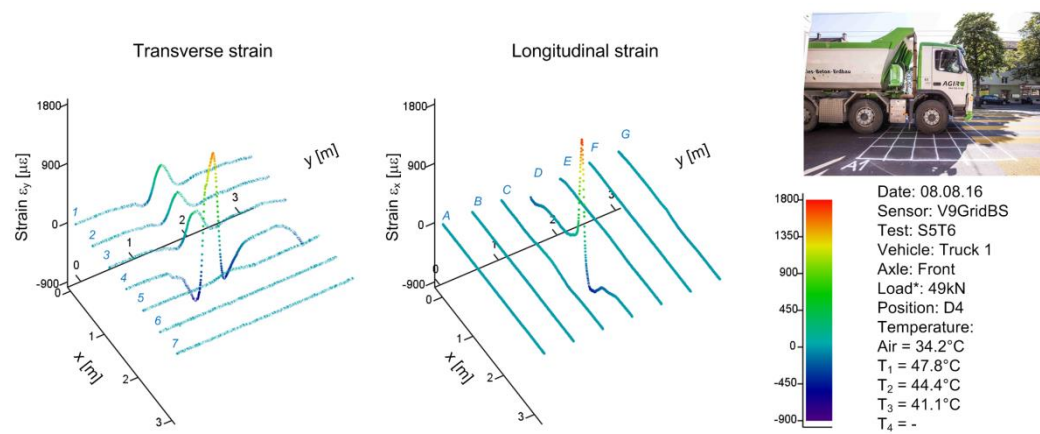
Fig. 66 *Strain measurement under the front axle truck 1, summer*
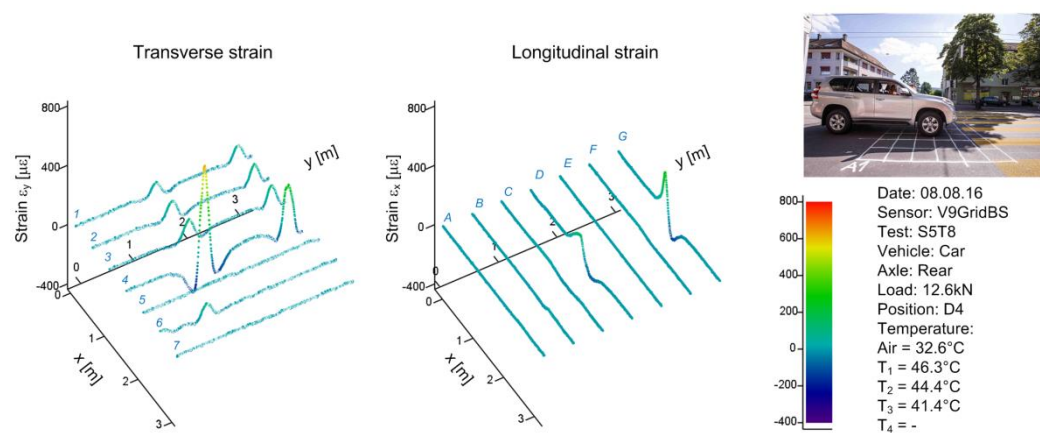
Fig. 67 *Strain measurement under the front of the car, summer*
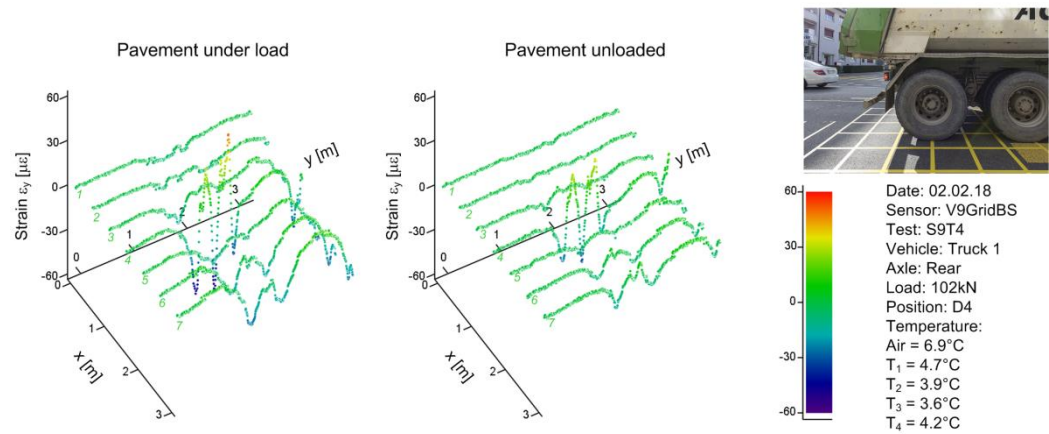
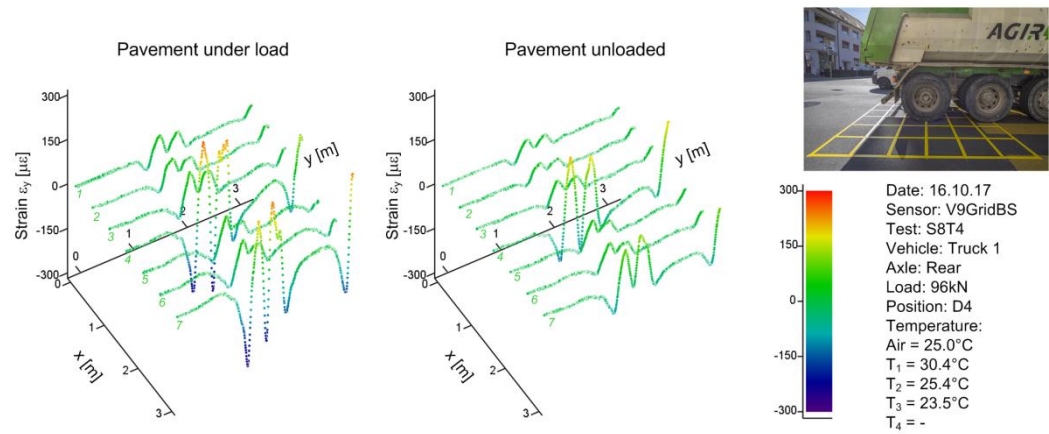**Fig. 68** *Transverse strain measurement under the rear axle of truck 1, winter*

Fig. 69 *Transverse strain measurement under the rear axle of truck 1, autumn*
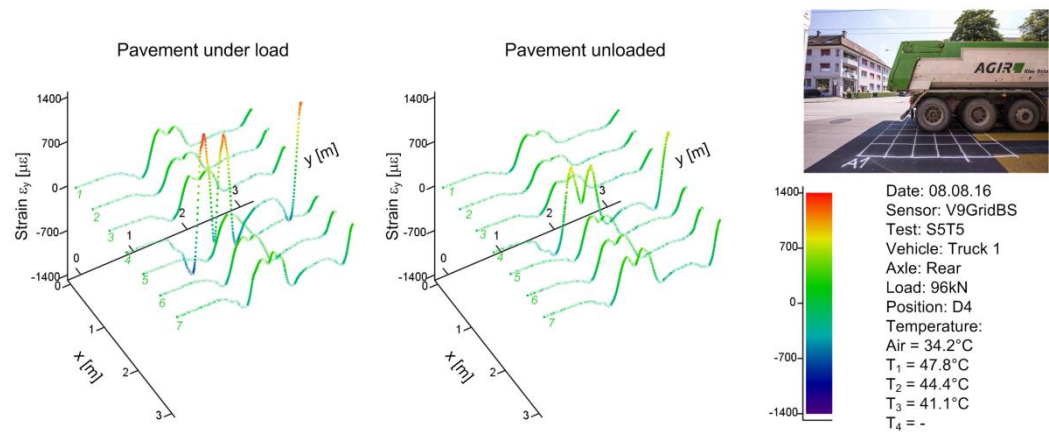
Fig. 70 *Transverse strain measurement under the rear axle of truck 1, summer*

Comparison of the measured strain distribution in different temperature conditions

The previous section pointed clearly out that the strains caused by the tires of truck 1 and the car strongly depend on the temperature of asphalt. In order to consider this more in depth, the measured strains along sensor section 4 (transverse) of the sensor V9GridBS were plotted against the transverse position y^* for different test series, which were conducted at various temperatures. This is shown in Fig. 71 (rear axle) and Fig. 72 (front axle). The position of the truck was not always perfectly located at $y = 1.5$m. In order to improve the visibility of the figures, the measured strain profile were, where necessary, slightly shifted to each other (indicated by the coordinate y^*). In order to assign a temperature to each test series, a representative value of $T_{3,rep}$ was taken (90mm depth).
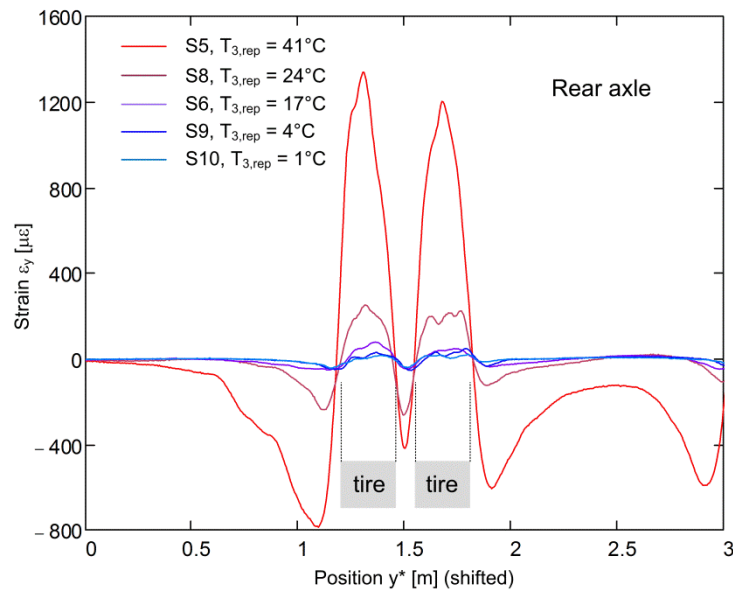
Fig. 71 *Comparison of measured strains for different temperatures (rear axle)*
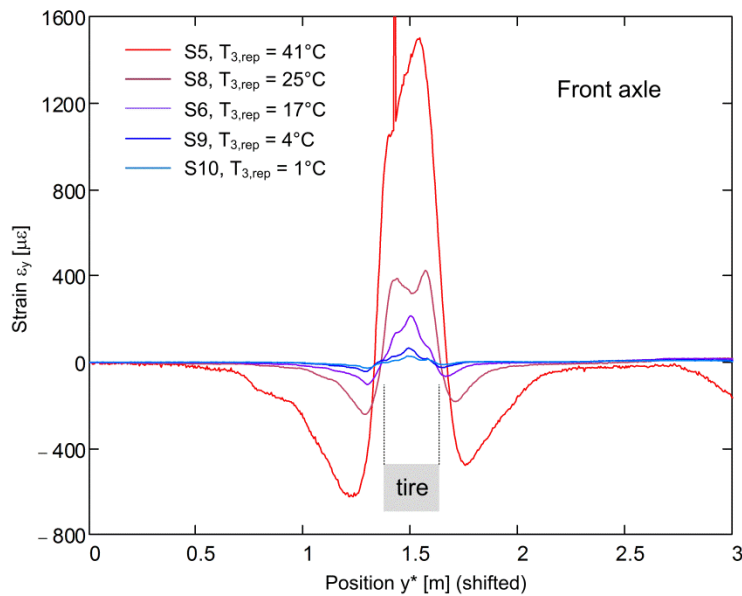
Fig. 72 *Comparison of measured strains for different temperatures (front axle)*

The comparison in Fig. 71 (rear axle) Fig. 72 (front axle) highlights again the strong dependence of asphalt stiffness on temperature. Between the maximum expansive strains of S10 ($T_{3,rep} = 3°C$) and S5 ($T_{3,rep} = 41°C$) is more than a factor or 50, a smaller

difference can be observed for the contractive strains beside the tire. At the bottom of these figures, the footprint of the single tire (front axle) and twin tire (rear axle) is shown schematically, which indicates that the range of expansive strains is limited quite well to the size of tire. Beside, contractive strains were measured. In summer, the two double wheels of the rear axle are influencing each other ($y* \approx 2.4m$), whereas this seems not to be the case for the front axle owing to the larger wheelbase.

In order to illustrate the strain distributions for cool temperatures in a better way, all distributions shown in in Fig. 71 (rear axle) and Fig. 72 (front axle) are repeated and plotted at individual scale in Fig. 73 (rear axle) and Fig. 74 (front axle). In all graphs the ratio between maximum (expansive) and minimum (contractive) strain on the ordinate of the figure is set to 2 in order to highlight the change of the strain distribution's shape towards cooler temperatures. Whereas in warm conditions the expansive strain directly under the tire is clearly larger than the absolute value of contractive strain beside the tire, it seems that expansive and the absolute value of contractive strain become approximately equal in cooler temperatures.
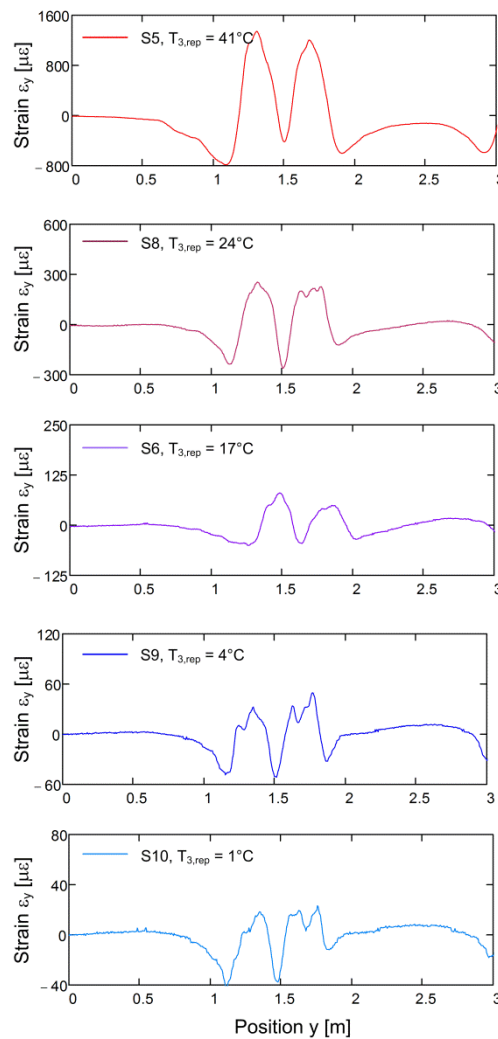
Fig. 73 Comparison of measured strains for different temperatures (rear axle)
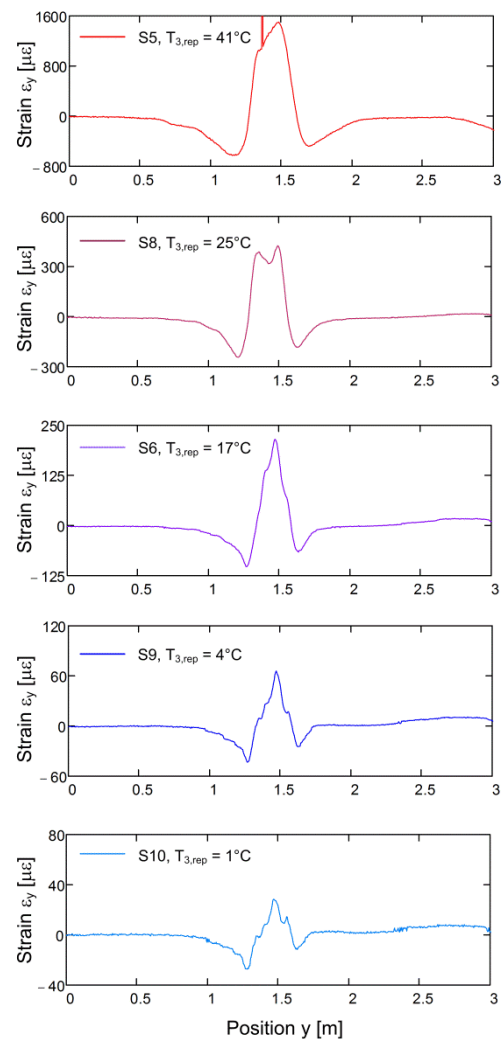
Fig. 74 Comparison of measured strains for different temperatures (front axle)

5.2.3 Measurements in 22cm depth using the sensor V3Trans FS

The sensor V3TransFS was foreseen to be used for static and dynamic measurements. Hence it has only a total length which is smaller than 10m and was therefore not installed in a reticular shape as the sensor V9GridBS, which was discussed in the section before. The sensor is embedded in 22cm depth on the subgrade at the interface between asphalt and gravel. Measurements were carried out in various temperature conditions and loads originating from different vehicles. The layout of this sensor is shown in Fig. 59. Strains were measured under the right side of the vehicle, whereas the wheels of the left side did not stand on the sensor V3TransFS.

Measurements in winter

Fig. 75 to Fig. 77 show the strains measured on February 2 in 2018 during static loading of the pavement by truck 1 (rear and front axle) and the car (front axle). In these figures, the strains immediately (a few seconds, indicated as "loaded", measurement time) after the load from the vehicle was brought onto pavement are shown, as in the previous figures using sensor V9GridBS. In addition, also the strain response immediately after unloading, when the vehicle drove away, is included (indicated as "unloaded", measurement time) and shows the delayed response owing to creep in asphalt. Interestingly, the sensor shows strains in a similar magnitude as the sensor V9GridBS during winter. Expansive strains can be measured directly under the tires of the vehicles with a maximum magnitude of around 60 to 80$\mu\epsilon$ (truck 1) and around 30$\mu\epsilon$ for the car. Also in 22cm depth, the twin tires of the truck lead to a double peak in expansive strain, whereas the single tire causes only a single strain peak. However, the distance between the two points, where the measured strain changes its sign and turns into contractive strain, became clearly larger than in the sensor in 4cm depth above and is significantly more than the tire dimension (truck 1 0.26m, car 0.18m). Furthermore, the contractive strains beside the tires do no show such a distinct peak as in 4cm depth and are distributed over a wider range. The non-symmetric distribution of strains, owing to the load brought by the left wheels of the vehicle, is clearly visible.

Measurements in autumn

Fig. 78 and Fig. 79 show the strains measured along the same sensor as before during October 16 in 2017. Owing to the clearly warmer environmental conditions, temperatures in the asphalt were around 20°C higher, which lead to strain magnitudes, which were around 3 times higher than in winter (February 2, 2018, previous section). Note that for these test series a different measurement device (although same nominal device type) had to be used and the strain measurement showed higher variability. Note that the measurements denoted with "unloaded" were taken after the whole truck left the sensor area, which means for the measurements with the front axle, that four further axles traversed the sensor before this measurement was launched.
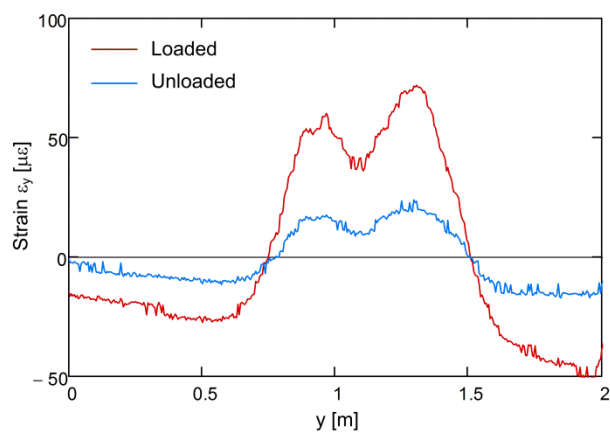
Date: 02.02.18
Sensor: V3TransFS
Test: S9T1
Vehicle: Truck 1
Axle: Rear
Load: 102kN
Position: A
Temperature:
Air = 8.5°C
T_1 = 11.1°C
T_2 = 6.2°C
T_3 = 5.2°C
T_4 = 4.7°C

Fig. 75 *Strain measurement under the rear axle of truck 1, winter*
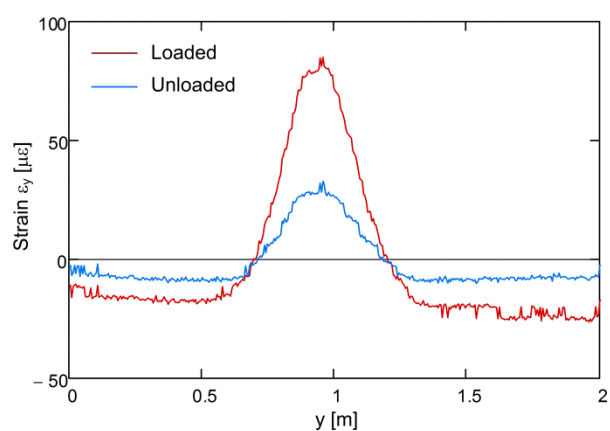
Date: 02.02.18
Sensor: V3TransFS
Test: S9T3
Vehicle: Truck 1
Axle: Rear
Load*: 49kN
Position: A
Temperature:
Air = 8.5°C
T_1 = 11.1°C
T_2 = 6.2°C
T_3 = 5.2°C
T_4 = 4.7°C

Fig. 76 *Strain measurement under the front axle truck 1, winter*
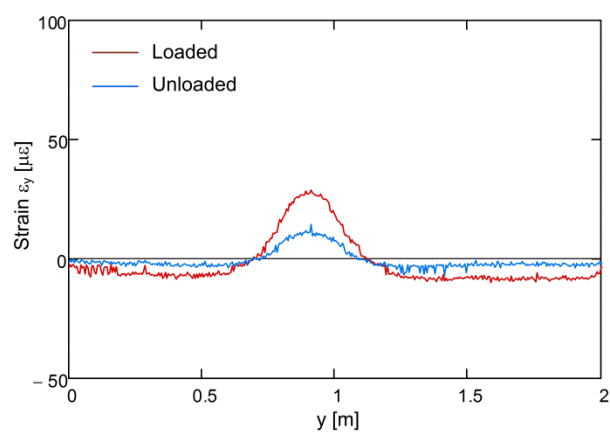
Date: 02.02.18
Sensor: V3TransFS
Test: S9T7
Vehicle: Car
Axle: Front
Load: 12.6kN
Position: A
Temperature:
Air = 6.0°C
T_1 = 6.4°C
T_2 = 7.2°C
T_3 = 6.8°C
T_4 = 6.3°C

Fig. 77 *Strain measurement under the front of the car, winter*

Date: 16.10.17
Sensor: V3TransFS
Test: S8T3
Vehicle: Truck 1
Axle: Rear
Load: 96kN
Position: A
Temperature:
Air = 26.6°C
T_1 = 32.3°C
T_2 = 28.0°C
T_3 = 26.8°C
T_4 = -

Fig. 78 *Strain measurement under the rear axle of truck 1, autumn*

Date: 16.10.17
Sensor: V3TransFS
Test: S8T6
Vehicle: Truck 1
Axle: Front
Load: 50kN
Position: A
Temperature:
Air = 26.6°C
T_1 = 32.1°C
T_2 = 28.2°C
T_3 = 27.0°C
T_4 = -
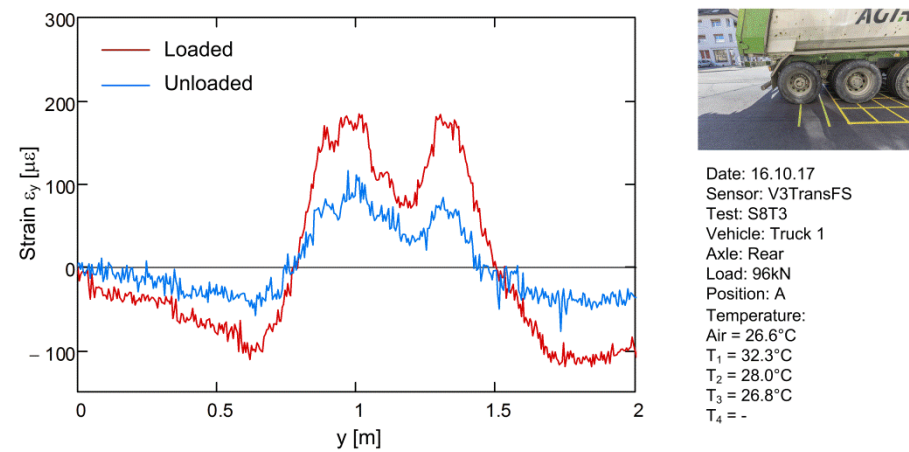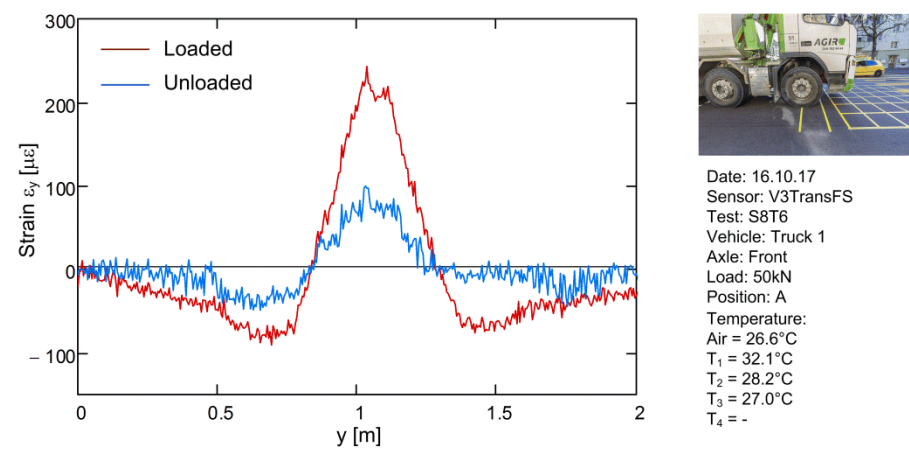
Fig. 79 *Strain measurement under the front axle truck 1, autumn*

5.2.4 Calibration measurements using ETH delta and concrete blocks

The strain distributions shown in the previous sections were gathered all by means of a standardized test procedure, described in section 5.1.7. Whereas these tests could be carried out without a strong disturbance of the traffic flow during the day, longer resting times of a load than a few seconds or measurements of the deflection trough were not possible. In order to collect further information about the behavior of the asphalt layers, which is of importance for the parameter determination in numerical modelling shown in the chapters towards the end of this report, one lane of the road was closed for several hours during the night of June 19 to 20 in 2017. This opportunity was used to gather settlement data of the road surface while it was loaded by the front axle of truck 2 and, furthermore, to study the behavior of asphalt under radial symmetric static loading with resting times of several minutes using concrete blocks. It is important to note that although the measurements were conducted during the night, the temperatures measured in the pavement are belonging to the highest recorded within this study. Furthermore, the temperature gradient changed its sign compared to the situation during the day: The layers in the center of the pavement were warmer than those close to surface. Moreover, it should be mentioned that during this night a malfunction of the connector on the measurement device OBR 4600 was detected, leading to the fact that more processing difficulties occurred. In order to still retrieve acceptable strains from the measurement, the spatial resolution (gauge length) and the sampling interval (sensor spacing) was doubled to 2cm and 1cm respectively, compared to the usual specifications of 1cm and 0.5cm used in this report.

Measuring the settlement trough using ETH Delta

For the measurement of the vertical displacements, a measurement device called "ETH Delta", developed at IGT of ETH Zurich a few years ago [45], was applied. The device was positioned directly in the center above the sensor sections 1, 4 and 7 of the sensor V9GridBS, in order to collect simultaneously both, strain in the asphalt layer and surface settlement. The test was repeated at each sensor section, hence, in total six tests were conducted. Fig. 80 shows the installed ETH Delta device above sensor section 1 of the sensor grid. A detailed description about the ETH Delta measurement procedure is provided in [45]. Fig. 81 shows the positioned front axle of truck 2 during a test, bringing an axle load of 90kN to the pavement. The deflections were measured be means of lasers while the truck was approaching the sensor line, while it stood for around a minute on the sensor line and while it left the sensor line again. The distance between the truck and the sensor line was measured also by means of a laser, making it possible to construct a full settlement trough, using the variable distance truck to sensor line. Distributed strain measurements were carried out in parallel before the truck drove onto the sensor section (reference measurement), immediately after it arrived on the sensor line (loading 1), before (loading 2) and immediately after (unloading) it left the sensor section. The results of the distributed strain measurement during test D3 carried out on the sensor section 4 are shown in Fig. 82.

Fig. 80 *Installed ETH Delta device before the test above sensor section 1 of the grid*
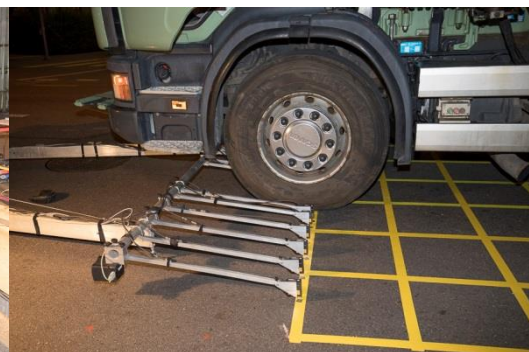
Fig. 81 *ETH Delta test combined with strain measurements directly underneath*
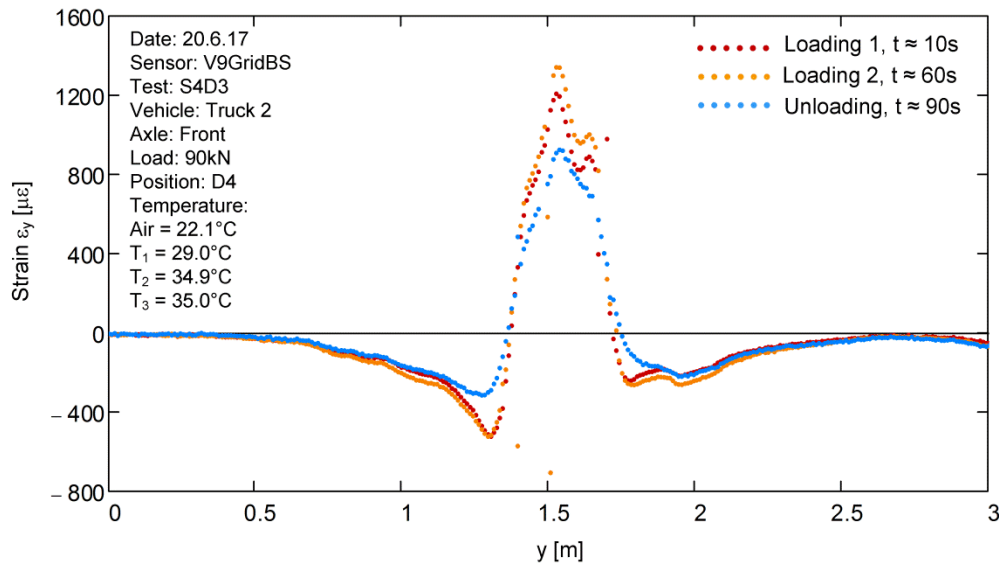
Fig. 82 *Transverse strains along sensor section 4 during test series 4 (ETH Delta, D3)*

The distributed strain measurements showed expansive strains directly under the tire of up to $1400\mu\varepsilon$ during test D3 shown in Fig. 82. Note that the measurement results were shown as dots and not as lines for the sake of a better visibility, owing to outliers in the measurement (data processing difficulties). The delayed strain response in unloading owing to creep is clearly visible. The resting time t of the load provided in Fig. 82 is an approximate parameter retrieved from the time stamp of the measurement. Note that the time of the careful slow positioning of the truck between the lasers is not included. t includes only the time after the truck was positioned correctly. The corresponding settlements measured beside the tire (but not underneath) were around 0.1mm to 0.15mm during these tests and are shown and discussed, together with the numerical modelling, in chapter 7. The combined simultaneous measurement of strains and deflections gave an interesting insight into the behavior of asphalt and was an important input data for the inverse analysis shown in the chapter 7 to 9.

Measuring the strain response under a radial symmetric loading using concrete blocks

In order to have longer resting times of the load on the pavement and to create a complete radial symmetric instantaneous loading of the pavement, which simplifies the parameter derivation in numerical modelling, the pavement was loaded during the night from June 19 to 20 in 2017 with concrete blocks, which were positioned by means of a crane (Fig. 83). The concrete blocks used were so called "Ebi-Blocs 0.8", manufactured by the company "Eberhard", having a mass of 1.2t. The blocks were placed on a wooden bearing, which was set on top of a thin sand cushion on the pavement. The circular bearing had a diameter of 0.3m. Four tests were carried out in total. A first test (K1) was conducted using a single block, whereas in the following three tests (K2 to K4) two blocks were used for the purpose of loading. Fig. 83 shows the applied bearing and the block during test K1, in which the load was applied on D4. Fig. 84 shows a picture taken during test K2 involving two blocks, loading the pavement on C4 and E4.

Fig. 83 *Positioning of the concrete block on a wooden bearing on top of a sand cushion during test series S4 (test K1)*

Fig. 84 *Position of two concrete blocks during test series S4 (test K2)*

Strains were measured during these tests along the whole grid (Sensor V9GridBS) as it was the case during the standard test involving truck 1, shown in the previous sections. However, in this report only the transverse strains ε_y and, out of the transverse strains, only those measured along section 4 directly under the load are included. Fig. 85 shows the transverse strain ε_y measured during test K1 of test series S4. The reference measurement was gathered right before the concrete block was put on the bearing. Immediately after the loading of the pavement with the concrete block, the measurement K1-1 was conducted (conducting a measurement takes up to around 10s). After the load was left for around 80s on the pavement, a second measurement (K1-2) was conducted. Afterwards the concrete block was removed and the measurements K1-3 to K1-5 were conducted and delayed strains owing to creep were measured. The development of the strain occurring around point P_1 in Fig. 85, with the approximate time taken from the timestamp of the measurement device, is shown in Fig. 86. Obviously, the change in strain owing to loading and unloading has clearly not the same magnitude.
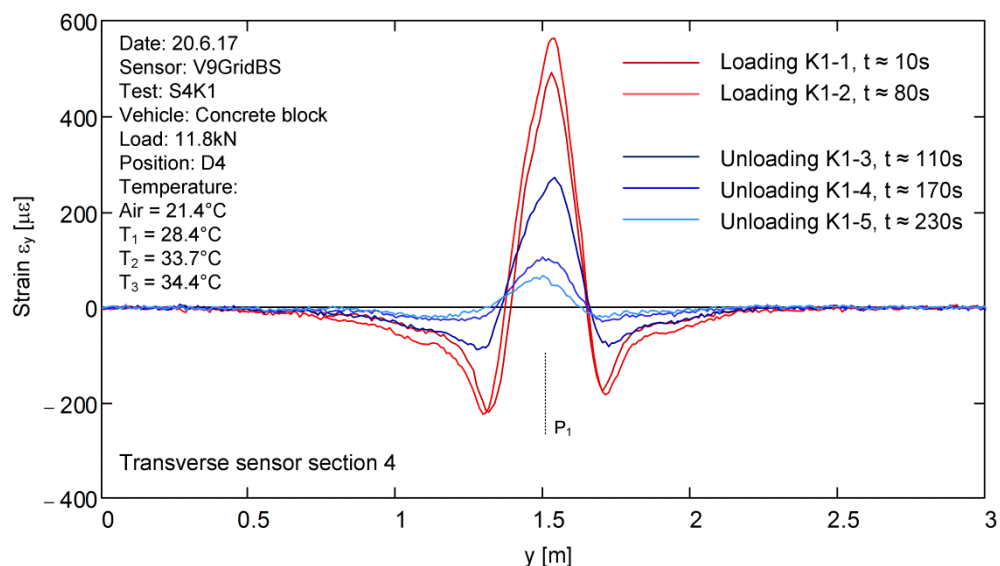
Fig. 85 *Transverse strains along sensor section 4 during test series 4 (test K1), pavement loaded by a concrete block*
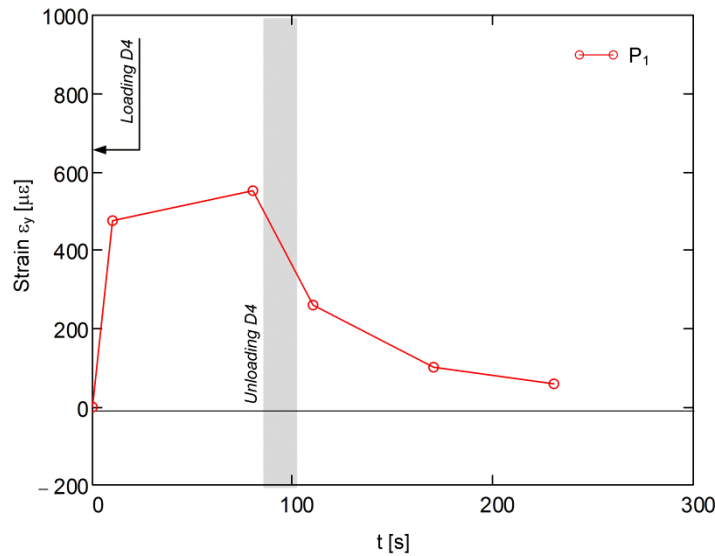
Fig. 86 *Development of strains around Point P_1 with time during test series 4 (test K1)*

In test K2, two blocks were used and the resting duration of the block was increased. Fig. 87 shows the strain distributions measured while the pavement was loaded by the two blocks. First the block on E4 (around $y = 2m$) was used for loading and the measurements K2-1 to K2-3 were conducted. Afterwards, the second block was placed on C4 and the measurements K2-4 to K2-6 were carried out. Between 6 and 7min of the test, the concrete block on C4 was removed again and the measurements K2-7 to K2-10 were conducted (Fig. 88). During this time window, the strain under E4 increased only marginally. Afterwards, also C4 was unloaded and the sensor response was measured with the readings K2-10 to K2-12. It is of interest to note that during Test K1 under D4 only a single expansive strain peak was measured under the load, whereas in test K2 under both loads the tendency of two expansive strain peaks can be observed (see also discussion in section 5.4).
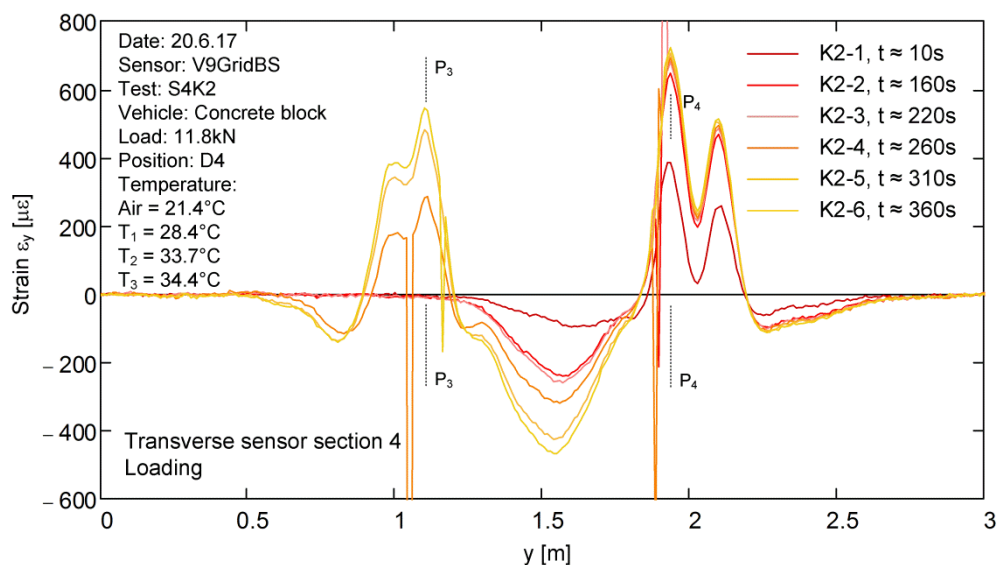
Fig. 87 *Transverse strains along sensor section 4 during test series 4 (test K2), pavement loaded by concrete blocks, loading phase*
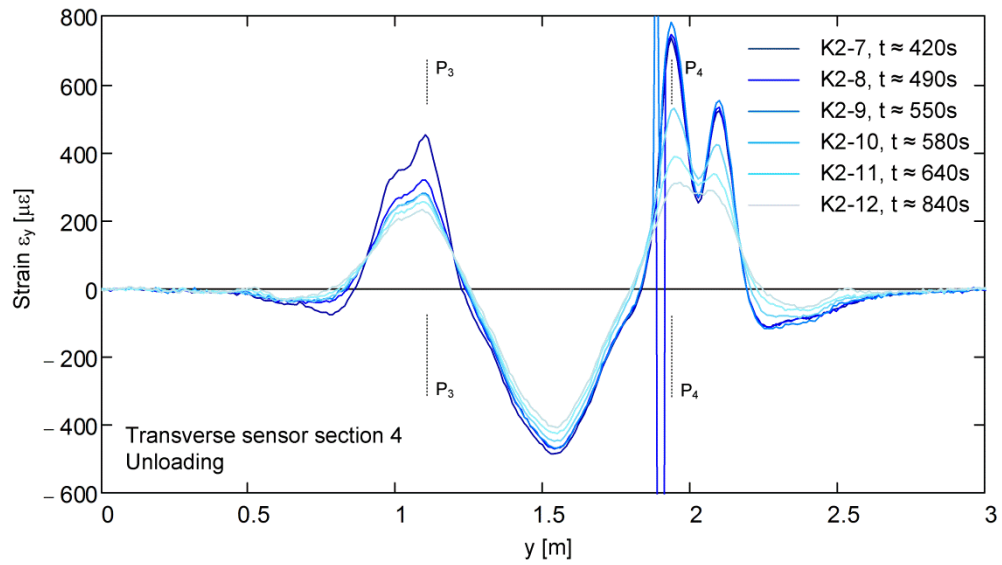
Fig. 88 *Transverse strains along sensor section 4 during test series 4 (test K2), pavement loaded by concrete blocks, unloading phase*

The development of strains with approximate time is shown in Fig. 89 for the strains around point P_3 and P_4 in Fig. 87 and Fig. 88. As in test K1, unloading leads also in test K2 not to the same amount of strain change as loading did.
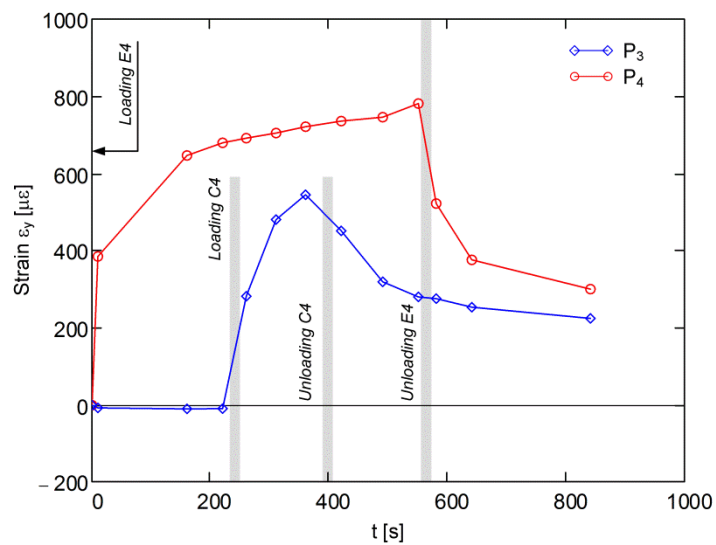
Fig. 89 *Development of strains around Point P_3 and P_4 with time during test series 4 (test K2)*

5.3 Dynamic measurements

5.3.1 Introduction

Whereas in the section before the strain distribution within the pavement was measured under a static load with short (seconds) and intermediate (minutes) exposure times, in this section, the results from strain measurements are shown, where the test vehicle did not stop above the sensors but traversed the sensors with a pre-defined nominal velocity v_{nom}. In order to be able to measure the strains with a sufficiently high temporal resolution, an ODiSI B device, manufactured by the company Luna Inc., was used which can acquire measurements much faster than the OBR 4600 device used for the static tests. This device allows for measuring strains in a distributed manner with spatial resolution of around 5mm and a scanning (acquisition) rate of 100Hz over a length of 10m. Higher frequencies would be possible, but this only on the cost of sensor length. Therefore, higher frequencies were not applied in this project. The nominal velocities for the tests were chosen to values according Tab. 17. Since the test site was within the city of Zurich, 50km/h could only be realized with sufficient security personal and traffic lights, which were taken out of order. The spatial distance d_{nom}, which the vehicle covers between two readings of the ODiSI B device (running at 100Hz), is for these velocities between 0.014 and 0.14m. Since d_{nom} for the largest velocity is smaller than the shortest length of the footprint of a tire (truck 1, 0.18m), it can be ensured, that the tires of each axle are always directly above the cable when a reading is taken. For the car, this statement holds only up to $v_{nom} = 30$km/h, since the tire of the car induces a footprint length of only 0.13m.

Tab. 17 Vehicle velocities during the dynamic tests

Nominal velocity v_{nom} [km/h]	5	10	15	30	(50)
Nominal velocity v_{nom} [m/s]	1.39	2.78	4.17	8.33	(13.89)
Spatial distance between two measurements d_{nom} [m]	0.014	0.028	0.042	0.083	(0.14)
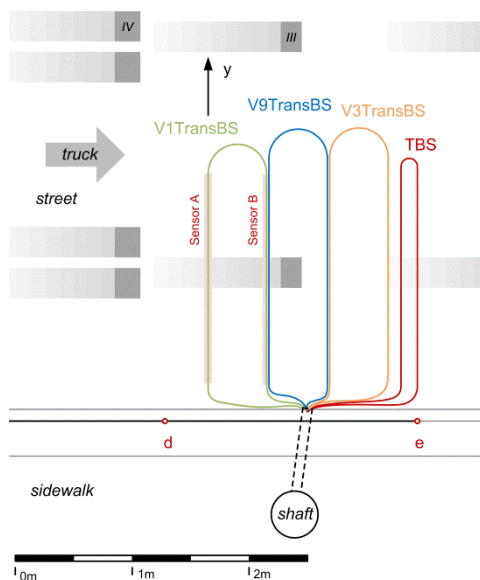
Fig. 90 Part of the footprint of truck 1 for dynamic tests using the sensor V1TransBSS

Dynamic measurements were conducted with different sensors as V1TransBS, V9TransBS, V9LongBS (all in 4cm depth) as well as V3TransFS (22cm depth). The situation, when truck 1 is traversing the sensor V1TransBS is shown in Fig. 90. Note that not all axles are drawn in this figure. The figure shows the situation when axle No. I to III (single tire) have already traversed the sensor, whereas axle No. IV and V (twin tires) did not cross the sensor V1TransBS yet. The fiber optic sensor loop is again divided in two sections: section A (traversed first) and section B, each around 1.8m long with a distance of 0.5m in between. The vehicles were passing the sensor with their right wheels approximately in the center. The situation, when the car is crossing the sensor, is shown in Fig. 91. Fig. 92 finally, shows the transit of truck 1 above the longitudinal sensor loop V9LongBS.
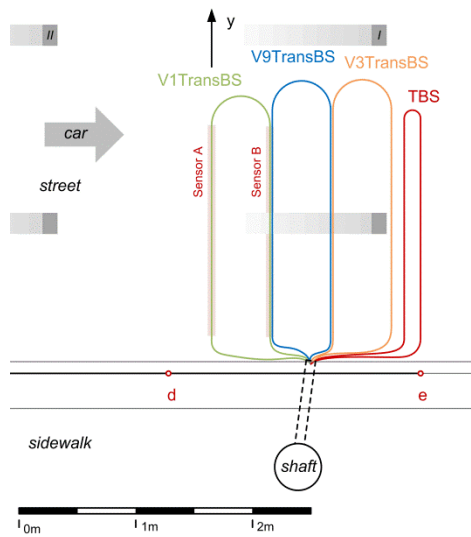
Fig. 91 Footprint of the car for dynamic tests using the sensor V1TransBS
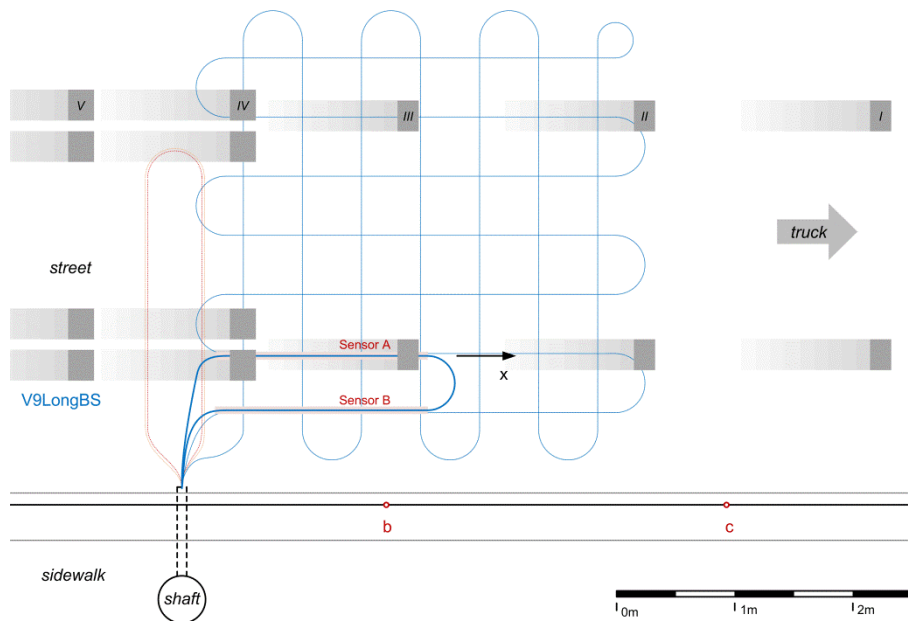
Fig. 92 Footprint of truck 1 for dynamic tests using the sensor V9LongBS

5.3.2 Results obtained during dynamic measurements

In order to illustrate the measurement results in the following section in a simpler way, an example of such a dynamic measurement is discussed here in depth. Fig. 93 shows the measurement results of section A, resulting from a transit of truck 1 with 5km/h above sensor V1TransBS on August 8 in 2016 in very warm conditions. On one abscissa the transverse coordinate y is plotted, whereas the other abscissa represents the time axis. The ordinate is the measured transverse strain ε_y (perpendicular to the driving direction). The plot consists of 1600 single distributed measurements, which were strung together, each of them representing a strain distribution at certain constant time. The five peaks, which were highlighted with black dots, represent the passage of the right wheels (left wheels are beside the sensor and not visible therefore) of an axle of truck 1. The delayed response owing to creep, once the last axle has passed, becomes clearly visible in this figure. Since the last two axles contain twin tires, smaller additional peaks occur for axle No IV and V at approximately y = 1.2m. Expansive and contractive strains of around 1000$\mu\varepsilon$ occur under and beside the wheels. This is, as expected, already slightly smaller than the strains measured under static load, although this result realized at only 5km/h.

The same result is again shown Fig. 94, simply the perspective was changed to a top view. The measurement results from sensor section A are repeated on the left side, on the right side, the strains from sensor section B are plotted. Since section B is located 0.5m behind section A, a time shift Δt of the transit of axles No. I to V can be observed. Axle No. I passes section A at 1.139s, whereas it passes section B at 1.559s. From that an effective velocity of around 1.2m/s (4.3km/h) can be estimated while the front axle of the truck passed. Note that at these low velocities, it was difficult for the truck driver to keep the velocity constant during the passage. Hence a slightly higher velocity of around 1.5m/s (5.3km/h) was observed towards the passage of the end of the vehicle.

Fig. 95 shows a section for y = 0.907m through sensor section A and B. The transit of the five axles, the different spacing of the axles as well as the time shift Δt between sensor A and B becomes clearly visible. In order to calculate the real velocity of the vehicle, which may differ somewhat from the nominal velocity, the length of the vehicle (6.77m) and the time difference between the first and the last axis could be used. However, in general, the length of the vehicle may not be known, and, therefore an additional analysis based on cross-correlation between the two signals was conducted around the center zone of the sensor. This additional analysis was carried out in order to define time a shift Δt and to compute the real velocity of the vehicle in an independent way for the reason of comparison. The last 10 seconds show the delayed response owing to creep, which may also consist partially of plastic strains.

Sections trough the measurement data with constant time allow comparing the strain distribution from the dynamic test to those observed during static loading. Fig. 96 shows a section at t = 1.139s (Sensor A) and 1.559s (Sensor B), when the front axle was exactly traversing the sensor. The same comparison is made in Fig. 97 for the rear axle. Although the strain distribution shows more variability and some measurement outliers (processing difficulties of the device) occurred, the double strain peak under the twin tires of the rear axle is still recognizable, whereas under the front axle still only a single strain peak develops.

It is important to note, that the application of this technology allows for counting the axles of a vehicle (and the number of tires), finding the driving direction and the position in the road where it drove and the velocity of the vehicle. A determination of the axle loads of the vehicle seems to be theoretically supposable; however, a precise temperature measurement and an adequate constitutive law would be required.
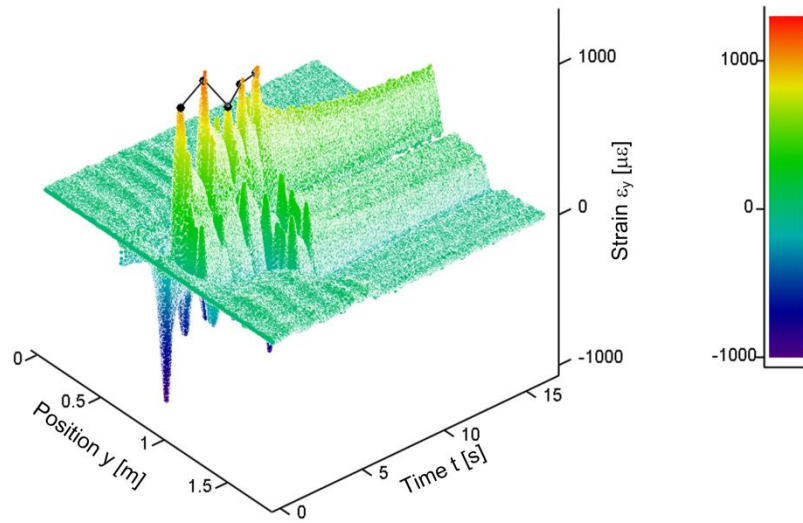
Sensor A, truck 1, S5, v_{nom}= 5km/h

Fig. 93 *Strains measured during transit of truck 1, sensor A, S5, v_{nom} = 5km/h*
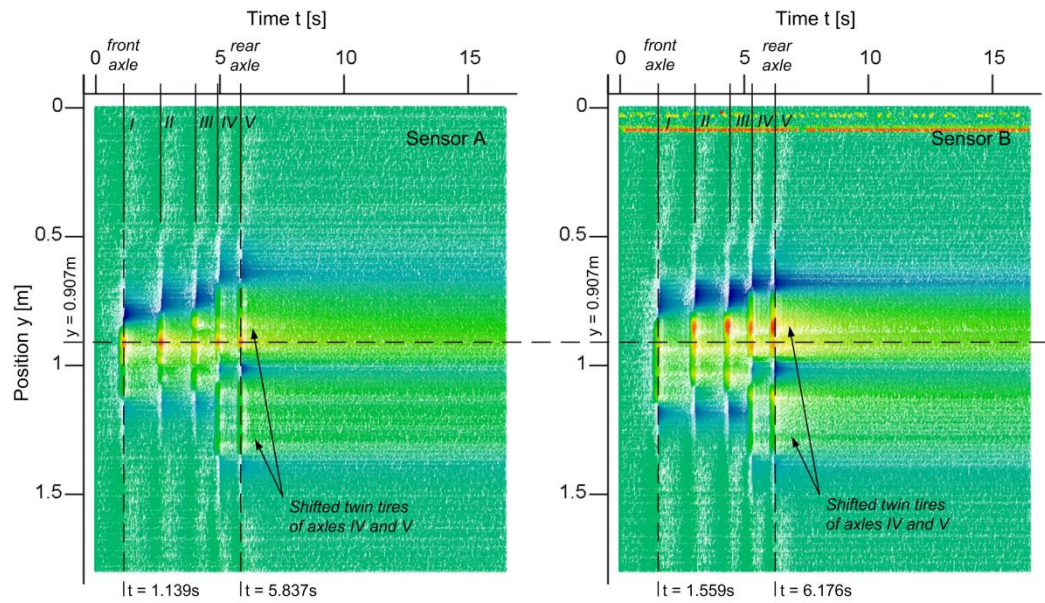
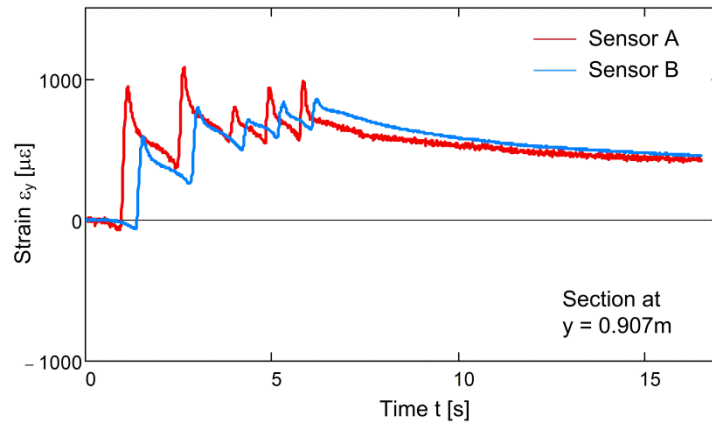**Fig. 94** *Response of sensor section A (left), response of sensor section B (right)*
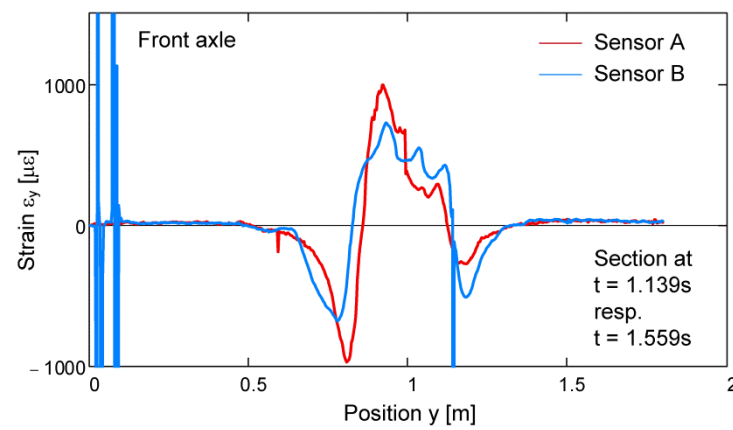
Fig. 95 *Section with constant position y = 0.907m*

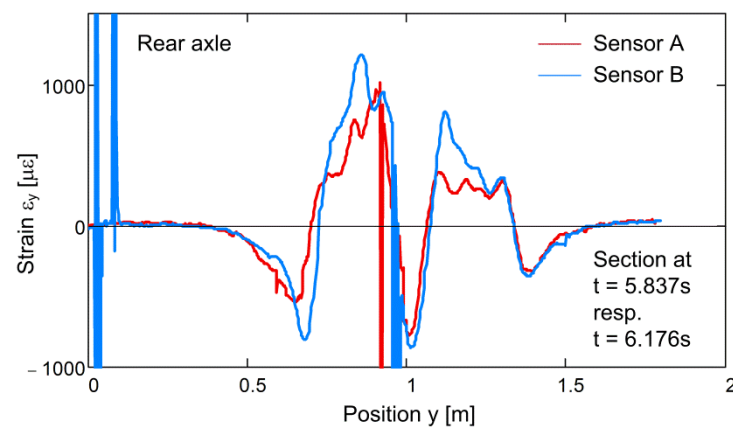**Fig. 96** *Section with constant time t = 1.139s (A) and 1.559s (B), front axle, single tire*

Fig. 97 *Section with constant time t = 5.837s (A) and 6.176s (B), rear axle, twin tire*

5.3.3 Measurements on the grade of the binder course

Transit of truck1 over sensor V1TransBS

In this section, the measurement results of the passage of truck 1 above the sensor V1TransTS in 4cm depth are presented. Fig. 98 to Fig. 100 show the strains measured at 100Hz and a spatial resolution of 5mm while truck 1 drove with the nominal velocity of v_{nom} = 5km/h over the sensor loop V1TransBS for three different temperature conditions (winter, autumn, summer). The figures are kept in the same format as in the exemplary measurement in the previous section 5.3.2: On the left side of these figures, the measured transverse strain ε_y is shown in a perspective view versus time t and transverse position y. On the right side, the same data is presented in a top view in order to improve the visibility of the axle passage. Note that axles No. I to III have single tires whereas axles No. IV and V have twin tires, which are slightly displaced from the other tires (Fig. 55). A direct comparison between the two extremes winter and summer is made in Fig. 101, in form of a side view, which shows the envelope of strains with time.

Although the nominal velocity v_{nom} = 5km/h was the same, the calculation of the velocity during postprocessing of the measurement results, using the known distance between the axles and applying a simple rough peak detection scheme (see e.g. Fig. 93), showed, that the actual velocity may differ slightly from the nominal velocity. Since the actual velocity is calculated as an average from the two sensors A and B including the four axle distances, it is denoted v_{ax} and regarded in this study as the true velocity of the vehicle. Of course, in general conditions the axle spacing of the vehicle is not known and, hence, two alternative velocities are being calculated and denoted v_{lp} and v_{cc}. Since they may not represent the true velocity of the vehicle as accurate as v_{ax}, they are denoted "estimated" velocities. v_{lp} results from the spacing of the loop (sensor A and B) and the time difference between the strain peaks in sensor A and B, whereas v_{cc} represents the outcome of a method applying cross-correlation based analysis between the results of sensor A and B. For this purpose, the strain distribution with time around the wheels, as shown e.g. in Fig. 95, is used in order to define a time delay between the signals. For the calculation of v_{lp}, the knowledge of the number of axles of the vehicle was used in this study (in a technically mature solution presumably not necessary). The calculation of v_{cc} required in this study no information about the vehicle (this of course on cost of accuracy). However, it also does not represent a completely automated method yet and requires currently still some input and further improvement if applied elsewhere. The different velocities and their denotation are shown in Tab. 18, the full information about the nominal, calculated and estimated velocities of the tests discussed in this section, is provided in Tab. 19. However, it should be noted that the values listed in Tab. 19 may vary slightly with the applied parameters for the used peak detection routine and the input parameters for the method using cross correlation analysis.

The effect of different thermal conditions on the dynamic measurement results is discussed after Tab. 19, in a similar way as already in section 5.2 before for the static tests. Sensor V1TransBS was not only traversed with a nominal speed of 5km/h, but also with higher velocities of 10, 15, 30 and partially also 50km/h. The effect of the different vehicle velocities on the strains measured in the asphalt is shown therefore in a further section after Fig. 102.
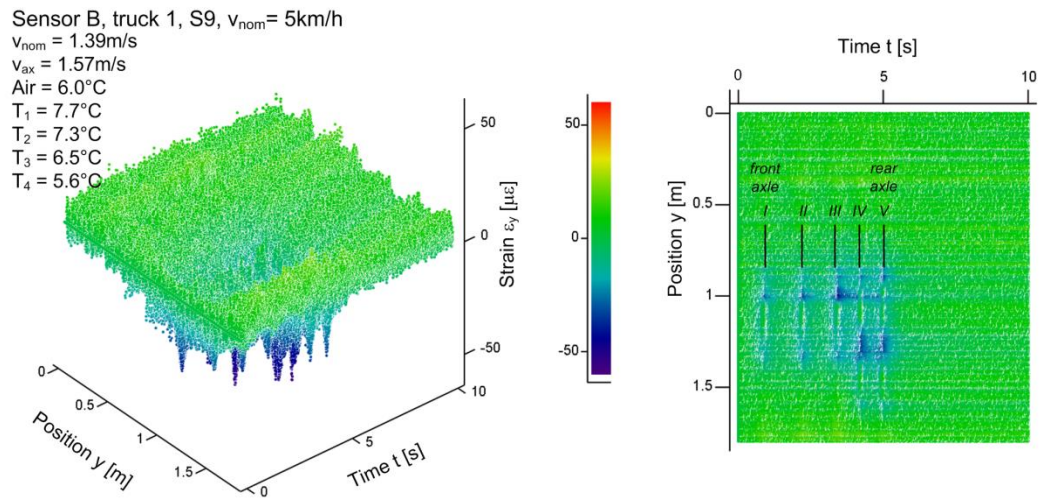
Sensor B, truck 1, S9, v_{nom}= 5km/h
v_{nom} = 1.39m/s
v_{ax} = 1.57m/s
Air = 6.0°C
T_1 = 7.7°C
T_2 = 7.3°C
T_3 = 6.5°C
T_4 = 5.6°C

Fig. 98 *Strain measured during passage of truck 1, winter, v_{nom} = 5km/h, 4cm depth*
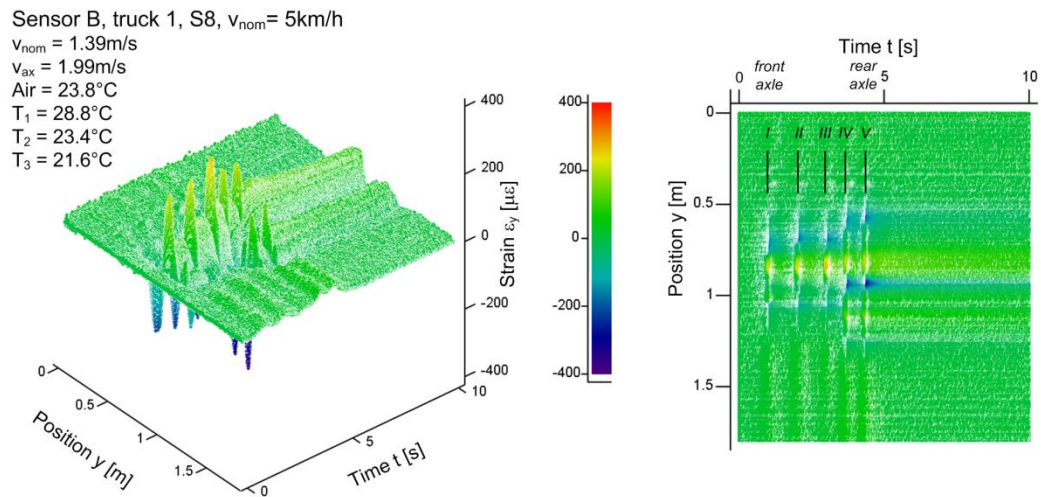
Sensor B, truck 1, S8, v_{nom}= 5km/h
v_{nom} = 1.39m/s
v_{ax} = 1.99m/s
Air = 23.8°C
T_1 = 28.8°C
T_2 = 23.4°C
T_3 = 21.6°C

Fig. 99 *Strain measured during passage of truck 1, autumn, v_{nom} = 5km/h, 4cm depth*

Sensor B, truck 1, S5, v_{nom}= 5km/h
v_{nom} = 1.39m/s
v_{ax} = 1.42m/s
Air = 26.6°C
T_1 = 40.4°C
T_2 = 35.8°C
T_3 = 32.9°C
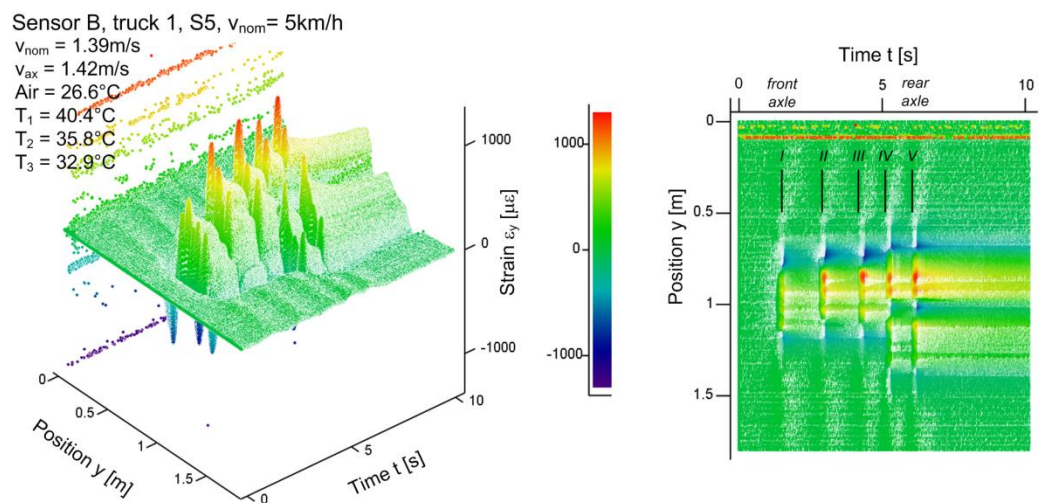
Fig. 100 *Strain measured during passage of truck 1, summer, v_{nom} = 5km/h, 4cm depth*

Sensor B, truck 1, S9, v_{nom}= 5km/h
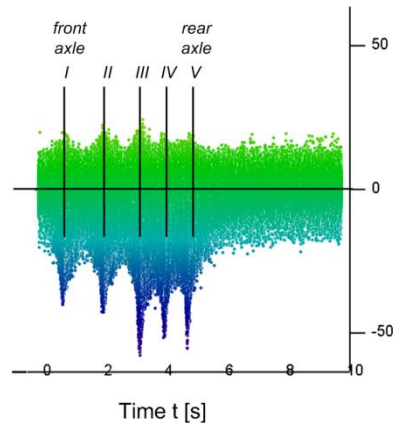
Sensor B, truck 1, S5, v_{nom}= 5km/h
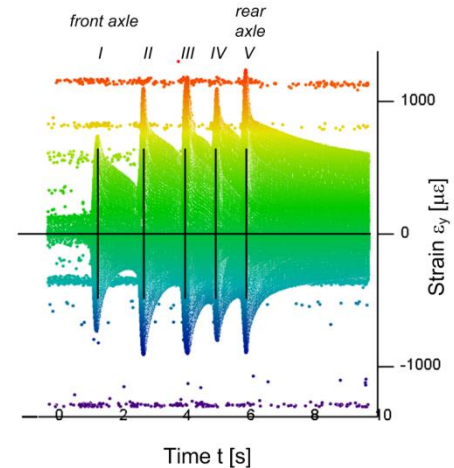
Fig. 101 *Comparison of strain envelope with time for winter (left) and summer (right)*

Tab. 18 Velocity definitions

Denotation	Symbol	Explanation
Nominal velocity	v_{nom}	Nominal, predefined speed of the vehicle before the test
Calculated velocity	v_{ax}	Calculated true velocity of the vehicle using the strain peaks in sensor A and B and the known axles distances of the vehicle
Estimated velocity	v_{lp}	Estimated velocity using the time difference between the strain peaks in sensor A and B (0.5m spacing), only the number of axles of the vehicle is used
Estimated velocity	v_{cc}	Estimated velocity using the time delay between the strain distribution in sensor A and B (0.5m spacing) resulting from a method applying cross-correlation analysis around the zone where the wheels passed the sensor, no prior knowledge about the vehicle used

Tab. 19 Nominal, calculated and estimated test vehicle velocities

Test series	Nominal velocity v_{nom} [km/h]	Nominal velocity v_{nom} [m/s]	Calculated velocity v_{ax} [m/s]	Estimated velocity v_{lp} [m/s]	Estimated velocity v_{cc} [m/s]
S5	5	1.39	1.42	1.41	1.49
S9	5	1.39	1.57	(2.12)	(1.04)
S8	5	1.39	1.99	2.04	2.09
S8	15	4.17	3.84	3.79	3.82
S8	30	8.33	7.19	7.14	7.09
S8	50	13.9	12.8	12.5	13.5

Effect of different thermal conditions at constant nominal velocity of 5km/h

As for the static tests, also for the dynamic tests the thermal condition in the asphalt layer represents the key parameter, which is influencing the strain within the asphalt. Clearly, with increasing temperature, the stiffness of asphalt becomes smaller and the strains under the same load increase, as already shown in the static tests. However, in the dynamic tests not only the strain magnitude, but also the strain distribution experienced a small variation with temperature.

Fig. 98 shows the strain measured in sensor B with time and space during the passage of truck 1 with v_{nom} = 5km/h in rather cool conditions ($T_{3,rep}$ = 7°C, test series S9, winter). The same test was carried out in warmer conditions ($T_{3,rep}$ = 22°C, test series S8, autumn, Fig. 99) and even very warm conditions ($T_{3,rep}$ = 33°C, test series S5, summer,

Fig. 100). Although the actual velocity of truck 1 varied slightly in these three tests between 5.1km/h and 7.2km/h (Tab. 19), the test conditions are regarded to be comparable. Whereas in summer and autumn the five axles of truck 1 become clearly visible, owing to the expansive strains (positive) directly under the tire, this is not the case in cold conditions in winter. In winter, the strains directly under the tire are indeed different from those beside of the tire as in summer or autumn, but in general, they do not exceed zero and remain contractive as beside of the tire. This was not the case during static measurements in winter, where the strains directly under the tire were of expansive nature for all temperatures. However, as the top view perspective in Fig. 98 indicates, the passage of each individual axle remains still visible in the results as distinct contractive strain peaks beside the tire. This is also pointed out in Fig. 101, where the strain distribution of the winter and the summer measurement is compared to each other by means of a side view of the strain distribution, which shows actually the strain envelope over all positions y with time t. Also in winter, the passage of the five axles remains visible, simply the expansive peaks under tire do not occur.

A direct comparison of the recorded strain distribution for different thermal conditions with space is made in Fig. 102, where strain for a constant time t is shown, when the tire was during the passage for an instant above the sensor. In Fig. 102 on the left, the strain distribution is shown for four thermal conditions (S6, winter, in addition to S5, S8 and S9). In order to enable a simpler interpretation of the results, the individual strain distribution were shifted slightly to each other (indicated by the coordinate y*), since the truck did not pass the sensor always exactly at the same position. This comparison was made for the passage of the front axle (No. I) of truck 1 and it reminds to Fig. 72, where the comparison was made for the static tests. However, owing to the different measurement device and the dynamic nature of the test, the strains in Fig. 102 contain slightly more irregularities. Between the maximal contractive strains of S5 (summer) and S9 (winter) is more than a factor of 30.

On the right side of Fig. 102, each measured distribution is shown individually at a different scale and along the coordinate y (not shifted). These individual distributions highlight again the relative decrease of expansive strains under the tire, compared to the contractive strains beside of the tire, up to the conditions in winter, where under as well as beside the tire no expansive strains are measured anymore (S9).
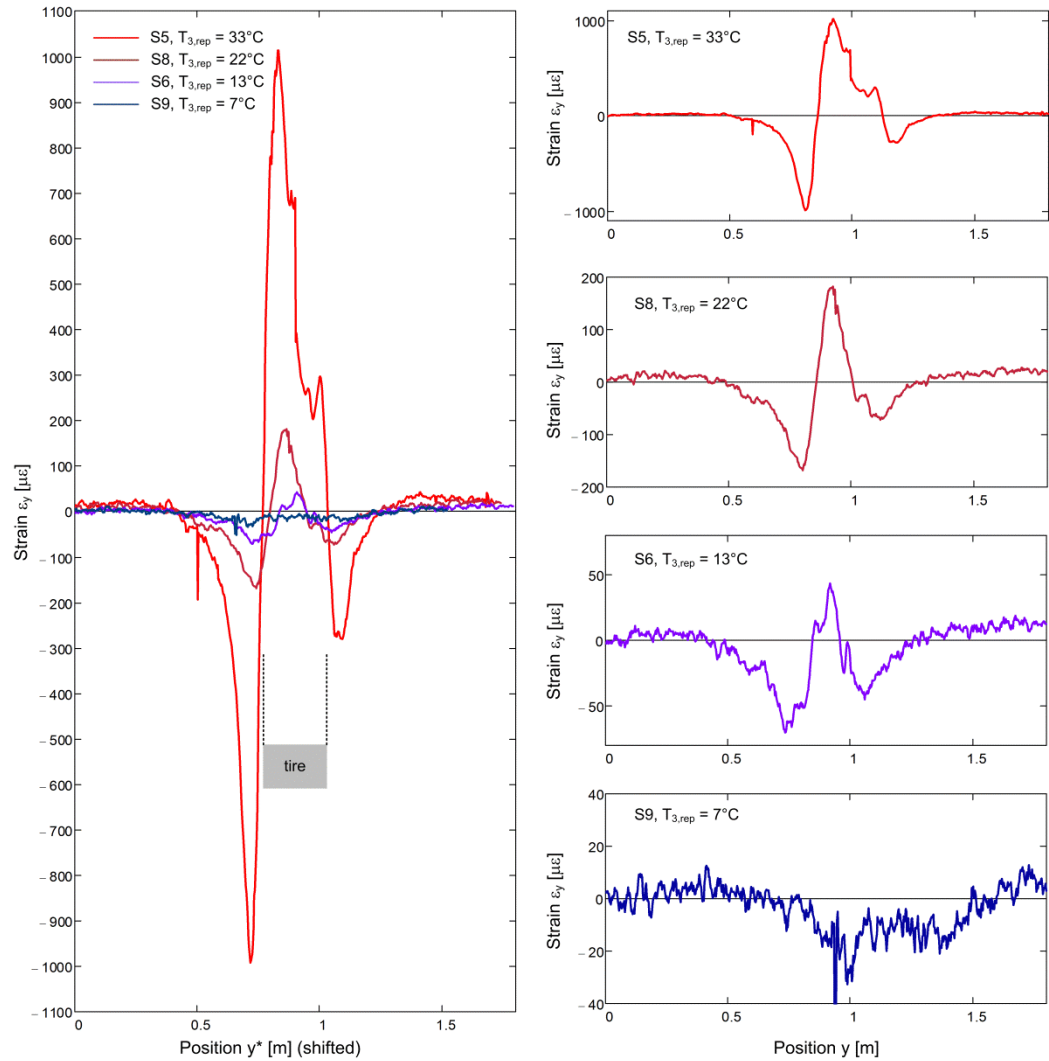
Fig. 102 *Comparison of the strains measured during the passage of the front axle of truck 1 while the tire is located above the sensor, in different thermal conditions at $v_{nom} = 5km/h$*

Effect of different vehicle velocities

In order to be able to study the effect of different velocities on strain, the results of a certain test series are considered in order to ensure approximately constant thermal conditions in asphalt. In this study, the test series S8 in autumn was chosen for this purpose. Fig. 103 to Fig. 106 show the transverse strains ε_y measured with the sensor V1TransBS during the passage of truck 1 with a nominal speed v_{nom} of 5km/h, 15km/h, 30km/h and 50km/h. Owing to the fact that during the test with $v_{nom} = 5km/h$ a slightly higher velocity than desired was realized and during the test with $v_{nom} = 10km/h$ a slightly lower velocity resulted, the calculated velocity v_{ax} of both tests was practically the same and, hence, only the results from the test with $v_{nom} = 5km/h$ are shown here.

The measurement results are presented in the same way, as introduced in the beginning of section 5.3.3 explained. In addition, in the perspective view of the figure, the strain peaks, found by an applied simple rough peak detection scheme, are marked with black dots. The presented time window in these figures is always scaled to six seconds. Owing to the increasing vehicle velocity, the time difference between the passage of the front and the rear axle becomes smaller. Owing to the minimal contact length of 0.18m between the tire of truck 1 and asphalt, also at the speed of 13.9m/s (50km/h), at least one measurement is available, while the tire was above the sensor, since the acquisition run at 100Hz. Owing to the fact that center of the tire may be in maximum misplaced by around 0.07m, it may be, that at the speed of 50km/h not the absolute maximum of the

strain magnitude was recorded, however, the effect is not expected to be large. In general, an increase of the acquisition rate would improve the situation, which represented, owing to the required sensor length, unfortunately the technical limit of the device at that time.

As the measurement results in Fig. 103 to Fig. 106 show, there exists a trend of smaller strains at higher velocities, as could be expected owing to the partially viscous nature of asphalt. However, it is interesting to note that this decrease of strain with increasing velocity is again not homogenous along the position of the sensor. Similar to the effect of decreasing temperature on strain also higher velocities lead mainly to a decrease of the expansive strain in asphalt directly under the tire. At a velocity of 50km/h, the expansive strain under the tire is below $40\mu\varepsilon$ or approximates even zero, whereas the contractive strain beside the tire has still a magnitude of around $100\mu\varepsilon$ or larger. This can be illustrated at best with Fig. 107, where for the two extreme cases of v_{nom} = 5km/h (left) and v_{nom} = 50km/h (right) again side view of the measured strain envelope in space with time is shown. Whereas the time scale for the left figure (5km/h) was left by 6s, the time scale for the right figure (50km/h) was changed to 2s in order to improve visibility. These two figures point clearly out that firstly, the strain distribution does not decrease homogenously along the position y and secondly, that also for 50km/h the passage of the individual axles remains still visible as contractive strains in the measured transverse strain ε_y.

Interestingly, compared to the situation with the static tests, in the results of the dynamic measurements, the transverse strain in positions located more than 0.5m away from the tire changes again its sign and becomes expansive. It seems to resemble the situation where the asphalt layer acts like a plate on an elastic foundation with a zone of hogging (expansive strains at the top of the plate, 4cm depth) for $|y| > 0.5$m and a zone of sagging (contractive strains at the top of the plate, 4cm depth) for $|y| < 0.5$m. In the center of the distribution, directly under the tire, depending on the velocity and temperature, the lateral extension (Poisson's effect) resulting from the contact pressure may turn the sign of the transverse strain again. The effect of expansive strains for $|y| > 0.5$m was clearly less distinct, or even not visible, during the static tests.
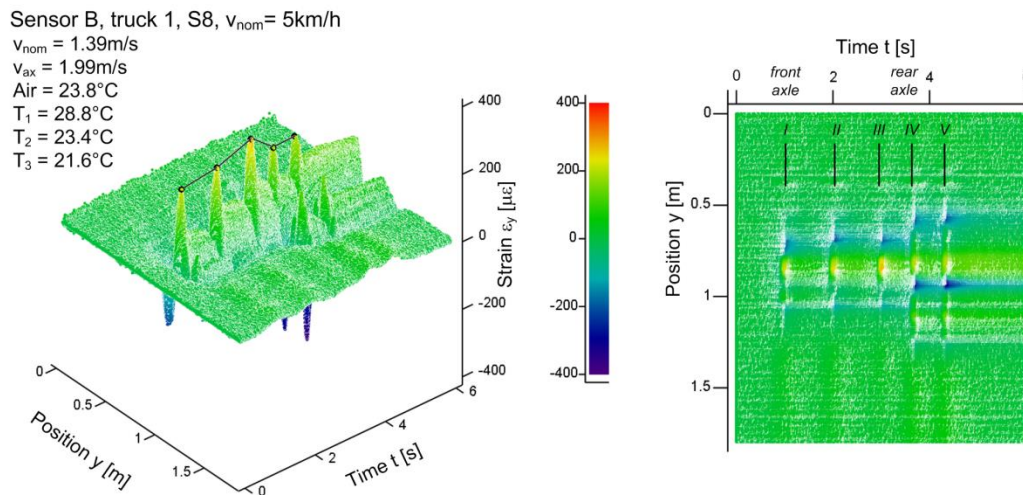
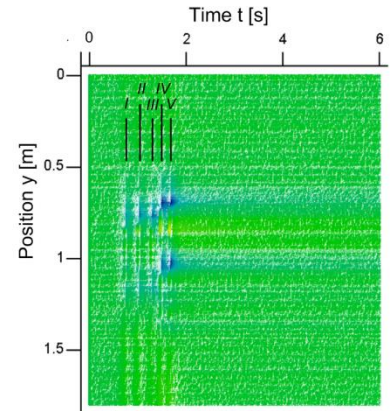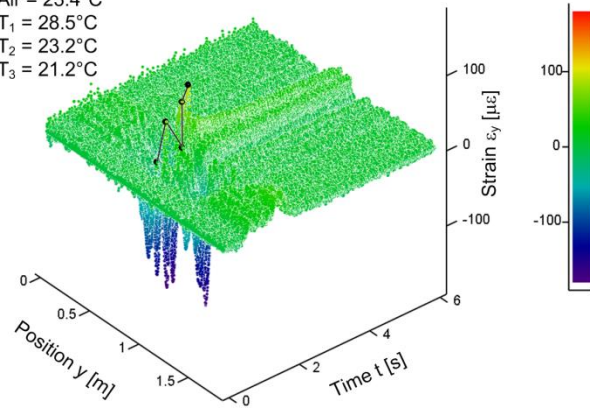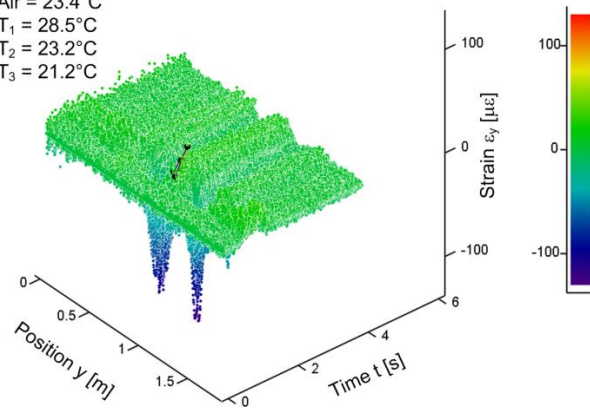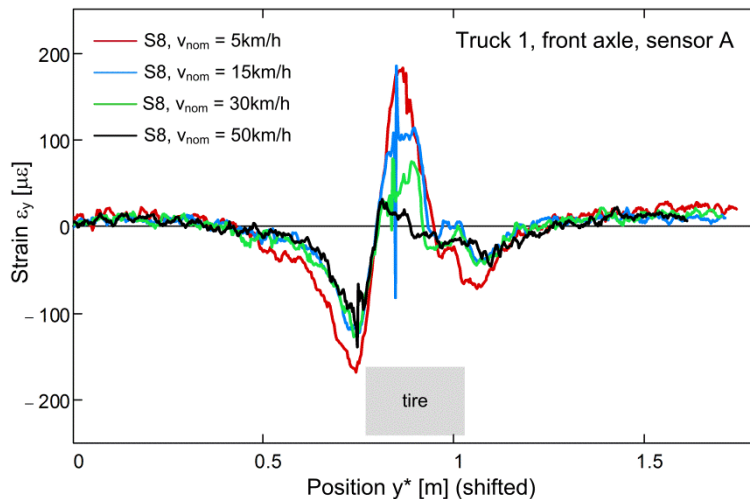**Fig. 103** *Strains measured during passage of truck 1, autumn, v_{nom} = 5km/h, 4cm depth*

Sensor B, truck 1, S8, v_{nom}= 15km/h
v_{nom} = 4.17m/s
v_{ax} = 3.84m/s
Air = 22.5°C
T_1 = 28.0°C
T_2 = 22.1°C
T_3 = 20.6°C
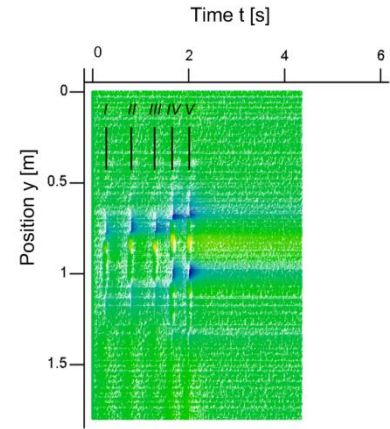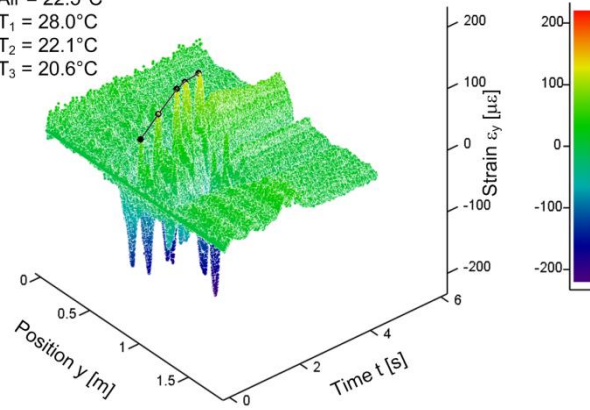
Fig. 104 *Strains measured during passage of truck 1, autumn, v_{nom} = 15km/h, 4cm depth*

Sensor B, truck 1, S8, v_{nom}= 30km/h
v_{nom} = 8.33m/s
v_{ax} = 7.19m/s
Air = 23.4°C
T_1 = 28.5°C
T_2 = 23.2°C
T_3 = 21.2°C

Fig. 105 *Strains measured during passage of truck 1, autumn, v_{nom} = 30km/h, 4cm depth*

Sensor B, truck 1, S8, v_{nom}= 50km/h
v_{nom} = 13.9m/s
v_{ax} = 12.8m/s
Air = 23.4°C
T_1 = 28.5°C
T_2 = 23.2°C
T_3 = 21.2°C
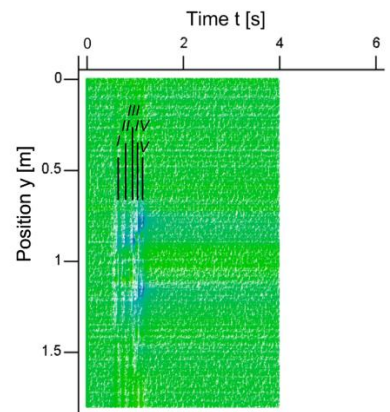
Fig. 106 *Strains measured during passage of truck 1, autumn, v_{nom} = 50km/h, 4cm depth*

Sensor B, truck 1, S8, v_{nom}= 5km/h
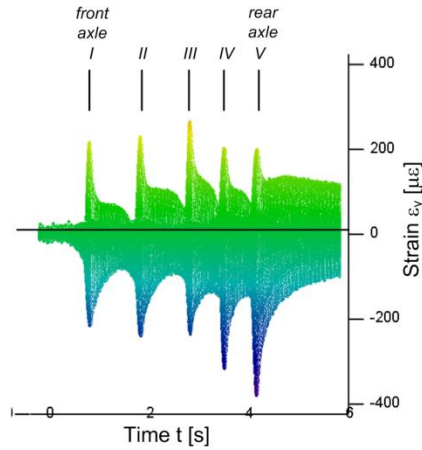
Sensor B, truck 1, S8, v_{nom}= 50km/h
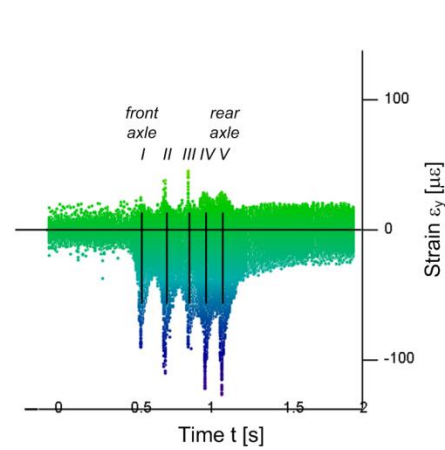
Fig. 107 *Comparison of strain envelope in autumn with time for $v_{nom} = 5km/h$ (left) and $v_{nom} = 50km/h$ (right)*

A further study of the effect of increasing vehicle velocity is made in this report by analyzing the response of the fiber optic sensor at the time, when the strain peaks and the tire is directly above the sensor. For this purpose, the strain results presented in Fig. 103 to Fig. 106 were cut at the constant time when the strain peaked (according to the applied peak detection routine and the used parameters in order to find the maxima while ignoring local outliers). The distribution which was measured at this specific time is shown in Fig. 108 to Fig. 112 in comparison to the distributions of the tests with other vehicle velocities. In order to exclude interaction with thermal effects, the comparison was made again with test series S8, where during the dynamic tests the thermal conditions can be characterized by $T_{3,rep} = 21°C$. Fig. 108 and Fig. 109 show the results of sensor section A and B while the front axle of truck 1 traversed the sensor. The general trend of smaller strain magnitudes with increasing vehicle velocity becomes clearly visible in these figures. In addition, also the alteration of the strain distribution, with reduction of expansive strain to almost zero directly under the tire, can be observed.
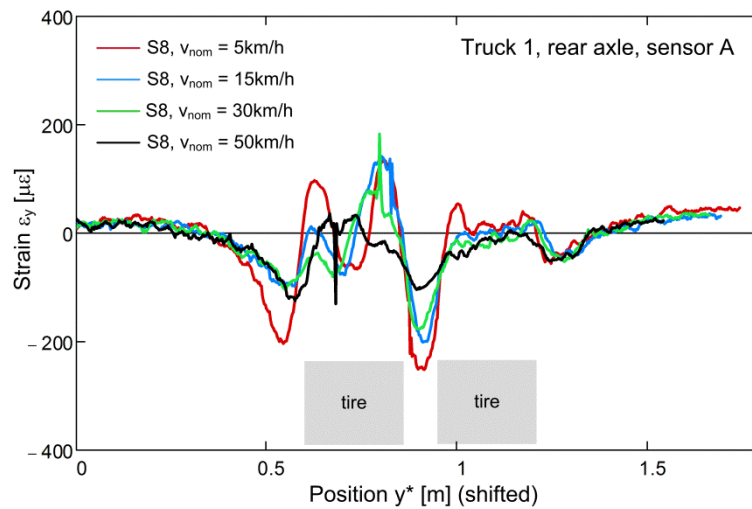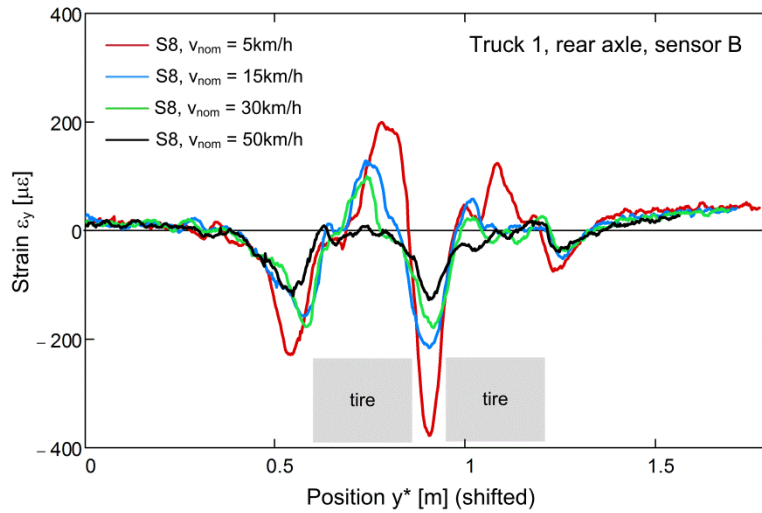

Fig. 108 *Comparison of the strains measured during the passage of the front axle along sensor section A for different velocities in test series S8 ($T_{3,rep} = 21°C$, 4cm sensor depth)*
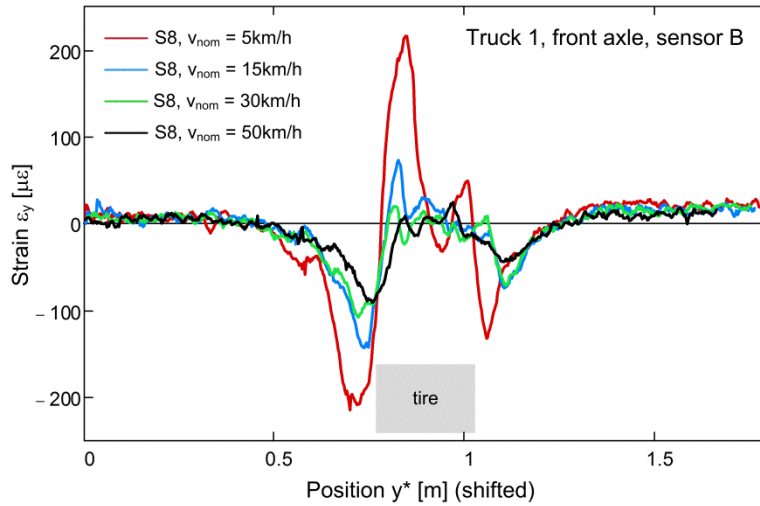
Fig. 109 *Comparison of the strains measured during the passage of the front axle along sensor section B for different velocities in test series S8 ($T_{3,rep} = 21°C$, 4cm sensor depth)*

The same comparison, as discussed above, is made in Fig. 110 and Fig. 111 for the rear axle of truck 1. As already discussed on basis of the measurement results of the static tests, the effect of the twin tire is clearly visible in the dynamically measured transverse strain distribution and high contractive strains can be measured between the twin tires. Also here exists the same trend of reduced strain magnitudes at high velocities and a change in the shape of the measured distribution.

Fig. 110 *Comparison of the strains measured during the passage of the rear axle along sensor section A for different velocities in test series S8 ($T_{3,rep} = 21°C$, 4cm sensor depth)*

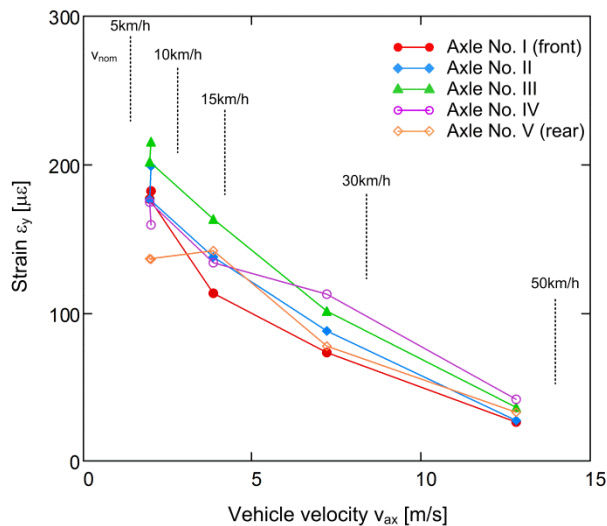**Fig. 111** *Comparison of the strains measured during the passage of the rear axle along sensor section B for different velocities in test series S8 ($T_{3,rep} = 21°C$, 4cm sensor depth)*

The effect of vehicle velocity in terms of strain magnitude can be even highlighted directly: For this purpose, the maximum expansive strain detected (neglecting local peaks and irregularities) during the transit of axles No. I to V is plotted versus the true velocity v_{ax} of truck 1 in test series S8 in Fig. 112 (sensor section A) and Fig. 113 (sensor section B). These two figures include also the results of the test with the nominal velocity $v_{nom} = 10$km/h, which were omitted before, since for this test a similar true velocity v_{ax} as for the test with $v_{nom} = 5$km/h was realized. However, in these two figures the additional test highlights that the test produces at similar velocities results, which are quite close to each other. As these two figures show, there is a reduction of the peak expansive strain directly under the tire with increasing velocity. The strain magnitudes decreases from around $200\mu\epsilon$ at $v_{nom} = 5$km/h to around $30\mu\epsilon$ at $v_{nom} = 50$km/h.

Fig. 112 *Comparison of the peak strains measured during the passage of truck 1 with sensor section A for different velocities in test series S8 ($T_{3,rep} = 21°C$, 4cm sensor depth)*
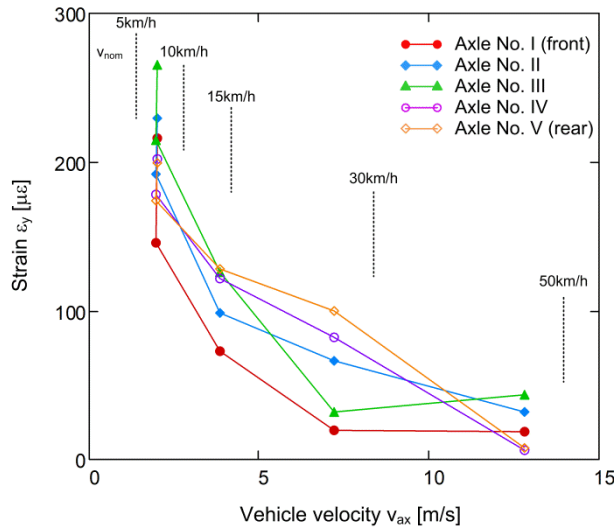
Fig. 113 *Comparison of the peak strains measured during the passage of truck 1 with sensor section B for different velocities in test series S8 ($T_{3,rep} = 21°C$, 4cm sensor depth)*

Note that for this comparison only the strain peak in expansion was considered. The reduction of the contractive strain magnitude is not included in these figures. Furthermore, it has to be mentioned that the magnitude of the strain peaks in Fig. 112 and Fig. 113 represents the black dots in Fig. 103 to Fig. 106. These maximum values were found by applying a strain peak detection scheme to the measurement results, using specific parameters. This specific scheme was chosen in order to ignore local outliers in the measurement. Hence, the results plotted in Fig. 112 and Fig. 113 are slightly dependent on the parameter choice in the detection scheme and they do not represent the absolutely largest strain magnitude measured. However, they do still reflect very well the overall trend within the measurement results.

Transit of truck 1 over sensor V9LongBS

The strain caused in the pavement by the transit of different vehicles, was measured with distributed fiber optic sensors perpendicular to the driving direction. Whereas the results of the sensors in transverse direction were shown and analyzed in depth in the past few sections, the tests with the longitudinal sensor had only the character of a trial test and its results are shown in this report only in extracts. There is only one longitudinal sensor V9LongBS embedded in the pavement (4cm depth). The response of the transverse sensors was measured and discussed for different vehicles, depths and temperature conditions. The longitudinal sensor on the other hand was only embedded in order to figure out, whether is possible to obtain also in longitudinal direction a meaningful strain response. Fig. 114 shows such a strain response of the sensor V9LongBS while truck 1 is driving along it (layout see also Fig. 92). For a deeper evaluation of the measurement results, further tests and analysis would be required. However, Fig. 114 shows already at this preliminary stage that the five axles of truck 1 with their different spacing are clearly visible in the measurement. The velocity of the vehicle, driving along the sensor, can be obtained via the inclination of the resulting traces of the axles in the time – position plot (Fig. 114, right). In the present example, the truck drove with a nominal speed of 1.39m/s (5km/h) along the sensor. A first rough estimation, based on the measurement results, shows that the truck was in reality slightly faster, as the inclination of around 1.6m/s indicates.
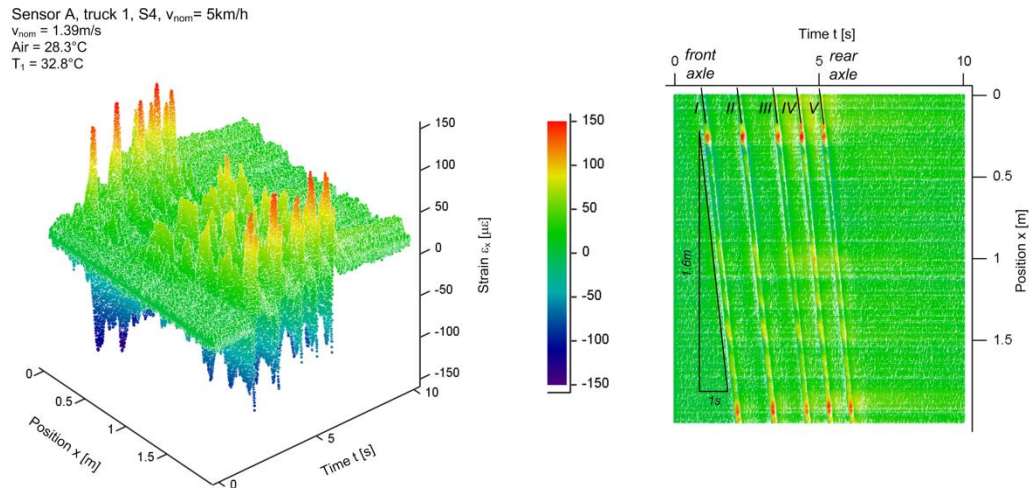
Fig. 114 *Strains measured during passage of truck 1, summer, $v_{nom} = 5km/h$, 4cm depth, longitudinal sensor V9LongBS*

5.3.4 Measurements on the grade of the base layer

Dynamic measurements were not only conducted close to road surface but also in 22cm depth, at the bottom of the asphalt layer. Owing to the large amount of data generated in these tests, only selected results are shown in the present report.

5.3.5 Current limits of dynamic strain measurements in the test field

In the foregoing sections, dynamically measured strains, while truck 1 was traversing the sensor, were shown. It was shown that the truck could be clearly identified at all tested velocities (up to 50km/h) and this even in the coldest temperature tested (around 0°C). But what about the car? Can it also be detected in cold temperatures at high velocities? Tests conducted with the car showed that detection at high velocities or in cold temperatures is still possible, however, cold temperatures and high vehicle speeds occurring together seem to form a current limit of application for this specific road design, measurement device and sensor specification. The resulting strain in these cases is very small and disappears in the current noise level of the measurement. Hence, further improvements on the sensor specifications should be carried out in order to reduce the noise level.

5.4   Discussion

Static and dynamic distributed strain measurements of a pavement, loaded with different vehicles, were presented in this chapter. In general, the discussion and the assessment of the measurement data as well as their designated use were provided at the end of each individual section of this chapter. Hence, in the present section of this chapter only some specific issues concerning all measurements are discussed.

The strains measured in the different asphalt layers were highly temperature dependent, as also indicated by the stiffness test of asphalt cores. Large strain magnitudes of up to $1500\mu\epsilon$ were observed in summer conditions, directly under the tire, in 4cm depth. This magnitude was reached in static tests with truck 1 when the exposure time of the load was around 10 to 15s. At low velocities of 5km/h, still a maximum expansive strain magnitude of around $1000\mu\epsilon$ was observed under the truck. Beside the tire, contractive strain was measured, at warm temperatures and low velocities in general clearly smaller than the expansive strain directly under the tire. However, in cold temperatures the strain directly under the tire was observed to be smaller than the absolute contractive strain magnitude nearby and, at higher velocities, the strain did not even become expansive anymore. In the following lines, a specific observation of the strain directly under the tire is discussed more in depth: In certain conditions the transverse strain under the tire showed not an ordinary peak but rather two strain peaks.

The strain directly under the tire is caused by bending deformation of the asphalt layers and by the transverse extension of asphalt. The latter is caused by Poisson's effect owing to the high local contact normal stress between asphalt and the tire. Moreover, also shear stress at the interface tire – asphalt may significantly contribute to the transverse strain measured with the fiber optic sensor in 4cm depth. The presence of double strain peaks was observed during different tests. The true nature of the interaction between tire and asphalt is rather complex and different reasons for the occurrence of a double peak could be introduced for tests where the load originated from a tire. However, double peaks were sometimes also observed under the radial symmetric loading conditions of the concrete blocks, placed on a wooden bearing on top of a sand cushion. In the following section this effect is briefly discussed using Boussinesq's elastic half space solution.

5.4.1   Elastic horizontal strains close to surface under the circular load

In order to discuss the possible occurrence of double peaks below the load and close to the surface, the elastic solution of Boussinesq's half space problem, involving a vertical force on the surface, is used. Although the asphalt is not linear isotropic elastic and, furthermore, a two-layer solution according to Burmister would be more appropriate in order to account for the base material below the asphalt, Boussinesq's solution is used in order to study this effect in a first preliminary step.

Fig. 115 shows the parameter definition of the problem. A circular normal stress is considered by means of a large number of vertical forces acting within this area on the surface of the elastic medium. The center of this circular area with radius r has a distance of y_p and z_p to the cable axis and strains are being computed as an integral of Boussinesq's solution along the cable axis x. The eccentricity of the load was introduced in order to study the effect of a non-perfectly positioned load, originating for example from positioning imprecision of the load or from potential imprecisions in defining the exact cable location in the field. Moreover, a further potential source of imprecision may also be found in the variability of the asphalt layer thickness owing to construction works. The present parametric study has only the goal to highlight the effects originating from geometry, material parameters and pressure distribution on the strains measured along the cable. No matching of the applied rough model to the measurement data is sought. An inverse analysis and the modelling of the test results, including a comparison to the measured strains, is shown in the later chapters of this report.
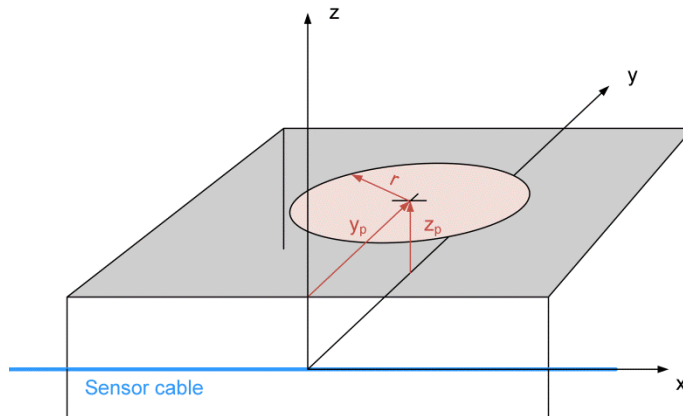
Fig. 115 *Parameter definition*

In order to study the effects of different parameters, a Young's modulus of 100MPa was used. The specific choice of the Young's modulus is in so far uncritical for the following parametric study, as it simply scales the strain magnitude but does not affect the shape of the strain distribution. The diameter of the circular load was chosen to 0.3m and the total load was chosen to be 11.8kN in order to fit exactly the test conditions present during the tests with the concrete clocks reported in section 5.2.4. In a first step, the normal contact stress distribution of this load was chosen to be uniform, resulting in a magnitude of 167kPa.

Fig. 116 shows the strains present along a line which simulates the sensor cable in 4cm depth below the surface ($z_p = 4$cm) and a load eccentricity of $y_p = 0$cm (perfectly centered load) for different Poisson's ratio ν between 0 and 0.5. Hence, the strain ε_x is in this radial symmetric problem identical to the radial strain ε_r. The dimension of the load is marked in this figure by means of two dashed lines. Clearly, Poisson's ratio has a large effect on the shape of the distribution. Without considering further effects, such as time and temperature, Poisson's ratio of asphalt is considered to be around 0.4 in this small analysis, as the shape of the distribution for $\nu = 0.4$ seems to match also roughly what was measured during the static experiments (expansive strains under the load, no or limited expansive strains in the region x > 2r). It is of interest to note that independently of the choice of ν in this specific depth and with the uniform pressure distribution, a double strain peak was found under the load.

The effect of the vertical distance between the surface load and the cable (cable depth) is investigated by means of Fig. 117. The parameter used for this figure are the same as in the previous figure, however, ν was set to 0.4 and the z_p is varied between 1cm and 8cm considering a potential imprecision of the wearing layer thickness or embedment depth. The circular load is still assumed to be uniform and centered above the cable. Hence, the computed strain ε_x corresponds still to the radial strain ε_r. The results in Fig. 117 clearly show that the closer the cable is positioned to the surface the more distinct the double peak in strain is. On the other hand, for a depth of $z_p = 8$cm the double peak in strain already disappeared. Note that in the deeper embedded cables within this report never such a double peak was measured (e.g. in 22cm depth in this chapter or in 13.5cm depth in the following chapter). Hence, based on this simple isotropic linear elastic half space considerations, the presence of the double peak under the load is limited to ratios of z_p/r smaller than 0.5.

Finally, the effect of an eccentricity y_p between the sensor cable and the load is studied in Fig. 118. For this purpose ν was set again to 0.4 and z_p was chosen to be 4cm. The load eccentricity was varied between $y_p = 0$cm and $y_p = 21$cm, which is almost 1.5 times the load radius r. Owing to the eccentricity, the computed strain ε_x along the cable does not correspond anymore to the radial strain ε_r. As Fig. 118 shows, the double peak in 4cm depth becomes less distinct if the load is not fully centered. Although the eccentricity of

the load in the field is not expected to vary greatly, it can be seen that also this parameter affects the strain distribution present in the pavement.
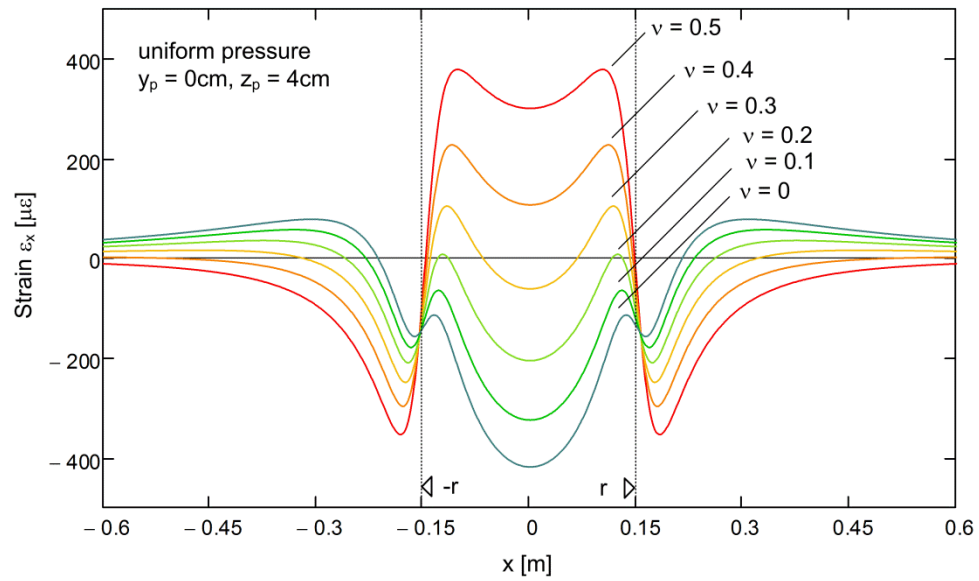

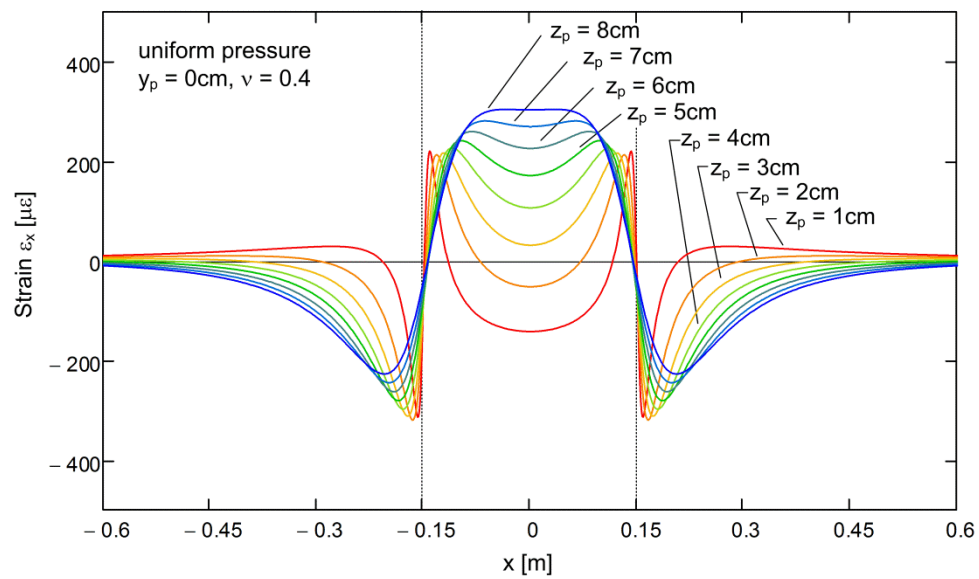**Fig. 116** *Computed elastic horizontal strains for different Poisson's ratios*

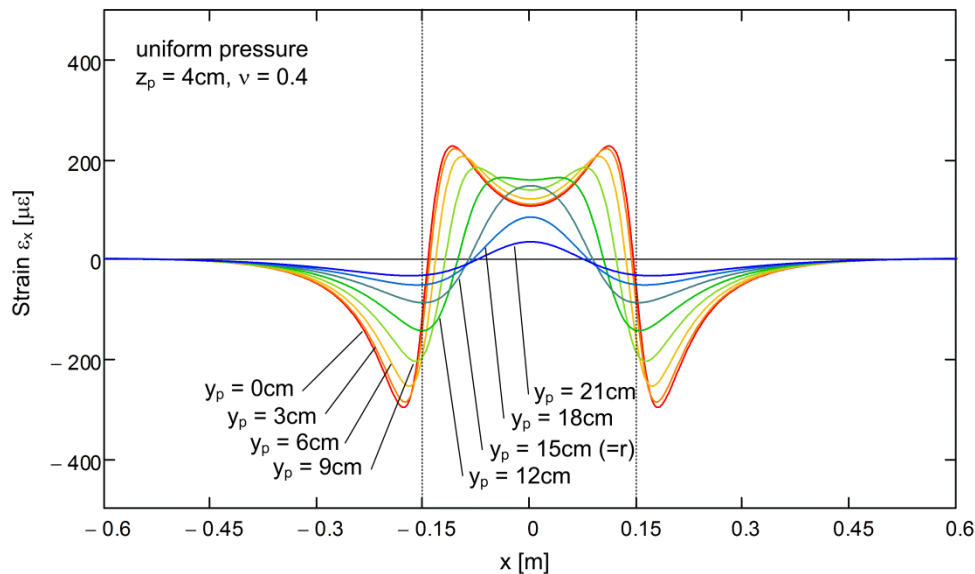**Fig. 117** *Computed elastic horizontal strains for different depths*

Fig. 118 *Computed elastic horizontal strains for different eccentricities*

Whereas in the foregoing figures only a material parameter and the geometry was varied, in Fig. 119 and Fig. 120 additionally also the effect of the contact normal stress distribution at the surface is studied. For this purpose, three circular radial symmetric load distributions are shown in Fig. 119 with a cross-section through the center of the load. A first load distribution was chosen to be again uniform for the reason of comparison. The other load distributions were chosen to follow a quadratic function over the load area, one having the maximum in the center and zero load on the boundary (denoted "convex"), the other having the maximum on the boundary and zero load in the center (denoted "concave". Clearly, these two load distributions represent extreme cases of what may be found in reality as contact normal stress under the circular wooden bearing on the sand cushion. Note that the total load applied onto the pavement still corresponds for all distributions to 11.8kN, which represents the concrete block used in the test. The strains ε_x computed for these three distributions are shown in Fig. 120. Owing to the fact that no eccentricity was considered ($y_p = 0$), these strains correspond also to the radial strain ε_r. Furthermore ν was set to 0.4 and z_p to 4cm as in the previous figures. As expected, also the distribution of the load has a strong effect on the shape of the horizontal strain close to surface. The concave distribution amplifies the effect of the double peaks, leading even to contractive strains in the center under the load, whereas the convex distribution results in a single strain peak under the load and to a more narrow strain distribution with a contractive strain maximum, which lies around the boundary of the load.

5.4.2   Implications for measuring strains in asphalt

Although the validity of the applied model for this small elastic parametric study is limited, the consideration of the foregoing figures leads to the conclusion that the shape of the specific strain distribution present in asphalt, underneath the load and close to the surface, is strongly dependent on material and geometric parameters as well as on the distribution of the load. The fact that the strains under the load vary greatly in space and depend strongly on the applied parameters, is also a strong argument for measuring strains in a distributed manner using e.g. distributed fiber optic systems rather than pointwise strain measurements provided by other technologies as Fiber Bragg Grating (FBG) or classical strain gauges. If strains are being measured pointwise, the reliability of data originating from a single sensor has limited explanatory power since already a few centimeters beside, a strain with different magnitude may be present and possible imprecisions in the range of a few centimeters often occur in field experiments. It is therefore a great advantage for the understanding of the behavior of pavements to benefit from the unprecedented amount of strain data which can be gathered by the usage of spatially high resolved distributed fiber optic strain data.
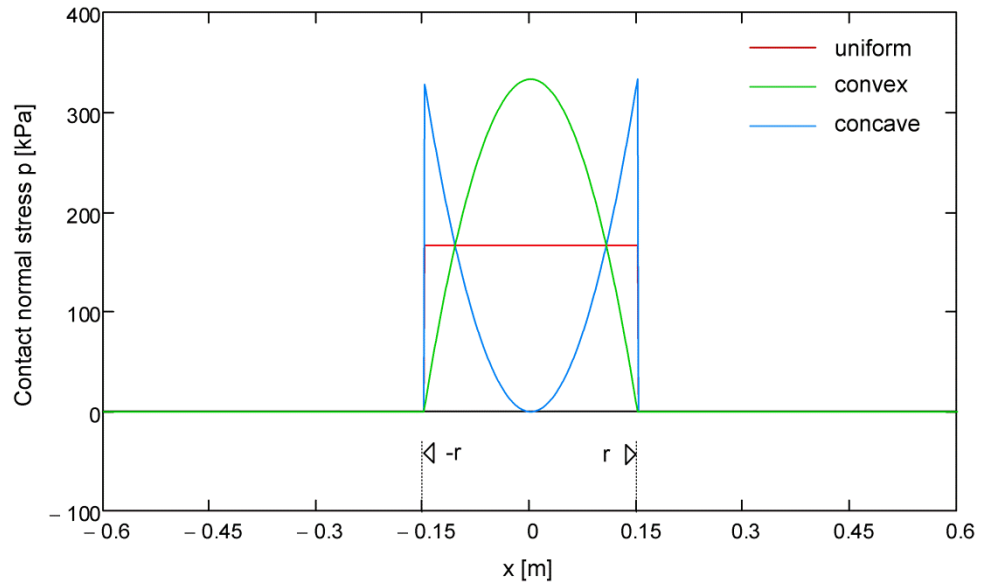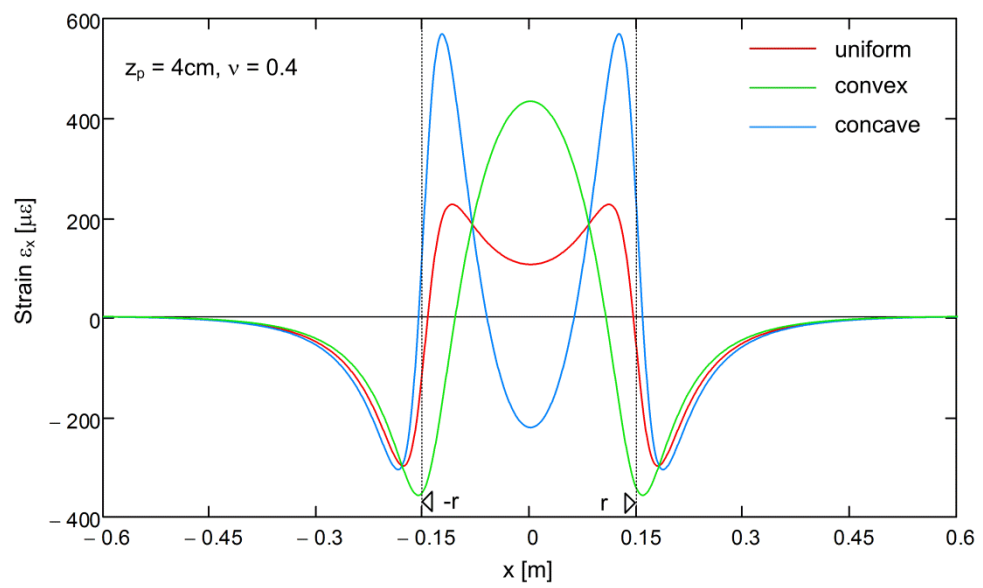
Fig. 119 *Definition of the applied load distribution*

Fig. 120 *Computed elastic horizontal strains for different load distributions*

5.5 Conclusions

Fiber optic cables were embedded successfully in different depths into the pavement of a road. Strains were measured afterwards continuously with high spatial resolution along these cables by means of distributed fiber optic sensor technology. Different vehicles and test procedures were used in order to apply load to the road and induce the strains. Beside of static tests, where the pavement was exposed several seconds to the axle load of a truck or car, also dynamic tests were conducted, where the vehicles traversed the sensor at a constant velocity. The test site was operated for more than 2.5 years and strain data was collected in different seasonal temperature regimes. Many different sensors were installed at the test site Hohlstrasse and, moreover, many test series were conducted. This generated a large amount of measurement data, which can be shown only partially in this report.

The following conclusions can be drawn on basis of the measurements conducted at the test field Hohlstrasse.

- The installation procedure in a real construction industry project was successful and did not create too many interference with the process of road construction.
- No sensor was lost owing to cable damage in the asphalt environment during installation or operational time. All cable damages which were observed occurred in the access shaft. Owing to the sensor length limit, the cable guidance in the access shaft had to be carried out unfortunately non-ideal. However, this can be improved by slightly longer cable ends in the shaft, which allow for a simple repair of the sensor.
- The spatial variability of the strain distribution measured close to surface is high. Thanks to the high spatially resolved strain data, it was possible to gain an insight into the strain field present in asphalt, which would never have been possible by means of simple point sensors.
- A strong dependency of the strain magnitude and its distribution on temperature was observed, which confirmed the expectations regarding the temperature dependency of asphalt material parameters.
- Large expansive strains of up to $1500\mu\varepsilon$ were measured in warm temperatures 4cm below the tire. This expansive strain decreased faster with decreasing temperatures than the contractive strain beside the tire. Clearly smaller, but also of expansive nature, was the strain, which was observed under the tire in 22cm depth.
- An interesting characteristic of the near surface strains is the double expansive strain peak, which occurred sometimes in the measurement data. The presence of this double strain peak could be verified and understood by means of a simple linear isotropic elastic model. Such detailed insight into the strain field of asphalt was only possible thanks to the continuous and highly resolved strain data observed by means of distributed fiber optic strain sensors.
- The strains, measured while the test vehicles traversed the sensor with a certain velocity, allowed for defining the driving position and direction of the vehicle as well as its number of axles, axles spacing and wheelbase of the vehicle. In case of trucks, even twin tires could be clearly distinguished from single tires. Clearly, higher axle loads could be distinguished from lower ones; however, owing to the strong dependency of asphalt behavior on temperature, a precise determination of axle loads might require further efforts and calibration.
- Whereas the strains owing to a 40t truck could be measured in all tested temperature conditions and velocities (up to 50km/h) clearly, the dynamic detection of light vehicles as cars in cold temperatures at high velocities was in the current sensor configuration not always successful. The detection became difficult, owing to the fact that the small strain quantities vanished in the measurement noise. By improving the sensor specifications and reducing the random fluctuations along the sensor, such detection might become also possible in future without changing locally the road design. However, the static load of the car could always be detected in cold environment.
- The applied acquisition (or scanning) rate for the dynamic measurements was 100Hz, in order to achieve an active sensor length of 10m. Higher scanning rates are with the applied device only possible on cost of sensor length. 100Hz scanning rate was

shown to be adequate for vehicle velocities up to 50km/h. Above 50km/h, it cannot be guaranteed that a frequency scan is conducted while the vehicle is directly above the sensor, which would lead to an even stronger reduction of measured strains at higher velocities. Hence, higher scanning rates are required at higher vehicle velocities.

- The large strain magnitudes in summer occurred in a highly localized manner. Regarding the sensor grid, a narrower grid spacing towards the center of the grid than the chosen equidistant grid (0.5m spacing), would be recommended.

- Distributed fiber optic sensors have at this test site proven to be a valuable source for gaining a better understand of the behavior of asphalt and providing high quality input data in order to calibrate numerical models.

A new insight into a topic, as e.g. distributed strain sensors provide in the present research project, generates often new questions which could be investigated with further research. In this particular research project and concerning the presented measurements in this chapter, it would be interesting to compare the measurement results and the behavior of the different fiber optic cables (V1, V3, V9) applied in the same temperatures under the same load in asphalt. This would allow studying, whether the more robust cable versions, consisting of more cable sheath layers, may follow the strain present in asphalt as close as the less protected cable versions. This becomes in particular important if large strains in very warm temperatures are being measured leading to spatially very high strain gradients. Furthermore in the case of static measurements accomplished with the OBR 4600 device, it would be interesting to compare in detail those measurements (gathered within 10s) to a measurement which shows the strain development with time (within this 10s measurement time). This would allow for studying more in depth to which sort of averaged strain the strain measured with the OBR 4600 belongs, if the strain changes slightly during the measurement time of 10s owing to viscosity of the asphalt. This comparison could be achieved by applying the ODiSI B device (running at 100Hz) to a static test.

5.6   Acknowledgements

6   Test field at Zurich Airport

Abstract

In the present chapter, the testing procedure and the measurement results from the test field at Zurich Airport are shown and discussed. This chapter starts with a brief introduction containing the specific conditions of the test site; afterwards the testing procedure with the positioning of the aircraft, which was used as test vehicle in order to apply loads, is shown. These sections are followed by another section which comprises the strains measured in the asphalt under the aircraft using distributed fiber optic sensors. The chapter closes with conclusions about the field test at the end.

6.1   Measurement setup

6.1.1   Site conditions

During summer 2015, the construction works for the renewal and the adjustment of the aircraft stands "Delta Süd" were conducted at Zurich Airport. Owing to specific project boundary conditions and the foreseen temporary usage of the stands, the stands of Delta Süd were built in the form of two asphalt layers instead of concrete (4cm AC 11S and 9.5cm AC T 22S), lying on two layers of cement treated base material, which were in total 53cm thick (see also Fig. 123). Thanks to the courtesy of the airfield maintenance team, it was possible to embed distributed fiber optic sensor cables into the two asphalt layers and use them for the purpose of the present research project. Both, embedding the sensor during construction of the pavement and conducting later on measurements with these sensors, had to be carried out under the usual safety restrictions of an airport. Since for the loading of the pavement aircrafts were used, measurements could only be carried out at pre-defined time windows. Although the access to the test site was limited, thanks to the great support from the airfield maintenance team it was possible to gather measurement results with different aircrafts and in different thermal conditions.
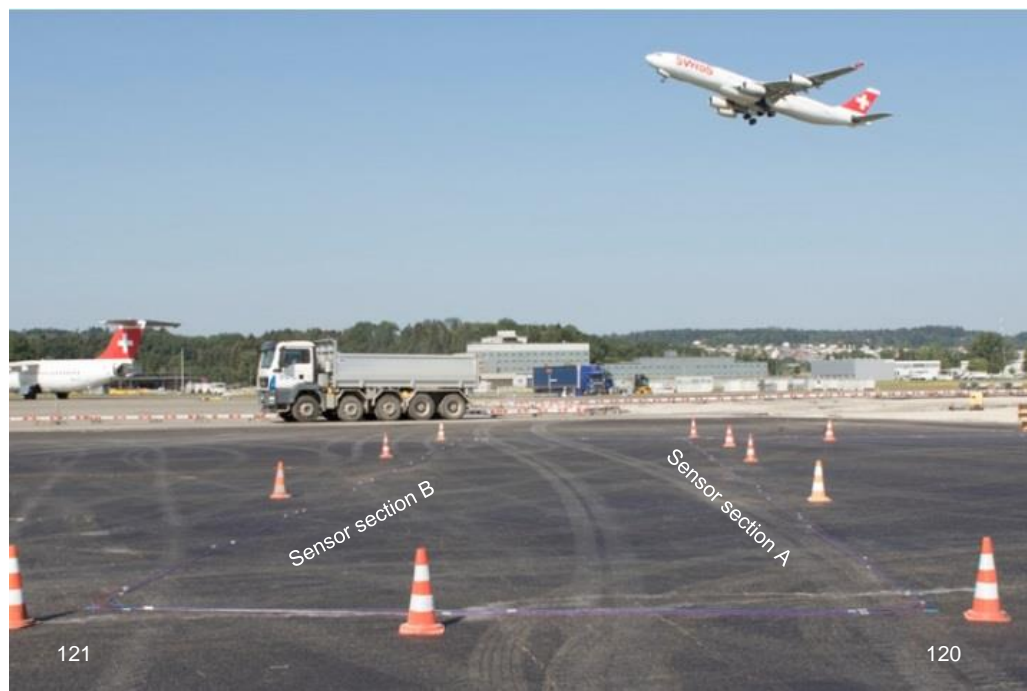

Fig. 121 *Stands Delta Süd of Zurich airport with sensor cables close to points No. 120 and 121 (line of sight from east towards west) during construction*

6.1.2   Test project description

The test project at Zurich airport consists of different tests, which were conducted between July 2015 and February 2018. Some of them (as discussed in section 6.1.7) were carried out only in order to check and optimize the performance of the fiber optic sensors which were embedded at the test site. The measurements conducted with the fiber optic sensors were of "static" nature and each test was conducted within one day. The aircraft was moved into a pre-defined position using an airfield tractor, afterwards measurements were conducted using all embedded sensors and in a further step, the aircraft was moved into the next position. No "dynamic" measurements, as it was the case on the test site Hohlstrasse, were conducted. Strains were measured in two different depths in the asphalt layers, in two different thermal conditions using two different types of aircrafts. Compared to the situation on the test site Hohlstrasse, where trucks and a car were used as test vehicles, the loads and the contact pressures under the aircraft gears are here clearly larger. However, the two rather thin asphalt layers lie on a cement treated base, which is expected to be significantly stiffer than a granular unbound base layer. The field test at Zurich Airport was the first installation within this project and hence, served also as testing environment in order to gain experience with the different cable fixation methods reported in chapter 4. The extent of different tests, used vehicles, various thermal conditions and other boundary conditions is clearly smaller than in the field test Hohlstrasse. Parts of the present chapter are also included in [46].

6.1.3   Distributed fiber optic sensor layout

An overview of the installed fiber optic sensors is provided in Fig. 122 and Fig. 123. The process of the installation was already discussed in detail in chapter 4 and is not repeated here. Fig. 122 shows the situation around the stand T64 of Delta Süd, which was instrumented with fiber optic cables. The cables were installed in a loop configuration of slightly less than 150m length each including the free cable ends. On the cement treated base course, a V3 cable was installed, on the asphalt base course, a V3, V9 and a T cable were installed in parallel. Whereas V3 and V9 are tight buffered cables which can register temperature and strain changes, the T cable is a loose tube cable, which was installed for the purpose of potential temperature compensation. In order to have access to the cable ends and to connect them to the measurement devices, the cables were guided to an electro shaft nearby. Owing to the predefined position of the aircraft stand and the location of the electro shaft, it was decided to install the sensor in a loop configuration. This enables for measurements using BOTDA based measurement devices as well as the SWI based OBR 4600 device with its maximum sensor length of slightly more than 70m (at full performance), since the cable with around 150m length is accessible from both sides. From point No. 0 in the electro shaft, the sensor cable is guided within a plastic tube up to point No. 101. There, all cables leave the protection tube and run from point No. 101 over 109, 120, 121, 134 back to point 101 and from there back to the electro shaft. The distance between point No. 0 and No. 109 is only used to guide the light to the relevant sensor location under test, which are the sections between point No. 109 and 120 (sensor section A) as well as point No. 134 and 121 (sensor section B). The two parallel sections A and B are 29m long and have a distance of 6m to each other. The fiber optic sensor lying on the cement treated base is divided into sensor section "V3FSA" and "V3FSB", the fiber optic sensors lying on the asphalt concrete layer are denoted "V3TSA", "V3TSB", "V9TSA", "V9TSB", "TTSA" and "TTSB". Fig. 122 contains also the contour of an Airbus A340-300, including main gears as well as centerline and nose gear and is drawn in its usual parking position on stand T64. The SWI measurements were usually conducted by bringing the measurement device through the manhole into the electro shaft and connecting it there individually to the cable ends (Fig. 124). The larger BOTDA measurement device was plugged to all sensors, connected together to one loop, from outside the shaft using extension cables (Fig. 125).
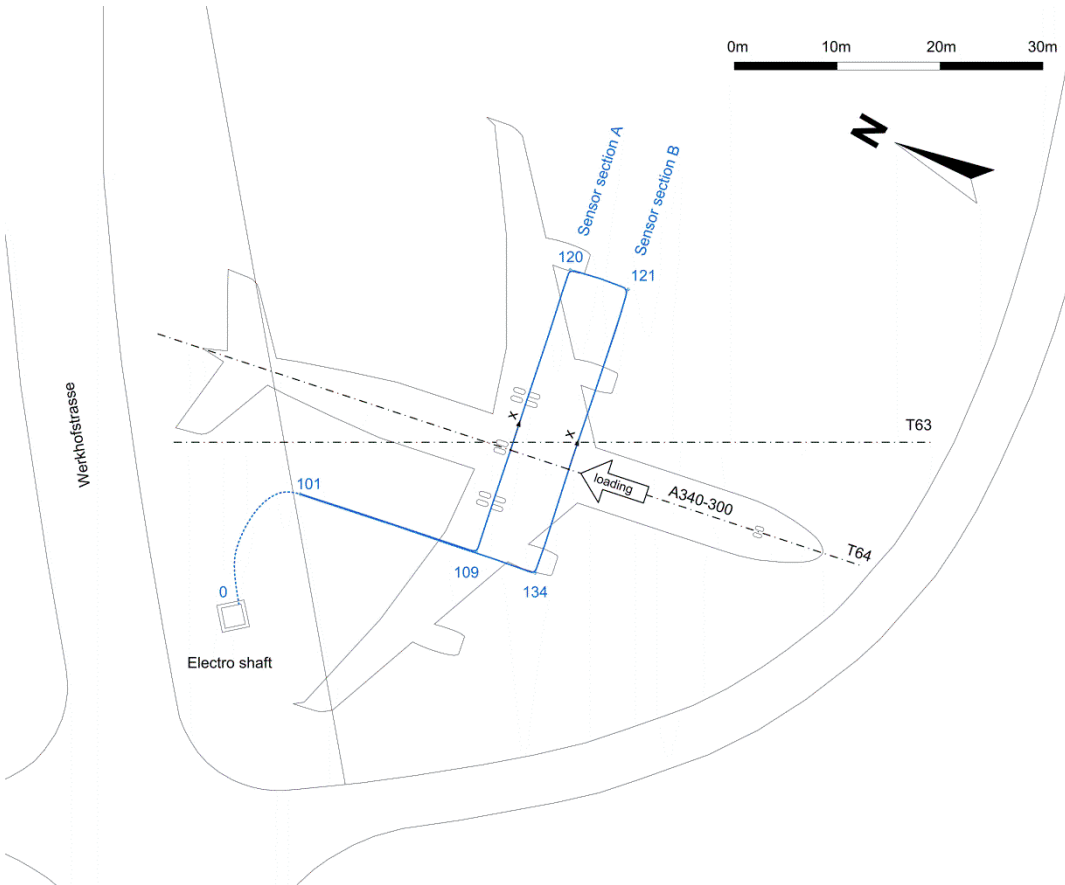
Fig. 122 *Fiber optic sensor layout including the contour of an A340-300 aircraft in its parking position on the instrumented stand T64*
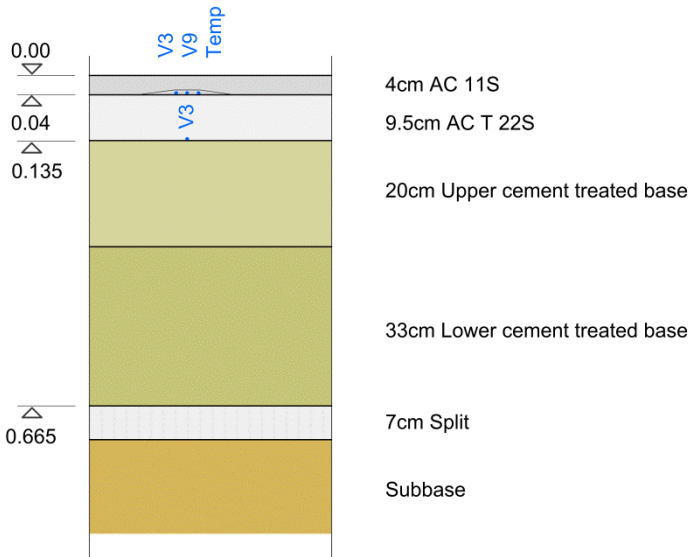

Fig. 123 *Cross section of the new pavement structure in the vicinity of the instrumented area*

Fig. 124 *Cable ends in the electro shaft directly after installation (left) and stored in access box (right) after packaging*

Fig. 125 *Electro shaft close to T64 while conducting measurements*

6.1.4 Distributed fiber optic measurement devices

For this field tests at Zurich Airport the Rayleigh based SWI technology and the Brillouin based BOTDA technology were applied in form of the OBR 4600 device from Luna Inc. and the DITEST STA 202 device from Omnisens SA. Although the wheels and the contact zone between the tires and asphalt are larger compared to the situation with a truck or a car at the test field Hohlstrasse, also here mainly the SWI technology was used, owing to its high spatial resolution. SWI measurements were usually conducted within this field test using a spatial resolution (gauge length) of 10mm and sampling interval of 5mm. The BOTDA measurements using 1m spatial resolution and a sampling interval of 0.1m were only used for the reason of internal comparison and for a potential compensation of temperature effects in the measurement results. However, within the present report, the results of the BOTDA measurements are not included.

6.1.5 Temperature measurements

The environmental temperature as well as the temperature of the different asphalt layers was measured, owing to the specific test location, to clearly less extent than at the test field Hohlstrasse. The temperature of the asphalt was only measured at surface (T_{sf}), using a needle thermometer with a specific temperature transmitter. In addition, the temperature of the air outside (T_{air}) and inside of the shaft (T_{sh}) was registered. Furthermore, a Pt100 element was set in to the protection tube between point No. 0 and 101, located around 2m from the shaft in a depth of 0.8m from the ground surface, measuring the temperature below the cement treated layers in soil (T_{sl}).

6.1.6 Aircrafts

Gear geometry

Two different types of aircraft were used in order to load the pavement: an Airbus A340-300 and an A330-300. The footprint (contact zone and wheels) for this two aircrafts are shown in Fig. 126 and Fig. 127. Interestingly, both aircrafts have the same spacing between the gears and the wheels; however, the A340-300 has between the two main gears an additional centerline gear. Whereas the main gears contain four wheels, the centerline gear contains only two wheels, as the nose gear does too. The tires of the centerline gear have the same dimensions as the main gears, but their spacing is smaller. Further information about the gears can be found in [47] and [48]. Whereas the tire of a main or centerline gear has an outside diameter of 1.4m and a width of approximately 0.5m, the contact area between the tire of a main gear and the asphalt has a width of 0.4m and a length of approximately 0.3m in the present weight configuration, the tire pressure is around 1.4MPa.
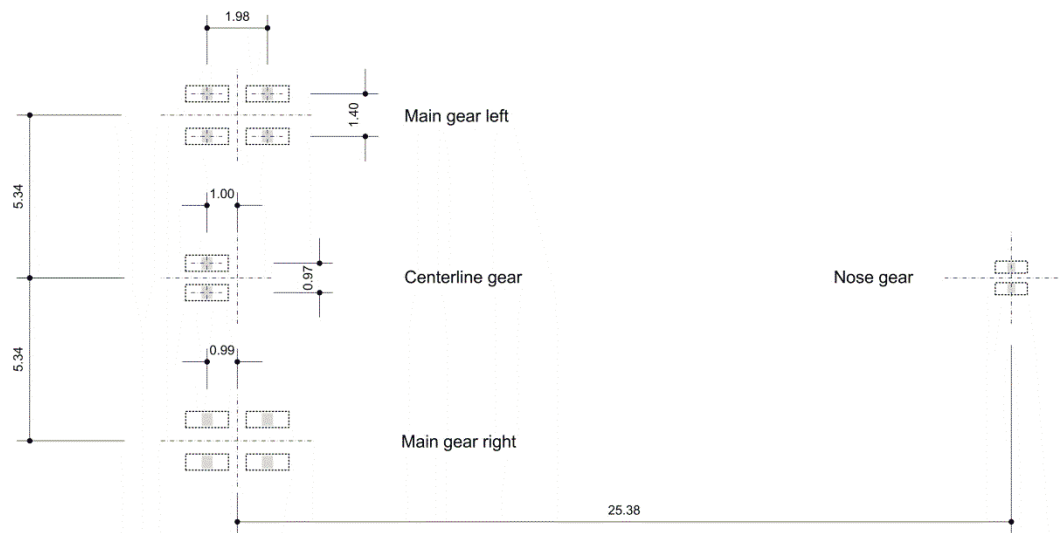
Fig. 126 *Footprint of an A340 – 300 aircraft*
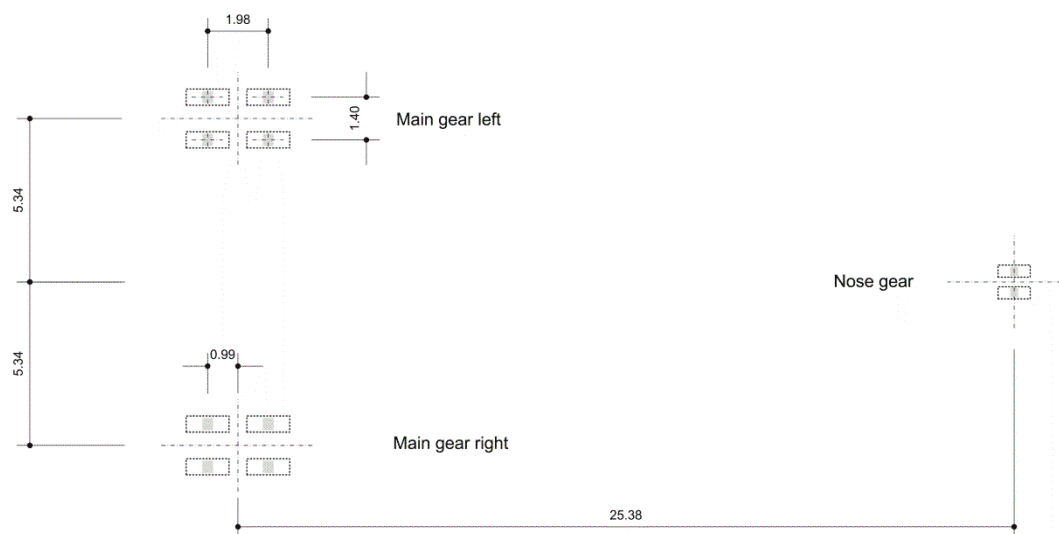
Fig. 127 *Footprint of an A330 – 300 aircraft*

Aircraft mass

Beside the gear geometry, also the mass of the aircraft and the distribution of the resulting gravity forces on the gears are of importance. The aircrafts which were used for the tests were always empty in the sense that no passengers, luggage or cabin crew was aboard. The information about the rest fuel mass, which remained in the tanks after the flight, was obtained from aircraft technicians who were on site. Hence, the gross mass of the aircraft is estimated within this project to be the "empty operating mass", which can be gathered from aircraft documentations ([47], [48]) plus the reading about the current fuel mass. Although this approximation neglects the mass of e.g. hydraulic fluids, it is sufficiently accurate for the present purpose. Information about the aircrafts used in the relevant test No. 5 to 7 is shown in Tab. 20. The assumed gross aircraft mass for the tests within the present project is around 135t for the A330-300 and around 140t for the A340-300, owing to the empty aircraft and almost empty fuel tanks. Note that the maximum allowable ramp mass for these aircrafts can be as high as 230t for the A330-300 and 270t for the A340-300.

Tab. 20 Aircrafts used in selected tests

Date	Test No.	Type	Reg.	Operating Empty mass	Fuel mass	Assumed aircraft gross mass
26.09.2016	5	A340-300	HB JMK "Aarau"	131t	8t	140t
11.09.2017	6	A330-300	HB JHG "Glarus"	127t	6t	135t
26.02.2018	7	A330-300	HB JHQ "Chamsin"	127t	6t	135t

Gravity load distribution

According to the aircraft documentation ([47], [48]), depending on the "weight variant" of the aircraft, only 5% to 10% of the gravity load is carried by the nose gear, the rest is distributed via main gear group to the pavement. For the present purpose, it is assumed that around 93% of the gravity load is carried by the main gear group. For the A330-300 this means, that a gravity load of approximately 630kN is being transmitted per main gear to the pavement, which results in average in around 160kN per gear wheel. Since the A340-300 possesses a centerline gear, which is assumed to carry a gravity load of around 90kN ([47])), around 600kN are transmitted per main gear to the pavement. This results in a load of around 150kN per main gear wheel and around 40kN to 50kN per centerline gear wheel.

Although the aircraft was empty and the fuel mass was low, the resulting gravity load per main gear was for both aircrafts around 600kN. This load is transmitted to the pavement within a rectangle of around 1.8m times 2.3m, whereas at the test field Hohlstrasse truck 1 transmitted a gravity load of around 400kN within a rectangle of 2.3m times 6.8m. The resulting contact normal stress is expected to be around 2 to 3 times higher for the aircraft than for truck 1.

6.1.7 Test procedures

The fiber optic sensor layout is shown in Fig. 122 and Fig. 123. Relevant for the measurements during the test are actually only the sensor section A and B, which are formed by the two 29m long parallel sections of the fiber optic sensor loop having a distance of 6m to each other. In order to measure strains at different distances of the aircraft to the sensor sections, the aircraft was moved with an airfield tractor into different positions. While the aircraft was remaining in a certain position, "static" measurements were conducted using mainly the OBR 4600 device and using the SWI technology. The whole test excluding reference and unloading measurements but including moving the airplane lasted, depending on the procedure, around half an hour. In the relevant tests No. 5 to 7, two slightly different test procedures were applied, which will be discussed in the following lines.

Test procedure A

Test procedure A was used during Test No. 5 with an A340-300 aircraft and is shown in Fig. 128. Before the aircraft was moved in the zone of influence, close to the sensor sections A and B, a reference measurement was conducted with every fiber optic sensor. This position is denoted A_0 and the distance a_0, from sensor section A to the axle of the main gear group, was clearly larger than 10m. Since four sensor loops with an individual length of slightly less than 150m were installed, but the OBR 4600 device enables only for sensor lengths of slightly more than 70m, the four loops had to be read out from both sides. Afterwards, the aircraft was moved with the tractor to position A_1, corresponding to a distance $a_1 = 10$m. In the following few minutes, measurements were launched in the three tight buffered fiber optic cables from both sides. By the time the measurements in position A_1 were finished, the aircraft was moved into position A_2, corresponding to a distance of $a_2 = 4$m. Note that sensor section B has been already traversed by that time. Also in this and the following positions, six measurements were carried out within a few minutes (typically 5 minutes). In the next position A_3, the aircraft was moved to the point where the axle of the main gear group was 1m away (distance a_3) from the axis of the fiber optic sensors, but the wheels of the main gear and the centerline gear stood directly above the sensors. For the following position A_4, the aircraft was moved a further meter, resulting into the distance $a_4 = 0$m and the circumstance that the axis of the main gears is located directly above the fiber optic sensor, but nor tire of the gears is directly above the sensor. Depending on the availability of the aircraft, the aircraft was afterwards uncoupled from the tractor and left in its position a_4 for a certain time and further measurements were conducted under load. Alternatively, the aircraft was immediately pulled away by the tractor to another stand and some further measurements were carried out under unloading conditions. At the end of the test procedure, always a further measurement, including also the loose tube cables, was conducted.

Test procedure B

Test procedure B was used during Test No. 6 and 7 with an A330-300 aircraft and is shown in Fig. 129. This slightly modified procedure was introduced, since the test with procedure A showed that an influence of the aircraft on sensor section A with $a_2 = 4$m is hardly detectable. Hence, the aircraft positions where moved slightly closer to sensor section A and one further position was introduced. Whereas the start of procedure B with position B_0 and the reference measurement is the same as in procedure A, position B_1 corresponds to a distance $b_1 = 7$m, leading to the situation that the rear tires of the main gears are positioned exactly above sensor section B. After the measurements were conducted in this position, the aircraft was moved to position B_2, corresponding to distance of $b_2 = 3$m, which means that the axis of the main gears is in the middle of sensor section A and B. Afterwards, the distance b_i of the main gear axis to sensor section A was reduced in steps of 1m towards $b_5 = 0$m in position B_5, where again the axis of the main gear is directly above the sensor and the tires are located beside the sensor. Note that in both test procedures effects owing to the delayed response of asphalt (creep) of the foregoing position may be present (in particular position A_4 and B_5 as discussed later).
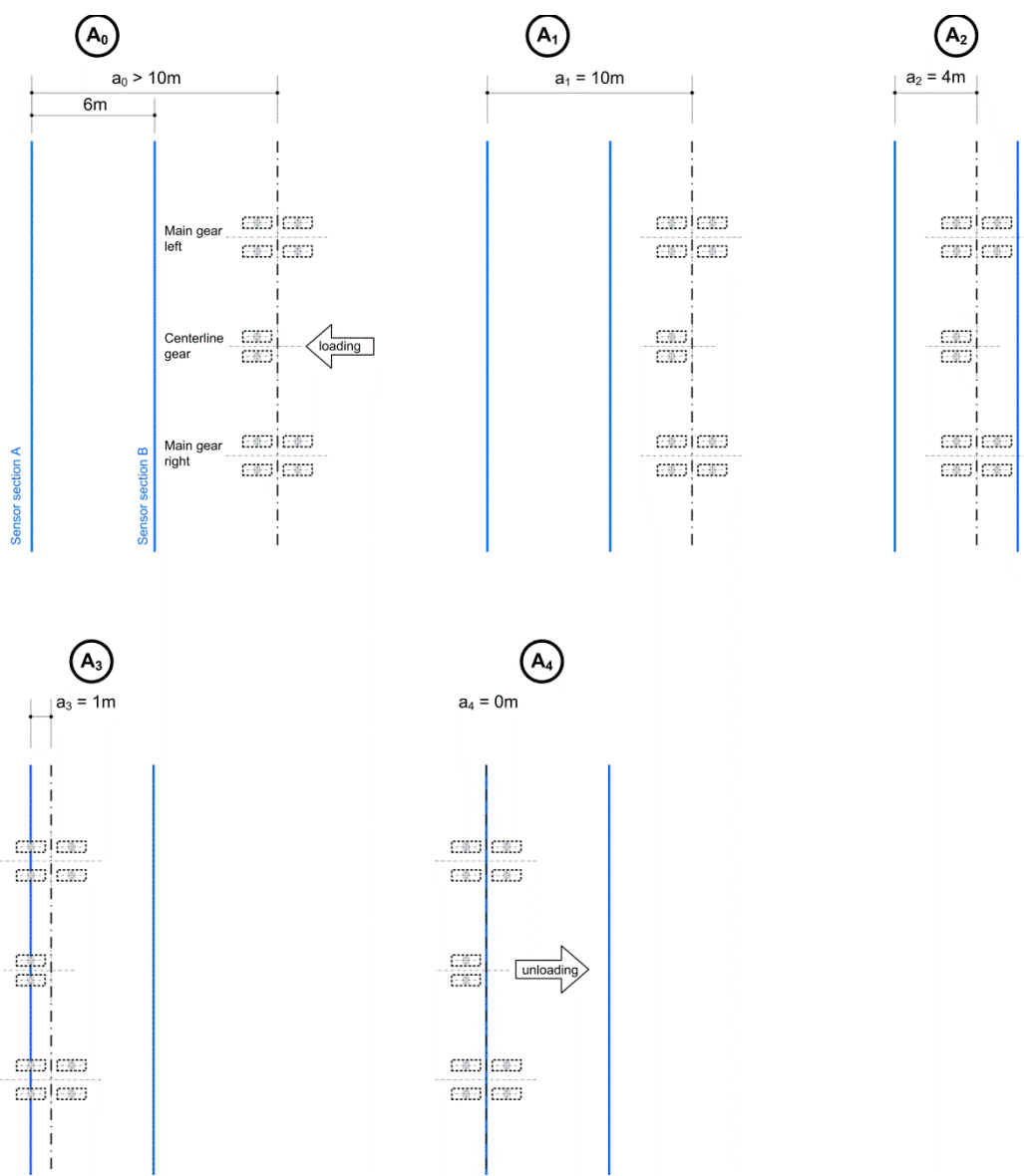
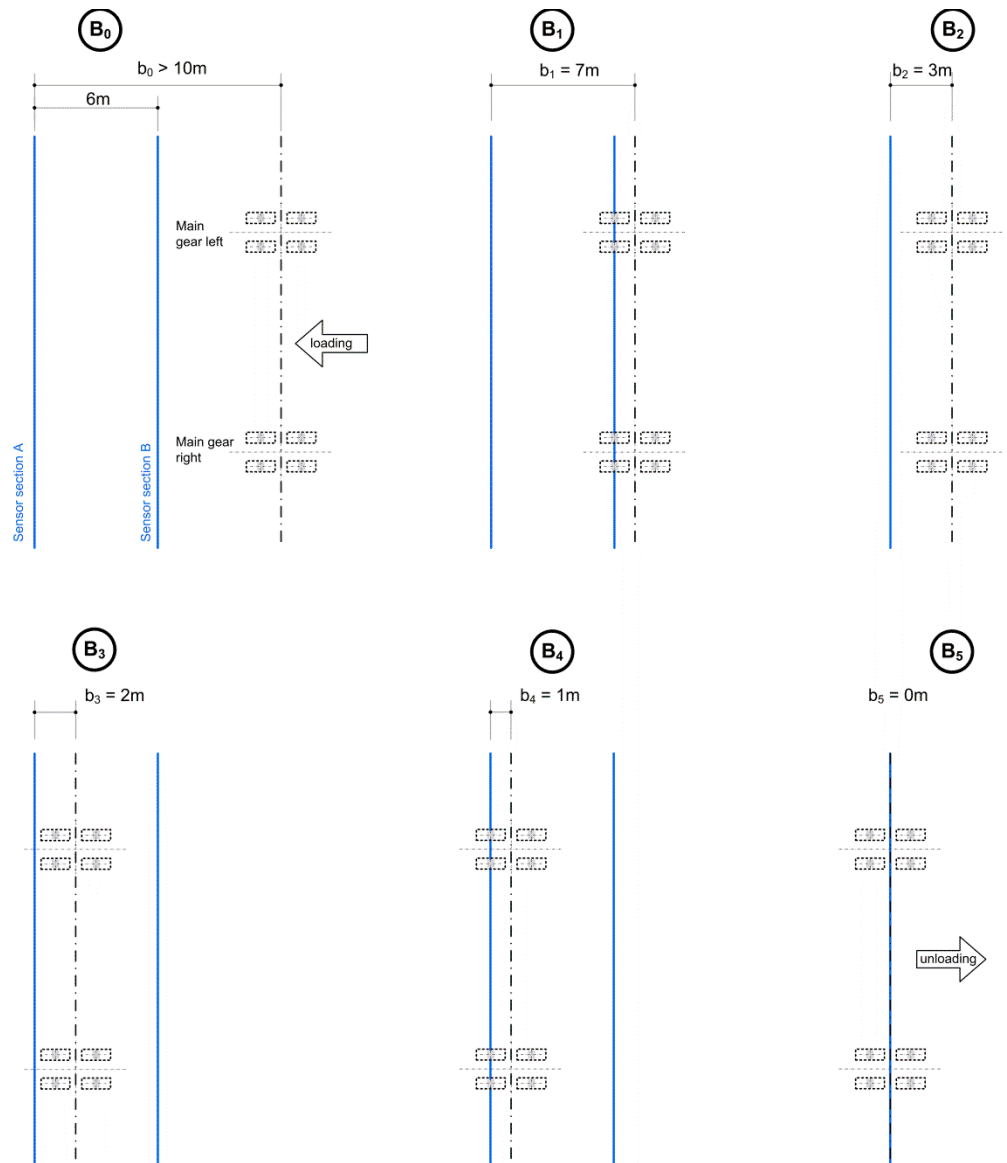**Fig. 128** *Test procedure A using a A340 – 300 aircraft*

Fig. 129 *Test procedure B using a A330 – 300 aircraft*

Illustration of the test procedures

Some impressions of the test procedures are shown by means of Fig. 130 to Fig. 137. Whereas Fig. 130 to Fig. 133 are pictures taken during Test. No. 5 using an A340-300, Fig. 134 to Fig. 137 are pictures taken during test No. 6 and 7 when an A330-300 of two different airlines was used. The A340-300 in Fig. 130 to Fig. 133 can be recognized owing to its four jet engines and its additional centerline gear, having smaller wheel spacing than the main gears beside.

Fig. 130 and *Fig. 131* *Positioning of an A340-300 on August 19, 2016*

Fig. 132 and *Fig. 133* *Position of the main gear group (A340-300) on August 19, 2016*

Fig. 134 *Positioning of an A330-300 on February 26, 2018*

Fig. 135 *Positioning of an A330-300 on September 11, 2017*

Fig. 136 *Position of the main gear group of the A330-300 on September 11, 2017*

Fig. 137 *Position of the main gear right of the A330-300 on February 26, 2018*

6.1.8 Test series overview

The field test at Zurich Airport consisted of 7 tests as shown in Tab. 21. Test No. 1 was only a functioning test, a few days after the installation of the sensors and no load was brought to the pavement. In the measurement results of test No. 2 and 3, unusual disturbances were found and it became obvious that the specific long loop layout of the sensors at the airport required different measurement parameters than those, which were applied so far. A further functioning test in September 2016 showed that the sensors can be operated at the usual performance from now on. Hence, the successful tests which are discussed in the following sections are Test No. 5 (using an A340-300) and Test No. 6 and No. 7 (using an A330-300). The warmest conditions were met during test No. 5 in September 2016. Similar conditions, but slightly cooler temperatures, were observed during the test in September 2017. Significantly colder temperatures were measured during the last test No. 7 in February 2018. During test No. 5, unfortunately the main gear group of the aircraft was slightly shifted from the axis T64 and, even more relevant, the axis of the main gears was not fully perpendicular to the axis T64, which resulted in the fact that the aircraft stood not everywhere perfectly above the sensor cables. Measurement results of test No. 5 can also be found in [46].

Tab. 21 Overview about the tests conducted at Zurich Airport

Date	Test No.	Aircraft	Thermal conditions	Test procedure	Comment
31.07.2015	1	-	-	-	Functioning test
27.11.2015	2	A330-300	Cold	A*	Disturbances in the measurement results
19.08.2016	3	A340-300	Warm	A	Disturbances in the measurement results
08.09.2016	4	-	-	-	Functioning test
26.09.2016	5	A340-300	Very warm	A	Aircraft positioned slightly inclined
11.09.2017	6	A330-300	Warm	B	
26.02.2018	7	A330-300	Very cold	B	

6.2 Measurement results

The strains measured during tests No. 5, 6 and 7 are shown in different figures of the following three sections. For the sake of simplicity, they are presented always in the same way: In a first group of figures, the measured transverse strains ε_y are shown for each sensor of section A (V9TSA, V3TSA and V3FSA) in different aircraft positions. This enables for studying the effect of the distance between main gear axis and the sensor axis in asphalt. In a second group of figures, the same strain distributions are shown again, but now each figure includes the results of all sensors for one specific aircraft position. This, in contrast to the figures before, enables for comparing the strains measured in different cables and in different depths for the same aircraft position. In addition to that, at the end of this section, some further selected results are being discussed. Note that the legend, and also some additional information, is included only in one figure of the group, but is also valid for all other figures of the group. Owing to the fact that between the reference measurement and the last measurement was not too much time, no compensation of temperature effects in the measurements were carried out and the full frequency shift measured was converted into strain. As the following figures will show, the effect of temperature appeared to be negligible, making a further data processing including temperature compensation unnecessary.

6.2.1 Test No. 5

An A340-300 was used to load the pavement around the stand T64 during test No. 5 in September 2016. Test procedure A according to Fig. 128 was applied during this test. The average air temperature during the measurements was $T_{air} = 23°C$, the surface temperature of asphalt was measured in average to be $T_{sf} = 30°C$ and the temperature in the protection tube was $T_{sl} = 24°C$. A large part of the measurement results from test No. 5 are also in included in [46].

Fig. 138 shows in the upper part the transverse strains ε_y measured with the sensor V9TSA in a depth of 4cm versus the position y* along the sensor section A. The diagram in the center represents the strains measured with the sensor V3TSA in 4cm depth, whereas the diagram at the bottom shows the results from the sensor V3FSA in 13.5cm depth. Up to a distance of $a_2 = 4m$, the effect of the main gear on the pavement is almost not visible. However, for the aircraft position A_3, where the main gear axis is located 1m away from the sensor axis of section A and the rear tires of the main gear group theoretically stood directly above the sensor, large strains were measured. Each gear, main and centerline gear, becomes clearly visible in the measured transverse strains. The tire positions of the different gears are marked with grey rectangles, indicating that directly under the tire expansive strains and directly beside the tire contractive strains occurred in both depths. In position A_4, when the main gear axis is located above the sensor but no tire stands directly on the sensor, clearly smaller strains were recorded. Of course one should note that the result of position A_4 include still some delayed strains owing to creep from position A_3 a few minutes before.

Conspicuous is the fact, that, mainly during position A_3, the strain magnitudes for the three gears are clearly not the same. Whereas some smaller strains could be expected under the centerline gear, owing to the smaller load present there, the difference between the left main gear and the right main gear has a different reason: During the positioning procedure, the aircraft was moved using an airfield tractor and its position became slightly inclined, as shown in Fig. 139, where the planned and the approximately realized position of the aircraft are drawn. Hence, during position A_3, the rear tires of left main gear did not stand directly above the sensor section A, whereas the rear tires of the right main gear were located directly above the sensor. Note that because of the imprecise positioning, the aircraft was not only inclined but also slightly shifted and a shifted coordinate y* was therefore chosen as the position variable in test No. 5. Of interest is furthermore the rather high magnitude of expansive strain directly under the tire of the right main gear. Up to 3000$\mu\varepsilon$ were measured already after a few minutes under load during an autumn day, which is likely to be exceeded during summer after several hours of parking on the stand T64.
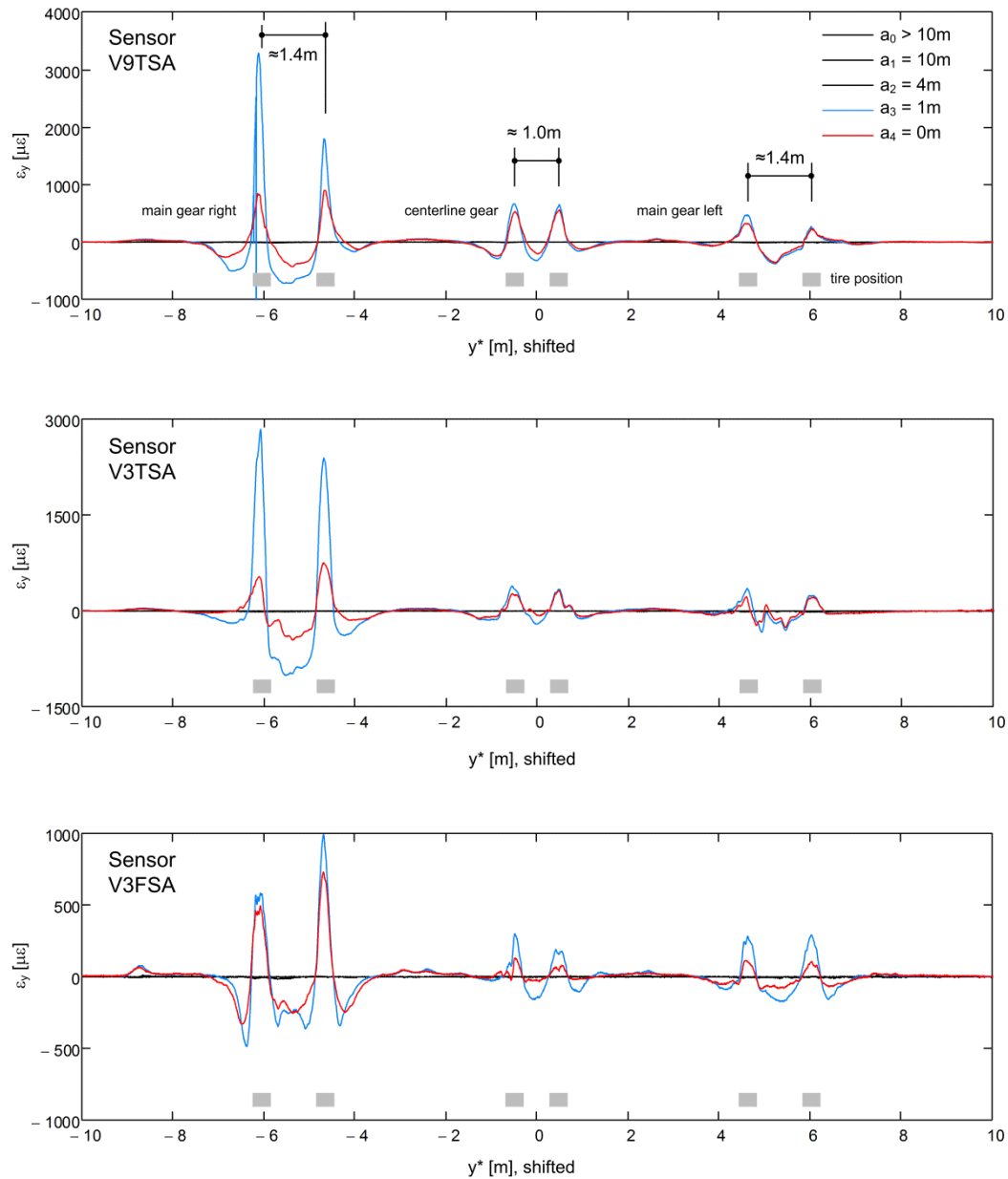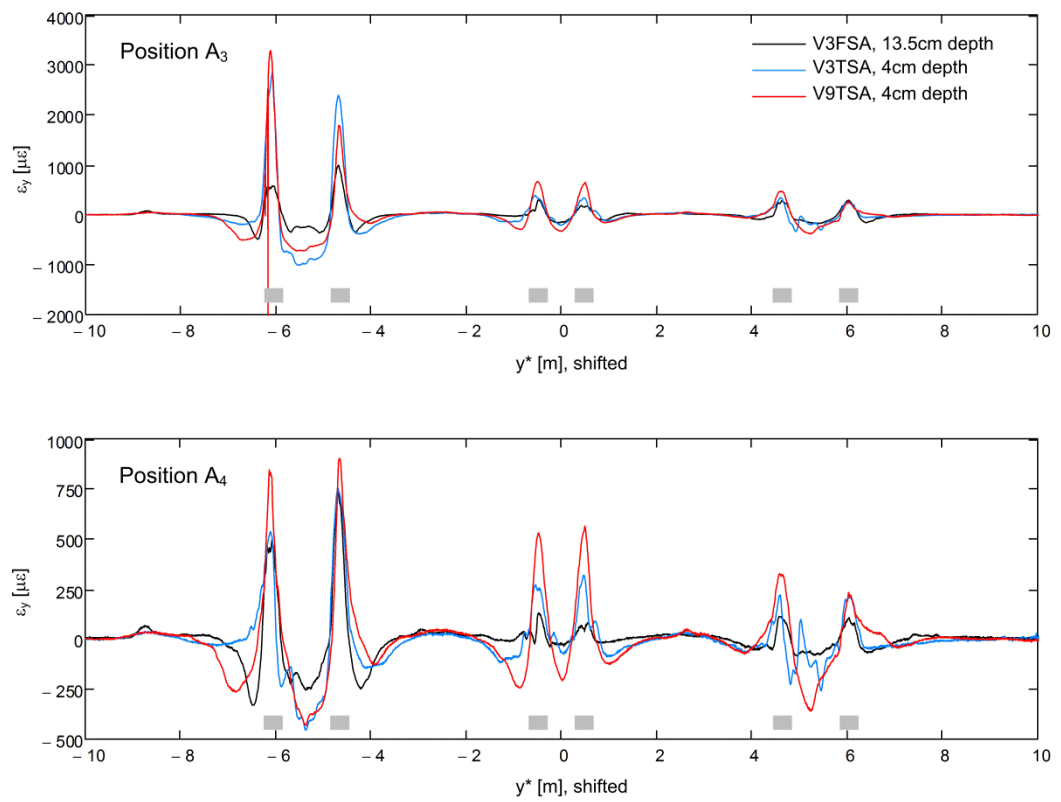
Fig. 138 *Transverse strains measured in three sensors for different positions of the A340-300 aircraft in September 2016 (inclined aircraft position, adapted from [46])*

Fig. 139 shows the same measurement data as already included in Fig. 137. However, the data gathered with each sensor is now compared in a certain position to the data of all other sensors recorded in this position. Fig. 17 shows that all sensors measured a similar distribution and that the effect of the imprecise positioned aircraft, leading to smaller strains on the left main gear side becomes clearly visible. Note that some differences in the measured strain along the sensors can be expected, owing to the fact that they were placed with a horizontal spacing of a few centimeters to each other and different types of sensor cables were used. Furthermore, the heterogeneity of surrounding asphalt may also play a role and finally, it is important to note that the measurements were not conducted perfectly simultaneous: While the aircraft rested for a few minutes in a certain position A_i, measurements were conducted with each sensor individually. As some figures towards the end of this chapter will show, a certain part of the strains occurs owing to creep and introduces therefore also a certain time dependency. Hence a certain discrepancy concerning majorly the magnitude of strains is caused by the order how the measurements were conducted.
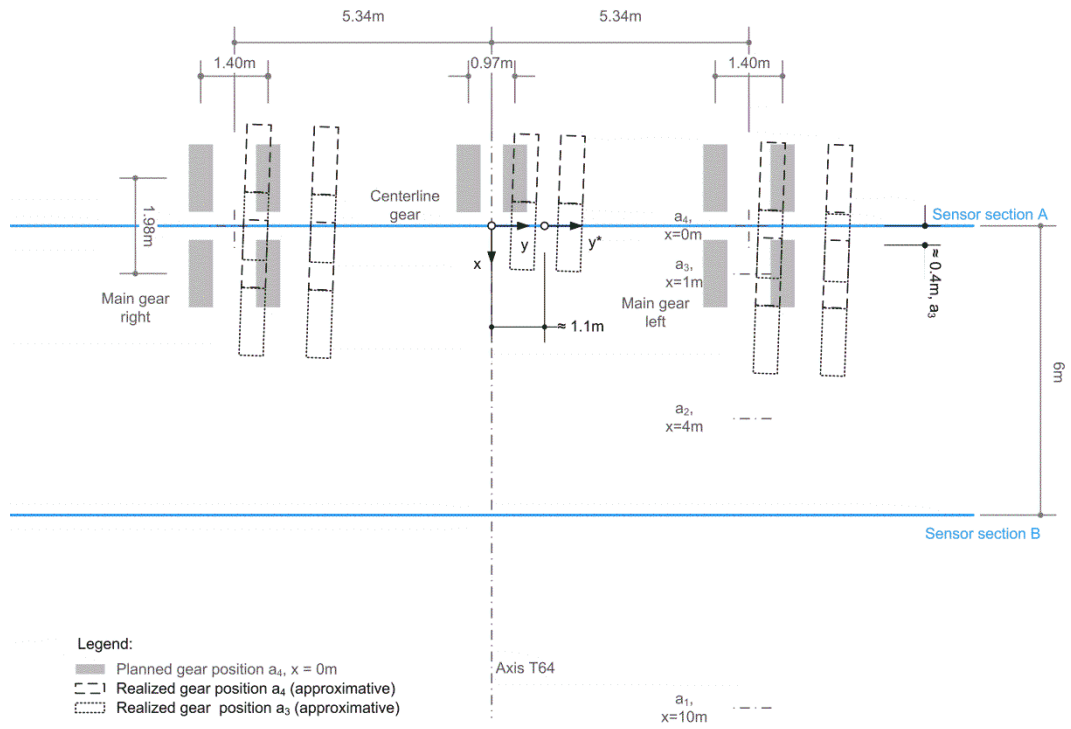
Fig. 139 *Imprecise positioning of the aircraft during test No. 5 (adapted from [46])*

Fig. 140 *Transverse strains measured along three sensors for positions A_3 and A_4 of the A340-300 aircraft in September 2016 (inclined aircraft position, adapted from [46])*

6.2.2   Test No. 6

An A330-300 was used to load the pavement around the stand T64 during test No. 6 in September 2017. Furthermore, test procedure B according to Fig. 129 was applied during this test and the aircraft could be positioned as foreseen. The temperatures were slightly cooler than in test No. 5: The average air temperature during the measurements was $T_{air} = 19°C$, the surface temperature of asphalt was measured in average to be $T_{sf} = 21°C$ and the temperature in the protection tube was $T_{sl} = 22°C$.

Fig. 141 shows the measured transverse strains along the three sensors V9TSA, V3TSA in 4cm depth and V3FSA in 13.5cm depth, for different aircraft positions B_i with spacing b_i ranging from 3 to 0m. Both main gears are clearly visible in the measurements and the distribution is also the same as during test No. 5, showing expansive strains directly und the tire and contractive strains beside the tire (excluding the missing centerline gear of the A330-300 compared to the A340-300). The strain distribution gathered during this test is now in good approximation symmetric with respect to the aircraft axis. This confirms that not a larger heterogeneity around T64 in asphalt caused the asymmetry in the strain distribution measured during test No. 5. However, as in test No. 5, also here the strains of the aircraft position where the distances from the rear axis to the sensor are larger than 1m, are found to be rather small. This even though, the test procedure was changed in order to have also distances of 2m and 3m instead of only 4m as in test No. 5. The largest transverse strain magnitudes ε_y occur again during the position B_4 while the rear tires of the aircraft main gears stood directly above the sensor. With sensor V9TSA strains of $2000\mu\varepsilon$ to partially more than $3000\mu\varepsilon$ were measured, whereas sensor V3TSA indicated maximum expansive strains of around $1000\mu\varepsilon$ to $2000\mu\varepsilon$. Possible reasons for this discrepancy (different cables, non-simultaneous measurements, creep) were already discussed in the previous section describing test No. 5 and apply also here. Whereas these two sensors indicate the strains in 4cm depth, V3FSA in in 13.5cm depth shows almost an identical strain distribution, with clearly lower expansive strain magnitude of around $500\mu\varepsilon$ to $1000\mu\varepsilon$ directly under the tire. Interestingly, during position B_4 and directly under the tire, a more or less clearly distinct double peak in the transverse strain becomes visible, as it was also the case e.g. under the load of the concrete blocks at the test field Hohlstrasse (see section 5.2.4). This effect is separately discussed in section 5.4. In position B_4, under the left tire of the left main gear, some outliers in the measured strain data can be seen, occurring owing to the specific sensor layout and the locally high spatial strain gradient, which is also further addressed in section 6.2.4.

Fig. 142 shows again the same measurement data but owing to the different arrangement, the vertical scale of the figures could be adapted for each aircraft position. This enables for a magnified view into the strain distribution prior to position B_4. Regarding the transverse strain distributions belonging to the positions B_2 and B_3, it becomes obvious that the strains in this specific pavement layout are highly localized. In position B_2, when the rear tires of the main gears are only 2m away from the sensor (axis distance 3m), around $25\mu\varepsilon$ were registered and still, during position B_3 when the rear tires of the main gears are only 1m away from the sensor (axis distance 2m), only around $50\mu\varepsilon$ were measured. Moving the aircraft 1m further, towards the sensor into position B_4, increases the strains dramatically and leading to the large strain magnitudes discussed above. Regarding this, the strain distributions measured during position B_5, when the axis of the main gears is located directly above the sensor but no tire, appears in a different light. Although not exactly comparable to position B_2, where the tires are also 1m away from the sensor owing to the second group of tires, the strains occurring during position B_5 are around 20 to 60 times higher than those measured during position B_3. This leads to the conclusions that the strains measured during position B_5 are merely the result of delayed strains owing to creep of position B_4 and not representing the strains belonging to the specific geometric position of the main gear during position B_5. Significantly smaller strains could be expected, if the aircraft could be brought directly into position B_5, without stopping in position B_4 or even, in a gedankenexperiment, without crossing the sensor in order to get into position B_5.
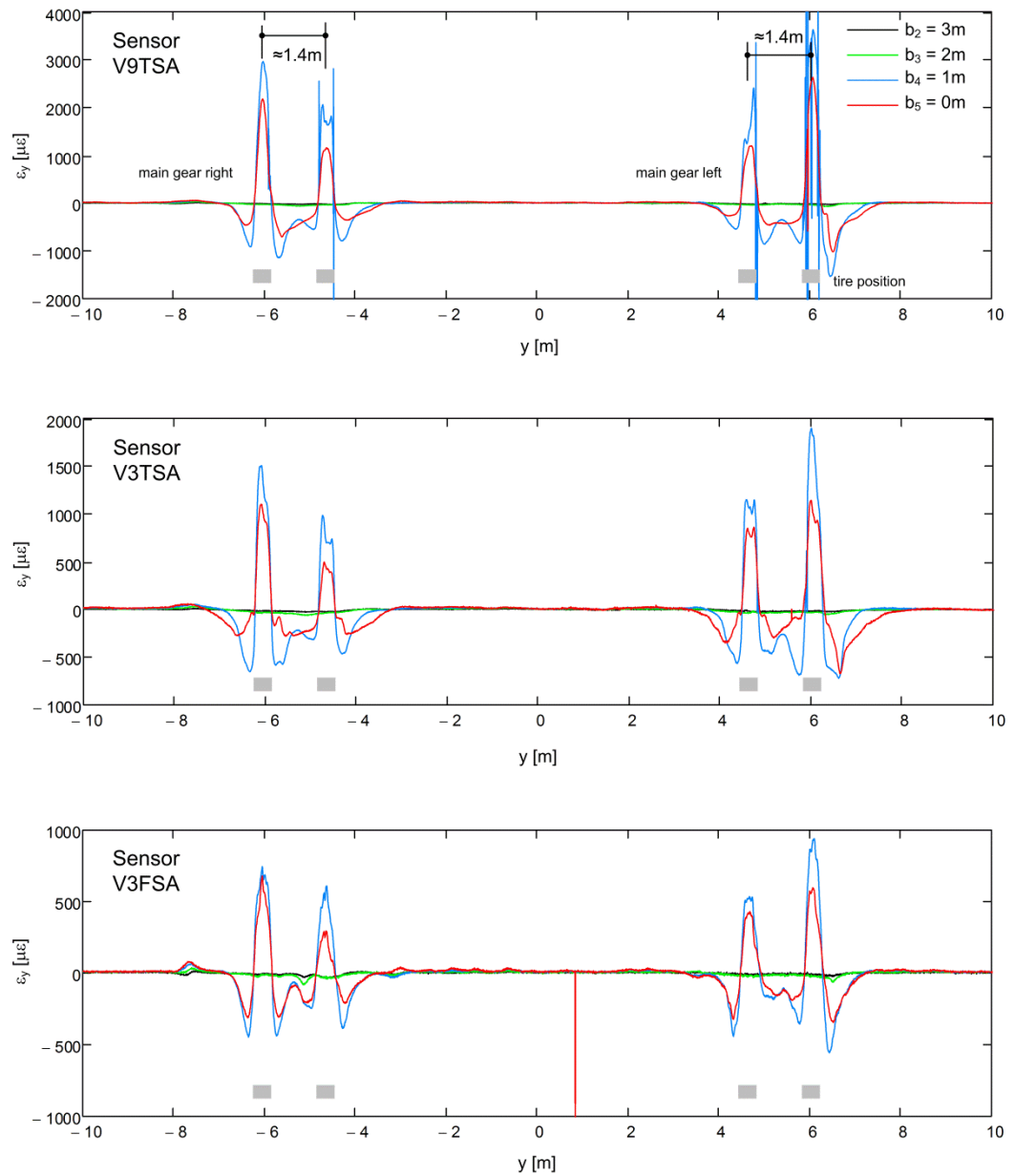
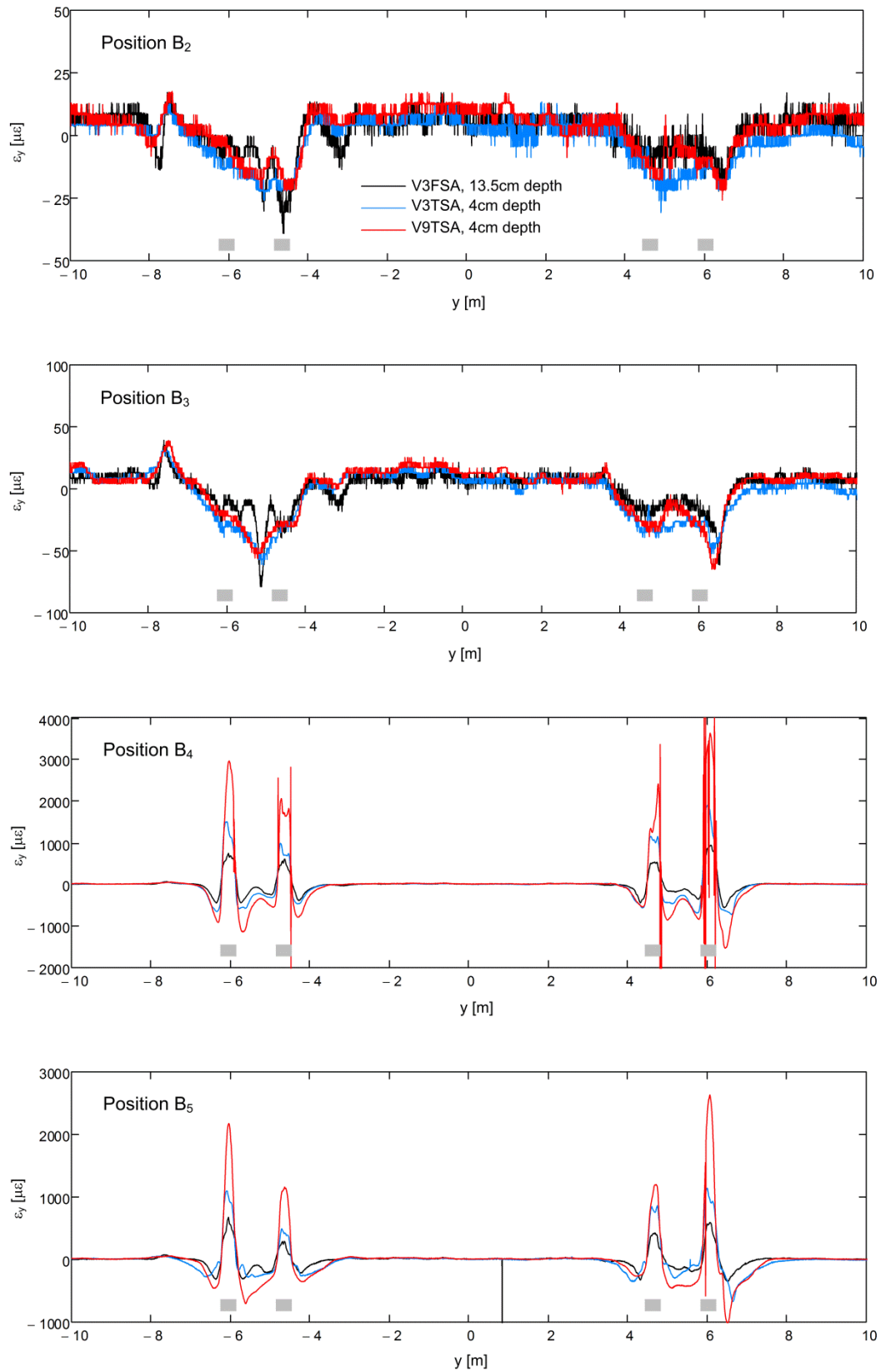**Fig. 141** *Transverse strains measured along different sensors for positions B_2 to B_5 of the A330-300 aircraft in September 2017*

Fig. 142 *Transverse strains measured along three sensors for positions B_2 to B_5 of the A330-300 aircraft in September 2017*

6.2.3 Test No. 7

During test No. 7 in February 2018, an A330-300 was used to cause strains in the pavement around the stand T64. Furthermore, procedure B according to Fig. 129 was applied. The temperatures were significantly colder than in test No. 5 and 6. The average air temperature during the measurements was T_{air} = -10°C, the surface temperature of asphalt was measured in average to be T_{sf} = -9°C and the temperature in the protection tube was T_{sl} = 4°C. The fact that in the electro shaft, where the OBR 4600 measurement device was temporarily installed, significantly higher temperatures of almost 3°C were met, made measurements at the lower bound of the suggested operating temperature range of the device only possible.

Fig. 143 shows, as in the previous sections, the strains measured along the three different sensors. Unfortunately it was not possible to obtain during these tests for all sensors and aircraft positions meaningful results. In some measurements the level of disturbances was, owing to the challenging temperature and humidity conditions in the shaft, rather high and therefore not included in this report. However, the remaining measurements allow for an interesting study of the effect of temperature change on the strain distributions, since the same type of aircraft with identical weight configuration was used, applying the same test procedure as in Test. No 6 in clearly warmer thermal conditions.

As expected and already confirmed by the measurement results in Hohlstrasse, the asphalt is significantly stiffer owing to the reduced temperature and hence, the strain magnitude is only a fraction compared to what was measured in autumn (September 2017). The effect of the approaching main gear becomes again visible in Fig. 143 during position B_2 (b_2 = 3m). The strains measured during this position around the main gears are of expansive nature, but rather small and almost vanishing in the fluctuation of the measurement. During position B_3, the strains seem to be merely contractive around the main gears and reach in maximum approximately $25\mu\varepsilon$. In position B_4, when the tires stood directly above the sensors, a similar strain distribution as observed in cold temperatures in the test field Hohlstrasse was measured: In a depth of 4cm, the strains under the tire are not expansive anymore. Directly beside the tire, still contractive strains can be observed and towards the center of the tire, the strains tend to be less contractive but they do not change their sign and do not become expansive anymore as observed during autumn. It is of interest to note that the strain magnitude observed during position B_3 is approximately half of what was measured in autumn for B_3, when the temperature of the asphalt surface and the air was around 30°C higher. However, for position B_4 temperature has a very large effect, turning even the sign of the strain distribution directly under the tire. Interestingly, the strains in 13.5cm depth remain expansive directly under the tire or at least they approach zero. The largest strain magnitude in winter conditions was recorded during position B_4 in 13.5cm depth and not in 4cm depth, although the expansive strain under the left wheel of the left main gear seems to be extraordinary high compared to the others and also rather unusual, since exactly under this wheel also in 4cm depth the strain distribution exhibited an anomaly (almost no sharp change in strain directly beside and under the tire) compared to the other three tires. This can be observed at best in Fig. 144 (Position B_4), where the strains from all sensors are compared to each other for a certain position. Of further interest is also the comparison of strains measured during position B_3 and B_5 shown in Fig. 144: Whereas in autumn a factor of 20 to 60 was observed between the strains measured during these two aircraft positions, in winter it is only around a factor of two. This result could also be expected, owing to the fact that the sensors have in both positions a distance of 1m to the next wheel. However, in position B_5 there is on both sides of the sensor in a distance of 1m a wheel located, whereas during position B_3, there is a wheel only on one side of the sensor (Fig. 129). Hence, in contradiction to the measurements in autumn, the field experiment confirms that viscous effects, as delayed strains owing to creep, seem to be clearly less important during winter, as could be expected from the material behavior of asphalt.
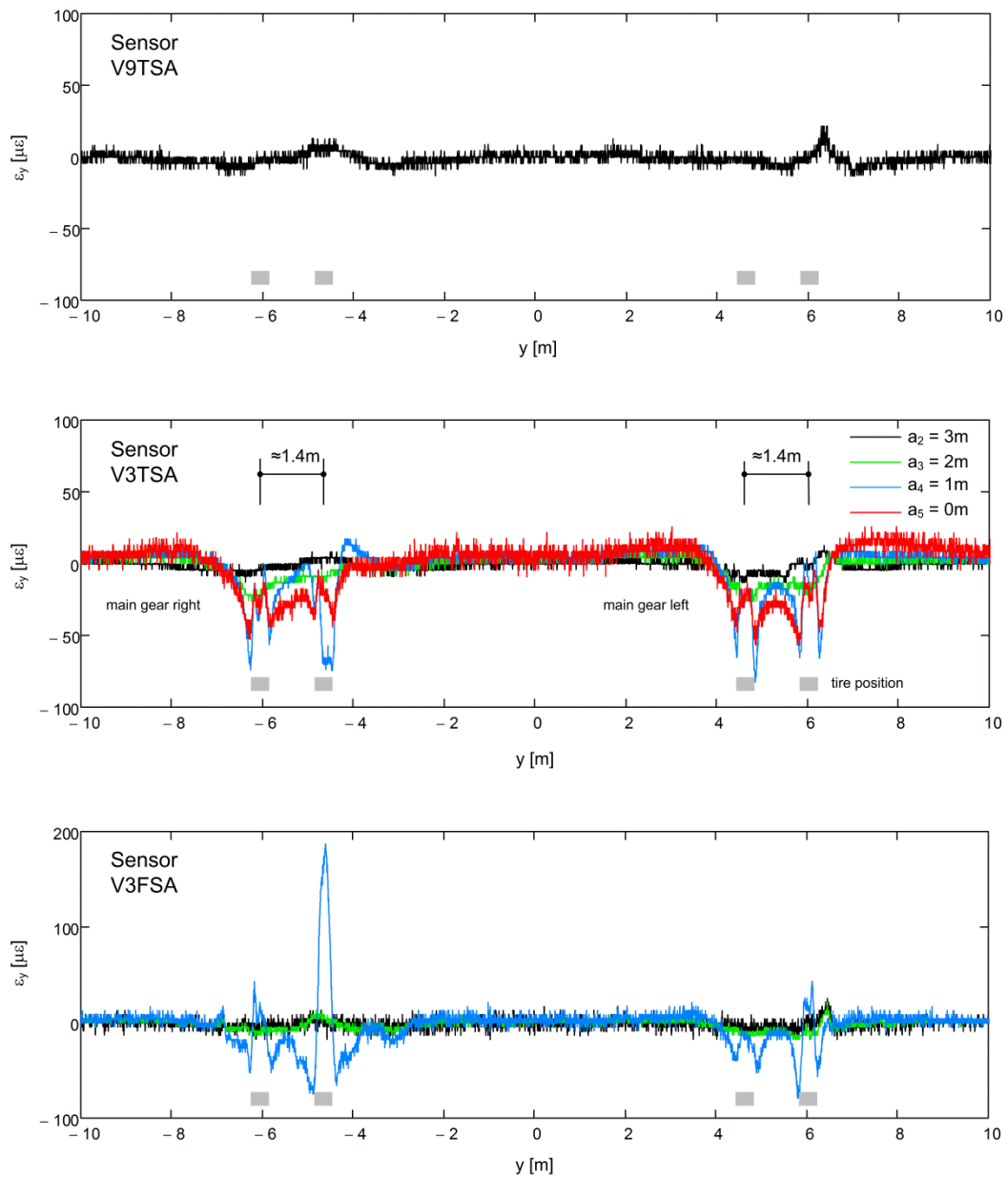
Fig. 143 *Transverse strains measured along different sensors for positions B₂ to B₅ of the A330-300 aircraft in February 2018*
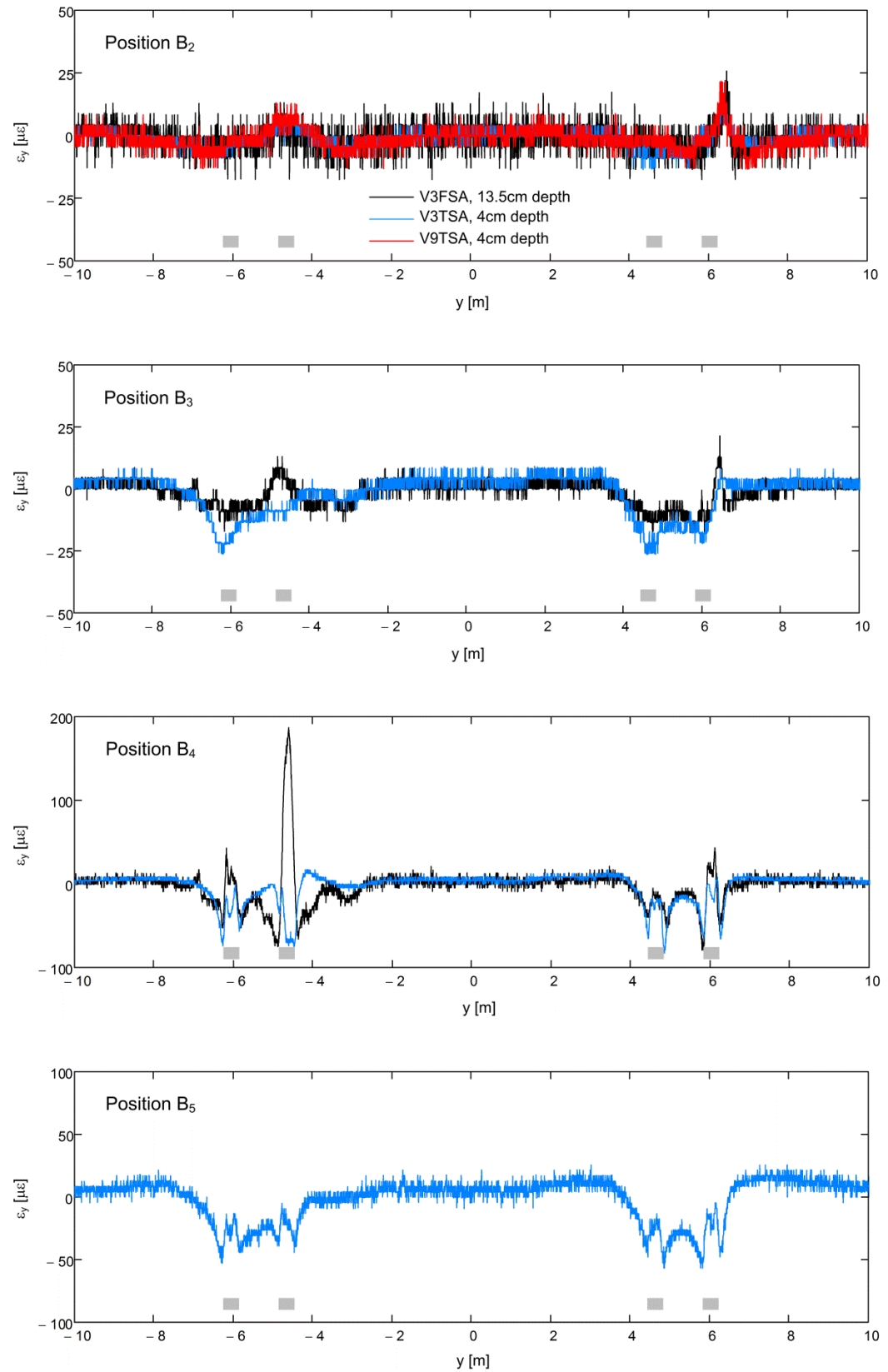
Fig. 144 *Transverse strains measured along three sensors for positions B₂ to B₅ of the A330-300 aircraft in February 2018*

6.2.4   Selected measurement results

In the present section, some selected details of the measured strain distribution are shown.

Strain distribution around the main gear

The figures of the previous sections included always a sensor section of 20m in order to show the full influence zone of the main gears. However, the spacing between the wheels of the main gear from tire axis to tire axis is only 1.4m and hence, a more detailed insight into the strain distribution by means of a 5m section around the right main gear, is shown in Fig. 145 for all three sensors on the example of test No. 6 (September 2017). These illustrations highlight that the strain distribution changes, in good approximation, from contractive to expansive strain at the boundary of contact zone between tire and asphalt. Furthermore, they point out that a very high strain gradient is present in this zone. Whereas often the strain culminates ordinarily in the center under the tire, in certain conditions the strain distribution forms a double peak with a small decrease of strain in the center under the tire. The latter type of strain distribution was already observed at the test field Hohlstrasse. As at the airport, it was also at Hohlstrasse registered to occur close to surface in a depth of 4cm. Potential reasons for the occurrence of this specific type of distribution are discussed in section 5.4. Interestingly, the double strain peak occurs in this specific test only under one tire of the main gear, but not under the other. However, as Fig. 23 shows, it was observed along both sensors (V9TSA and V3TSA) in 4cm depth, but not along the sensor (V3FSA) in 13.5cm depth.

Of interest is also the comparison of the detailed strain distribution around a main gear in autumn (September 2017, Fig. 145, center, V3TSA, right main gear) to the one measured in winter (February 2018, Fig. 146, V3TSA, left main gear), when the air and asphalt surface temperature was approximately 30°C cooler. As discussed before, the strain directly under the tire is not expansive anymore and the strain magnitude measured in the different positions b_3 to b_0, does not vary by orders of magnitudes in winter. Furthermore, the strains are clearly less localized in winter compared to the situation in summer. Additionally, by comparing the strains of positions b_3 and b_5 to each other, it can be concluded that creep effects in winter are, as expected, rather small.

Outliers

As discussed above, the maximum strain magnitude (around $3000\mu\varepsilon$ to $4000\mu\varepsilon$) under the tires measured in autumn conditions at the airport, clearly exceeds the maximum strains measured at the test field Hohlstrasse (around $1500\mu\varepsilon$). Whereas strains in this range are not a problem for the sensor cable and measurement device, the applied sensing technology SWI in the form of the measurement device OBR 4600, is sensitive to high spatial strain gradients, as present e.g. in September 2017 at the airport. Depending on the processing parameters, high spatial strain gradients lead increasingly to processing difficulties and local outliers in the strain distribution. If the strain gradient is very high, this may lead locally even to an erratic strain distribution, which of course does not represent the strain state present in the sensor cable or the host material. A situation where locally high spatial strain gradients occurred, is shown Fig. 147 on the example of the strains under the outer tire of the left main gear in September 2017. During position B_4, the determination of frequency shift (and with that also strains) in the zone of high strain gradient fails. If the computed strains are plotted as individual dots and not as line (Fig. 147), the measurement result remains still recognizable since individual outliers do not govern the whole picture. This point of view also highlights that the predominate amount of data points is still computed correctly.
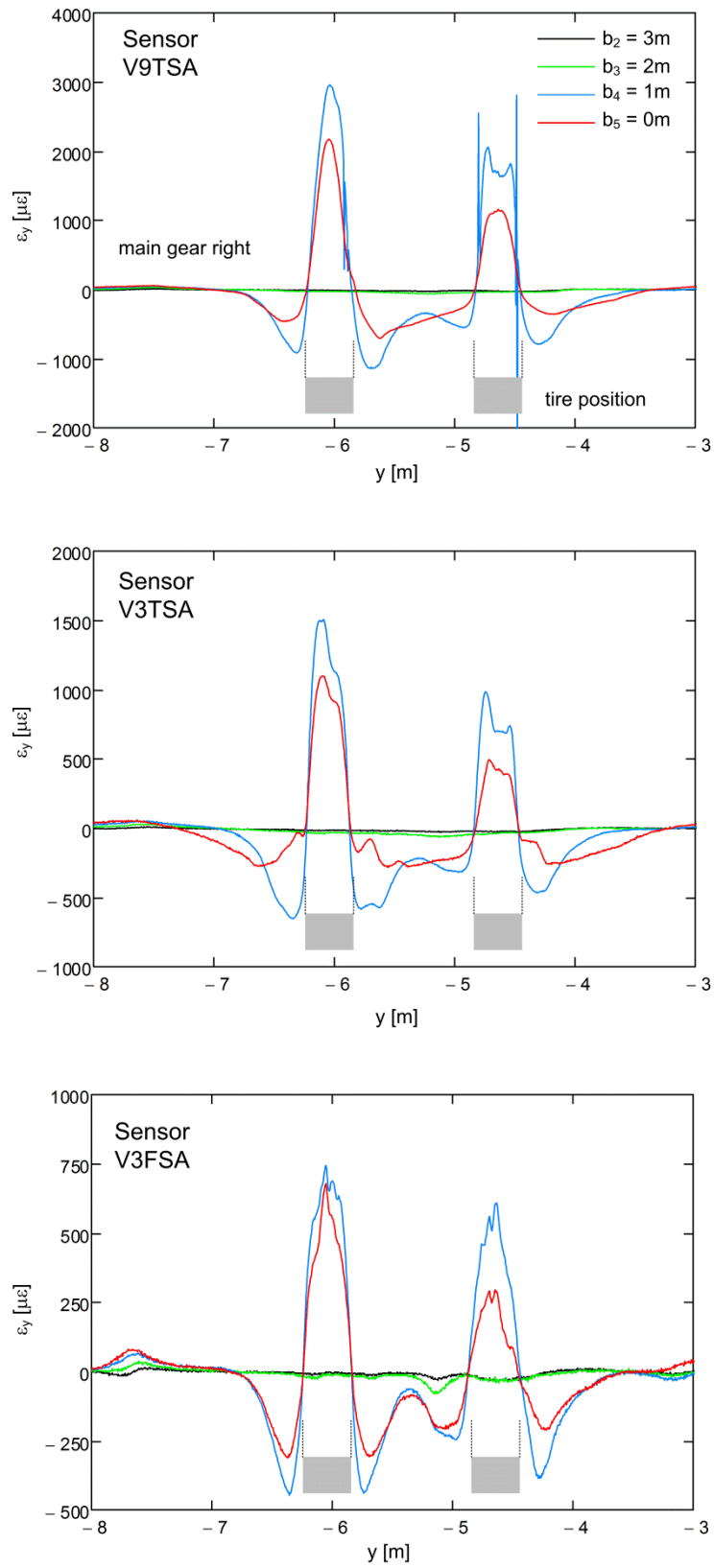
Fig. 145 *Detailed strain distribution under the right main gear in September 2017 for three sensors and different aircraft positions (A330-300)*
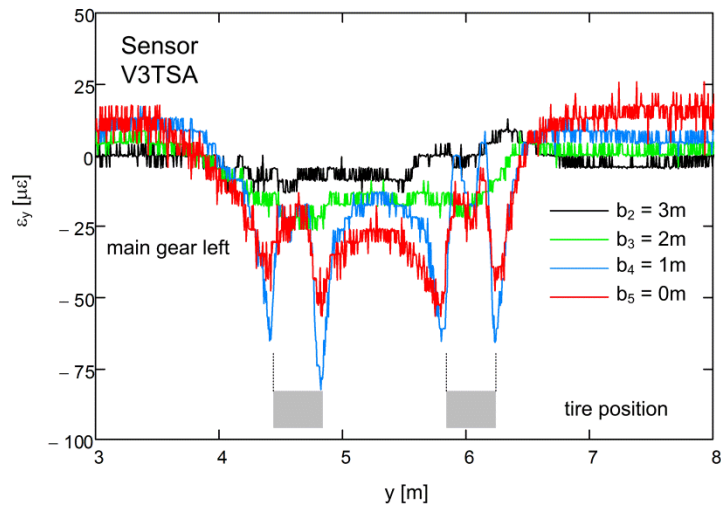
Fig. 146 *Detailed strain distribution under the left main gear in February 2018 for the sensor V3TSA and different aircraft positions*
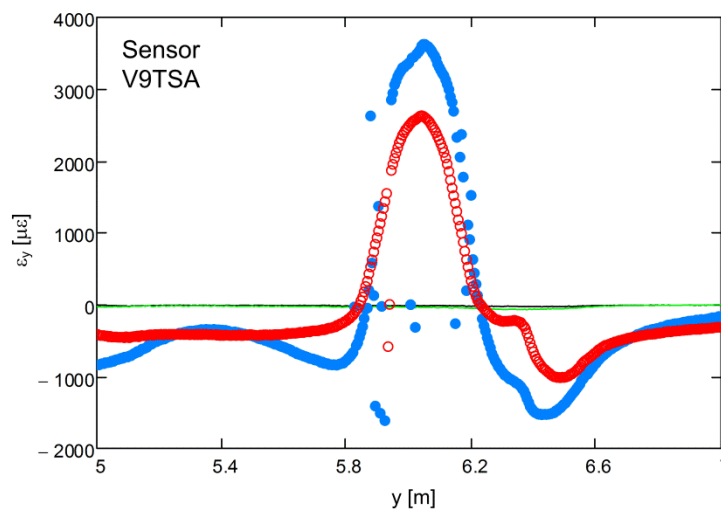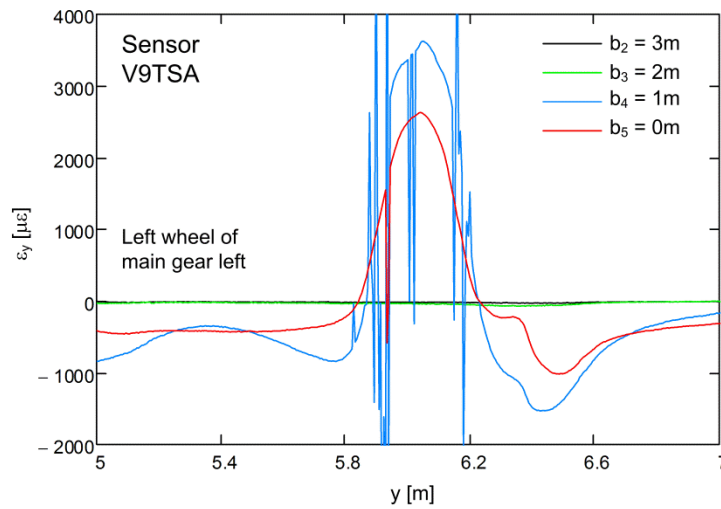

Fig. 147 *Processing difficulties in zones of high spatial strain gradients, illustration of the measurement data using lines (top) and points (bottom)*
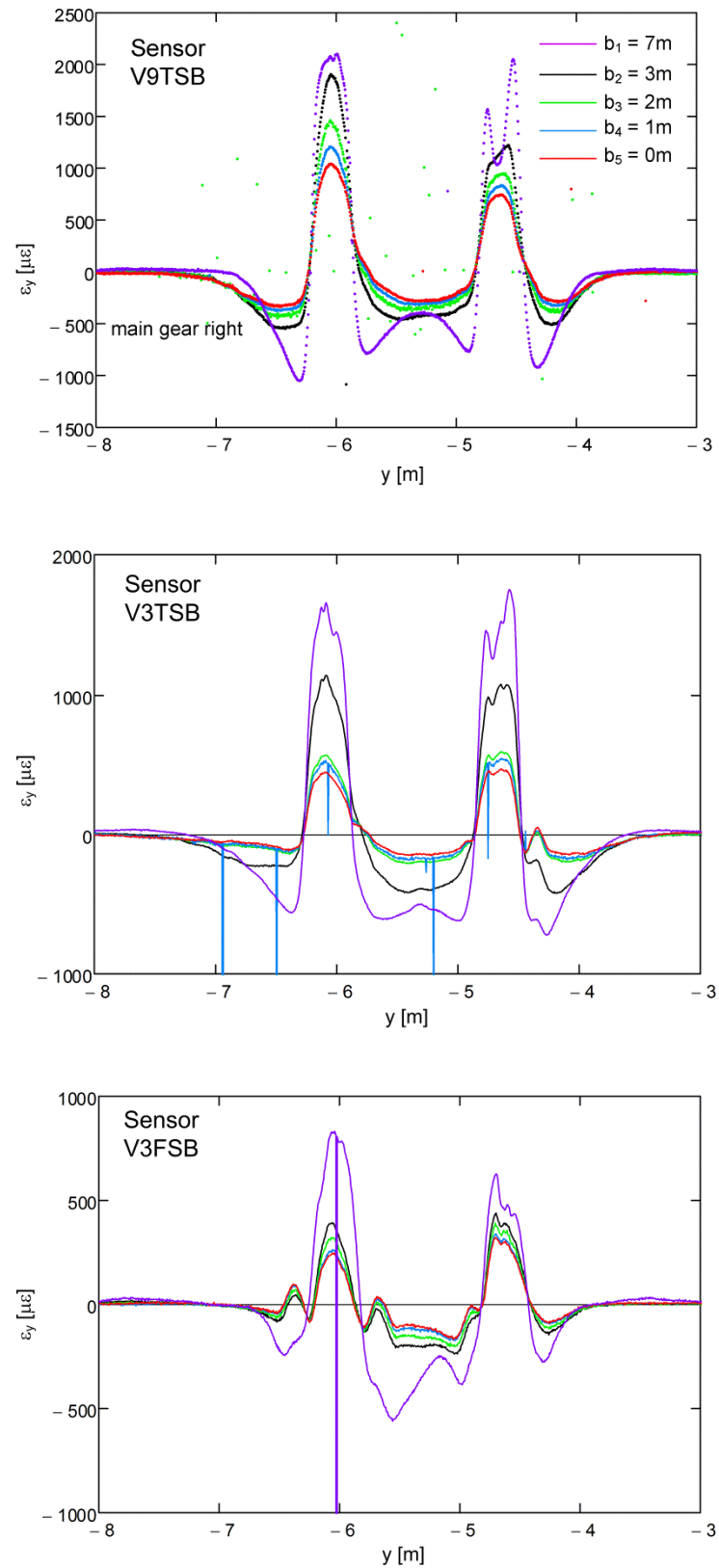
Fig. 148 *Development of strains (with time) in subsequent measurements for three different sensors of sensor section B, loading (b₁ = 7m) and unloading (b₂ = 3m) in September 2017*
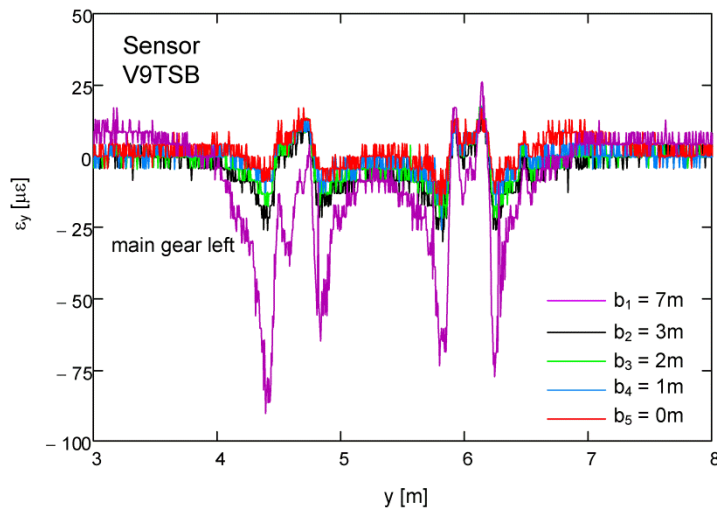
Fig. 149 *Development of strains (with time) in subsequent measurements for the sensor V9TSB of sensor section B loading (b_1 = 7m) and unloading (b_2 = 3m) in February 2018*

Creep

So far only the results of sensor section A were discussed. However, there is also roughly the same amount of measurement data available along sensor section B. Owing to the specific test procedure, mainly made for sensor section A, a series of measurements after unloading are available for sensor section B. In test procedure A, these unloading measurements are the result of traversing the sensor, whereas in test procedure B the unloading measurements result from a stop of several minutes of the aircraft on the sensor (Position B_1, b_1 = 7m). Fig. 148 shows strain distributions measured along the sensor section B under the right main gear of the A330-300 during autumn 2017. For the sensor V9TSB on top, the data was plotted as individual points without connecting lines, since processing difficulties occurred, resulting in many outliers. Although the different strain distributions are labelled according to the aircraft position with respect to the sensor section A, this denotation is actually meaningless, since the different distribution represent not the effect of the increasing distance to the sensor but rather the development of viscous strains with time. Whereas during position B_1 the rear tires of the main gear stood directly on the sensor, all further aircraft positions B_2 to B_5 represent actually the effect of unloading with time. The load was resting several minutes above the cables in position B_1 and between the further following measurements are always around 5 to 10 minutes and the different distributions are showing the unloading process within the following around 30min (more detailed time information could be retrieved from the measurement time stamp). Whereas creep strains seem to be the governing effect in autumn, in winter this effect is rather limited, as Fig. 149 on the example of sensor V9TSB in 4cm depth for Test No. 7 in February 2018 shows.

6.3 Discussion

Compared to a normal road, as e.g. represented by the test field in Hohlstrasse, the operational demands of an airfield stand are quite different. Both, the load per wheel of a main gear, but also the resulting normal contact stress are larger on an airfield. Furthermore, the loads are expected to rest for a clearly longer time on the stand than on the road and the aircraft is positioned, owing to the marks on the pavement, always exactly at the same location. On the other hand, the number of load cycles is clearly lower at the stand compared to the road. In order to reduce the tendency of local permanent deflection under the tires of the main gears, stands are often built from concrete plates. However, the stand T64, from which the measurement results were gathered, is built in a different layout consisting of two asphalt layers with a total thickness of 13.5cm on two cement treated base layers with a total thickness of 53cm (Fig. 123). This is owing to the specific boundary conditions of the project and the foreseen temporary usage. Compared to the design at Hohlstrasse, where the asphalt layers were in total 22cm thick, resting on a base layer with 60cm thickness consisting of recycled concrete material, the asphalt layer itself seems to be stiffer at the road, whereas the base layer itself is expected to be significantly stiffer at the airport, owing to the cement treatment. Hence, the design at the airfield seems to resemble a rather soft asphalt layer (depending on the temperature), lying on rather stiff cement treated base layer. Despite of the different design, the strain distribution in 4cm depth shows some similarities to what was found at the test field Hohlstrasse. In both cases large expansive strains were found directly under the tire, which was also the case in 13.5cm depth (Zurich Airport) and 22cm depth (Hohlstrasse). Furthermore, in 4cm depth sometimes double peaks in the strain distribution were observed at both test sites. Directly beside the tire, the strain was found to be contractive and changed its sign with large spatial strain gradients. However, the strains measured in the pavement of the airfield were in general clearly larger. Although a direct comparison between these two test sites is difficult, since the resting time of the load until the measurement was carried out was different (a few seconds at Hohlstrasse compared to a few minutes at the airport) one can state that the strains at the airport were in general clearly higher. Furthermore, it was observed that the strains were strongly localized around the tires. Unfortunately the high strain magnitudes seem already to have induced first remaining local permanent deflections in the pavement, as illustrated in Fig. 150 and Fig. 151.

Fig. 150 *Local permanent deflections on stand T64 in September 2017, aircraft position B₄*

Fig. 151 *Local permanent deflections on stand T64 in February 2018, aircraft position B₄*

6.4 Conclusions

The test field on Zurich Airport was the first test field for the project team where distributed fiber optic sensors were installed. The experience of the installation process could be directly used on the second test field at Hohlstrasse. Although in the beginning the quality of the measurement data gathered at this test site was not satisfying, successful measurement campaigns could be conducted in the second half of the project, since the measurement procedure was adapted to the specific sensor layout present in this test field. The results gathered during installation and operation of this sensor over more than 2.5 years lead to the following conclusions:

- The specific distributed fiber optic sensor layout, which had to be applied in order to measure with high spatial resolution, created initially some difficulties, which were overcome by adapting the parameter of the measurement procedure. Hence, longer fiber optic loops providing access from both sides are more delicate to measure but possible.
- The measured strain distributions have some similarities to those measured in the test field Hohlstrasse, however, the strain magnitude was in general clearly larger.
- Expansive strains were measured in warm conditions in autumn in 4cm and 13.5cm depth directly under the tire of the aircraft main gears, whereas in cold winter conditions the strains directly under the tire in 4cm depth became mainly neutral or even contractive.
- Large local expansive strains were measured directly under the tire, leading to high spatial strain gradients, which implicated partially processing difficulties in the applied measurement technology. This can be observed as outliers in the measured strain distributions.
- The large expansive strain magnitudes of several thousand microstrains, measured under relatively short exposure times of several minutes of the aircraft on the stand, are likely to be exceeded in even warmer conditions in summer and usual exposure times of several hours.
- The specific design of the aircraft stands with two asphalt layers on a cement treated base, the large local strains under the tires as well as the recurring identical positioning of the aircraft caused already some local permanent deflections in the pavement.
- A double peak of expansive strains was observed directly under the tire in some measurements, as it was already observed on the test field Hohlstrasse.
- The fast change of the strain distribution in space, showing two contractive and one or two expansive peaks within a distance of less than one meter, requires the application of a distributed strain sensing technology with high spatial resolution in order to resolve the local strains properly.

6.5 Acknowledgements

7 Modelling of ETH Delta tests in Hohlstrasse

Abstract

The spatial settlement measurement data obtained with the ETH Delta device are used in this chapter to back-calculate the material parameters with the help of a finite element model. The model and the back-calculated parameters are initially described and then the simulated and measured settlements are compared and discussed.

7.1 Finite element model

In order to validate the strain measurements, the tests results from the three dimensional static deflection tests were adopted for the back calculation procedure of the asphalt stiffness.

A three dimensional finite element model was implemented in the commercial finite element code ABAQUS reproducing the loading conditions and the pavement structure. The model length and width are 5m (Fig. 152). The layer thicknesses correspond to those obtained from the sample boring.

- Wearing course (asphalt AC 11): 4cm
- Binder and asphalt base layer (asphalt AC B 22 & AC T 22): 2 x 9 = 18cm
- Base course and subgrade: 400cm

The model has an axis of symmetry, and it represents one half of the half of one axle load. The axis of symmetry is the middle of the axle load and of the tire respectively. The tire footprint was modelled as a rectangle with a width of 30cm and a length of 25cm (12.5cm in the model = one half). The tire pressure was taken equal to 6bars.

The layers have been modelled with a linear elastic constitutive model (soil and asphalt) as well as a hyperviscoelastic model for the asphalt according to Puzrin and Rabaiotti [49]. Between all the layers, a frictional interface was considered (coefficient of load transfer $\mu = 0.5$).
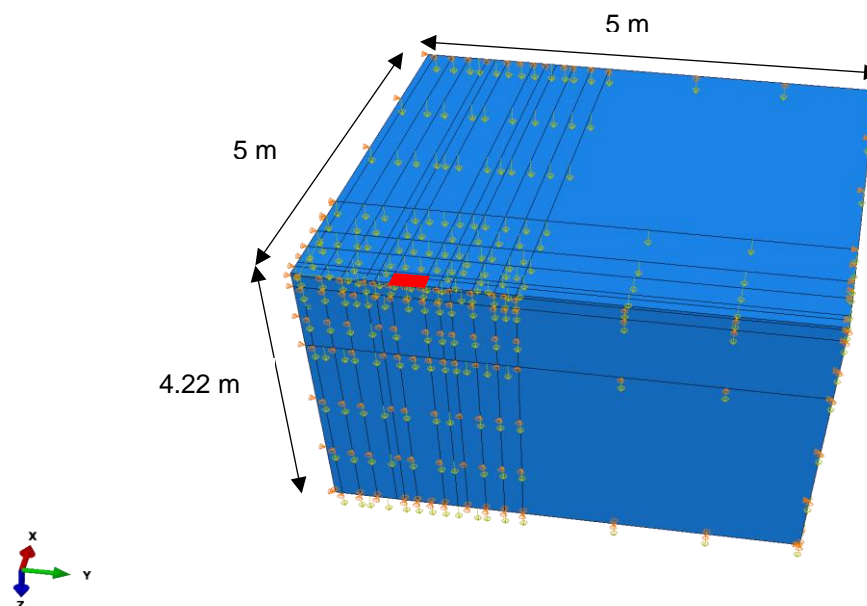

Fig. 152 *Three-dimensional finite element model adopted for the simulation. Red = applied load surface (tire footprint)*

The mesh of the model is shown in Fig. 153. The chosen element is a linear hexahedral element of type C3D8R (reduced integration).
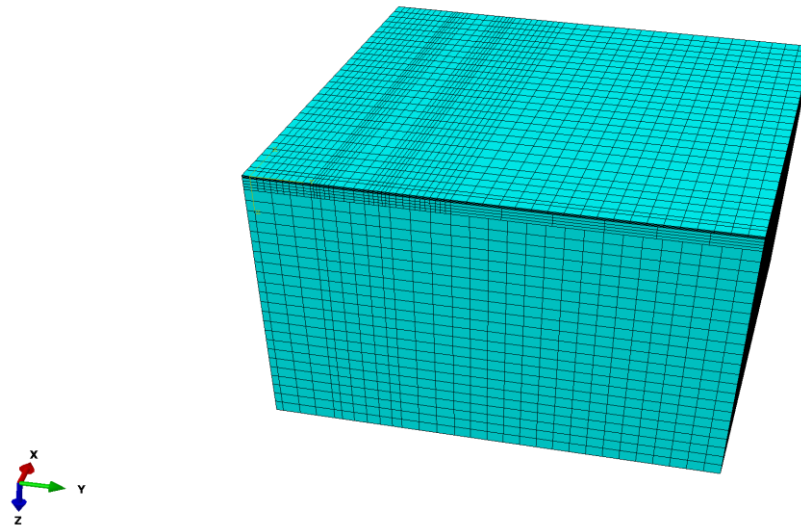

Fig. 153 *Adopted finite Element mesh of the boundary value problem at the Hohlstrasse*

The back-calculated elastic and hyperviscoelastic material properties are shown in Tab. 22 and Tab. 23. The constitutive model (elastic) and the parameters are the same for the sub-base and the subgrade layer. The analysis has been carried out minimizing the sum of the mean squared errors between measured and calculated displacements.

The inverse analysis has shown that the parameters for the wearing course and the asphalt base layer do not influence the shape of the measured deflection bowl. In particular the calculation carried out with the time dependent hyperviscoelastic model show that the viscous deformations of the asphalt take place under or in close proximity (few centimeters) to the tire (see also Fig. 154 und Fig. 155) . The pavement settlements in this region cannot be measured by the ETH Delta device, therefore neither the elastic nor the viscoelastic properties of the wearing course and the asphalt base layer can be successfully analyzed.

Tab. 22 *Backcalculated elastic material properties*

	E	ν
Layer	**[kPa]**	**[-]**
Wearing course	800'000	0.4
Binder + Asphalt base layer	800'000	0.4
Base +Subgrade	420'000	0.2

The obtained parameters for the asphalt in Tab. 22 represent the long term elastic stiffness. The hyperviscoelastic material properties shown in Tab. 23 represent the long term elastic moduli (G_{inf} and K_{inf}) as well as the short term ones ($G_{inf} + G_1$, $K_{inf} + K_1$). These values are based on assumptions since the effects of the asphalt stiffness have no influence on the deflection measured by the ETH Delta on this pavement.

Tab. 23 *Backcalculated hyperviscoelastic material properties*

	G_{inf}	K_{inf}	m	G_1	K_1	τ_{G1}	τ_{K1}
Layer	[kPa]	[kPa]	[-]	[kPa]	[kPa]	[s]	[s]
Wearing course	285'700	1'330'000	1	300'000	0	30	1
Binder + Asphalt base layer	285'700	1'330'000	1	300'000	0	30	1

7.2 Comparison of numerical and experimental results

Fig. 154 shows the measured (dots) and back-calculated (curves) deflection lines of the pavement surface at different distances of the tire from the measurement section. The distance 0m means that the device measure the pavement deflection on both sides of the tire. The distance 1.4m means that the device measures the same section, but the tire is now 1.4m away from the measured section.
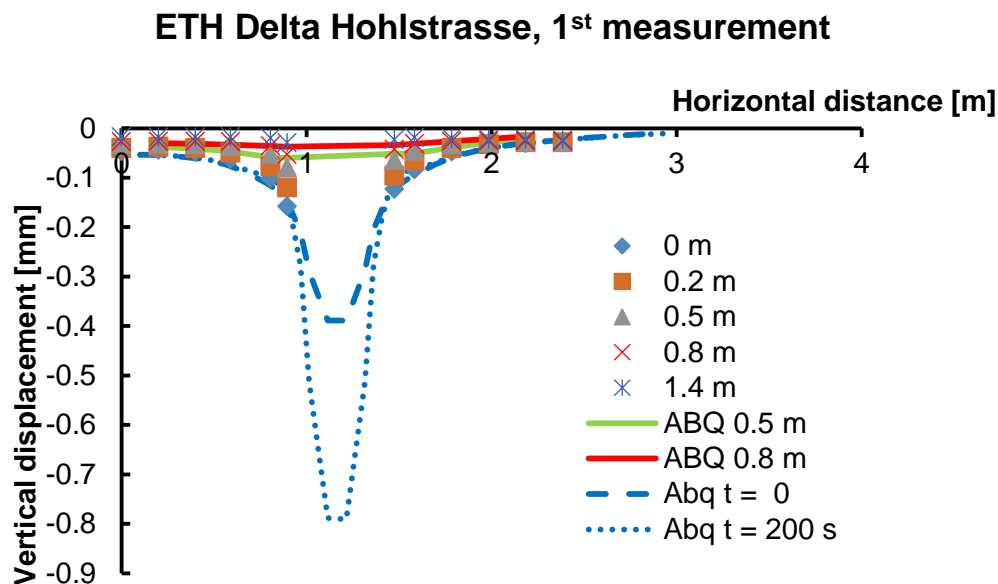
Fig. 154 *Measured (dots) and calculated (lines) deflections of the road surface*

Fig. 156 shows the calculated and measured cross horizontal strains at the top of the binder layer. The back calculated asphalt stiffness varies from 200MPa (short term) to 130MPa (long term).

The match between measured and calculated strains is not completely satisfactory for the negative (compressive) strains. A possible explanation is that asphalt stiffness at high temperature in tension is different than those in compression. It has also to be noticed, that the measured strains are mainly elasto-plastic, while the back-calculation has been carried out with linear elastic constitutive models for all the involved layers. Therefore the elastic stiffness has to be considered as a pseudo elastic properties.

The back-calculated base and subgrade parameters are the same as those from inverse analysis of Tab. 22.
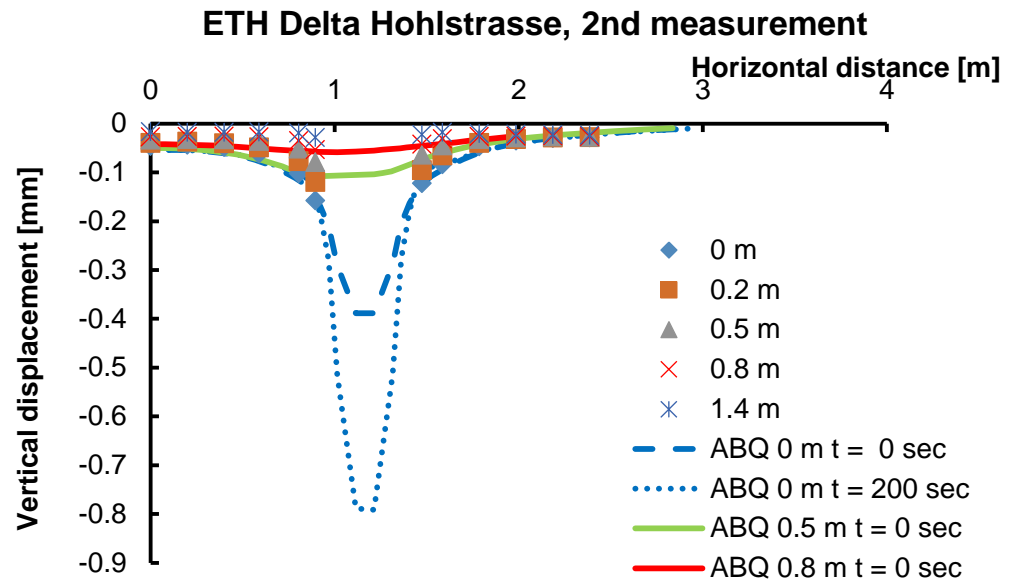
ETH Delta Hohlstrasse, 2nd measurement

Fig. 155 Measured (dots) and calculated (lines) deflections of the road surface

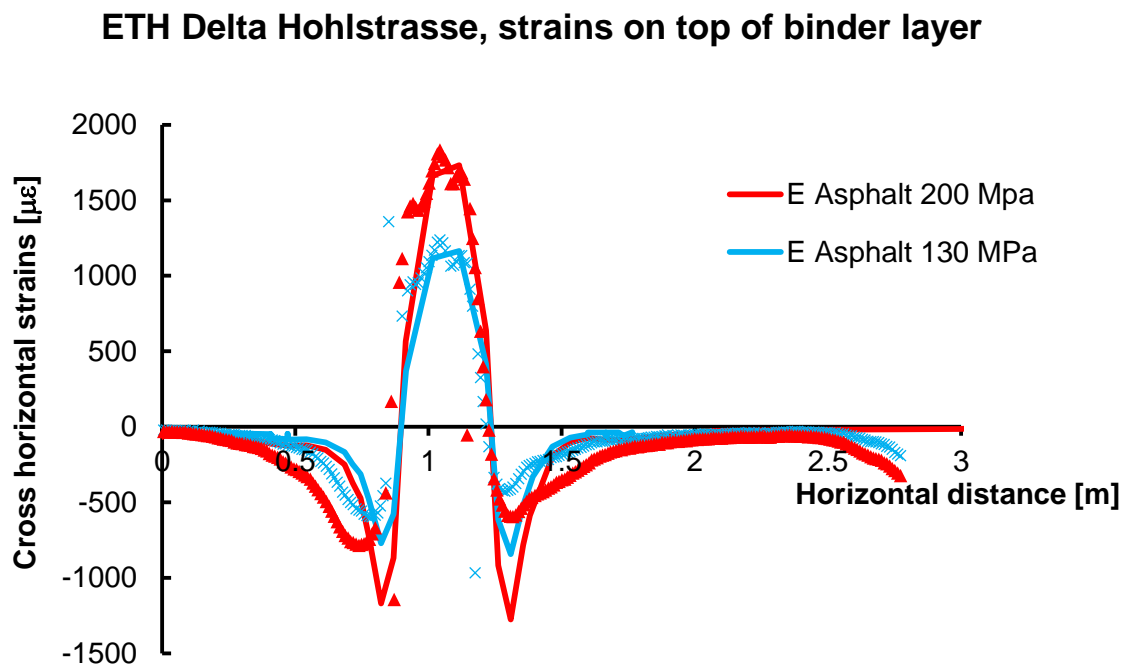**ETH Delta Hohlstrasse, strains on top of binder layer**

Fig. 156 Calculated strains at the top of the binder layer for short and long term asphalt stiffness

7.3 Conclusions

The subgrade properties are back-calculated with the help of a finite element model and the spatial settlement measurement acquired with the ETH Delta device. It is shown that the settlement distribution measured with the ETH Delta, unlike the strain measurement with the fiber optic cables, is not sensitive to the viscoelastic properties of the asphalt concrete.

8 Modelling of the tests in Hohlstrasse Zurich

Abstract

The current chapter presents the finite element simulation of the tests in Hohlstrasse Zurich. Initially, the utilized finite element models are described and the assumptions concerning the application of the tire contact pressure for the modelling of the static and dynamic field tests are elucidated. The material models used in this analysis both for the asphalt concrete and the subgrade as well as the procedure for their calibration are subsequently described, and the stress and strain fields computed with the calibrated models are shown. Finally, the results of the numerical simulations of the static and dynamic tests are presented and compared with the results of the field tests.

8.1 Finite element models

8.1.1 Model structure

As already described in chapter 5.1.2, "static" and "dynamic" loading tests were performed in different temperatures at Hohlstrasse Zurich, with the help of different types of vehicles. In order to gain a better insight into the behavior of the asphalt concrete during the aforementioned experiments, a finite element analysis of the boundary value problem has been conducted.

Axisymmetric model

As a first step for the modelling of the field test, a parametrical analysis has been performed with the help of a simplified axisymmetric finite element model. The scope of this analysis was to identify the influence of the different parameters on the induced strains.

For this investigation, only the tests conducted with the front axle have been simulated, as a simulation of twin tires cannot be modelled in the axisymmetric model. For the sake of consistency, only the field experiments performed with truck 1 were considered.

The three asphalt courses were individually modelled on the top of the base course and the subgrade, which have been modelled as a sole homogeneous layer. The nominal thickness of the asphalt layers has been used (see also Chapter 5):

- Wearing course: 4cm
- Binder course: 9cm
- Asphalt Base Course: 9cm
- Base Course & Subgrade: 1.78m

Between the individual asphalt layers, as well as between the asphalt and the subgrade, the existence of an interface has been investigated. The wearing course has further been divided into four sublayers (fully bonded one to another), to account for different elastic moduli within the layer as a result of a large temperature gradient close to the surface for some test series.

An equivalent circular area for the footprint shown in chapter 5.1.6 was calculated for this model. The assembly and the discretization of this model are illustrated in the following figure. To obtain results of high quality, finite elements of a minimum size of 1cm x 1cm (at least 4 elements along the vertical direction for the wearing course) have been implemented close to the loading area. A total of 7480 axisymmetric quadratic elements of full integration (CAX8) have been used in the whole model.
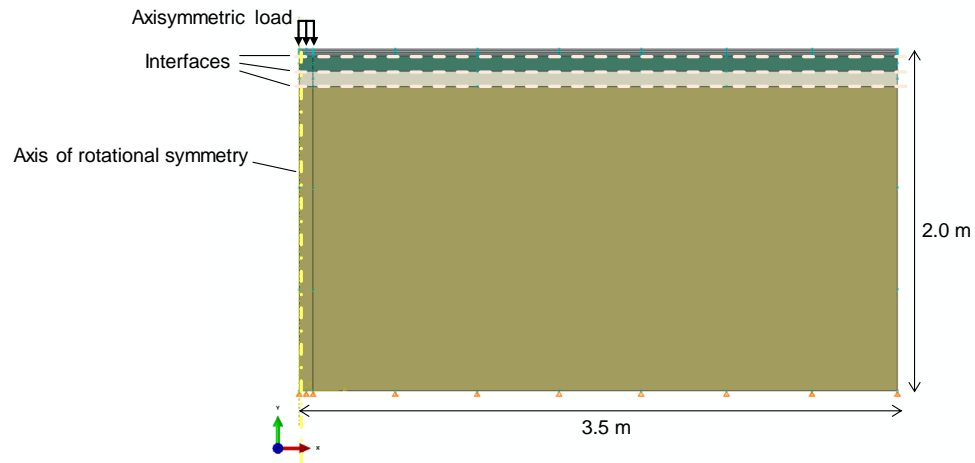
Fig. 157 *Axisymmetric finite element model assembly*

Three-dimensional model

For the final simulation of both the static and dynamic tests, a three dimensional finite element model has been used, the dimensions and assembly of which are shown in Fig. 158. The asphalt concrete layers have been modelled individually and with the thicknesses given for the axisymmetric model.

The optimal parameters for its test obtained with the help of the axisymmetric model have been implemented in this model. An interface has been utilized between the base course and the subgrade. The implemented material models and the parameters which were used are summarized in sections 8.2.1 and 8.3.

In order to reduce the computational cost, the longitudinal (in the driving direction) symmetry plane has been taken into account and only the half boundary value problem has been modelled. On the symmetry plane, the symmetry boundary conditions were imposed ($U_Y = U_{RZ} = U_{RZ} = 0$, where U the respective displacement). The boundary conditions at the rest boundaries are the following:

- Bottom boundary: $U_X = U_Y = U_Z = 0$
- Vertical boundary along the longitudinal direction: $U_Y = 0$
- Vertical boundary transverse to the longitudinal direction: $U_X = 0$

The vertical boundaries were placed in an adequate distance from the loading area, to avoid erroneous symmetry effects caused by the restrained deformations on the boundaries.

The advantage of the axisymmetric finite element model to the three-dimensional one is clearly shown in Fig. 159, where the discretization of the latter one is depicted. Indeed, this model comprises of 113482 quadratic elements. To assure satisfying precision, at least two elements were modelled along the vertical direction within a single layer, resulting into a minimum element size of 2cm x 4cm in the loading area. In order to place the model boundaries in an adequate distance and simultaneously retain a reasonable number of elements, the model was accomplished of three sub-models (Fig. 159) with different meshes which were eventually tied together into one model.

For the asphalt concrete layers, fully integrated quadratic elements have been implemented, in order to minimize potential shear locking and hour-glassing effects. For the subgrade, quadratic elements of reduced integration have been used.
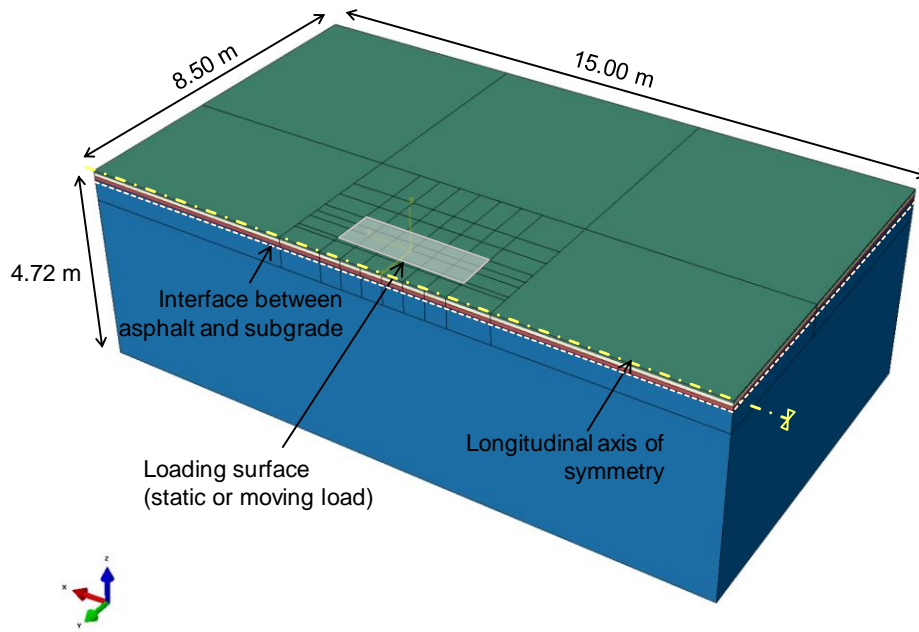
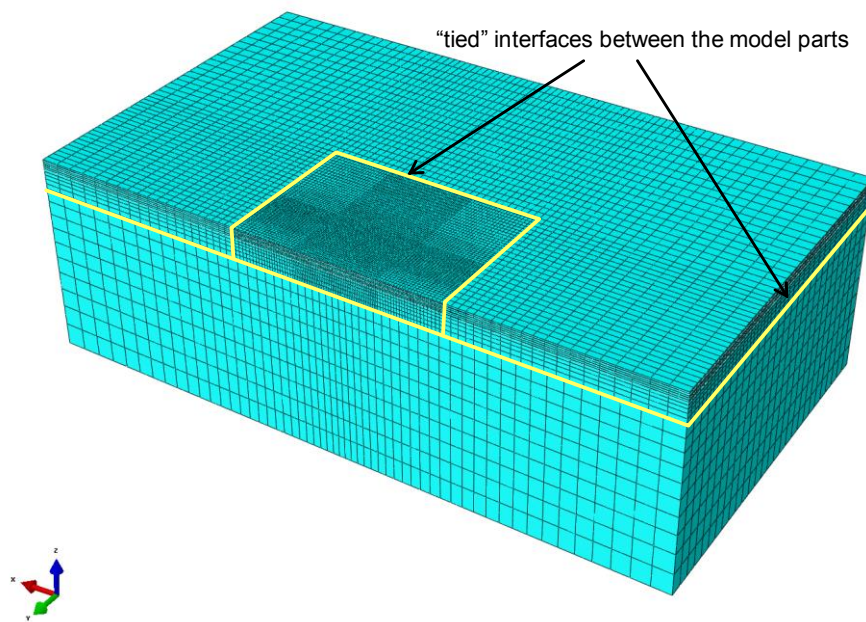**Fig. 158** *Finite element model assembly*

Fig. 159 *Finite element model discretization*

8.1.2   Static Loading

Contact pressure

The contact pressure has been modelled as surface pressure in Abaqus finite element code, applied on an area equal to the footprint shown in Fig. 55, chapter 5.1.6. For the static tests, the load of the front and for the rear axles has been used, in accordance with the field experiment described in chapter 5.1.6.

Initially, a short literature review about the possible configurations of surface pressure was conducted. According to experimental results of Yap [46] the vertical contact pressure between the tire and the pavement might follow various distributions, dependent on tire inflation pressure, tire load as well as the tire specifications. The average contact pressure and the inflation pressure of the tire have been shown to have a similar value, whereas the maximum contact pressure could substantially exceed these values. The investigation of the contact pressure distribution for different tires under various loading conditions and inflation pressures has thoroughly been measured by De Beer et al [51].

Yue and Svec [52] have conducted a parametrical study with a multilayer program, showing that tensile strains due to measured contact stress distribution might exceed the induced strains under the conventional assumption of constant contact distribution equal to the inflation pressure of the tire close to the surface. They observed further that for deeper layers, the contact pressure distribution is not important. For the static tire load, an inward traction between the tire and the pavement has been reported by Tielking et al. [53] and Hansen et al. [54].

The tire pavement interaction by means of sophisticated numerical modelling has been investigated by Wang et al. [55] in detail. This study has also shown that higher inflation pressures lead to a convex stress distribution and high loads lead to an approximately constant one. The inward traction for the static load in the transverse direction has been shown to change direction at each rib of the tire.

In the current study, truck 1 has an inflation pressure of 8.5bar and an approximate load per tire of about 2.5t for the front and rear axles. Therefore, the contact stress distribution is expected to be typical of tires with low axle load and high inflation pressure, hence convex. In the preliminary parametrical analysis, both the constant and convex vertical surface pressure distributions, as well as the influence of surface traction, were investigated. The investigated loading configurations for the axisymmetric model are illustrated in Fig. 160.
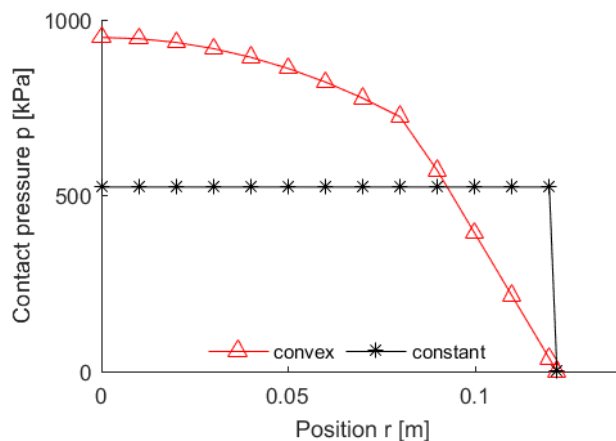

Fig. 160 *Surface pressure distributions investigated in the current analyses for the axisymmetric model*

Loading steps

Three loading steps have been modelled:

1. Gravity loading (geostatic field)
2. Loading for $\Delta t = 15s$
3. Unloading for $\Delta t = 15s$

The same loading duration of $\Delta t = 15s$ has been chosen for all the tests, as representative duration for one measurement (10s to 15s, chapter 5). The unloading has also been evaluated after the same duration. Some deviation from this time is in reality

plausible, and they might cause deviation between the model and the experimental results.

8.1.3 "Moving" Load

The dynamic tests have been simulated with the help of a "moving" load. No full dynamic analysis has been conducted, i.e. the inertia forces caused by the moving vehicles as well as the subsequent propagation of waves have been neglected.

On the other hand, the velocity dependent viscous behavior of the asphalt has successfully been modelled. The moving load was modelled with the help of the Abaqus subroutine DLOAD With the help of the sub-routine, the position of the tire pressure is updated at each time increment according to the given velocity. The motion of the vehicle is hence simulated with a sequence of discrete load positions with the time.

The material model used to describe the viscous behavior of the asphalt concrete and its calibration is discussed in the following paragraphs. The chosen time increment however also affects the response of the viscoelastic material and a good calibrated finite element model will give erroneous results, if a too large time increment, which leads to a too large position change, is chosen. In order to obtain accurate results, a time increment which corresponds to a position change of less than the 1/3 of the tire footprint length in the driving direction was chosen. Moreover, the position change of the load has been chosen the same in all the conducted analyses regardless of the velocity, with the use of the appropriate time increment.

The dynamic field tests of truck 1 have been simulated. The distances between the axles are according to chapter 5. The axle loads for truck 1 used in the simulations are summarized in the following table. It should be noted that only the front and rear axles, as well as the whole truck have been weighed. The axles II, III and IV are merely rough estimations. The contact pressure distribution has been considered constant for all moving load analyses.

Tab. 24 Loads per axle (Truck 1), No. I & No. V measured, II to IV estimated in accordance with the total mass

Axle	No. I	No. II	No. III	No. IV	No. V
Load	50kN	70kN	70kN	100kN	100kN

Neither accelerating nor braking forces have been considered in this analysis, although in the field experiment such forces cannot be fully eliminated. The friction under the rolling tires has also been neglected. Therefore in the following, only the strains across the moving axis, which are the least affected by such forces, have been evaluated.

8.2 Material models

8.2.1 Asphalt concrete

According to comprehensive research of Lytton et al. [56] on pavement materials, the behavior of asphalt concrete is reported to show viscoplastic behavior for high temperatures and viscoelastic for lower temperatures. The plasticity parameters governing its behavior are reported similar with soil properties and include cohesion, peak friction angle and friction angle at constant volume. Power-law constitutive models are used to describe the plastic, elastic and viscoelastic components according to this work. The Poisson ratio is reported to be stress dependent, and for high stress levels the behavior of the asphalt concrete is dilatant. Kim and Little [57] proposed that three different mechanisms are responsible for the behavior of asphalt concrete: fatigue which has as result the damage increase with the repetition of loads on the one hand and relaxation due to the asphalt concrete viscoelasticity and chemical healing of the micro-cracks on the other hand for periods when no loading occurs. A constitutive model based on the nonlinear viscoelasticity developed by Schapery [58] is proposed for the asphalt concrete, to consider the dependence of the asphalt concrete on the stress history. Kim et al. [59] have proposed a viscoelastic behavior with rate dependent damage evolution.

In the following preliminary analysis with finite element models, the asphalt concrete has been simulated in a first simple approximation as a merely viscoelastic material. No plasticity and no stress history have been considered.

Laboratory testing

In order to determine the properties of the asphalt concrete at the Hohlstrasse, fatigue and stiffness modulus tests were conducted by EMPA on cores drilled from the site [60]. Initially, the individual layers of asphalt concrete were measured in the samples and the results are summarized in Fig. 161 and Tab. 25. It can be seen that although the average measured thickness of the three courses is in good agreement with the nominal one, the standard deviation is quite high. The thickness of the courses substantially varies from specimen to specimen, sometimes in very close distances. These irregularities in the asphalt concrete layer thicknesses were not investigated with the finite element models discussed in this chapter. As the properties of the three different types of asphalt concrete used in the tested site do not differ considerably, the results of the analysis are not expected to be significantly affected.
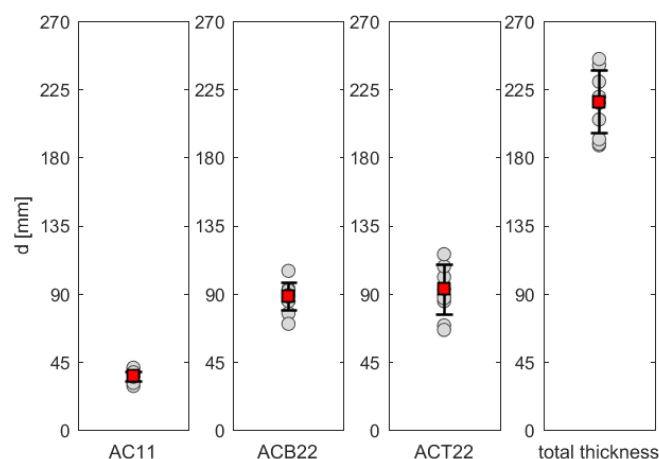

Fig. 161 *Asphalt concrete layer thicknesses according to EMPA technical report [60]*

The stiffness modulus of the binder and base course was determined with the help of force-controlled indirect tension tests on cylindrical species with diameter d = 150mm under harmonic sinus loading. The maximum induced horizontal strains have been limited between 500 and 1000$\mu\epsilon$. The stiffness moduli have been determined in temperatures varying from -5 to 25°C and for the frequencies 0.1, 1 and 10Hz. For each temperature and frequency, four specimens have been tested. The average and standard deviation of the resulted values are shown in the following figures and tables.

***Tab. 25** Asphalt concrete layer thickness according to EMPA technical report [60]*

|	**AC11**	**ACB22**	**ACT22**	**Thickness**
Average	35.5mm	88.5mm	93.0mm	216.9mm
Standard Deviation	3.2mm	9.0mm	16.6mm	20.7mm
Nominal	40.0mm	90.0mm	90.0mm	220.0mm
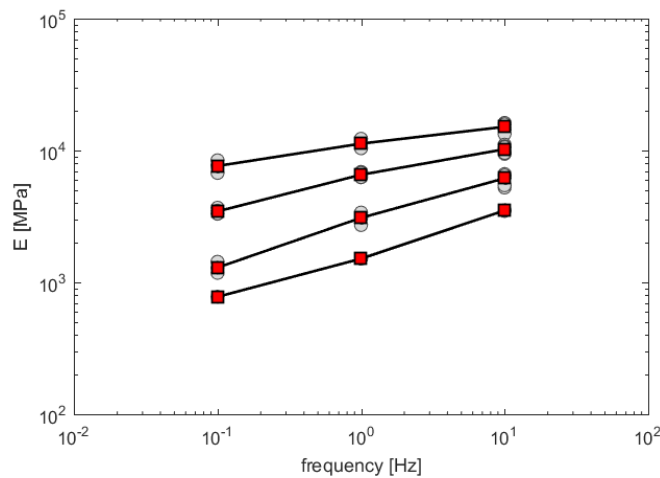
***Fig. 162** Asphalt concrete properties (binder course) according to EMPA technical report [60]*

***Tab. 26** Stiffness of ACB22 according to EMPA laboratory report [60]*

f = 10Hz	**T = -5°C**	**T = 5°C**	**T = 15°C**	**T = 25°C**
Average	15'131MPa	10'227MPa	6'152MPa	3'506MPa
Standard Deviation	1'002MPa	595MPa	521MPa	35MPa [1]
CV	0.07	0.06	0.08	_[1]
f = 1Hz	**T = -5°C**	**T = 5°C**	**T = 15°C**	**T = 25°C**
Average	11'275MPa	6'549MPa	3'088MPa	1'513MPa
Standard Deviation	759MPa	313MPa	275MPa	_[1]
CV	0.07	0.05	0.09	_[1]
f = 0.1Hz	**T = -5°C**	**T = 5°C**	**T = 15°C**	**T = 25°C**
Average	7'636MPa	3'455MPa	1'295MPa	777MPa
Standard Deviation	680MPa	170MPa	103MPa	_[1]
CV	0.09	0.05	0.08	_[1]

The mean and standard deviation values, as well as the coefficients of variation are summarized for the ACB22 layer in Tab. 26 and for the ACT22 layer in Tab. 27. It is

---

[1] For this test only one specimen (tested twice for the f = 10Hz) has been successfully tested.

observed that similar mean values are obtained for both layers, with the stiffness values of the ACT22 layer tending to be slightly higher. The results for the binder course show a higher quality, having very low coefficients of variation CV < 0.1. On the contrary, the coefficients of variation for the ACT layer are quite higher, varying between 0.15 and 0.71. The deviation of the results tends to increase for increasing temperatures and falling frequencies.

It has to be noted that for the samples tested in temperature T = 25°C, three failed for the binder course. For the bearing course, one specimen failed, but the coefficient of variation for the remaining three specimens lies between 0.34 for f = 10Hz and 0.71 f = 0.1Hz. The stiffness for this temperature is hence anticipated to deviate from the mean values obtained in these tests.
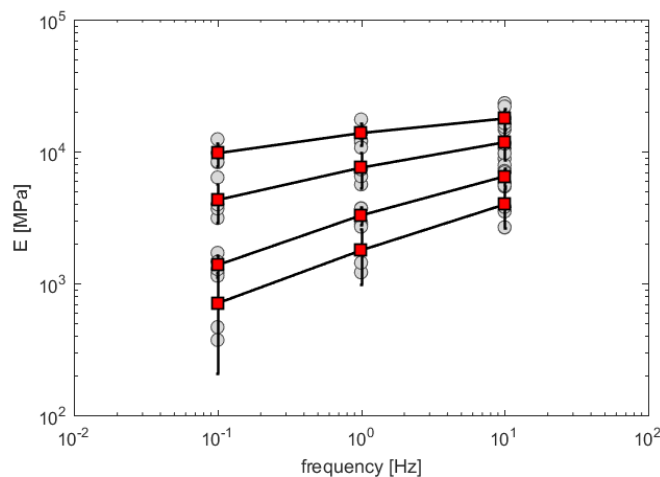
Fig. 163 *Asphalt concrete properties (base course) according to EMPA technical report [60]*

Tab. 27 *Stiffness of ACT22 according to EMPA laboratory report [60]*				
f = 10Hz	**T = -5°C**	**T = 5°C**	**T = 15°C**	**T = 25°C**
Average	17'783MPa	11'740MPa	6'476MPa	3'976MPa*
Standard Deviation	3'208MPa	3'093MPa	961MPa	1'338MPa[2]
CV	0.18	0.26	0.15	0.34[2]
f = 1Hz	**T = -5°C**	**T = 5°C**	**T = 15°C**	**T = 25°C**
Average	13'796MPa	7'543MPa	3'278MPa	1'780MPa
Standard Deviation	2'690MPa	2'233MPa	496MPa	798MPa[2]
CV	0.19	0.30	0.15	0.45[2]
f = 0.1Hz	**T = -5°C**	**T = 5°C**	**T = 15°C**	**T = 25°C**
Average	9'707MPa	4'290MPa	1'376MPa	706MPa
Standard Deviation	1'918MPa	1'422MPa	258MPa	499MPa[2]
CV	0.20	0.33	0.19	0.71[2]

---

[2] For this test only three specimen (tested twice for the f = 10Hz) have been successfully tested.

Abaqus time domain viscoelasticity

The behavior of all three asphalt concrete layers has been modelled with the time domain viscoelasticity material model embedded in Abaqus in combination with linear elasticity. The time domain viscoelasticity model in Abaqus is numerically implemented with the help of the Prony series expansion.

In order to describe the material, the long-term Young modulus and the Poisson ratio need to be defined. Then for each Prony series component, the relaxation time with the corresponding dimensionless shear and volumetric relaxation moduli are given. In Abaqus, the number of the Prony series components is unlimited. The volumetric and shear relaxation moduli can be independently defined.

The model is not able to describe the viscoplastic behavior of the asphalt concrete observed in high temperatures, and the subsequent accumulation of damage leading to fatigue. Moreover, no anisotropy is considered.

For the specific model, a Prony series with 8 components has been used for the static tests. For the "dynamic" tests, the behavior of the asphalt concrete for short relaxation times has to be determined in more detail. As a result, the viscoelastic behavior of the asphalt concrete is described by a Prony series consisting of 22 components. The Prony series coefficients for both cases are summarized in Tab. 28. The same coefficients have been used for the modelling of all test series regardless the temperature at which they were performed, implying thus the assumption of a temperature independent viscosity.

Tab. 28 *Prony series coefficients used in the Abaqus model*

Static tests			"Dynamic" tests		
g_i	k_i	τ	g_i	k_i	τ
[-]	[-]	[s]	[-]	[-]	[s]
0.2	0.2	5	0.01	0.01	0.005
0.15	0.15	10	0.01	0.01	0.01
0.1	0.1	15	0.05	0.05	0.02
0.1	0.1	20	0.093	0.093	0.03
0.05	0.05	30	0.14	0.14	0.04
0.03	0.03	50	0.14	0.14	0.05
0.04	0.04	75	0.14	0.14	0.08
0.02	0.02	160	0.13	0.13	0.1
			0.03	0.03	0.2
			0.012903	0.012903	0.25
			0.018065	0.018065	0.4
			0.023226	0.023226	0.8
			0.010323	0.010323	1.25
			0.012903	0.012903	2.5
			0.012903	0.012903	5
			0.012903	0.012903	10
			0.012903	0.012903	15
			0.025806	0.025806	20
			0.012903	0.012903	30
			0.007742	0.007742	50
			0.010323	0.010323	75
			0.005161	0.005161	160

In order to illustrate the viscoelastic behavior of the chosen models, one-element tests for both models were conducted in Abaqus. The model used for the one-element test is shown in Fig. 164 and consists of one eighth of a cubic specimen (3 planes of symmetry)

under uniaxial compression. Initially, a constant distributed pressure of 900kPa is applied for 200s and in a second, relaxation step the load is removed for additional 200s. The long-term elastic modulus used is 65MPa, corresponding to a temperature of approximately 35°C, as it was recorded during the EBI-Bloc test (test series 7) described in the next section. The stress and strain histories for the one element tests of the models used both in the static and "dynamic" tests are shown in Fig. 165 and Fig. 166.
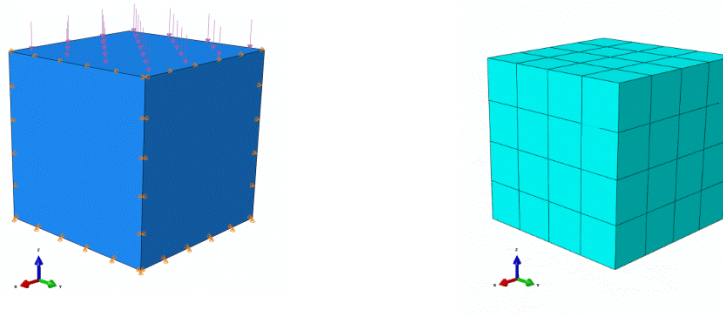

Fig. 164 *Finite element model for the one-element test*
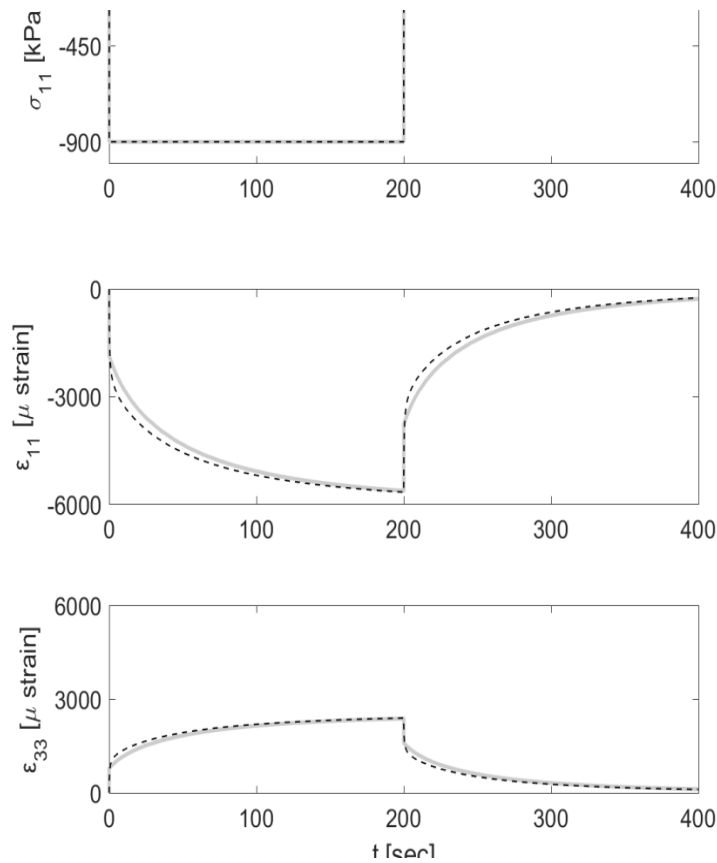
Fig. 165 *Strain evolution with the time under constant stress (one element test)*

8.2.2 Subgrade

For the reversible behavior of the subgrade, the following different constitutive models have been investigated:

1. Linear elasticity
2. Porous elasticity

The latter allows the modelling of the stress dependency of the subgrade stiffness. Although the modelling of the stiffness stress dependency might lead to more accurate results, the porous elastic model in Abaqus cannot be combined with viscoelastic behavior. Therefore, in combination with a porous elastic subgrade, the asphalt concrete has been modelled as a linear elastic material with a Young modulus suitable for the respective loading time.

Moreover, the effect of a possible irreversible behavior of the subgrade, particularly under high temperatures, has been investigated. For this case, Drucker Prager plasticity with non-associative flow rule has been used.
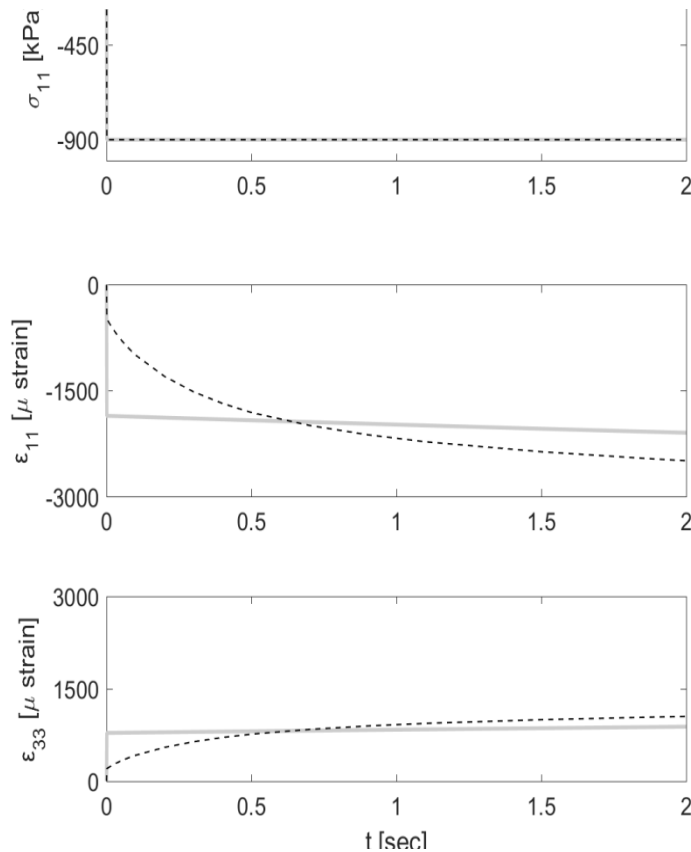
Fig. 166 *Detail of the strain evolution with the time under constant stress for short relaxation times (one element test)*

8.3   Calibration of material model

8.3.1   The concrete block test (Test series 7)

The viscoelastic parameters for the asphalt concrete have been calibrated in a first step with the help of the concrete block test. As already described in chapter 5.1.8, one EBI-Block has been placed on a wooden circular base with radius r = 0.15m and then on a thin sand layer on the top of the asphalt concrete. After approximately 150s, a second block has been placed in a distance of 2.0m to the first one, above the same transverse cable. After another 120s the second block was again removed and after a total time period of approximately 400s, the first block was removed too. The above described field test (K3) was modelled with the help of a simplified axisymmetric finite element model, in which only one concrete-block has been modelled. The viscous parameters of the Prony series were subsequently calibrated against the maximum values measured in the field test at different time instants. In order to neglect the influence of the loading due to the second block, the strains measured in the longitudinal direction have been considered.

This test was performed during the night after a hot summer day. The temperature in the pavement varied between 28°C at the surface and 35°C deeper. The calibration of the model for the measured strains under the concrete block gave as long-term elastic properties of asphalt concrete E = 65MPa and ν = 0.45. These properties are insofar in accordance with the results obtained from the EMPA laboratory report [60], taking into account that that the temperature is up to 10°C higher than at the laboratory testing, that no long-term modulus has been determined in the lab, and the great variance of the asphalt concrete stiffness already for T = 25°C.

In the following figure, the measured maximum expansive strains due to the concrete block loading are plotted against the maximum extensive strains from the finite element model.
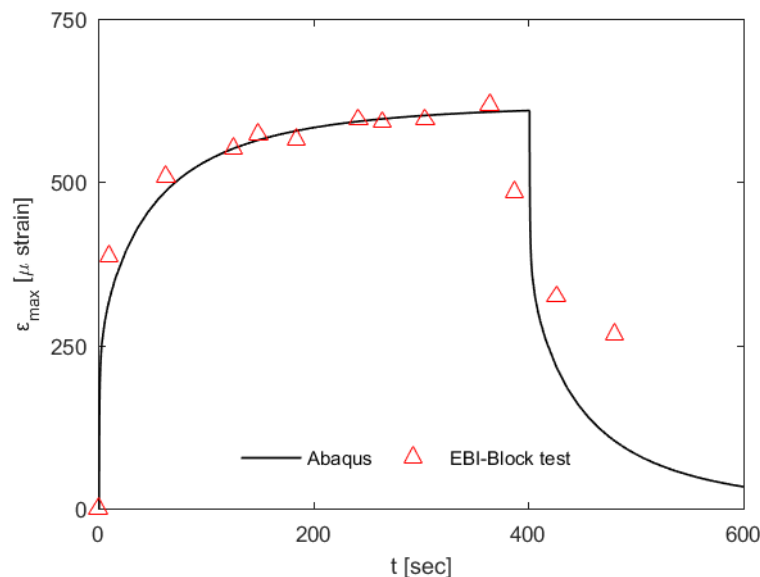
Fig. 167 *Validation of material model with the concrete block test (Prony series parameters for the "dynamic" test). Hint: μstrain = με = 10⁻⁶*

In the above figure, it can be seen that with the help of this test a good estimation of the evolution of the relaxation moduli/creep compliance for loading/relaxation times from 30s to 380s can be made. The test does not give any information about short relaxation times and the estimation of instantaneous elastic modulus. The finer calibration for short relaxation times has been verified with the help of the dynamic field tests. It is also evident, that this model cannot reproduce the non-reversible compliance measured. This

behavior is typical for asphalts in high temperatures, but cannot be reproduced by viscoelastic models like the Prony series used in the current analysis.

8.3.2   Parametrical investigation

Initially, a parametrical investigation was performed for the tests 5, 6, 8, 9 and 10. Scope of this analysis has been to examine the influence of the different parameters on the results and then determine the parameters with which the model optimally reproduces the measured strains.

For the test series 5, which was conducted in a temperature of 40°C, the different parameters examined are summarized in Tab. 29 and the results of the parametrical investigation are presented in Fig. 168 to Fig. 183. The same coefficients of the Prony series, which were determined according to the previous section, were used in all models, unless it is otherwise stated.

Tab. 29 Investigated parameters, summer (test series 5)

Contact pressure	Vertical		Constant	Convex	
	Traction		No	Inwards	Outwards
Subgrade					
Elastic Behavior	Linear elastic	E [MPa]	200	420	
		ν [-]	0.15	0.2	0.3
	Porous elastic[3]	κ [-]	10^{-2}	10^{-5}	10^{-7}
Failure Behavior	No plasticity	-			
	Drucker Prager	c [kPa]	0.1		
		φ [°]	35		
		ψ [°]	5		
Asphalt	Prony Series[4]	$E_{Longterm}$ [MPa]	50	100	200
Interface	Subgrade – Base course		Full bonding	$\mu = 0.8$	$\mu = 0.0$
	Between asphalt layers		Full bonding	$\mu = 0.8$	
Temperature gradient[5]			No	Yes	

In Fig. 168, the strains due to the two different contact pressure distributions described in section 8.1.2 are compared. It can be observed that the constant contact distribution creates a distribution of strains which does not resemble the measured results. Two peaks, symmetrical to the tire center are observed rather than a single, smooth peak. Moreover, the expansive strains measured in the field test prevail in a much wider region than these from the model, and the strain gradient according to the experimental results is much milder. Finally, the ratio of maximum absolute expansive to contractive strain is much larger for the experimental results.

The convex contact pressure distribution on the other hand induces a smoother strain distribution. It is noticed that although the total load of the tire is the same for both distributions, the peak expansive strain significantly increases for the convex contact pressure distribution, whereas the absolute increase in the contractive strain is only marginal. The results are hence improved in terms of the ratio of maximum absolute expansive to contractive strains. However, the strain gradient appears to be even steeper

---

[3] This material model cannot be modelled in a viscoelastic analysis. For analyses, at which the subgrade was modelled as porous elastic, the asphalt concrete was modelled as linear elastic.

[4] The material model is described in detail in chapter 8.2.

[5] The temperature gradient has been indirectly taken into account by a variation of the long-term Young modulus within the different asphalt layers.

than for the constant contact pressure distribution, thus not leading to a satisfying fit match.

Apart from the contact pressure distribution, the effect of traction between the tire and the binder course is investigated. Traction of constant magnitude of 35% of the inflation pressure has been induced. In figure Fig. 169 the results of traction both in the outward and the inward direction in combination with the convex contact distribution are shown. It is shown that the outward traction induces a greater maximum expansive strain with two symmetrical peaks, whereas the inward traction causes a slight decrease and only one spiky peak. The ratio of maximum expansive to maximum absolute contractive strain increases for the outward and decreases for the inward traction. Finally, the strain gradient remains the same for both traction types. The comparison of traction in the outward direction in combination with the constant and the convex contact pressure distribution is shown in Fig. 170.
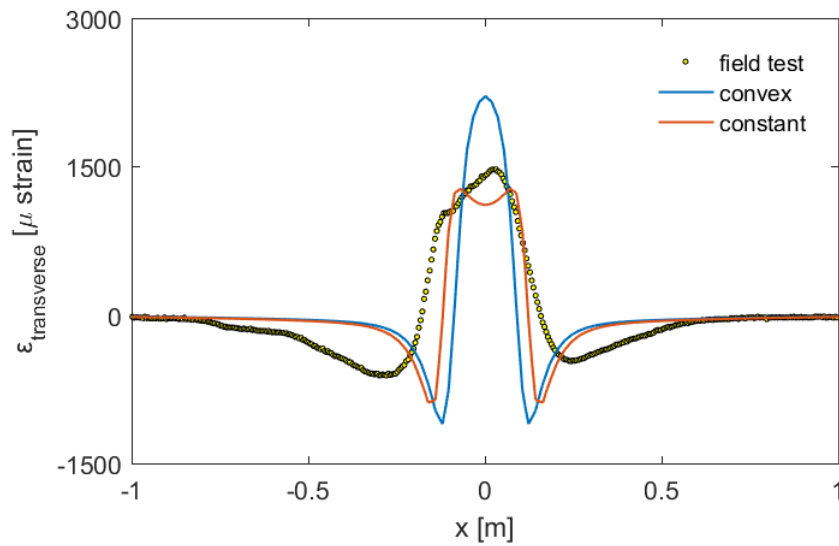
Fig. 168 *Comparison of the strains measured in summer under static loading with the strains according to the finite element model for convex and constant contact pressure distribution*

In Fig. 171, the effect of different volumetric and deviatoric viscous behavior is shown. Two extreme cases are examined; viscous volumetric behavior with purely elastic deviatoric behavior, and viscous deviatoric behavior with purely elastic volumetric behavior. As is seen in Fig. 171, the purely elastic deviatoric behavior in combination with the viscous volumetric behavior leads to a huge increase of strains, whereas the opposite case induces a slight decrease. This implies a prevailing deviatoric stress state of the asphalt concrete. However, the region where the asphalt concrete is under expansion is the same for all cases, and much narrower than the measured one, leading to the conclusion that a further variation of these parameters will not lead to the desirable strain distribution.
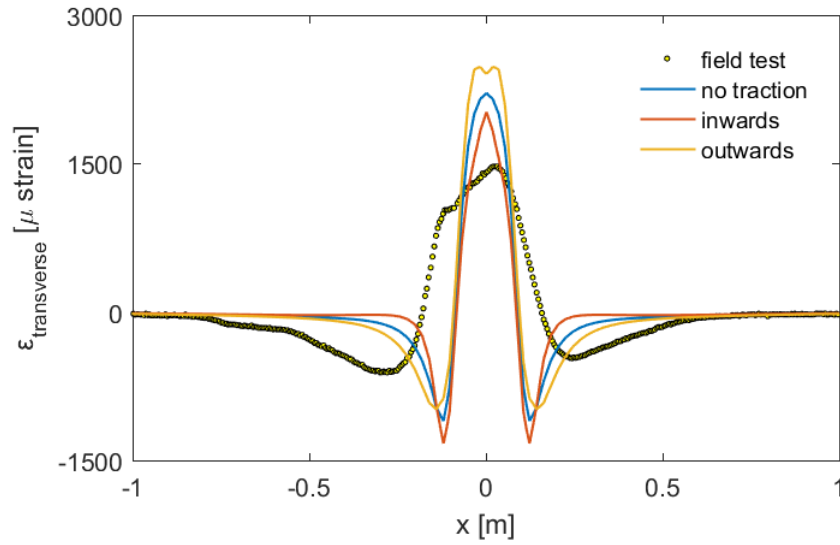
***Fig. 169** Comparison of the strains measured in summer under static loading with the strains according to the finite element model under different assumptions for the traction of the tire*
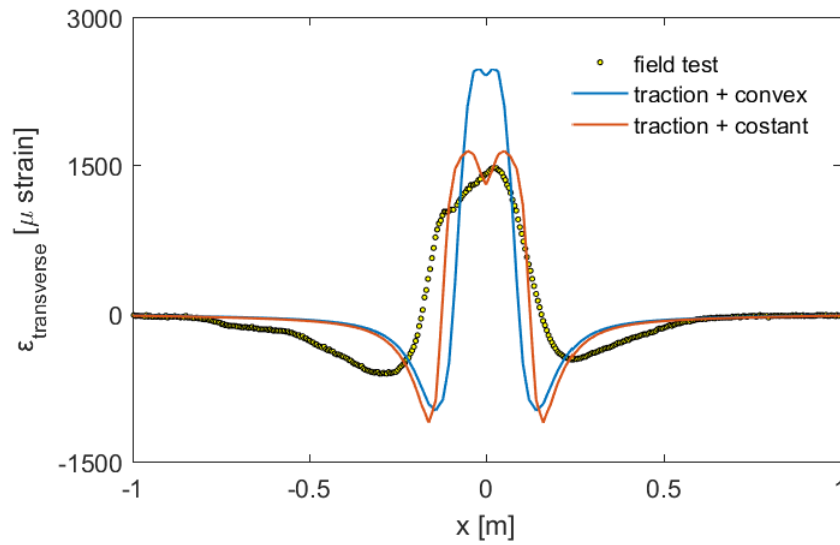

***Fig. 170** Comparison of the strains measured in summer under static loading with the strains according to the finite element model for convex and constant contact pressure distribution in combination with outward traction*
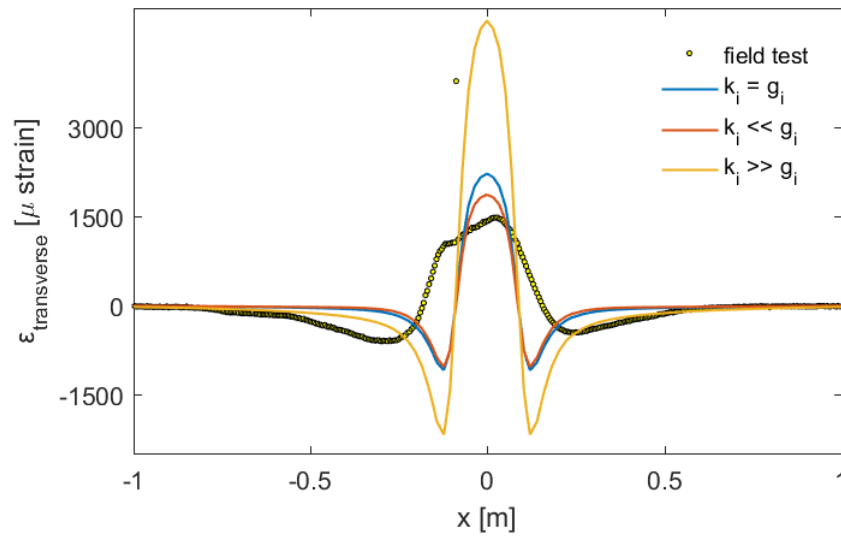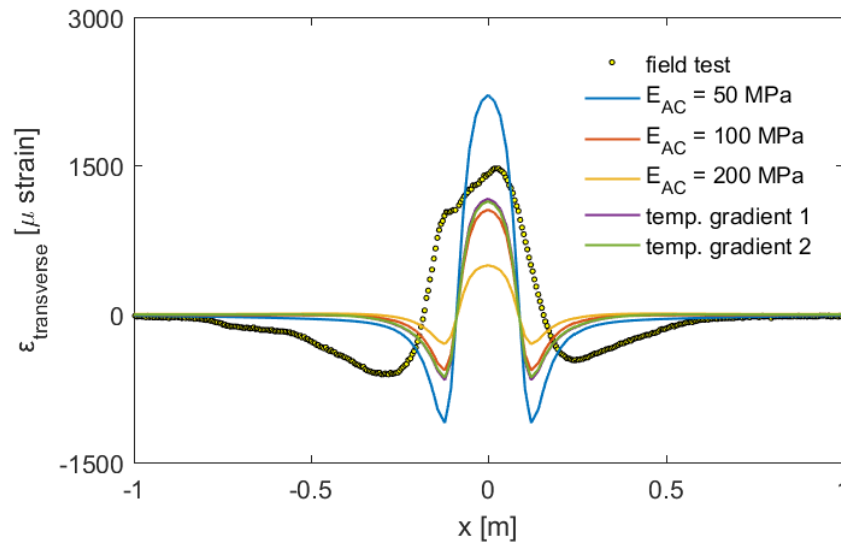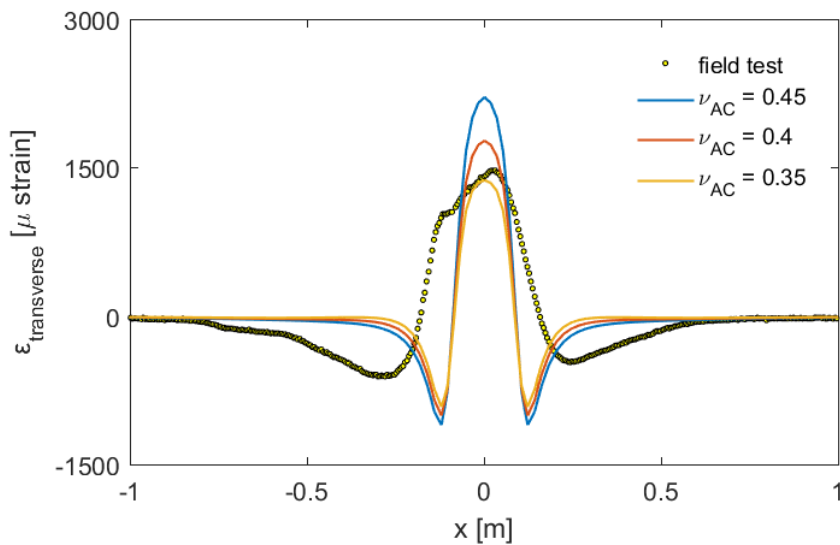
Fig. 171 *Comparison of the strains measured in summer under static loading with the strains according to the finite element model for different volumetric and deviatoric Prony coefficients*

In Fig. 172, the results for three different long-term moduli of asphalt concrete are shown. The stiffness of asphalt for these cases is kept constant for all the three layers, implying a constant temperature throughout the whole binder course. Additionally, the effect of temperature gradient through the binder course has been roughly investigated, by varying the elastic modulus among the different asphalt concrete courses. The two different stiffness distributions which have been examined are shown in Fig. 173. As expected, the strains are scaled down with an increasing stiffness modulus. The ratio of expansive to contractive peak strain as well as the location of strain change from contraction to expansion is not influenced. The variation of the AC moduli for the different binder courses, also led to similar results.
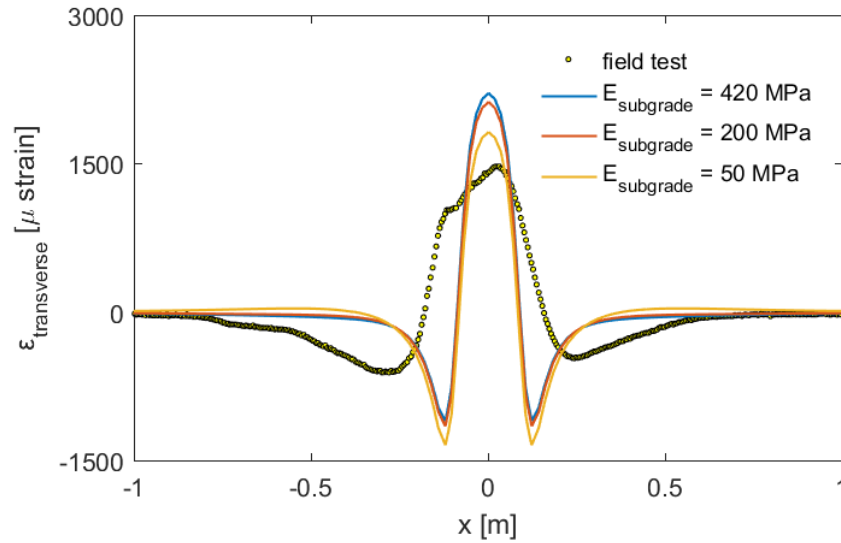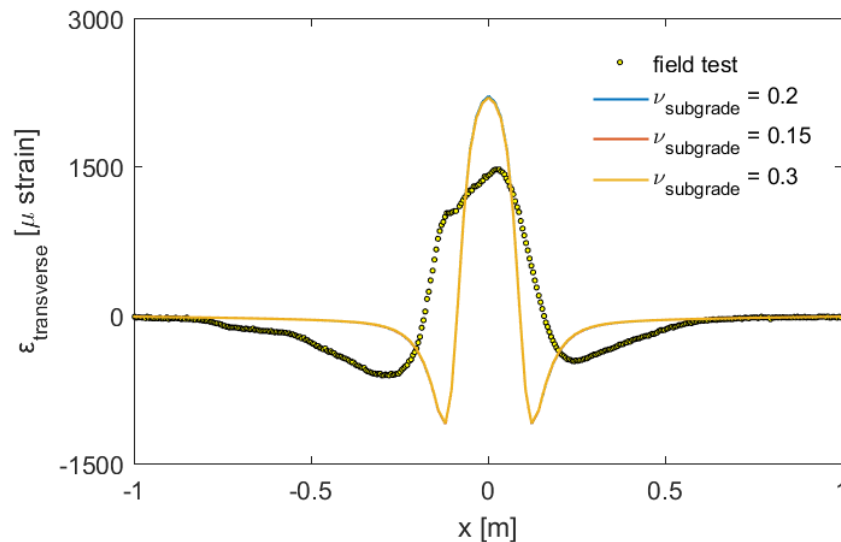

Fig. 172 *Comparison of the strains measured in summer under static loading with the strains according to the finite element model for different long-term elasticity moduli gradients of asphalt concrete*
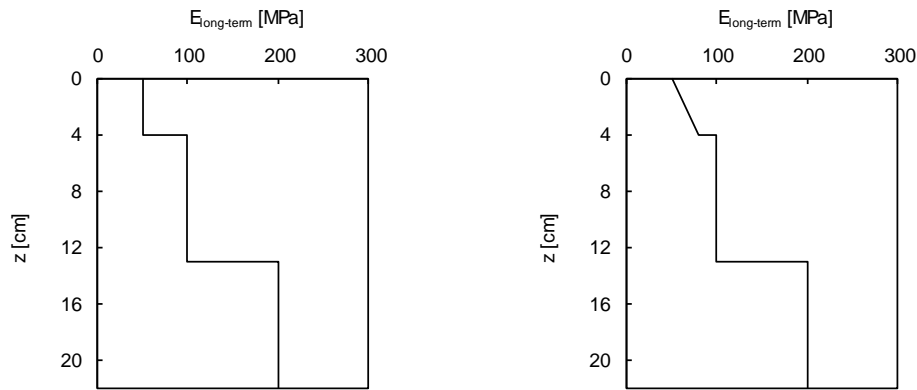
Fig. 173 *Stiffness distribution in function with the depth for temperature gradient 1 (left) and temperature gradient 2 (right)*

On the other hand, the reduction of Poisson ratio, shown in Fig. 174, leads to a significant decrease only for the expansive strains. The contractive strains are only slightly reduced. The location of the sign change of the strains remains the same.

The variation of the subgrade stiffness does not considerably affect the induced strains. The reduction of one order of magnitude of the stiffness causes just about 20% reduction of the peak expansive strain, as well as some small increase of the absolute peak contractive strain. The Poisson ratio of the subgrade is shown not to be affecting the strain distribution at 4cm depth at all.
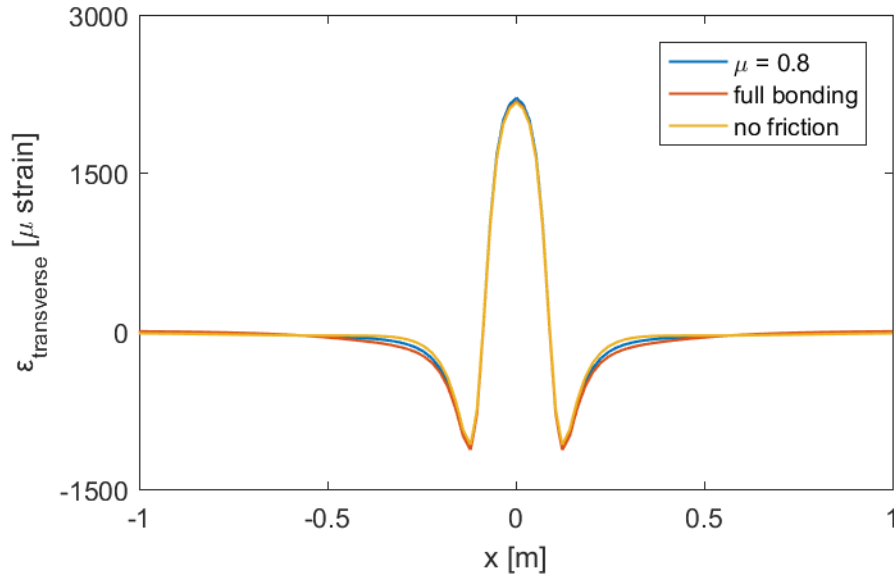

Fig. 174 *Comparison of the strains measured in summer under static loading with the strains according to the finite element model for different Poisson ratios of the asphalt concrete*

Fig. 175 *Comparison of the strains measured in summer under static loading with the strains according to the finite element model for different values of subgrade stiffness*

Both the existence of interfaces between the different binder courses, as well as between the binder and the subgrade are investigated. The strain distribution at 4cm depth is shown to be practically independent of the interface type between the subgrade and the base course. The interface between the different asphalt concrete layers on the other hand influences the results.

Fig. 176 *Comparison of the strains measured in summer under static loading with the strains according to the finite element model for different Poisson ratios of the subgrade*

For the case which friction between the different layers is assumed, the strain distribution in the wearing and the binder course at the same depth are no longer identical. In the wearing course, both the contractive and expansive strains increase, the ratio between the peak expansive to contractive strain decreases and the location of the sign change shifts slightly. The opposite effect is observed in the binder course.

***Fig. 177** Comparison of the strains measured in summer under static loading with the strains according to the finite element model for interface between the subgrade and the binder course with friction, full or no bonding*
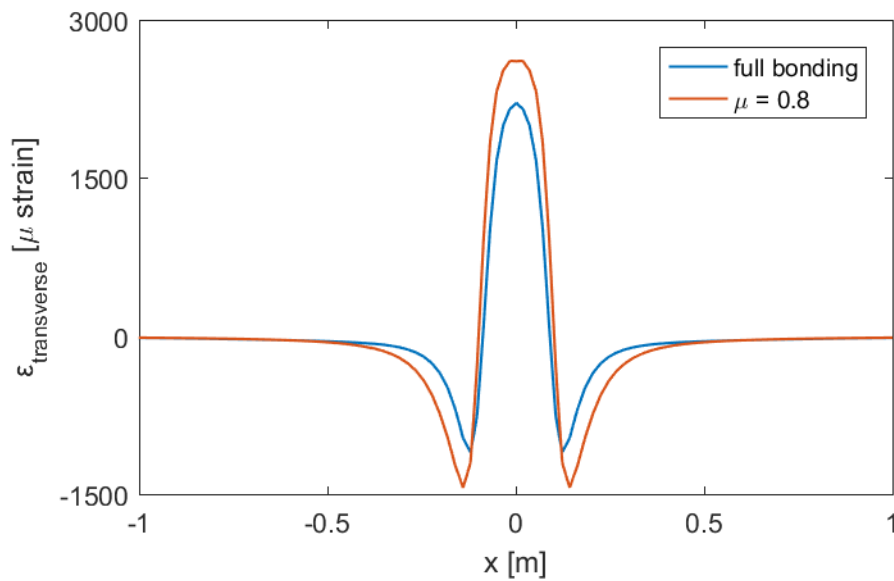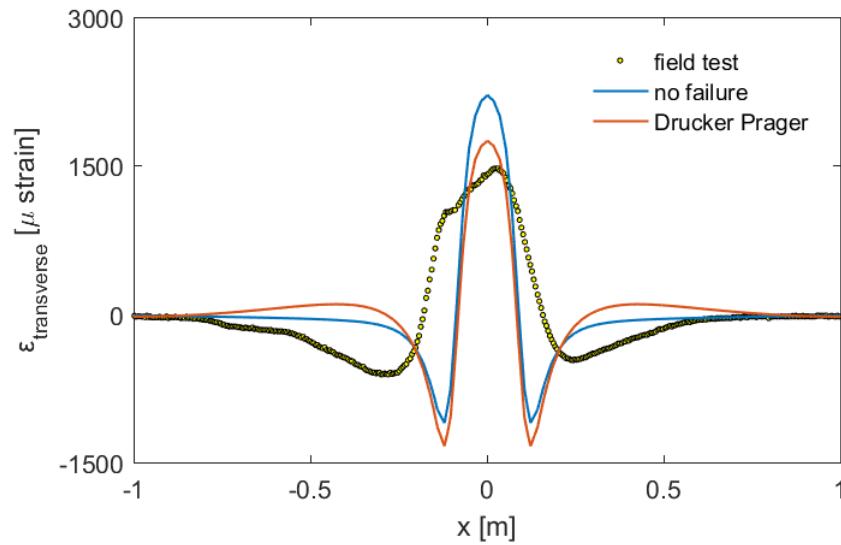

***Fig. 178** Comparison of the strains measured in summer under static loading with the strains according to the finite element model for interface with full bonding or with friction between the different AC courses*

Until now, the subgrade has been modelled as linear elastic without any failure surface. In an attempt to achieve a better simulation of the strain distribution, the existence of a Drucker-Prager failure surface has been modelled for the subgrade with the parameters summarized in Tab. 29. For these parameters, failure in the subgrade is observed, and the induced strain distribution in the binder course is shown in Fig. 179. However the results further deviate from the measured data (opposite curvature outside of the loading area), which let us conclude that this mechanism does not really occur at the field test.
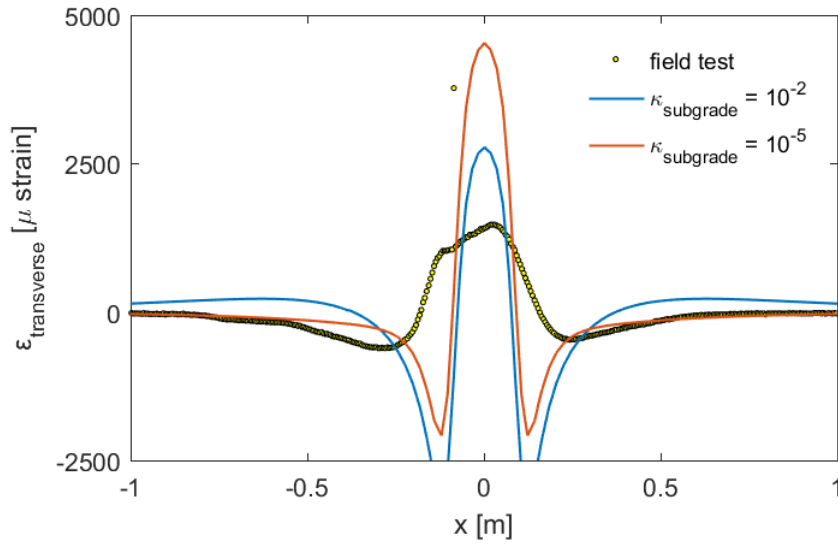
Fig. 179 *Comparison of the strains measured in summer under static loading with the strains according to the finite element model for subgrade with and without failure envelope*

Moreover, the effect of pressure dependent stiffness of the subgrade is investigated. Two different stiffness constants are examined and shown in Fig. 180. As already mentioned, this material model cannot be combined with viscoelasticity in Abaqus and therefore for the asphalt concrete has been modelled as a linear elastic material. The influence of the Poisson ratio of the subgrade, as well as the stiffness and Poisson ratio of the asphalt concrete are shown in Fig. 181 to Fig. 183. It can be seen, that although the strain distribution is different to the one for the linear elastic subgrade and fits better the outer part of the curve, the central part of the strain curve cannot be fitted.

Fig. 180 *Comparison of the strains measured in summer under static loading with the strains according to the finite element model for subgrade with pressure dependent stiffness; comparison of different logarithmic bulk moduli*
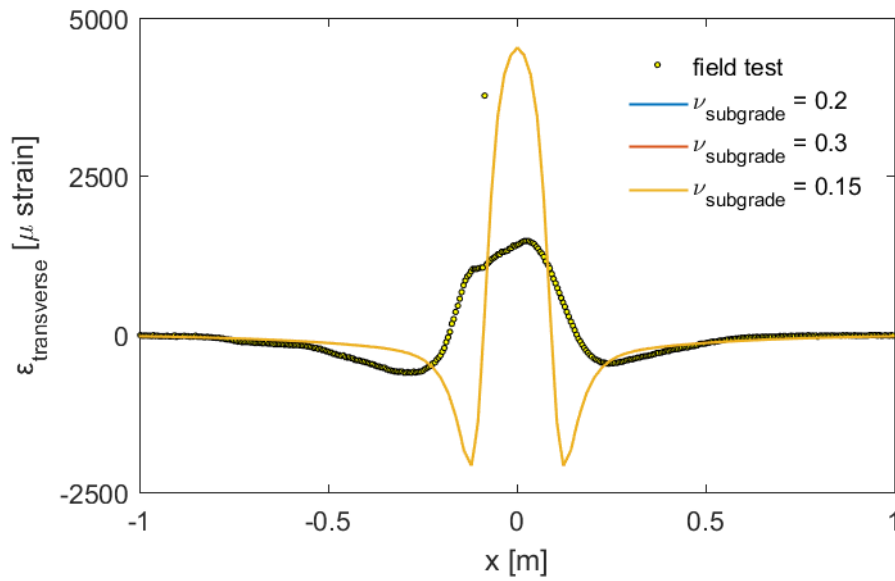

Fig. 181 Comparison of the strains measured in summer under static loading with the strains according to the finite element model for subgrade with pressure dependent stiffness; comparison of different values of the subgrade Poisson ratio
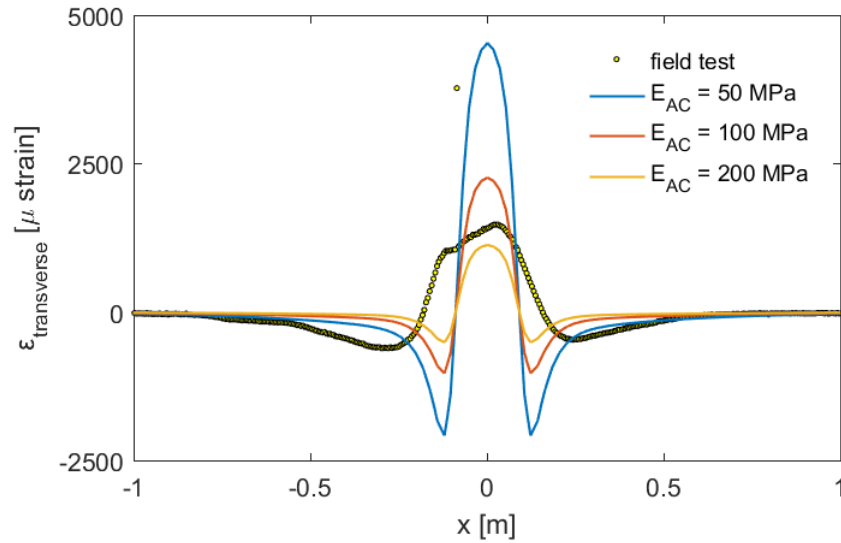
Fig. 182 *Comparison of the strains measured in summer under static loading with the strains according to the finite element model for subgrade with pressure dependent stiffness; comparison of different values of the asphalt concrete stiffness*
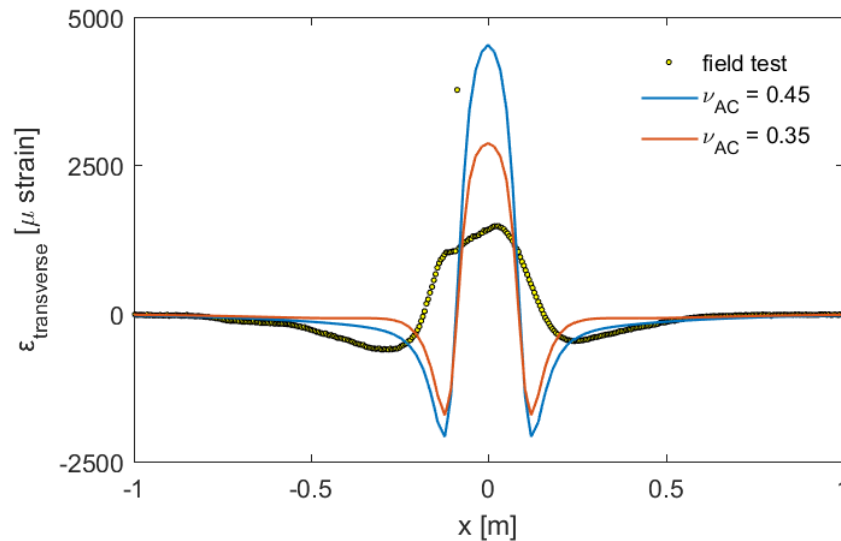

Fig. 183 *Comparison of the strains measured in summer under static loading with the strains according to the finite element model for subgrade with pressure dependent stiffness; comparison of different values of the asphalt concrete Poisson ratio*

The parametrical investigation regarding the test series 5 (summer) shows that none of the investigated parameters led to results similar to the measured strains. The region where the horizontal transverse strains change from expansive to contractive is shifted outwards not only compared to the numerical results, but also compared to the measurements under cooler temperatures. Under high temperatures similar to those during this test series, the utilized viscoelastic model is insufficient to explain the asphalt concrete behavior. In such temperatures, phenomena such as the reduction of stiffness and failure of the asphalt concrete under tension prevail. Hence, a constitutive model which considers pressure dependency (especially the stiffness reduction under tension) and a failure surface with could provide more accurate results.

In this chapter, however, only a preliminary finite element analysis based purely on the viscoelastic nature of the asphalt concrete is conducted. The test series 5 is therefore not further analyzed. For the other test series which were conducted in autumn and winter, a

parametrical analysis with the help of the axisymmetric model and the parameters which are summarized in Tab. 30 to Tab. 33 has been performed. The parameters leading to the best fits are summarized in Tab. 34 and will be further analyzed with the help of the three-dimensional model and compared with the measured values in the following section. It can be observed that the most satisfying results for these test series have been obtained with linear elastic subgrade and viscoelastic asphalt concrete modelled with the Prony series. The stiffness of the subgrade corresponds to the reloading modulus of a good quality subgrade, while the asphalt concrete stiffness reflects the temperatures measured during the test series. The convex contact pressure distribution has been shown to be the most satisfying. For the test series 8, a constant pressure distribution has been chosen, in order to further study the influence due to the different contact pressure distributions in the following chapter. No traction has been modelled at any of the models.

Tab. 30 Investigated parameters, spring (test series 6)

Contact pressure	Vertical		Constant	Convex	
	Traction		No	Inwards	Outwards
Subgrade					
Elastic Behavior	Linear elastic	E [MPa]	200	420	600
		ν [-]	0.15	0.2	0.3
	Porous elastic[6]	κ [-]	10^{-4}	10^{-5}	
Failure Behavior	No plasticity	-			
Asphalt	Linear elastic	E [MPa]	700	1000	1400
	Prony Series	$E_{Longterm}$ [MPa]	500	700	900
		ν [-]	0.35	0.4	0.45
Interface	Subgrade – Base course		Full bonding	μ = 0.8	μ = 0.0
	Between asphalt layers		Full bonding		
Temperature gradient[7]			No	Yes	

Tab. 31 Investigated parameters, autumn (test series 8)

Contact pressure	Vertical		Constant		
Subgrade					
Elastic Behavior	Linear elastic	E [MPa]	200	420	600
		ν [-]	0.15	0.2	0.3
Failure Behavior	No plasticity	-			
Asphalt	Prony Series	$E_{Longterm}$ [MPa]	200		
		ν [-]	0.4		
Interface	Subgrade – Base course		Full bonding	μ = 0.8	μ = 0.0
	Between asphalt layers		Full bonding		
Temperature gradient[7]			No	Yes	

---

[6] This material model cannot be modelled in a viscoelastic analysis. For analyses, at which the subgrade was modelled as porous elastic, the asphalt concrete was modelled as linear elastic.

[7] The temperature gradient has been indirectly taken into account by a variation of the long-term Young modulus within the different asphalt layers.

Tab. 32 Investigated parameters, winter (test series 9)

Contact pressure	Vertical		Constant	Convex	
	Horizontal		No	Inwards	Outwards
Subgrade					
Elastic Behavior	Linear elastic	E [MPa]	200	420	600
		ν [-]	0.15	0.2	0.3
	Porous elastic[8]	κ [-]	10^{-4}	10^{-5}	
Failure Behavior	No plasticity	-			
Asphalt	Prony Series	$E_{Longterm}$ [MPa]	1500	2000	2200
		n [-]	0.35	0.4	0.45
Interface	Subgrade – Base course		Full bonding	$\mu = 0.8$	$\mu = 0.0$
	Between asphalt layers		Full bonding		
Temperature gradient[9]			No	Yes	

Tab. 33 Investigated parameters, winter (test series 10)

Contact pressure	Vertical		Constant	Convex	
	Horizontal		No	Inwards	Outwards
Subgrade					
Elastic Behavior	Linear elastic	E [MPa]	200	420	
		ν [-]	0.2		
	Porous elastic[8]	κ [-]	10^{-5}	$5 \cdot 10^{-5}$	$5 \cdot 10^{-6}$
Failure Behavior	No plasticity	-			
Asphalt	Prony Series	$E_{Longterm}$ [MPa]	4000	6000	8000
		ν [-]	0.35	0.4	
Interface	Subgrade – Base course		Full bonding	$\mu = 0.8$	$\mu = 0.0$
	Between asphalt layers		Full bonding		
Temperature gradient[9]			No	Yes	

---

[8] This material model cannot be modelled in a viscoelastic analysis. For analyses, at which the subgrade was modelled as porous elastic, the asphalt concrete was modelled as linear elastic.

[9] The temperature gradient has been indirectly taken into account by a variation of the long-term Young modulus within the different asphalt layers.

Tab. 34 Best fit parameters for the different test series

Test series		6 (autumn)	8 (autumn)	9 (winter)	10 (winter)
Contact pressure	Vertical	Convex	Constant	Convex	Convex
	Horizontal	No	No	No	No
Subgrade	Elastic Behavior	Linear elastic	Linear elastic	Linear elastic	Linear elastic
	E [MPa]	420	420	420	420
	ν [-]	0.2	0.2	0.2	0.2
	Failure Behavior	No plasticity	No plasticity	No plasticity	No plasticity
Asphalt	Viscoelastic Behavior	Prony Series	Prony Series	Prony Series	Prony Series
	$E_{Longterm}$ [MPa] (AC/ACB/ACT)[10]	700/700/700	100/150/450	2000/2000/2000	5000/4000/1800
	ν [-]	0.4	0.45/0.42/0.4	0.4	0.4
Interfaces	Subgrade – Base course	$\mu = 0.8$	$\mu = 0.8$	$\mu = 0.8$	$\mu = 0.8$
	Between asphalt layers	Full bonding	Full bonding	Full bonding	Full bonding

---

[10] Different long-term Young moduli have been considered for each asphalt concrete layer to account for a rough consideration of the temperature gradient within the asphalt concrete.

8.4 Static tests

8.4.1 Comparison with the field measurements

In the following figures, the strains measured in the field experiment are compared with those calculated using the three-dimensional finite element model described in 8.1. The parameters used in the numerical model were determined with the help of the parametrical analysis described in 8.3.2 and are given in Tab. 34.

As already referred in 8.1.2, only the strains in the cross direction are analyzed. For each test, the strains due to both the front and rear tire are modelled. The results are compared at 4cm depth (in the binder course) for tests 6, 8, 9 and 10 and for the test 8, 9 and 10 at 22cm depth (on the subgrade). For test 6 no field test data on the subgrade are available. For all tests, the measurements are evaluated both at the end of the loading and the unloading step.

As expected, the strain magnitude drops for decreasing temperature, as a result of the decreasing asphalt concrete stiffness. Similarly with the field experiment results, the decrease of the ratio of the maximum expansive to the absolute maximum contracive strain is also observed in the finite element model results. Also in accordance with the experimental results, the strains measured on the subgrade are not reduced in the same extent because of the temperature decrease (Fig. 200, Fig. 201). Indeed, the ratio of stiffness between the asphalt and the subgrade is high for cold temperatures. As a result, the asphalt concrete layer under loading tends to behave as a bending plate founded on the subgrade, i.e. with expansion at the bottom and contraction at the top side.
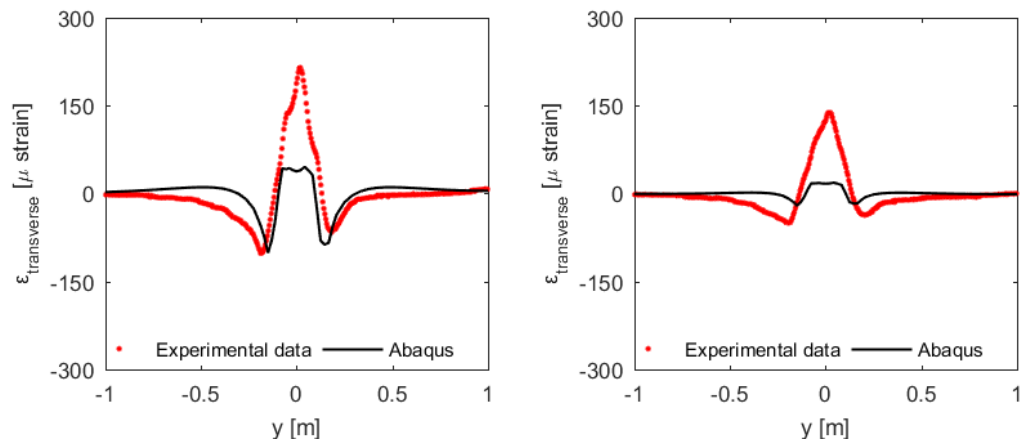
Fig. 184 *Comparison of the measured and modelled strains under the front axle on the binder course, autumn (test series 6), after loading (right) and unloading (left)*
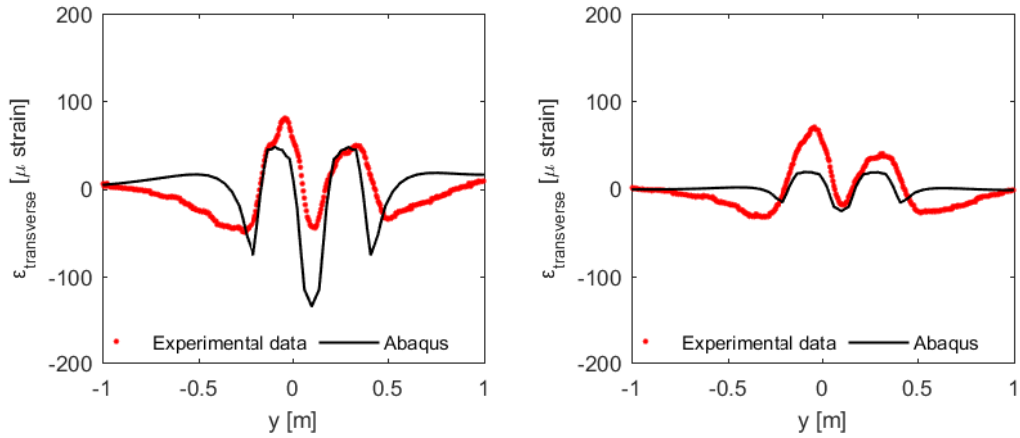
Fig. 185 *Comparison of the measured and modelled strains under the rear axle on the binder course, autumn (test series 6), after loading (right) and unloading (left)*
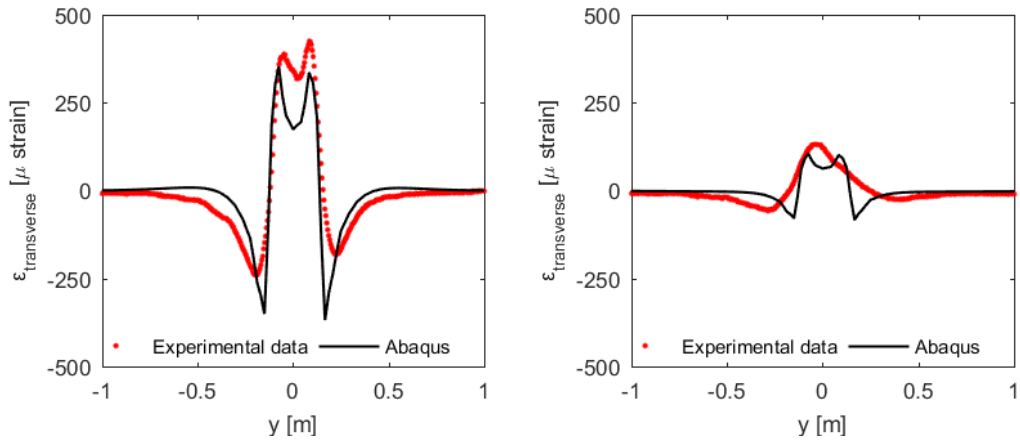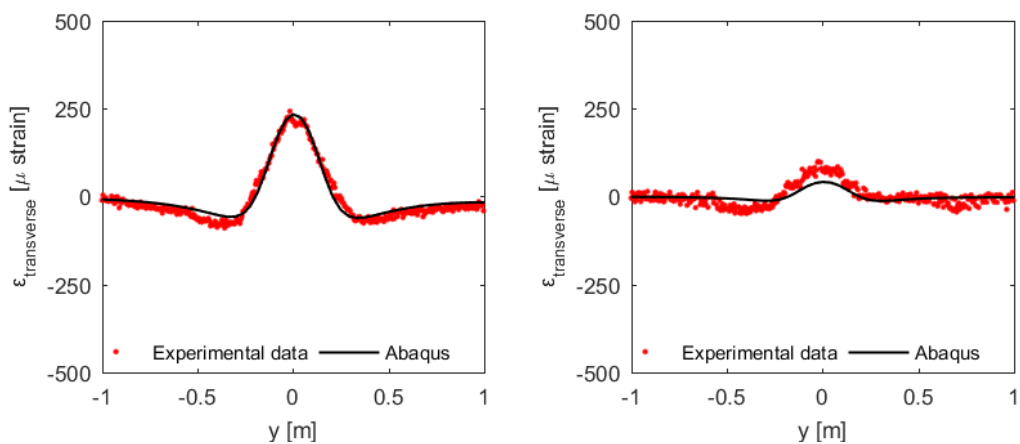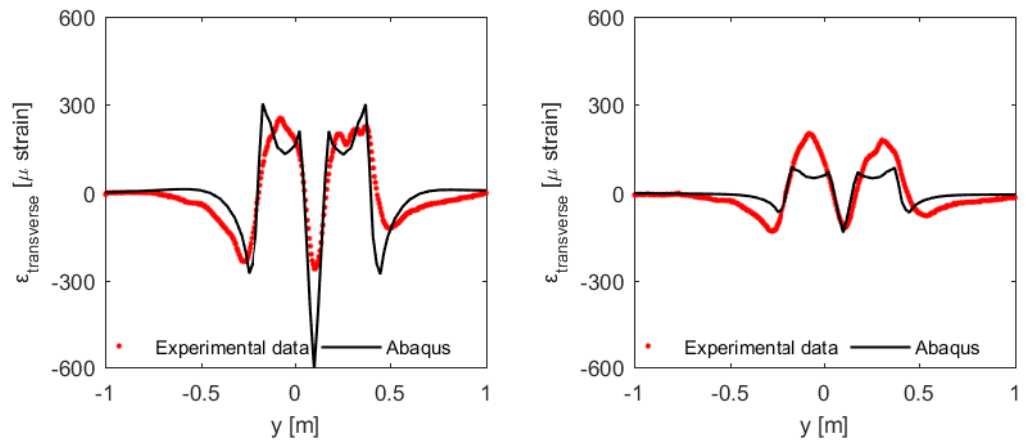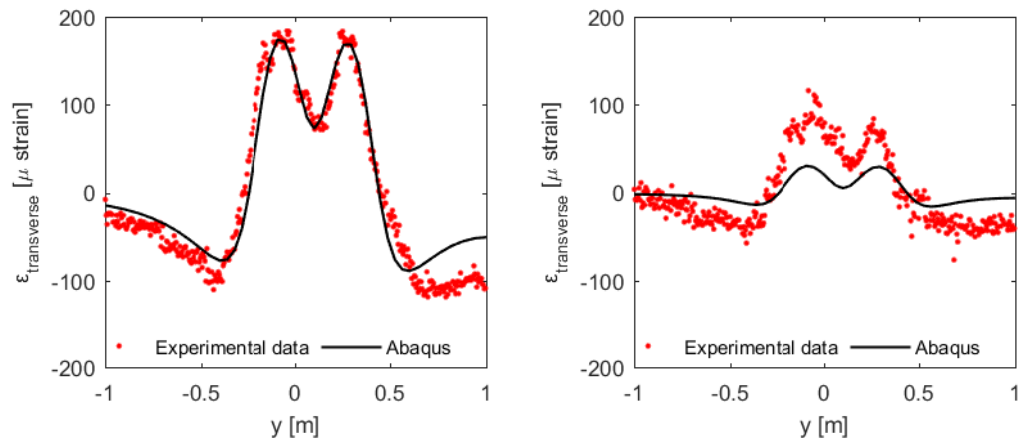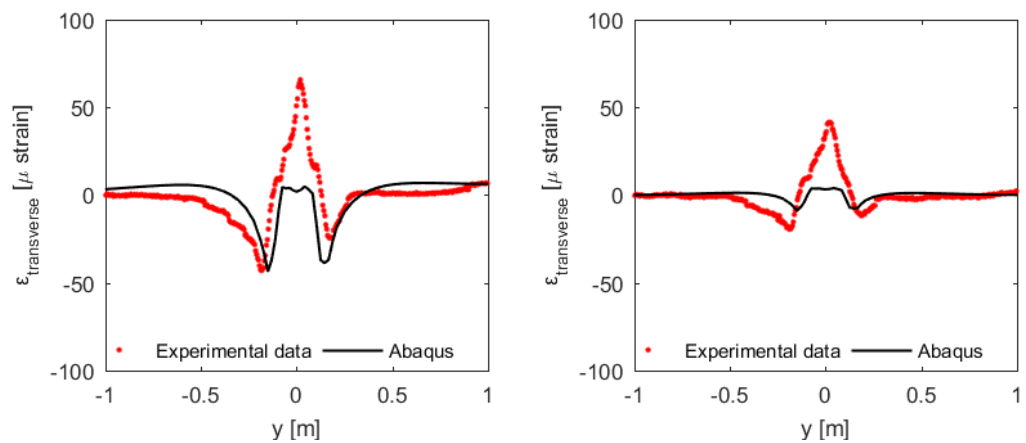

Fig. 186 *Comparison of the measured and modelled strains under the front axle on the binder course, autumn (test series 8), after loading (right) and unloading (left)*
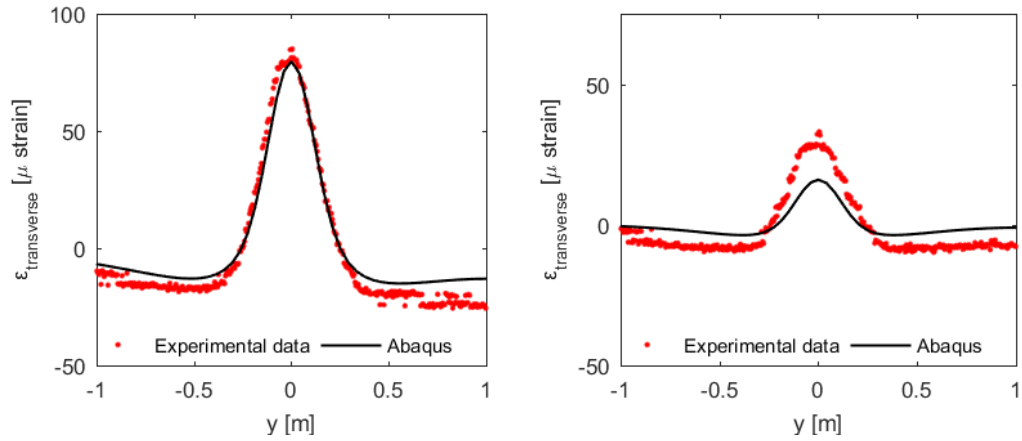

Fig. 187 *Comparison of the measured and modelled strains under the front axle on the subgrade, autumn (test series 8), after loading (right) and unloading (left)*
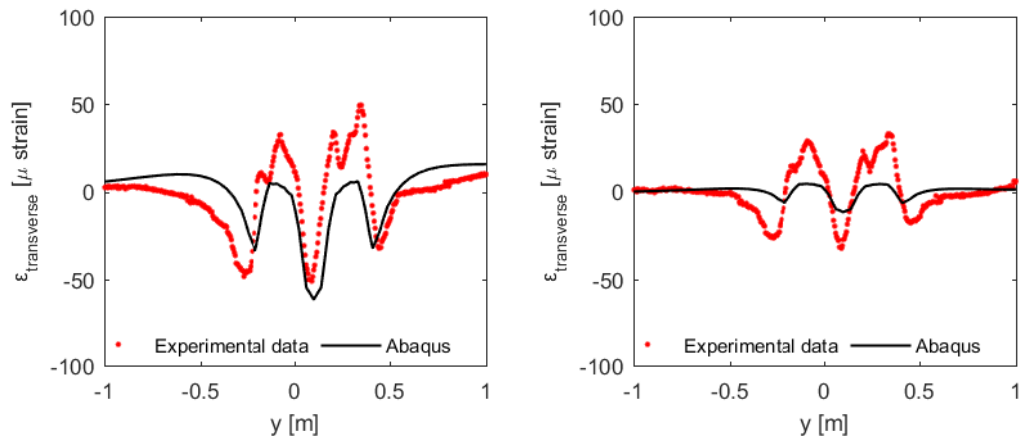
Fig. 188 *Comparison of the measured and modelled strains under the rear axle on the binder course, autumn (test series 8), after loading (right) and unloading (left)*

Fig. 189 *Comparison of the measured and modelled strains under the rear axle on the subgrade, autumn (test series 8), after loading (right) and unloading (left)*

Fig. 190 *Comparison of the measured and modelled strains under the front axle on the binder course, winter (test series 9), after loading (right) and unloading (left)*
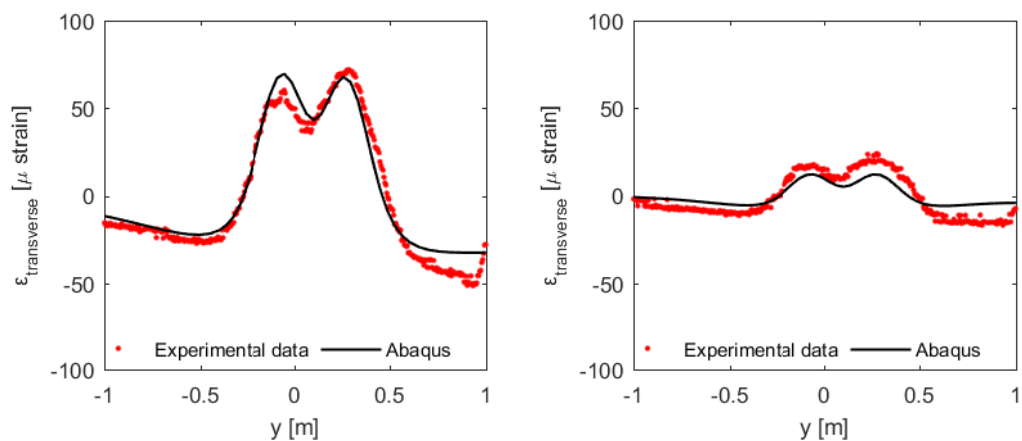
Fig. 191 Comparison of the measured and modelled strains under the front axle on the subgrade, winter (test series 9), after loading (right) and unloading (left)
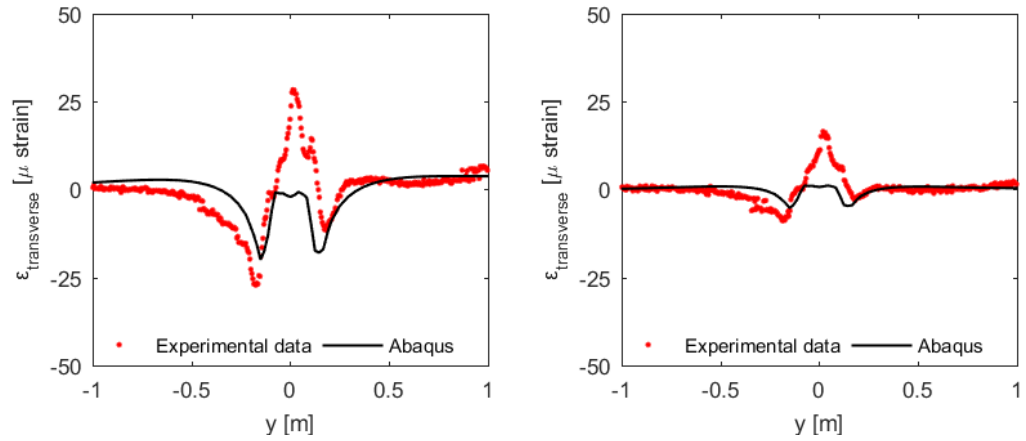

Fig. 192 Comparison of the measured and modelled strains under the rear axle on the binder course, winter (test series 9), after loading (right) and unloading (left)
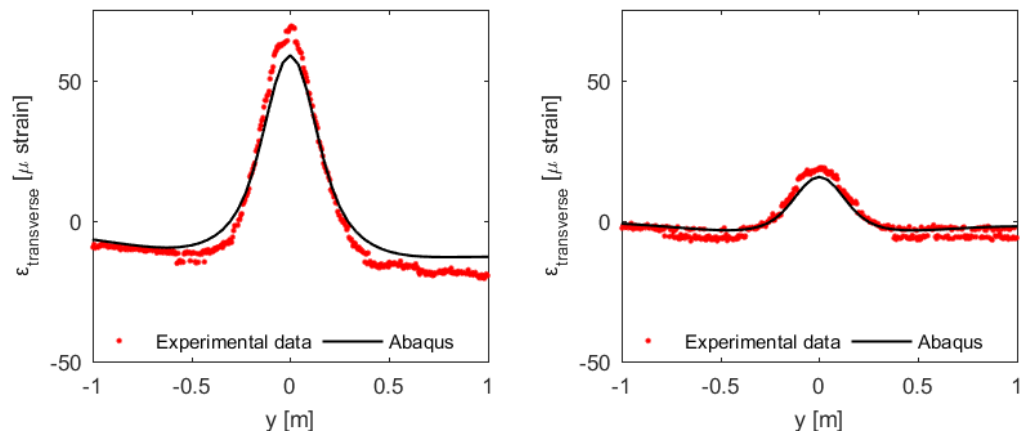

Fig. 193 Comparison of the measured and modelled strains under the rear axle on the subgrade, winter (test series 9), after loading (right) and unloading (left)

Fig. 194 *Comparison of the measured and modelled strains under the front axle on the binder course, winter (test series 10), after loading (right) and unloading (left)*

Fig. 195 *Comparison of the measured and modelled strains under the front axle on the subgrade, winter (test series 10), after loading (right) and unloading (left)*
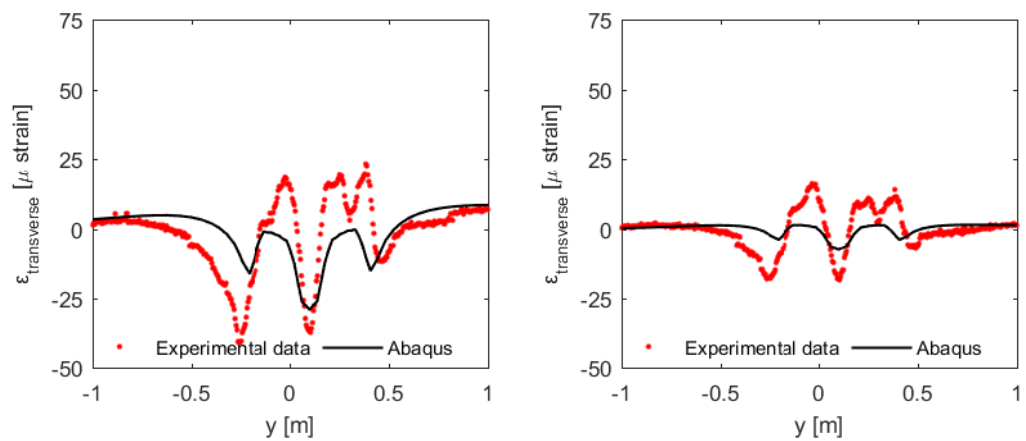

Fig. 196 *Comparison of the measured and modelled strains under the rear axle on the binder course, winter (test series 10), after loading (right) and unloading (left)*
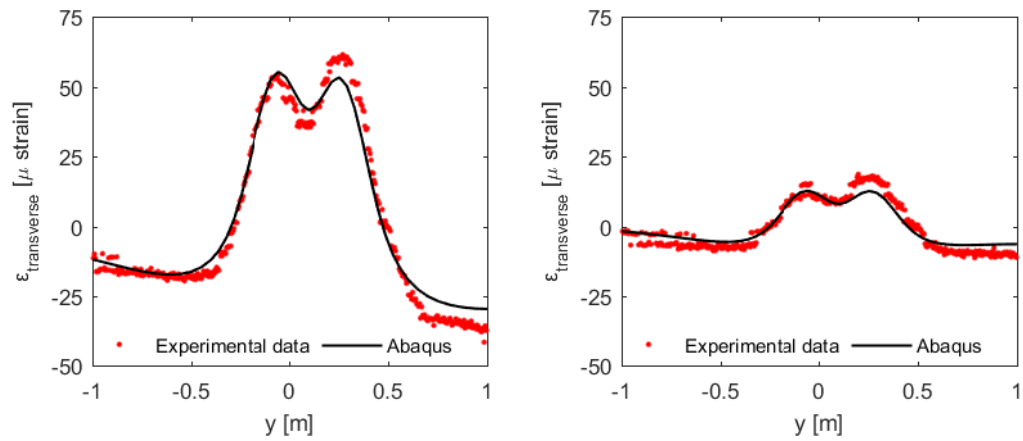
Fig. 197 *Comparison of the measured and modelled strains under the rear axle on the subgrade, winter (test series 10), after loading (right) and unloading (left)*
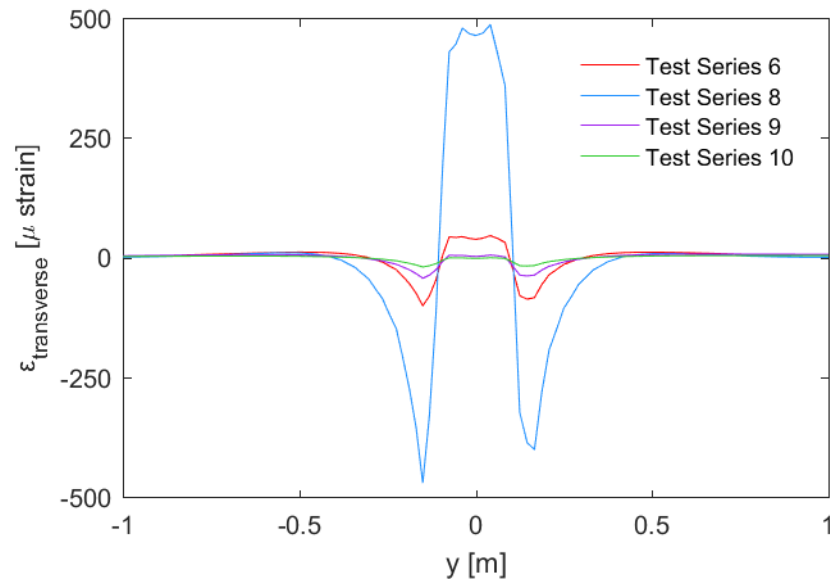

Fig. 198 *Comparison of the strains at 4cm depth due to the front axle of truck 1 for test series conducted in different temperatures*
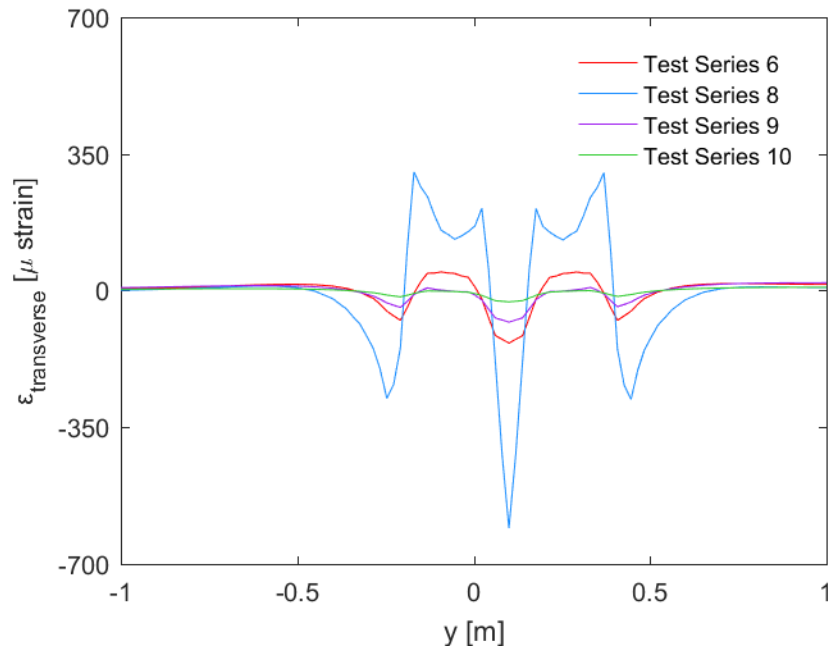
***Fig. 199** Comparison of the strains at 4cm depth due to the rear axle of truck 1 for test series conducted in different temperatures*
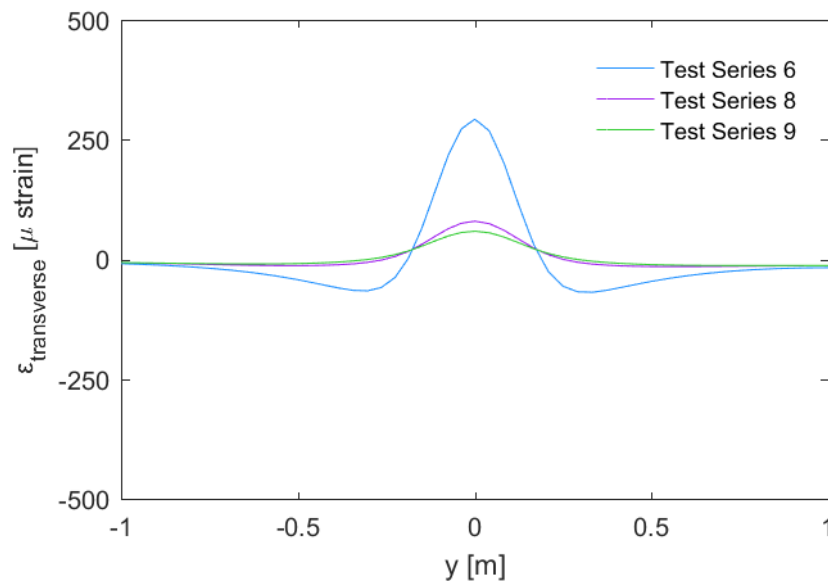

***Fig. 200** Comparison of the strains at 22cm depth due to the front axle of truck 1 for test series conducted in different temperatures*
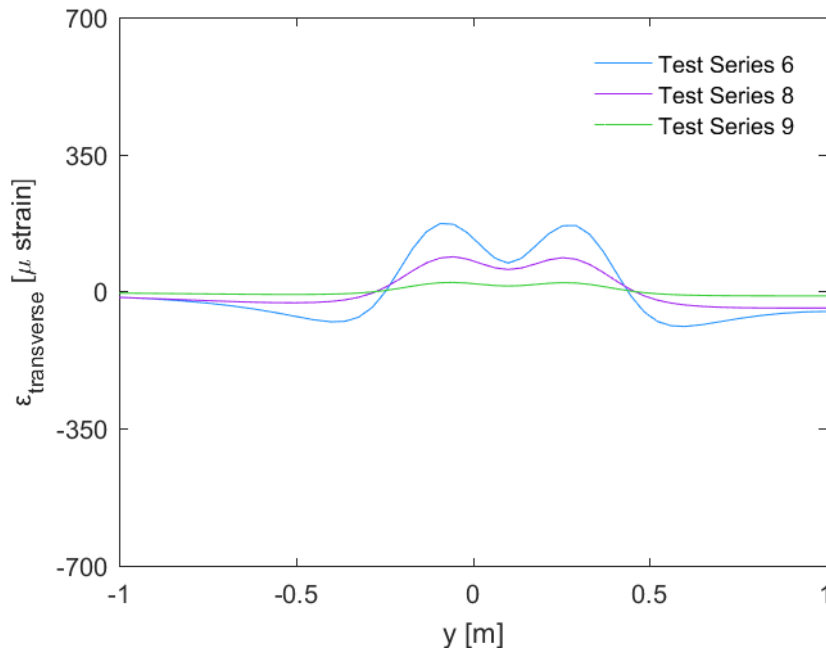
Fig. 201 *Comparison of the strains at 22cm depth due to the rear axle of truck 1 for test series conducted in different temperatures*

It can be observed, that the strains at 22cm depth are for all test and load cases almost perfectly reproduced by the model. To ensure the right interpretation of the results and the accuracy of the model, the measured strain distribution at 22cm depth is compared with the strain distribution at the same depth according to the finite element model both in the subgrade and in the base course. It is seen that a totally different strain distribution is obtained in the subgrade, hence verifying that the cable belongs to the asphalt concrete layer.

The modelling of the strains in the binder course has been more formidable however. Especially for the front tire, a spiky peak persistently appears in the measurements of test series 6, 9 and 10. Specifically for the test series 6, for which the asphalt concrete temperature ranges between 17 and 18, the strain distribution measured under the rear tires is much smoother and has almost the half amplitude compared to the strain under the front tire. In Fig. 73 and Fig. 74, section 5.2.2. .it can be clearly seen, that the measured amplitudes resulting from the rear and front axles for all test series are of similar magnitude with the exception of the test series 6. This could lead to the conclusion, that for this specific measurement some local imperfection might exist in the asphalt concrete.

For the winter measurements however (test series 9 and 10), spiky peaks of similar magnitude appear in the binder course under both the single and the twin wheels. None of these peaks could satisfactorily be modelled. More precisely, the modelling of expansive and contractive strains of small and simultaneously similar magnitudes has not been possible with the current model used. Both these test series were conducted in winter, at low temperatures. One possible mechanism to explain these peaks can be the following: For lower temperatures the stiffness of the asphalt concrete increases. The contact area of the tire expands due to the high stiffness of the pavement and as a result inward traction is applied on the pavement.

The second observation is that the strains computed after unloading have been consistently overestimated. This can be accounted for due to the fact that the used model can produce no irreversible strains. It has also to be noted here that fluctuations of the time between the unloading and the measurement might also vary, whereas in the finite element model it is 15s for all test series, leading thus to a potential deviation of the results.

For test series 8, unlike the rest test series, a constant contact pressure distribution has been used. It can be seen that the strain distribution caused under this assumption in the binder course, is different from the other results, with spiky peaks both for the contractive and expansive strain, and a ratio of maximum contractive to expansive strains close to 1. The strains on the subgrade are not, however, affected by the different distribution.

A further observation is that the asymmetries in the strain distribution caused by the existence of the neighbor tire can be reproduced in accordance with the measurements and are more evident in the winter as in the warmer temperatures. Particularly for the warmer temperatures, only minor asymmetries are noticed (test series 8 rear axle on the subgrade). As the temperature decreases, the following trend is observed: Towards the vehicle axle, a small expansive strain appears in the binder course, whereas on the subgrade a contractive strain of greater absolute magnitude is formed. The trend becomes more dominant for colder temperatures, which also indicates the plate behavior of the asphalt concrete in these temperatures, as previously referred. Additionally, the asymmetry is more evident for rear axle than for the front one, as the distance between the twin tires is smaller than the single tires.
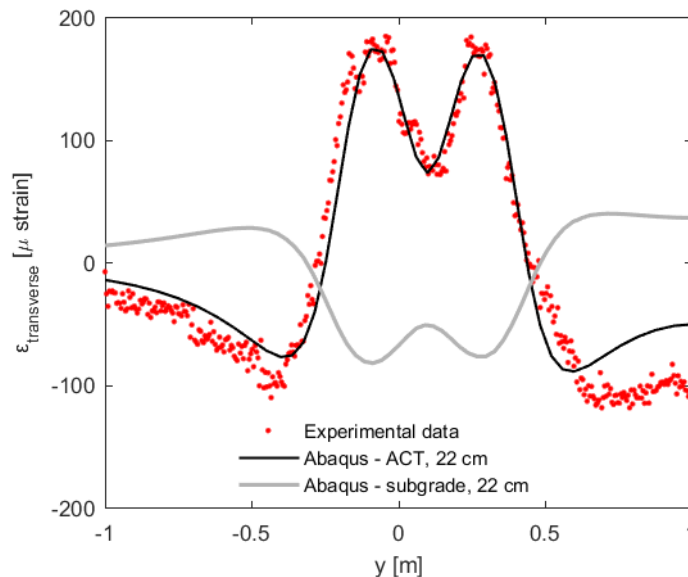

Fig. 202 *Comparison of the strains at 22cm depth on the subgrade and in the base course with the field measurement with approximation of the asymmetry, as mentioned in the text*

8.4.2 Stress and strain fields

During the field experiments, the strains along the fiber optic cables grid have been measured. These measurements provide valuable information about the strain field in the chosen region, and allow for the precise calibration of finite element models, as shown in the previous section. The stress and strain fields due to the tire loading can be subsequently calculated with the help of the finite element models.

In the current analysis, the asphalt concrete has been modelled as linear viscoelastic material, but as already mentioned, a constitutive model including failure would more accurately describe its behavior, especially under high temperatures. As the stress state of the material determines whether the material remains in the viscoelastic region, it begins to yield or eventually fails, the knowledge of the stress field is important for the choice of the appropriate constitutive model.

In Fig. 203, the computed transverse stresses and strains for the cross-section perpendicular to the driving direction are compared for the test series 8 (autumn) and 9 (winter) under the front axle. The transverse stresses and strains for both tests, both for single and dual tire loads, in two different cross-sections, one in the driving direction and one to the transverse to it, as well as in horizontal planes of different depths are illustrated in Appendix I.
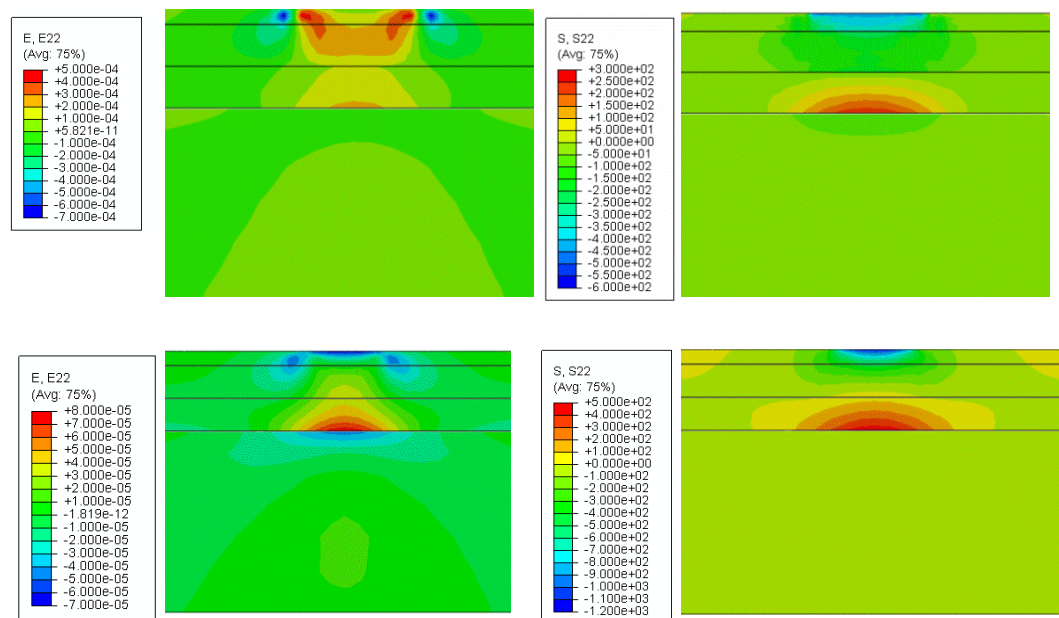

Fig. 203 *Distribution of transverse strains (left) and stresses (right) with the depth, under the front axle. Top: test series 8 (autumn), bottom: test series 9 (winter).*

It can be observed, that especially for the test series 8, which was conducted under mild temperature, the stress and the strain field show substantial differences. Whereas the maximum transverse expansive strains are calculated close to the pavement surface, the transverse stresses are compressive in the same region. Besides, although the maximum compressive stresses are located directly under the loaded area, the largest contractive strains are computed immediately next to it. The tensile transverse stresses of the maximum magnitude appear at the bottom of the asphalt concrete layer. For the test series 9, performed in winter, both the compressive stresses and strains appear close to the surface, and the expansive ones at the bottom of the asphalt concrete layer.

The results can be interpreted as follows: For the cold temperatures, the substantial stiffness contrast between the asphalt concrete and the underlying base has as a result the behavior of the asphalt concrete layer to resemble this of an embedded plate under bending due to loading, i.e. under expansion in the bottom and under compression at the top. For the warmer temperatures, the stiffness contrast is inadequate to cause this

behavior. In the region of the load application, the stress field is under compression; however the expansive strains due to the Poisson effect prevail. Finally, the large tensile strains which appear in the region next to the loading area close to the surface are a result of the shear stresses in this area both for the low and mild temperatures.

8.5   Dynamic tests

In this section the results of the numerical model for the dynamic field test are analyzed. In order to avoid the influence of either high or low temperatures, the test series 8 which was conducted in autumn is analyzed. The parameters used for the finite element model have been given in Tab. 28 and Tab. 34. Only the strains in the transverse to the traffic direction have been evaluated, on account of the neglect of inertia and friction forces in this analysis, as already explained in chapter 8.1.3.

In Fig. 204 and Fig. 205, two different snapshots of the model are shown for two different time instants. Both snapshots are located in the binder course, in 4cm depth and the velocity of the truck in this model is 5km/h. The results illustrated in the snapshots are strains in the transverse to the driving direction. In the first time instant the spatial distribution of the strains caused by the three front axles is shown. In the second snapshot, which is taken with a delay of 2.475s, the footprints of the third to the fifth axles in terms of transverse strains are illustrated. In both snapshots, the viscoelastic behavior of the asphalt concrete can be observed. The strains on the rear of each tire do not instantly disappear, but gradually fade away. This results to the accumulation of the strain caused by two subsequent axles, especially for the rear axles, which have shorter in-between axle distance.

This phenomenon can further be observed Fig. 206 in to Fig. 211. In these figures, the cross-section, for x = 0m is evaluated. The transverse strains are plotted according to the respective color code in the vertical axis versus the position in the transverse direction y and the time t. The transverse strains along this cross-section as a result of the passage of all five axles can therefore be seen in these figures.

The results are shown for the velocities of 5, 15 and 50km/h and both in the binder course (Fig. 206 to Fig. 208) and on the subgrade (Fig. 209 to Fig. 211), where the induced strains due to the viscoelastic behavior of asphalt concrete is demonstrated. The strains for the 5km/h velocity test have a maximum value of approximately 200$\mu\varepsilon$, whereas for the 50km/h test the maximum value is reduced to approximately 70$\mu\varepsilon$. The computed strains on the subgrade reduce similarly from 350$\mu\varepsilon$ to approximately 230$\mu\varepsilon$. Interestingly enough, for the results in the dynamic simulations, the maximum strains on the subgrade exceed those in the binder course. This observation is similar to the results obtained for the static tests conducted in the low temperatures. This phenomenon can be explained with the fact that the response of the asphalt concrete under moving load is stiffer than for a static load at the same temperature, and leads to similar strain distributions as the ones obtained for static tests at lower temperatures.

Additionally, the duration of the induced strains is different for different depths of the asphalt concrete when the load is moving. Indeed, although the stress distributes in larger surface, the duration of loading at the static tests remains constant with the depth. When the load is moving however, this is no longer true. The load distribution with the depth has as result that for the same cross-section, the distress duration increases with the depth. For a pseudo-plastic viscoelastic material, this will lead to larger strains depending on the viscoelastic parameters of the asphalt concrete, compared to the strains caused by static loading of equivalent duration.

On account of the difference between the nominal velocities, for which the simulations have been performed, and the actual velocity of the truck during the field experiment, the distribution of the stresses with the time differ between the respective plots (Fig. 113 and Fig. 214). It can be observed that the maximum tensile strain consequently appears under the third vehicle axle. This is a result of the combination of two factors: Firstly, the second and third axles have greater weight per tire than the other axles. As it was stated in Tab. 24 each of these axles has a total estimated weight of 7t, which gives 3.5t on each of the single wheels. In the other axles, the weight per tire is approximately 2.5t. The second factor is the viscoelasticity of the asphalt concrete. The peak strain because of the second axle does not entirely fade away before the third axle arrives, resulting in a slightly higher maximum tensile strain under the third axle. These results are in a good

but not full agreement with the measured values. One reason for that is that the loads of the axles II to IV are only estimated from the total weight of the vehicle and not measured. A slightly different load distribution might lead to different results. Additionally, small variations of the velocity, and the selected processing algorithm which identifies the strain peaks might influence the results.
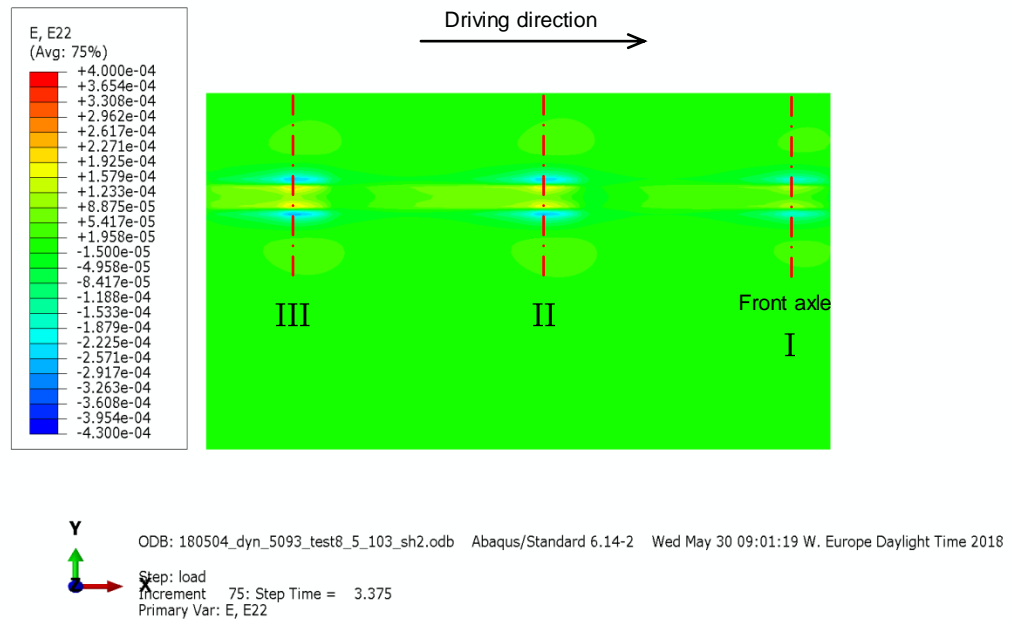

Fig. 204 *Strains on the binder course (transverse direction) according to the FE model for truck 1, autumn, v = 5km/h, 4cm depth, t = 3.375s*
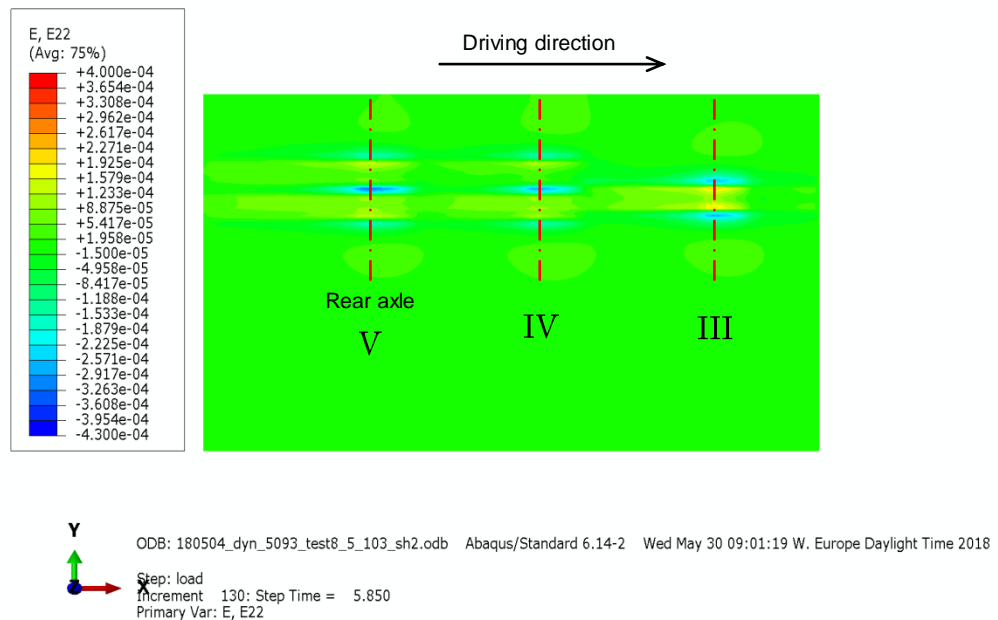

Fig. 205 *Strains on the binder course (transverse direction) according to the FE model for truck 1, autumn, v = 5km/h, 4cm depth, t = 5.85s*

Fig. 206 *Strains according to the FE model for truck 1, autumn, v = 5km/h, 4cm depth*

Fig. 207 *Strains according to the FE model for truck 1, autumn, v = 15km/h, 4cm depth*
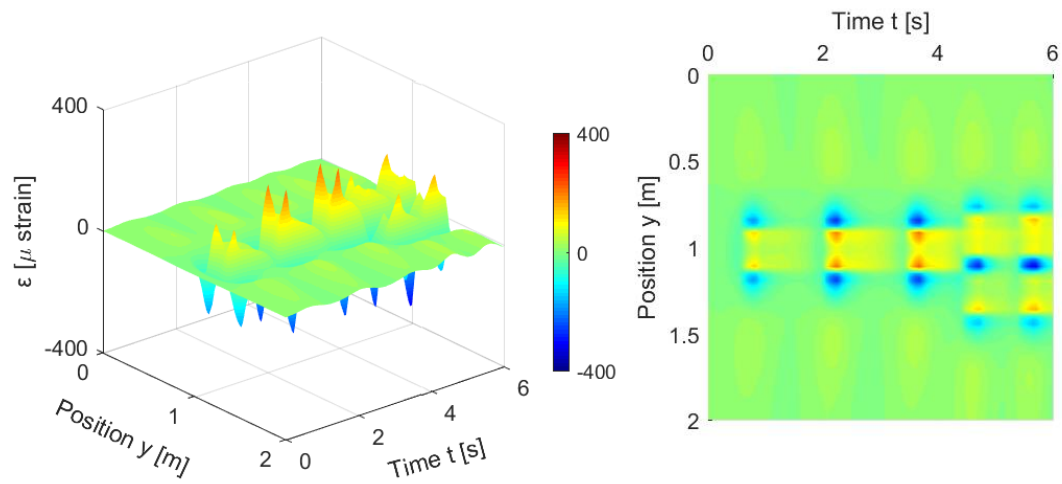

Fig. 208 *Strains according to the FE model for truck 1, autumn, v = 50km/h, 4cm depth*

Fig. 209 *Strains according to the FE model for truck 1, autumn, v = 5km/h, 22cm depth*

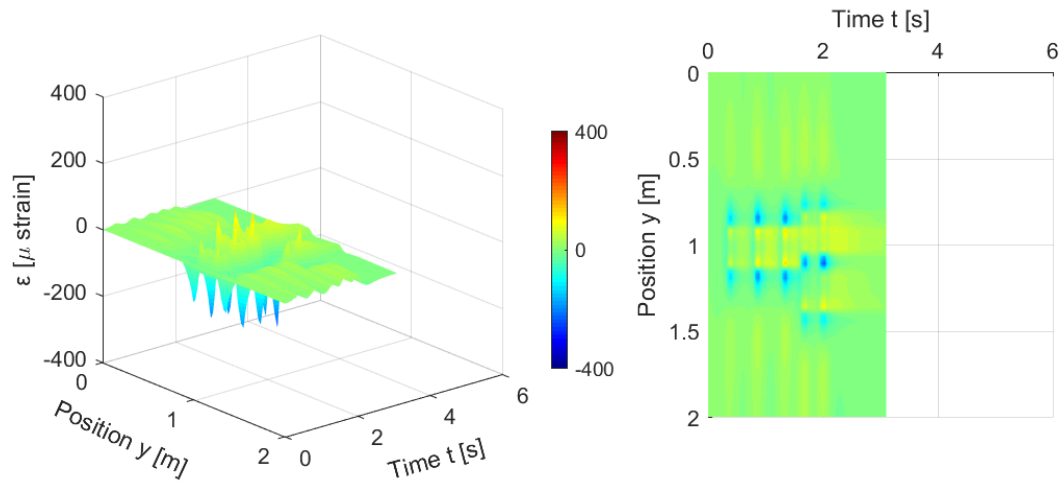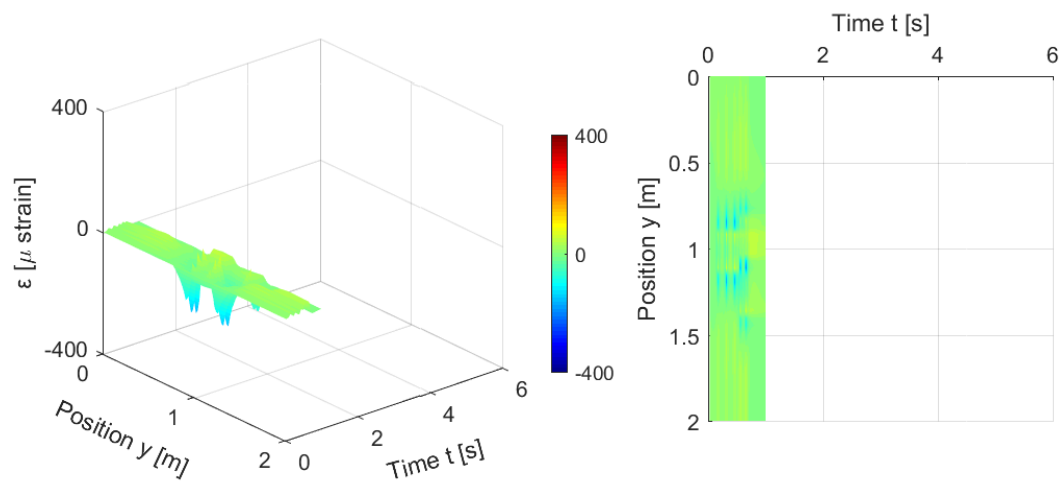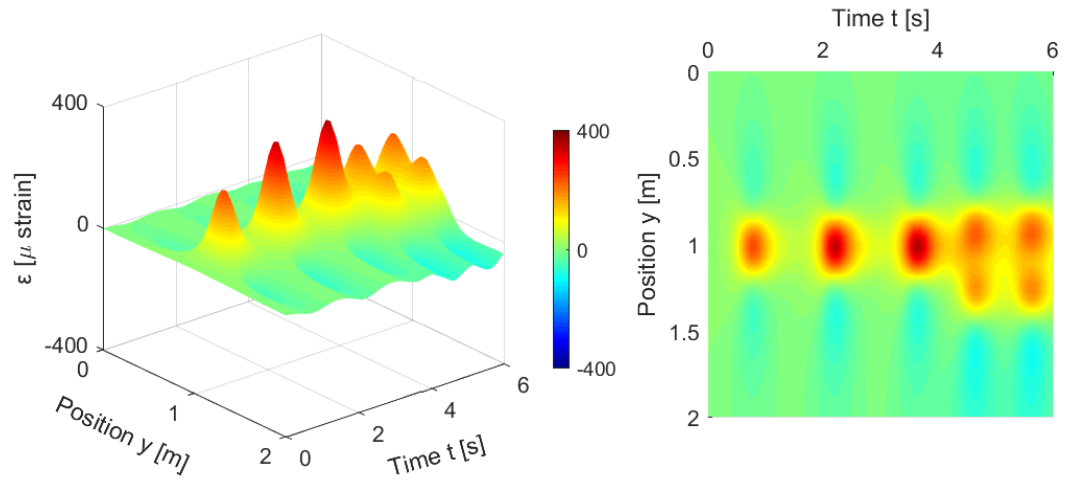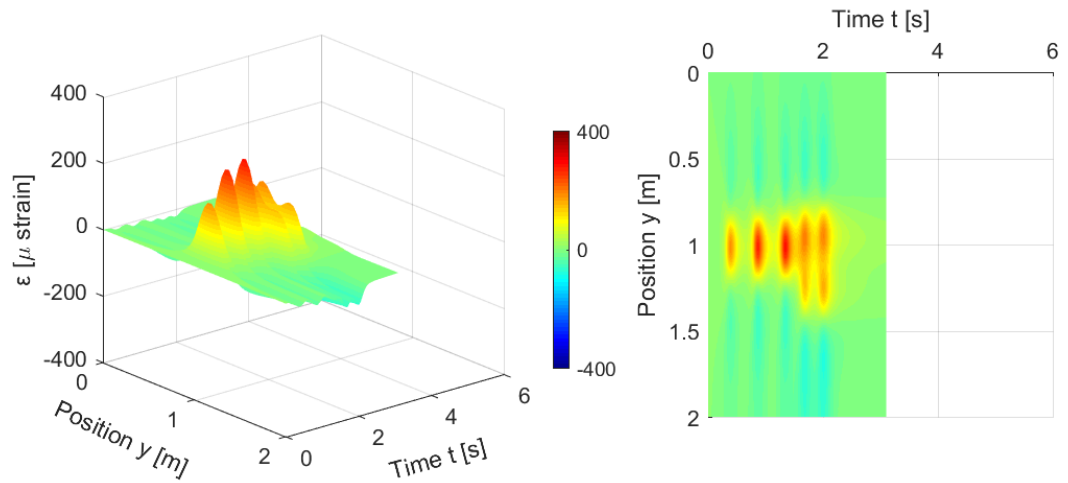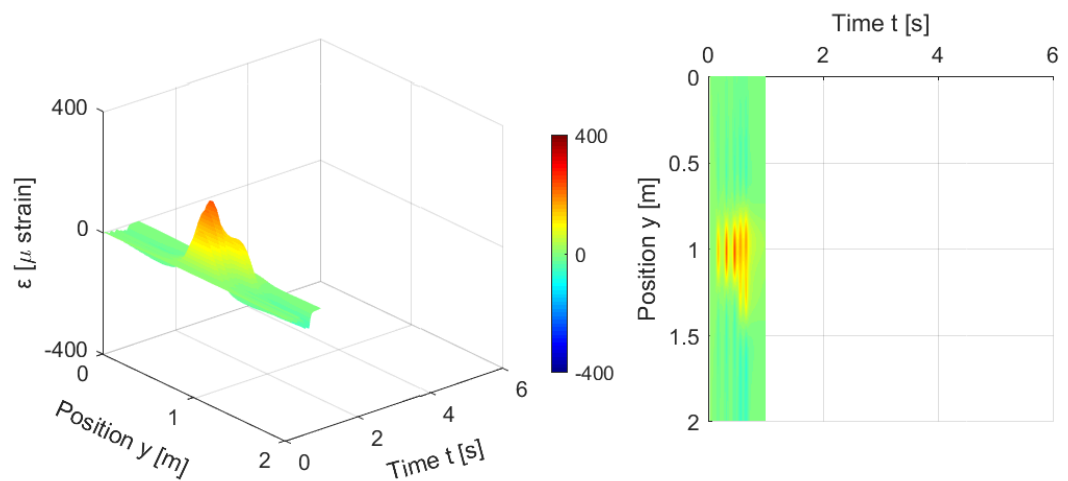**Fig. 210** *Strains according to the FE model for truck 1, autumn, v = 15km/h, 22cm depth*

Fig. 211 *Strains according to the FE model for truck 1, autumn, v = 50km/h, 22cm depth*

The maximum compressive strain however, appears consequently both at the numerical model and the experiment under the rear axle. This is owed to the fact that between the twin tires the compressive strain is a result of the superposition of the compressive strain duo to both tires. Although the fourth and fifth axles have the same load and configuration, slightly larger compressive strain is caused beneath the fifth axle, as a result of the accumulation of strains due to the viscoelastic nature of the binder.

Two different patterns are observed in the fading of the extensive and compressive strains. Both patterns appear consequently for all velocities and are in good agreement with the measurements (chapter 5.3.3, Fig. 107). These patterns are a result of the superposition of negative and positive strains which interchange with the load advancement, as a result of the viscoelasticity of the asphalt concrete. Initially, the negative (compressive) part of the strain "pulse" arrives at the evaluated cross-section. Due to the binder viscosity, the compressive pulse does not instantly fade out and superposes the actual tensile strain. This leads to the creation of the step-like strain distribution, which is observed in the tensile strains. The tensile strains do not follow the same trend, as the negative pulse arrives firstly, and is thus not influenced by any previous strains.

Despite being in good accordance with the field measurements, this step-like strain distribution is fading faster according to the model than in reality. It can also be seen, that the strain due to the last pulse fades almost totally after 2 seconds according to the finite element model, whereas according to the field measurement approximately 50% of the last strain peak remains (Fig. 107). As already referred above, this can be accounted for by the fact that the linear viscoelasticity used in this analysis cannot model the non-reversible compliance typical for asphalt concrete especially in high temperatures.

Another main difference of the results of this model with the dynamic field measurements is the strain distribution along the cross-section. Indeed, according to the finite element model the strain shows one smooth peak under each tire. The finite element model on the other hand, shows two pointed peaks, as a result of the constant contact pressure distribution used in this simulation for the tire loading. It was shown in the previous sections that a smoother, convex contact pressure distribution is more representative for the load and air pressure of the tires of the truck used in the field experiment and that it leads to more realistic strain distributions within the binder course.

Another observation regarding the two rear axles is the fact that the tensile strain on the subgrade beneath the outer tires is greater than this under the inner ones. Again, this is a result of the viscous asphalt concrete behavior and the passage of the three front axles, at a similar trail with the outer tire. This phenomenon is not observed results at 4cm depth according to the finite element model, in contrast to the field measurements. This is explained with the strain distribution in the cross-section. The pointed peak of the third axle is superimposed with the trough of the slightly displaced outward tire of the fourth axle. As a result, in the binder course under the outer wheel of the fourth axle an approximately constant strain is induced.

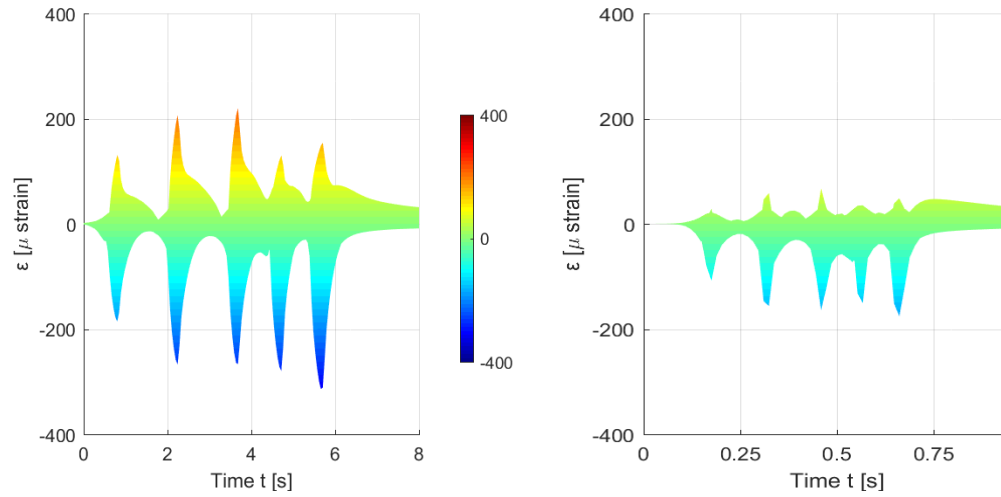**Fig. 212** *Comparison of strain envelope in autumn with time for v = 5km/h (left) and v =50km/h (right) at 4cm depth*
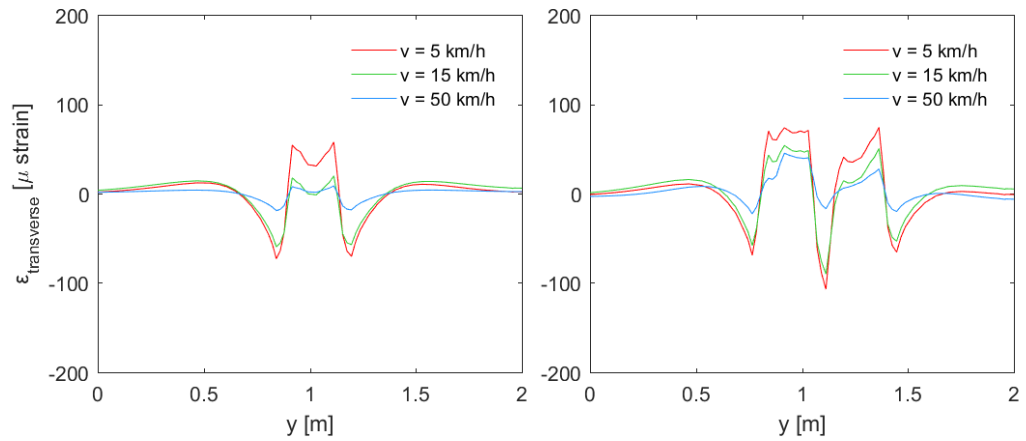

Fig. 213 *Comparison of the strains due to the front (left) and the rear (right) axle of truck 1 for different velocities in autumn and at 4cm depth*
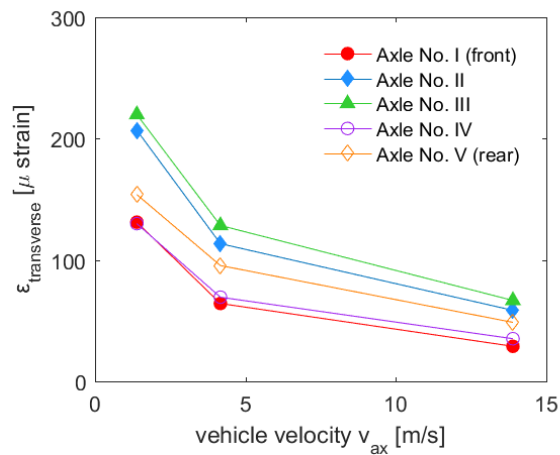

Fig. 214 *Comparison of the peak strains for the different axles of truck 1 in autumn and at 4cm depth for different velocities*

8.6 Discussion

In the current chapter, the finite element model simulation results of the tests at Hohlstrasse Zurich have been presented. An initial calibration of the viscoelastic parameters of the asphalt concrete was performed with the help of the EBI Block test (test series 7). Subsequently, a parametrical investigation with a simplified axisymmetric finite element model was conducted, in order to determine the exact material parameters and contact pressure distributions for each test. The optimized parameters were then applied in the three dimensional model for the exact simulation of the front and rear axle static tests as well as the passage of the vehicle with different velocities.

The asphalt concrete was modelled with the help of the Prony series implemented in Abaqus. This model is typically used for asphalt binders, as it can successfully describe their viscoelastic nature. It fails however to describe phenomena related to the asphalt behavior, like the non-reversible compliance, which is typical for higher temperatures. Also possible differences between the tensile and compressive stiffness and strength of the asphalt concrete cannot be reproduced by this model. Moreover, the viscoelastic behavior of the asphalt cannot be combined in the finite element calculation with any subgrade constitutive models which include pressure stiffness dependency. Finally, no damage due to the repetition of loads can be estimated.

The assumptions concerning the contact pressure distribution in the finite element model are a further discussion point. The typical assumption that the contact pressure is equal to the inflation pressure of the tires does not seem to be appropriate for this analysis. The reason is that the area of the tire footprint measured in field multiplied by the inflation pressure would lead to much higher axle weights than the ones measured in the field. Moreover, the parametrical investigation, verified by simple analytical calculations discussed in chapter 5, has shown that constant pressure distributions result in strain distributions totally different to the ones measured in the binder course. The ratio of the contractive to expansive strains is greater for a constant contact stress distribution. The peaks in the contractive strains are much narrower and of greater magnitude than the measured ones, whereas in the expansive strains, only two spiky peaks appear instead of a sole but mild peak. The argument that the contact pressure distribution is not constant is strengthened by the literature study, according to which a convex pressure distribution is expected for increasing inflation pressure and decreasing axle load.

In the parametrical investigation, the influence of a large number of parameters on the strain distribution is investigated. None of the investigated parameters led to a satisfying modelling of strains in high temperatures; a different strain distribution compared to the other experiments is measured. The change between expansion and contraction is shifted outwards, as are the absolute maxima of the contractive strains. Additionally, the ratio expansive to contractive strains is higher. This peculiar strain distribution could be a result of either pressure dependency with stiffness reduction under tension or tensile failure of the asphalt concrete, which could not be modelled with the different investigated constitutive models.

For the rest test series, reasonable results could be achieved. The linear viscoelasticity utilized for these analyses with the Prony series successfully described the asphalt concrete behavior for the winter and autumn temperatures. The greatest shortcoming of the model has been shown to be its incapability to produce non-reversible compliance strains. Traction was also not simulated in the finite element model, which might be the reason why the small expansive strains in the binder course could not be reproduced. Other factors leading to minor deviations with the static field test results could be a deviant loading duration, the existence of traction, as well as imperfections in the positioning of truck wheels on the sensors. The latter factor was minimized however as the best centered tests were selected to be fitted, verified with the help of the respective photos.

The simplified simulation of the dynamic field tests with the help of a pressure load the location of which updates at every time increment, had led to numerical results in

remarkable agreement with the experimental ones. As expected, the asphalt response is stiffer with increasing vehicle velocity, leading to lower peak strains. The remaining strains according to the finite element model, however, are lower than the measured ones. The use of a more suitable constitutive model, able to reproduce irreversible strains would be more appropriate. Finally, it should be noted, that for the dynamic tests, the tensile strains at 22cm depth are of greater magnitude than at 4cm, as a result of the higher effective asphalt stiffness and the different stress distribution due to the load motion. This lets us conclude that different distress mechanisms exist for the asphalt concrete for the static and the dynamic loading at mediocre temperatures.

All in all, as a further topic for future research in the numerical simulation of such field results would be the utilization of a unified temperature-dependent constitutive model, so that the long-term asphalt modulus and Poisson ratio are automatically adjusted in each model with only input the temperature. Furthermore, the implementation of a failure surface with limited tensile strength for the asphalt, could lead to a more accurate prediction of the strains in the binder course under high temperatures. Ultimately, the implementation of a damage parameter and its calibration with the help of the field measurements in combination with a finite element model able to accurately predict the asphalt response, will lead to a valuable tool for the non-destructive evaluation of the asphalt concrete pavements.

8.7 Conclusions

For this chapter, the following conclusions can be drawn:

- For the vehicle used in the tests, the utilization of a convex contact pressure distribution appears to be more suitable than the constant distribution. The assumption of the inflation pressure as contact pressure distribution does not seem to be appropriate.
- The contact pressure distribution influences the strain distribution close to the pavement surface and diminishes with the depth. For the depth of 22cm, its influence is already negligible.
- The strain distribution measured in the field can be reproduced satisfactorily with the use of linear viscoelasticity for temperatures of approximately 5 and 20°C both for the static and dynamic tests.
- For higher temperatures, viscoelasticity fails to describe the asphalt concrete behavior and a constitutive model with pressure dependency (stiffness reduction under tension) or viscoplasticity with limited tensile strength would be more appropriate.
- For temperatures colder than 5°C, the small deviation of the experimental to the numerical results can be accounted for by the existence of traction.
- The simple modeling of a moving load can satisfactorily reproduce the strains measured at the dynamic field tests.
- For the dynamic tests, the maximum expansive strains in the asphalt concrete are located at the bottom of the asphalt concrete layer.

All in all, although the results obtained with these preliminary finite element analyses are in quite a good accordance with the field measurements, the peculiar strain distribution under loading for high temperatures, as well as the existence of irreversible strains could not be properly modelled. It is hence proposed that further research on the topic shall be conducted, as a more sophisticated model which utilizes viscoplasticity as well as limited tensile strength would more accurately predict the asphalt concrete behavior under a broader band of environmental conditions.

9   Modelling of the tests at Zurich Airport

Abstract

In this chapter, a preliminary finite element simulation of the field tests at Zurich Airport is made. After the finite element model description, the measured and back-calculated strains are compared for different airplane gears, tests and depths in the asphalt concrete.

9.1   Finite element model

The finite element model adopted for the inverse analysis of the fiber optic measurement is similar to the one developed for the analysis of Hohlstrasse measurements.

The model length and width are both 5m. The layer thicknesses correspond with those obtained from the sample boring.

- Wearing course: 4cm
- Binder and asphalt base layer: 9.5cm
- Base (cement treated): 53cm
- Subgrade: 500cm

The model has two symmetry planes and it represents one fourth (one tire) of the main landing gear (Fig. 215).
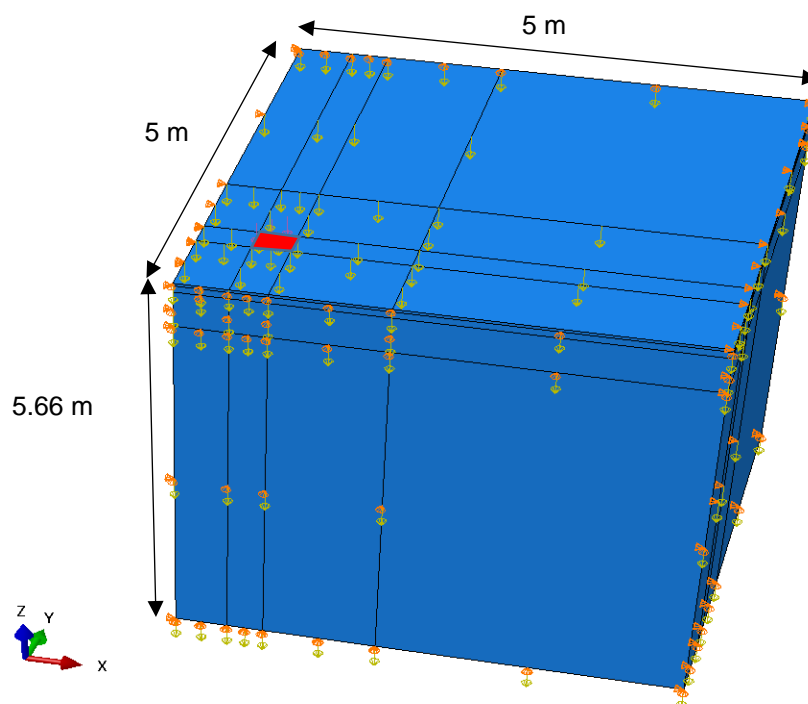

Fig. 215: *Three dimensional finite element model adopted for the simulation. Red = applied load surface (tire footprint)*

The tire footprint was modelled rectangular with a width of 36cm and a length of 30cm. The tire pressure was taken equal to 14.2bars (A340-300 and A330-300). The gear geometry is identical for the two airplanes types.

The layers have been modelled with a linear elastic constitutive model (soil and asphalt) model. The Interface between the asphalt base, base and subgrade layers is frictional with a horizontal load transfer coefficient $\mu = 0.5$. The interface between wearing course and the asphalt base layer was assumed to be rough.

The adopted mesh is shown in Fig. 216. The chosen element is a linear hexahedral element of type C3D8R (reduced integration).
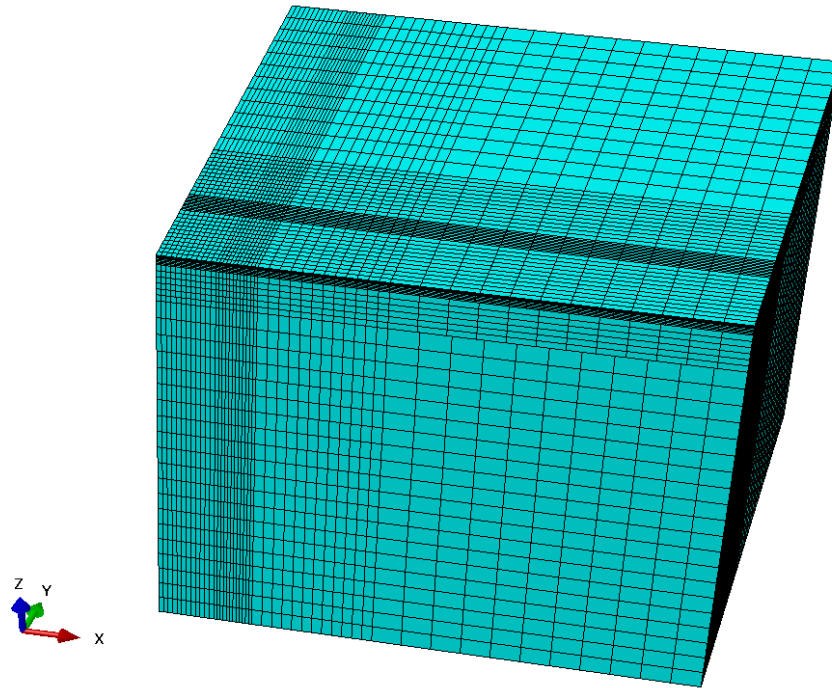

Fig. 216*: Adopted finite Element mesh of the boundary value problem at Zurich Airport*

9.2 Comparison of numerical and experimental results

Fig. 217 and Fig. 218 show the back-calculated strains at different depths for the measurement carried out the 27th of November 2016 with an A340-300 aircraft.

Main gear 2, top and bottom of base layer

Fig. 217 *Main gear 2: comparison between measured (dotted lines) and calculated (continuous lines) horizontal strains at different depths for 27th November 2016 measurement*

Main gear 1, top and bottom of the base layer

Fig. 218 *Main gear 1: comparison between measured (dotted lines) and calculated (continuous lines) horizontal strains at different depths for 27th November 2016 measurement*

It can be observed that for the measurements at shallow depths (~4cm) the calculated strains are not able to reproduce the correct shape of the strain field. This is due to the assumption of uniform tire load distribution, which is actually not realistic. A better correlation is found for the strains measured at larger depths (~13.5cm) where the effect of tire load distribution becomes negligible.

Fig. 219 and Fig. 220 show the back-calculated strains at different depths for the measurement carried out the 26th of February 2018 with an A330-300 aircraft.
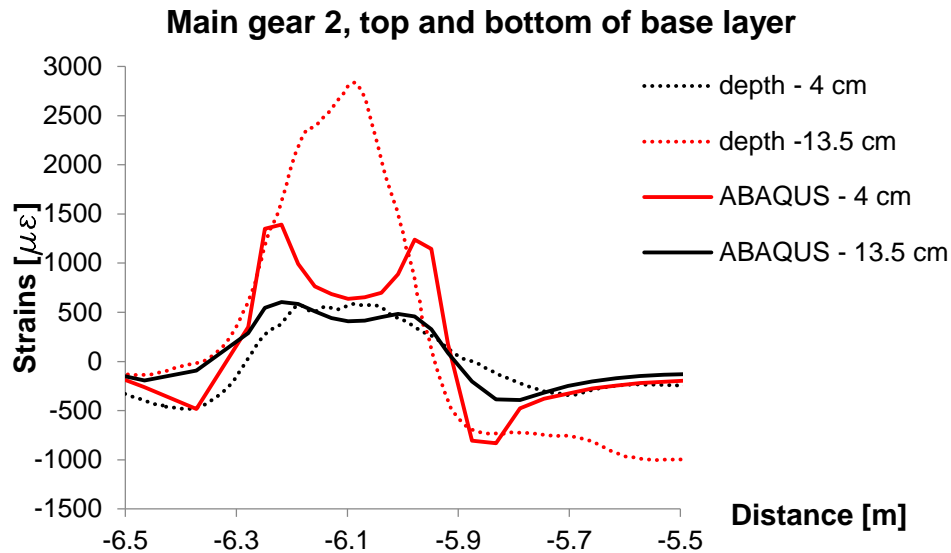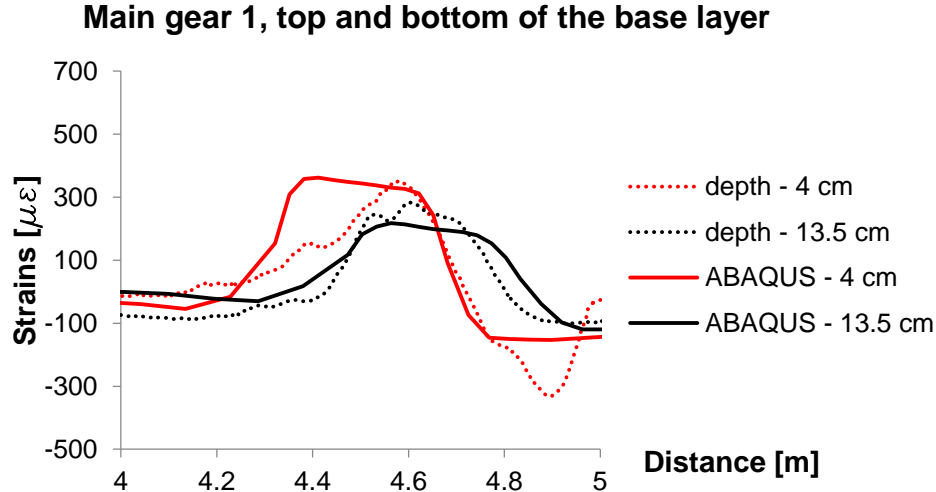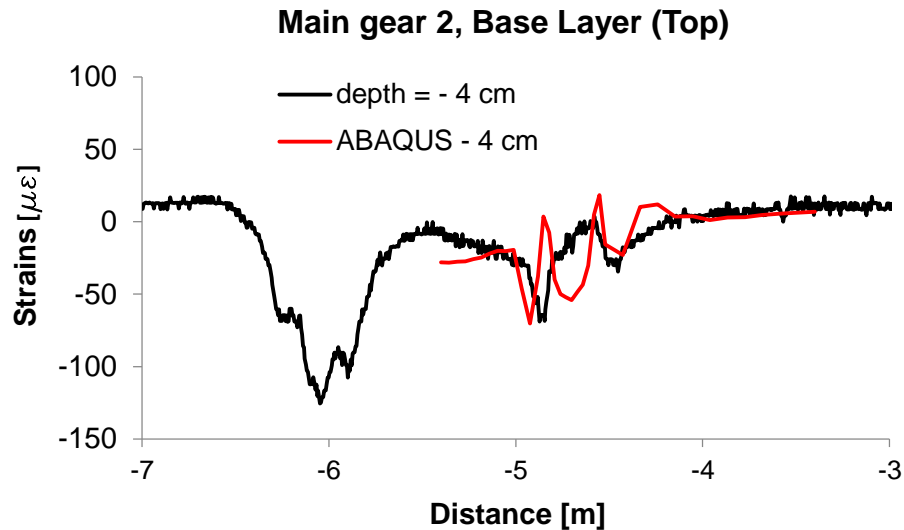
Fig. 219 *Main gear 2: comparison between measured (dotted lines) and calculated (continuous lines) horizontal strains at different depths (top of base layer) for 26th February 2018 measurement*
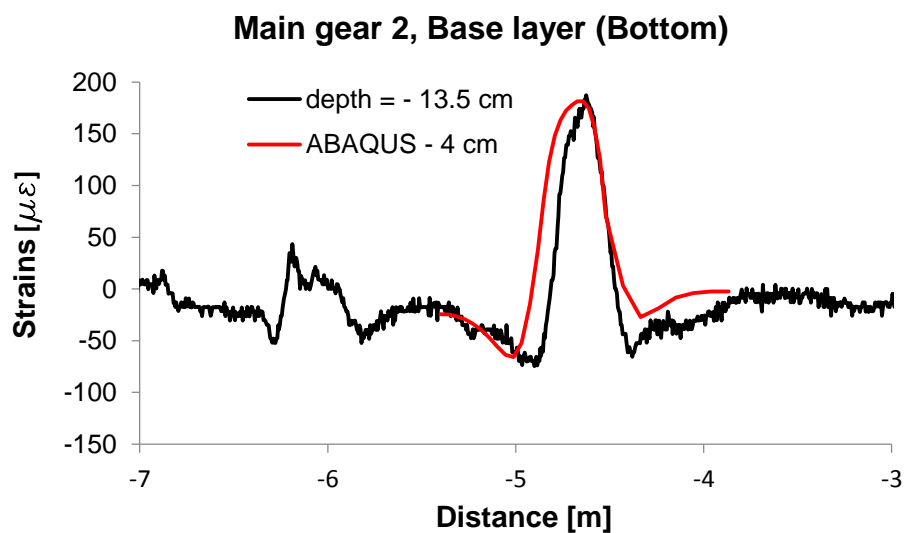
Fig. 220 *Main gear 2: comparison between measured (dotted lines) and calculated (continuous lines) horizontal strains (bottom of base layer) at different depths for 26th February 2018 measurement*

As for the previous measurements it can be observed that the calculated do not match accurately the measured ones at shallow depths (Fig. 219). A very good correlation can be observed between the measured and calculated strains at the bottom of the base layer. This is due to the vanishing effects of the irregular load distribution with depth.

Tab. 35 and Tab. 36 describe the obtained layer stiffness parameters obtained from the inverse analysis for the measurements carried out the 27th of November 2016 and the 26th of February 2018.

Tab. 35 *Backcalculated elastic material properties for the test of 27th November 2016*

	E	ν
Layer	**[kPa]**	**[-]**
Wearing course	400'000	0.4
Asphalt base course	800'000	0.4
Cement treated base	3'000'000	0.17
Subgrade	45'000	0.3

Tab. 36 *Backcalculated elastic material properties for the test of 26th February 2018*

	E	ν
Layer	**[kPa]**	**[-]**
Wearing course	3000'000	0.4
Asphalt base course	6000'000	0.4
Cement treated base	3'000'000	0.17
Subgrade	45'000	0.3

9.3   Conclusions

The back-calculation of the strains measured in the Zurich Airport has been challenging. Especially for shallow depths, the simulated strains deviate from those obtained in the field experiment. The implementation of a more appropriate strain field could lead to more satisfying results.

The simulation of a larger number of field experiments at different temperatures is additionally required in order to draw systematic conclusions for the behavior of the tested pavement under airplane loads. Moreover, the further investigation on this topic would help, in combination with the simulation of the field tests at the Hohlstrasse Zurich, to gain valuable insight in the overall behavior of asphalt concrete used in different pavement types and under different loads.

10   Conclusions and recommendations

The present project aimed to study the possibility of the embedment of distributed fiber optic sensors into pavements for the purpose of studying and characterizing the behavior of roads. The unprecedented amount of strain data, which can be gathered by means of this class of sensors, may contribute in conjunction with numerical models to the further understanding of the behavior of roads and stands loaded by different vehicles during their lifetime. The different field tests with fiber optic sensors in this project were accompanied with other state-of-the-art field experiments as ETH Delta measurements or laboratory tests on core drillings to further characterize the asphalt and base layers present in the field. The application of distributed fiber optic strain sensors in these projects was successful and gave promising insights into the behavior of the roads, both under static as well as dynamic loads caused by the traffic and aircrafts. Despite the general vulnerability of the fiber optic sensors, they have proven in this project to be robust sensors if they are embedded with care. Measurements could be conducted with these sensors for more than 2.5 years within this project and they are still active. Moreover, this robustness is underlined by the fact that the field tests were carried out within the framework of real construction industry projects and not only within experimental test sites.

10.1   Conclusions

Concerning the different research tasks within this project, the following conclusions can be drawn.

10.1.1   Fiber optic cables

The fiber optic cables used in this research project were produced by the project partner Brugg Kabel AG (now transferred to Solifos) in Brugg. Three strains sensing cable types (V1, V3 and V9, tight buffered) as well as one temperature sensing cable (T, loose tube) were applied on the test sites.

Laboratory test results

The research project started with laboratory tests on the fiber optic cables. Tests were carried out in the laboratory in order to figure out, whether the high temperatures present in asphalt during road construction may have a disadvantageous effect on the cables and in particular on the conversion coefficient between frequency shift and strain. As the test results showed, the cables were able to withstand temperatures of up to 138°C (higher temperature were not applied), in general without a noteworthy change of the behavior in the strain test bed. However, the temperature response gathered on loose cable sections was, beyond a cable specific temperature limit, observed to be nonlinear and the cables showed a tendency to shrink irreversibly after the heating cycle. Both effects are possibly caused by the plastic cable jacket. These effects are likely to create no problems when the cable is embedded in asphalt (bond to the surrounding asphalt material). However, the fact that the frequency shift measured along the cables, while they were exposed to the temperatures which may also be present in asphalt during operating time (up to around 40 to 50°C), is for some cables strongly non-uniform, has implications to the usage of these cables. In particular the V3 cable consisting of the largest amount of different layers and materials showed such a non-homogeneous response in this specific test. This behavior would make proper compensation of temperature effects on the measured frequency shift very difficult to achieve, if strain and temperature changes should be measured simultaneously. However, in the present research project application this was of no meaning, since always only the short term response under load was measured, assuming that no significant temperature change took place within the seconds or minutes (up to half an hour at the airport) of test duration.

The cables close to surface are not only exposed to strain and high temperatures, but also to significant transverse pressure resulting from the contact normal stress between the tire and the asphalt surface. Whereas the inflation pressure of tires for cars is around 250kPa and for trucks around 800kPa, for aircrafts magnitudes up to 1.4MPa are not unusual. Consequently, contact normal stresses in this order of magnitude act also at the asphalt surface under the tire. Since distributed fiber optic sensor technologies are also known to be weakly pressure-sensitive, tests in a pressure chamber, applying constant radial pressure to the cable were conducted. These tests should verify that the pressure from the tires does not create locally a frequency shift which will be misinterpreted as longitudinal strain, when the measurement results from the field tests are being processed. However, the laboratory test results showed that this effect plays for the present purpose a negligible role.

Mechanical robustness and behavior in the field tests

The different type of strain sensing cables applied in this research project, are protecting the vulnerable thin silica fiber in the core of the cable at different levels. Whereas cable V1 has only outer sheaths made from plastics, the more robust cable type V9 protects and seals the fiber by means of a thin metallic tube. The cable type V3 has even a steel wire armoring in addition to the metal tube. However, all cables survived the applied embedment procedure, even the most vulnerable cable type V1. From this point of view, the cable variety fulfilled the formulated requirements of sufficient robustness. Note that the overall probability of cable damage during installation is of course clearly reduced, if a more robust cable version is applied. Furthermore, the choice of the required cable robustness should be dependent on the layer in which the cable is embedded and also on the chosen embedment procedure. While selecting the type of cable, it should also be considered that, at least in theory, the involvement of cables, consisting of many sheath layers and materials, tend to redistribute (smear) the locally high strain gradient present in asphalt. Consequently, such a cable would indicate strain distributions slightly different from those present in asphalt owing the mechanical interaction of the sheath layers. Although in a parallel application of the different cables (airport) some differences in the measured strain magnitude of the different cable types were observed, it is not fully ensured that this is truly the effect of the different cable types, as it could also be caused by heterogeneities in asphalt, small differences in the distance from the cable to the center of the load or the different loading duration (viscosity) while measurements were taken in a certain order along the different cables. However, the detailed behavior of the different cable types should be investigated in future by means of a comparison of the performance of these cables e.g. by means of specific measurements in Hohlstrasse.

10.1.2 Embedment procedure

The embedment procedure of the fiber optic cables into asphalt plays an important role, both for the integrity of the sensor but also for the later measurement performance during the operation time. Several different embedment procedures were tested in this project. Placing the cable with clamps and screws or nails and covering it afterwards with fine asphalt material was e.g. a successful procedure. However, it turned out to be a rather time consuming and difficult procedure. Whether the application of the fine asphalt material could be omitted, was not investigated in this project. However, it seems to be a good measure against the possibility of tearing off the cables from asphalt, since the cable might stick on the wheels of the paver. The creation of a notch, using reinforcement bars while the pavement is rolled, seems to be a promising procedure. The fixation of the cables in these notches by means of a cold pouring compound was very efficient and the properties of the applied compound seemed to fulfill the requirements for a good strain transfer. Note that no damage to the fiber optic sensor occurred within the asphalt, neither during the embedment procedure nor during the sensor lifetime. All damages to the sensors occurred in the access shafts, where the fiber optic cable is spliced to specific connectors, which allow for plugging in the sensors into the measurement device. However, if there is sufficient cable over length foreseen in the shaft, these cable damages can also be repaired again.

10.1.3 Measurements results from the field tests

The distributed fiber optic sensors, proposed in this research project for the determination of the strains present in asphalt, proved to be a promising tool for this purpose. Strains were measured on two test fields, in Hohlstrasse, which is a classical road in Zurich, as well as on the Zurich Airport, where a stand was instrumented with these sensors. The high spatial variability of strains within the pavement, which was observed on these two test sites, is an important argument to use distributed fiber optic sensors instead of simple point sensors in order to quantify the strains present in asphalt. The highly resolved (1cm applied usually in this project) and continuous strain data along the sensor allows gaining clearly more and meaningful information about the strain field in asphalt compared to the situation where strain measurements are conducted with strain gauges only in some in some individual points. This is in particular the case if the sensor layout is chosen in a way that several sensor lines build a grid, which enables to understand the real strain field even closer.

Hohlstrasse Zurich

Strains were measured under static and dynamic loading originating from different vehicles with the sensors in the test field Hohlstrasse. As expected, a high dependency of strains on seasonal temperature variation was observed, but the temperature did not only scale the shape of the strain distribution, but changed also its characteristic shape. The large expansive strains, observed directly under the tire in summer, decreased clearly stronger with decreasing temperature than the contractive strain beside the tire. In the static tests, where the load from different vehicles rested for around 10 to 15s on the pavement, strains of up to around $1500\mu\varepsilon$ were measured under the truck. The strain magnitude under a car in winter was, on the other hand, approximately 100 times smaller, but remained still clearly detectable by the applied technology. This not self-evident, since the road is designed for a large amount of heavy traffic and the asphalt layers are in total 22cm thick. In order to milden the effect of the relatively long measurement time span in static tests (time dependent strains owing to viscous effects in asphalt), the measurement device applied for the dynamic tests could also be used in static tests for the purpose of a comparison (on reduced sensor lengths) and in order to study the effect of this time span and viscous behavior on the gathered strain distributions more in depth.

The dynamic measurements, which were carried out with an acquisition rate of 100Hz, allow for studying the behavior of asphalt under a real traffic load situation with subsequent axles traversing the sensor. A general trend of smaller strain magnitudes with increased vehicle speed was observed. However, the measured strains with a sufficiently high acquisition rate can serve not only for the purpose of characterizing the behavior of asphalt; it may have in future also potential for different applications, as driving direction and position as well as the number of axles and the velocity of the vehicle can be gathered from the sensor loop. However, a reliable and accurate quantification of the axle load seems, up to date, to be rather difficult and requiring a well-established model, accounting for temperature and potential aging effects in asphalt. Owing to the applied maximum frequency of 100Hz over 10m, strains originating from vehicles with velocities above 50km/h become difficult to properly resolve. However, higher frequencies for distributed measurement technologies are already available e.g. for lengths shorter than 10m and may also be increased in future for larger lengths. Owing to the smaller strain magnitudes in dynamic loading and the higher noise in the dynamic measurements, it became, in the current configuration, challenging to detect light vehicles as cars at high velocities of around 50km/h. However, also these limitations are expected to be brushed aside by a more careful sensor termination and further technological progress.

Zurich Airport

Compared to the test field in Hohlstrasse, the test field at the airport stand experiences a smaller number of load cycles but, on the other hand, it is exposed to longer loading periods. Measurements were conducted in an asphalt layer which was on top of a cement treated base material. During winter, almost no expansive strain was observed directly under the tire of the aircraft gear. However, already in warm autumn conditions,

expansive strains of up to 3000µε were measured directly under the tires and also at the bottom of the asphalt layer, up to 800µε resulted after exposure times of several minutes. Regarding the delayed strains owing to creep at longer exposure times and the possibility of warmer conditions than those met in autumn, even higher strains may be expected in summer on the stand. This seems also to be the reason for the local permanent deflections which could be observed around the aircraft main gears.

10.1.4 Numerical modelling

In a first step, it was investigated in the present project, whether the gathered measurement results can be approached by means of a simple constitutive relationship in numerical modelling using commercially available finite element (FEM) software. Whereas the measured settlements from ETH Delta were used to determine deformation parameters of the base and subgrade material, the parameters of asphalt were chosen in dependence on the laboratory tests on core drillings (EMPA). In general, it turned out to be challenging to match the measured response with FEM. The strain measurements gathered in cool to warm temperatures, could be modelled to a satisfying level with a viscoelastic model. On the other hand, the test results gathered in very warm conditions require further considerations as the introduction of viscoplastic behavior, in order to obtain a better fit. Hence, additional effort is required in order to model the test results numerically. Once the mechanical behavior is implemented correctly and matches the strain distributions measured in the field, the calibrated numerical models provide of course additional benefits as full information about other physical quantities than strain (displacements and stresses) and may be used in conjunction of the testing and understanding of new design methods, new pavement materials or for the simulation of damage processes in the road over its lifetime.

10.2 Recommendations

Distributed fiber optic sensors proved to be a promising tool for the measurement of the strain field present in the pavement under static and dynamic traffic load. In conjunction with numerical modeling, this method may be a powerful tool for testing and investigating new pavement materials and design methods outside the existing standard design practice. Furthermore, thanks to its large amount of highly resolved strain data, it represents an interesting new source for gathering measurement data in order to calibrate numerical models. Based on the present research, the following recommendations can be made:

- Since the sensor installation at the two test sites is still working, it is recommended to further conduct periodic strain measurements. This in order to investigate whether over time a change in the behavior of the road owing to aging effects could be observed. Such additional measurements could explore the further possibility of turning the fiber optic strain sensor into an instrument for monitoring the structural health of a road.
- Since all cable types demonstrated to be able to withstand the harsh environment, it seems to be worth it, to study their performance (potential for small slippage) in asphalt more in depth by additional specific measurement in Hohlstrasse in order to use an adequate cable type for the foreseen purpose.
- It is recommended to further investigate the potential of an inverse determination of individual axle loads by means of dynamic strain measurements.
- During this research project, a large amount of unique strain data in pavements under different thermal conditions, vehicle loads and velocities in different pavement depths was gathered. It is recommended to use this data for calibration of new or existing constitutive models of asphalt, in order to gain further understanding of its behavior.

10.3 Outlook

The field of fiber optic sensing is still a rather dynamic sector. During the last decade, several basic improvements or even break troughs were realized in terms of possible

spatial resolution, sensor lengths, acquisition rates and measurement precision. Hence, it appears not unlikely that, although some physical limits exist, in the next several years additional improvements as e.g. higher scanning / acquisition rates for distributed fiber optic sensors may become commercially available. Hence, currently existing application limits may be pushed forward in near future.

Appendix

Appendix

I Stress and strain fields

In this appendix, the stress and strain fields for the test series 8 and 9 at Hohlstrasse Zurich are shown. The stress and strain fields were computed with finite element models which were calibrated with according to the field measurements, as described in chapter 8.

I.1 Test series 8 (autumn)
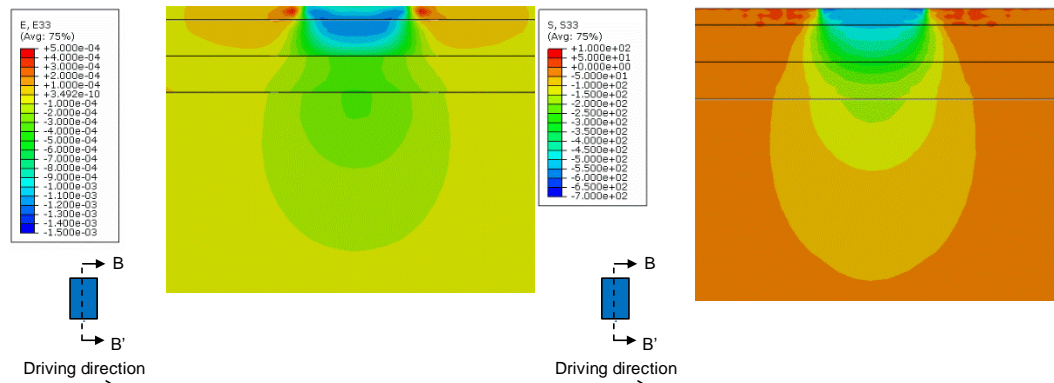
I.1.1 Front axle

Fig. 1 Distribution of vertical strains [-] (left) and stresses [kN/m²] (right) with the depth, under the front axle and during the test series 8 (autumn)

Fig. 2 Distribution of transverse strains [-] (left) and stresses [kN/m²] (right) with the depth, under the front axle and during the test series 8 (autumn)

Fig. 3 *Distribution of transverse strains [-] (left) and stresses [kN/m^2] (right) on horizontal planes of different depths, under the front axle and during the test series 8 (autumn)*
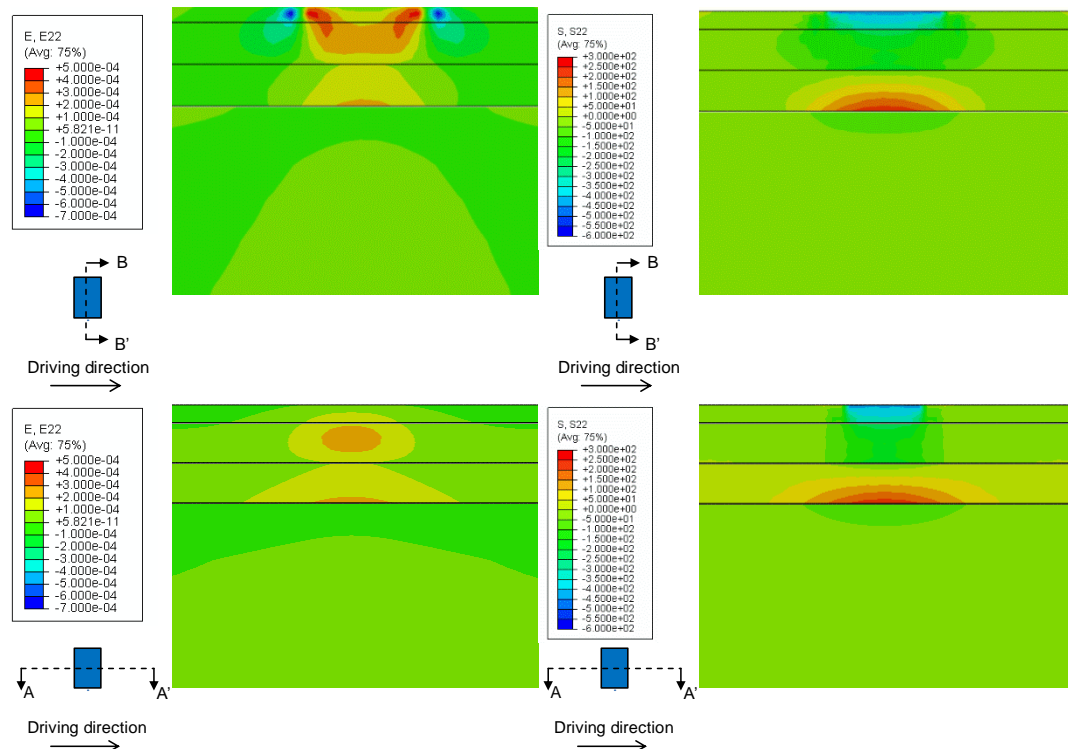
I.1.2 Rear axle

Fig. 4 *Distribution of transverse strains [-] (left) and stresses [kN/m²] (right) with the depth, under the rear axle and during the test series 8 (autumn)*
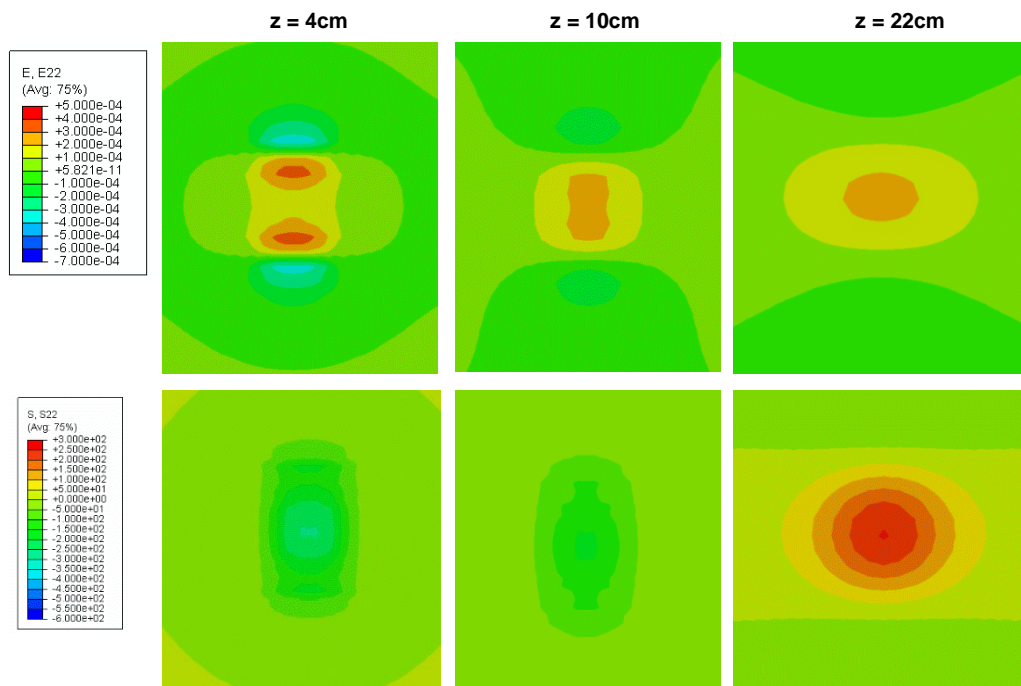

Fig. 5 *Distribution of transverse strains [-] (left) and stresses [kN/m²] (right) on horizontal planes of different depths, under the rear axle and during the test series 8 (autumn)*

I.2 Test series 9 (winter)

I.2.1 Front axle

Fig. 6 *Distribution of vertical strains [-] (left) and stresses [kN/m²] (right) with the depth, under the front axle and during the test series 9 (winter)*

Fig. 7 *Distribution of transverse strains [-] (left) and stresses [kN/m²] (right) on horizontal planes of different depths, under the front axle and during the test series 9 (winter)*
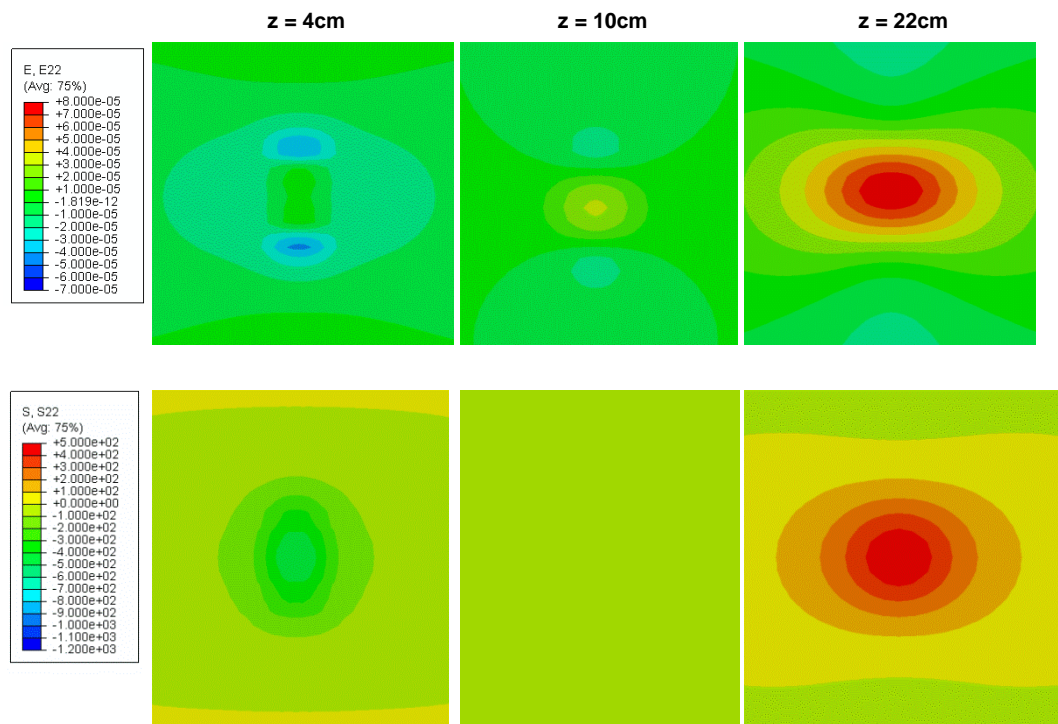
Fig. 8 *Distribution of transverse strains [-] (left) and stresses (right) [kN/m²] on horizontal planes of different depths, under the front axle and during the test series 9 (winter)*
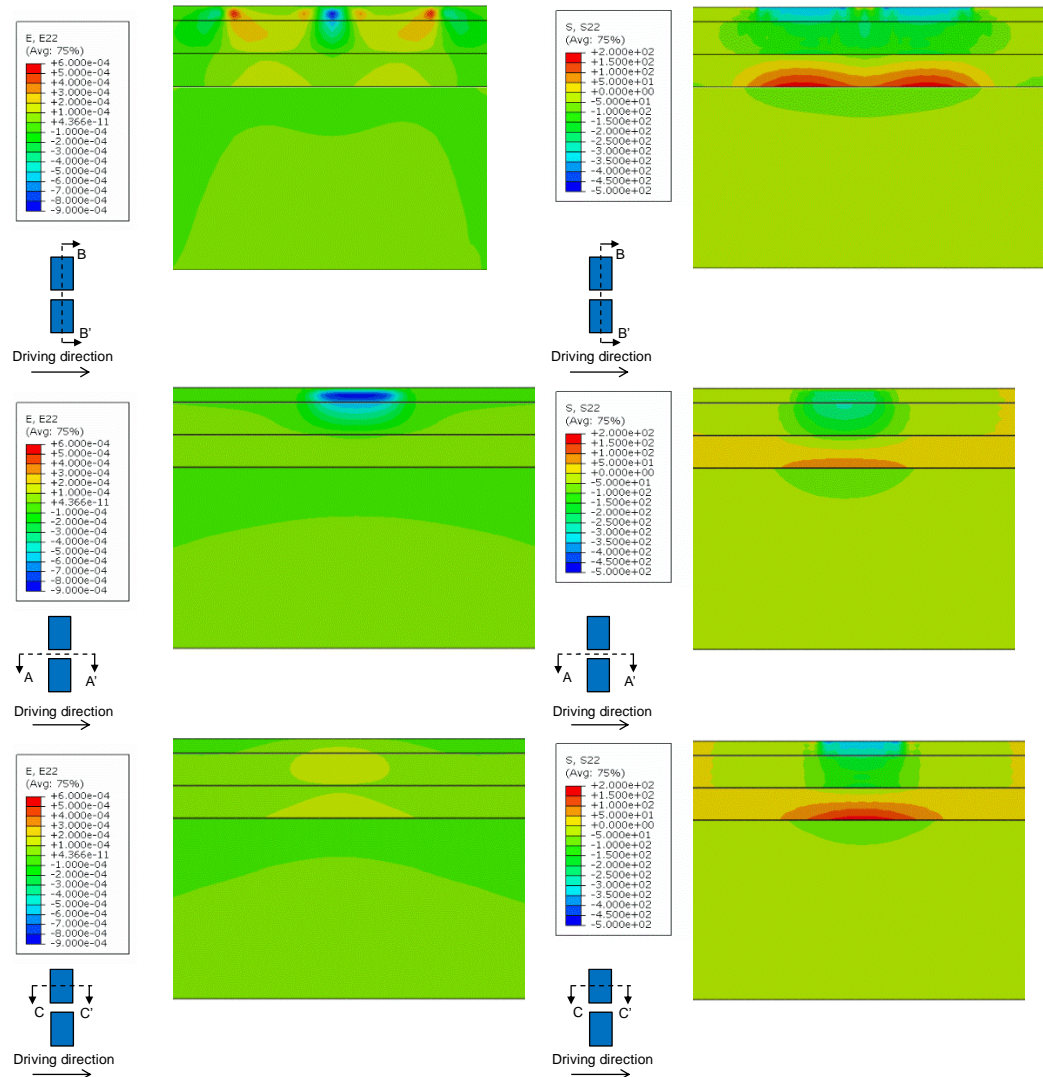
I.2.2 **Rear axle**

Fig. 9 *Distribution of transverse strains [-] (left) and stresses [kN/m²] (right) with the depth, under the rear axle and during the test series 9 (winter)*
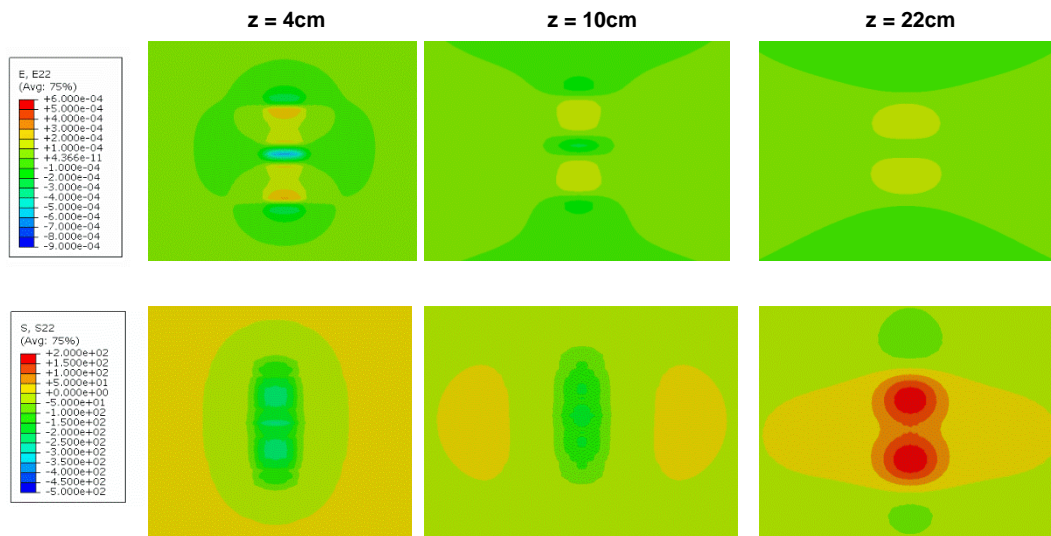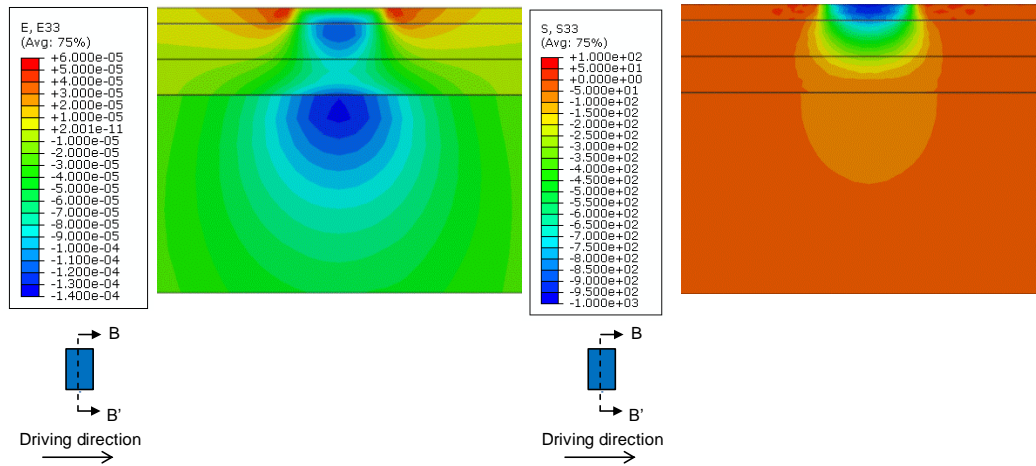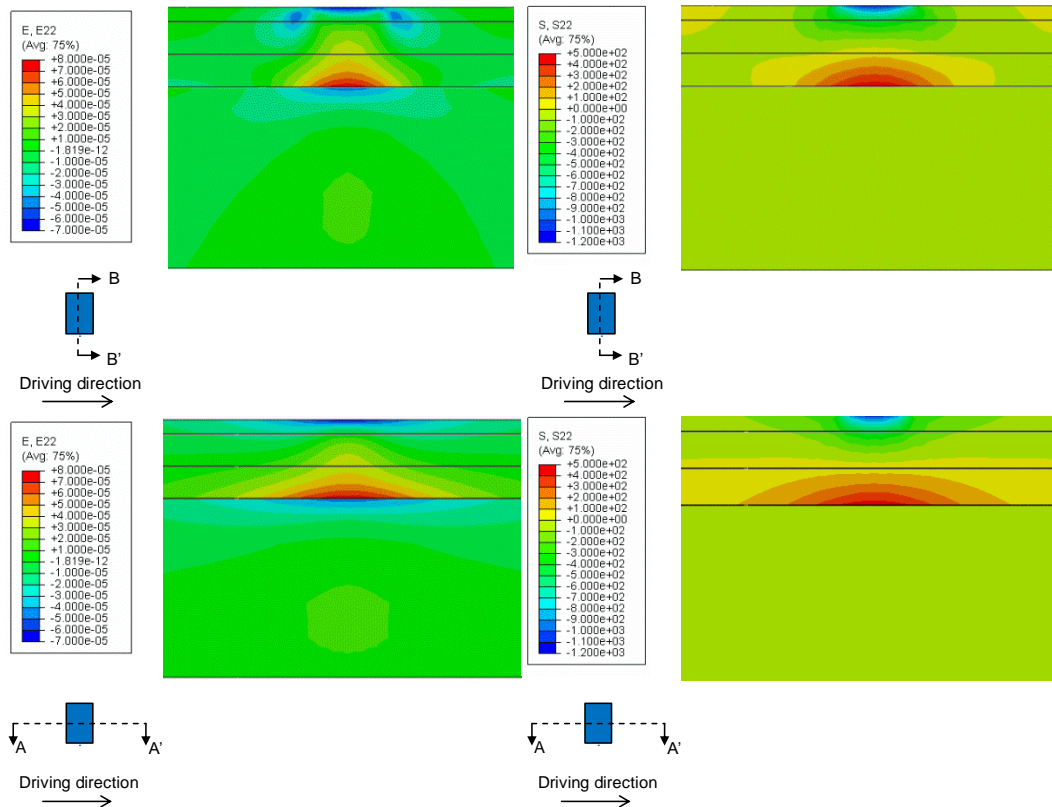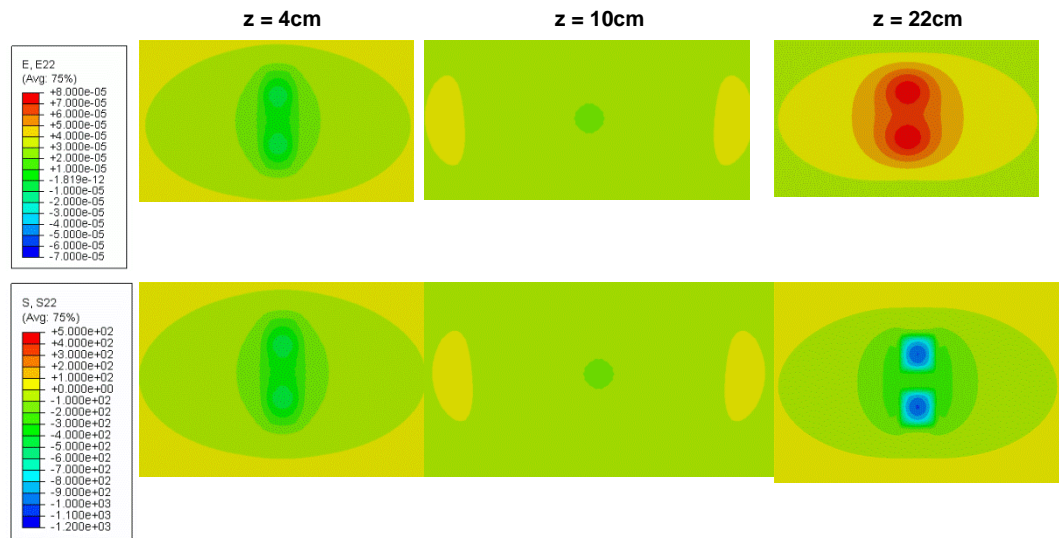
Fig. 10 *Distribution of transverse strains [-] (left) and stresses [kN/m^2] (right) on horizontal planes of different depths, under the rear axle and during the test series 9 (winter)*
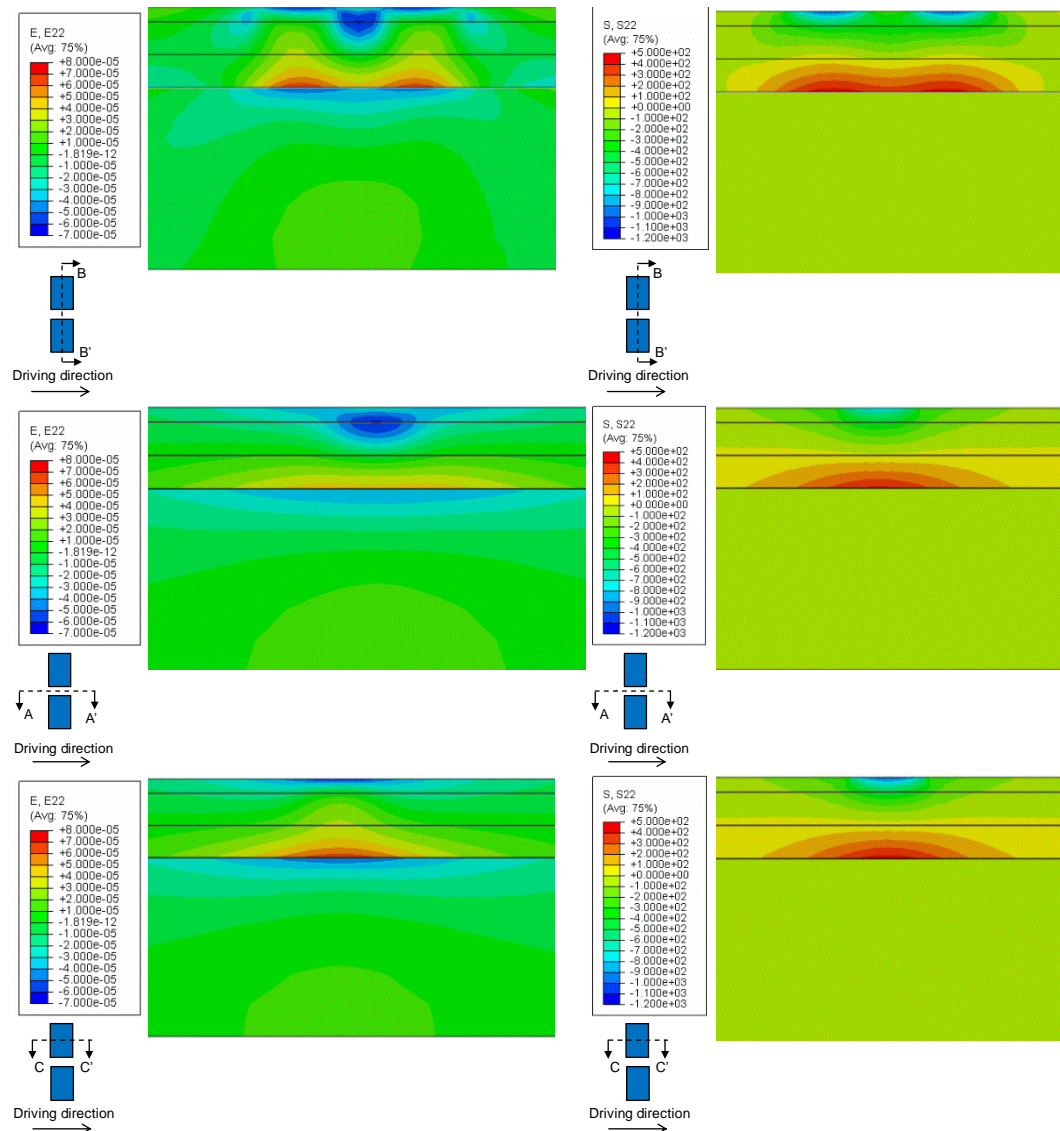
Glossary

Term	Meaning
BOTDA	Brillouin Optical Time Domain Analysis, a distributed fiber optic sensor technology
CTB	Cement treated base
DITEST STA 202	Distributed temperature and strain analyzer, a measurement device using BOTDA manufactured by Omnisens SA
IGT	Institute for Geotechnical Engineering, ETH Zurich
OBR 4600	Optical Backscatter Reflectometer, a measurement device using SWI manufactured by Luna Inc.
ODiSI B	Optical Distributed Sensor Interrogator, a measurement device allowing using SWI manufactured by Luna Inc.
SWI	Swept Wavelength Interferometry, a distributed fiber optic sensor technology, a distributed fiber optic sensor technology, sometimes also denoted c-OFDR
V1, V3, V9	Names of tight buffered strain sensing cable versions manufactured by Brugg Kabel AG
$\mu\varepsilon$, μstrain	Microstrain, a strain corresponding to a relative elongation $\Delta L/L$ of 10^{-6} or 0.001‰

References

Publications and documentations

[1] Inaudi D., (2002), **„Photonic sensing technology in civil engineering applications", in "Handbook of optical fiber sensing technology".** *Lopez Higuera J.M. editor, Wiley.*

[2] Froggatt M., Moore, J. (1998), **"High resolution strain measurement in optical fiber with Rayleigh scatter"** *Appl. Opt. 37, 1735–1740.*

[3] Gifford, D.K., Kreger, S.T., Sang, A.K., Soller, B.J. (2007), **„Swept-wavelength interferometric interrogation of fiber Rayleigh scatter for distributed sensing applications"**, *Proceedings of SPIE, 6770.*

[4] Bueche N., Rychen P., Dumont A.-G., (2009), **„Optical fiber feasibility study in Accelerated Pavement Testing facility"**, *The sixth international conference on maintenance and rehabilitation of pavement and technological control (MAIREPAV), Torino, Italy.*

[5] Doré G., Duplain G., Pierre P., (2007), **„Monitoring mechanical response of in-service pavements using retrofitted fiber optic sensors***", Proc. Advanced Characterizations of Pavement and Soil Engineering Materials, Athens, Greece.*

[6] Whelan B.E., Brunton M., Nosenzo G., Daryl Kay D., Buys H. (2012), **„Continuous monitoring of mining induced strain in a road pavement using fiber Bragg grating sensors***", Proc. of SPIE, Vol. 8351.*

[7] Doré G. & Duplain G., (2002), **„Monitoring pavement response during spring thaw using fiber-optics sensors***", Proc. 6th International conf. on the bearing capacity of roads and airfields, Lisbon, Portugal.*

[8] Loizos A., Plati C., Papavasiliou V., (2013), **„Fiber Optic sensors for assessing strains in cold in-place recycled pavements***", International Journal of Pavement Engineering, Vol. 14, No. 2, pp. 125 – 133.*

[9] Imacho M., Matsumiya N., Nakamura T., Sato O., Kawasaki R., Ochiai N., Suzuki T., Syoji T., (2000), **„Development of road temperature sensing system using optical fiber***", Proc. 7th World congress on intelligent systems, Torino, Italy.*

[10] Imacho M., Nakamura T., Hashiba K., (2002), **"Road icing detection and forecasting system using optical fiber sensors for use in road management in winter"**, *Hitachi Cable Review, No. 21, pp. 29-34*

[11] Chapeleau, X., Blanc, J., Hornych, P., Gautier, J.L., Carroge, J. (2014), **„Use of distributed fiber optic sensors to detect damage in a pavement. 7th European Workshop on Structural Health Monitoring"**, *July 8-11, 2014. La Cité, Nantes, France*

[12] Chapeleau, X., Blanc, J., Hornych, P., Gautier, J.L., Carroge, J. (2017), **„Assessment of cracks detection in pavement by a distributed fiber optic sensing technology"**, *Journal of Civil Structural Health Monitoring Vol. 7, No. 2, pp. 1-12.*

[13] Wang, H., and Xiang, P. (2016), **„Strain transfer analysis of optical fiber based sensors embedded in an asphalt pavement structure"**, *Measurement Science and Technology, Vol. 27, No. 7.*

[14] Xiang, P., Wang, H. (2016), **„Optical fiber-based sensors for distributed strain monitoring of asphalt pavements"**, *International Journal of Pavement Engineering, pp. 1 – 9.*

[15] Liu, W., Wang, H., Zhou, Z., Xing, X., Cao, D., Jiang, Z. (2015), **„Optical fiber-baser sensors with flexible encapsulation for pavement behavior monitoring"**, *Structural and Health Monitoring, Vol. 22, pp. 301-313.*

[16] Zhi Zhou, Wanqiu Liu, Ying Huang, Huaping Wang, Jianping He, Minghua Huang, Jinping Ou (2012) **"Optical fiber Bragg grating sensor assembly for 3D strain monitoring and its case study in highway pavement"**, *Mechanical Systems and Signal Processing 28, 36-49*

[17] Eric Udd, Marley Kunzler, Harold Martin Laylor, Whitten L. Schulz, Stephen, T. Kreger, John C. Corones, Robert McMahon, Steven M. Soltesz, Robert Edgar (2001), "**Fiber grating sensor systems for traffic monitoring**", *Health Monitoring and Management of Civil Infrastructure Systems*

[18] Paul J. Cosentino, P.E; Wulf von Eckroth; and Barry G. Grossman (2003), "**Analysis of Fiber Optic Traffic Sensors in Flexible Pavements**", *Journal of transportation engineering*

[19] Malla, R., Sen A. and Garick N. (2008), "**A special fiber optic sensor for measuring wheel loads of vehicles on highways**", *Sensors*

[20] Bailey, D. & Wright, E. (2003), **„Practical fiber optics",** *Newnes (imprint of Elsevier), Oxford.*

[21] Thévenaz, L. (ed.) (2011), "**Advanced fiber optic – Concepts and technology**", *EPFL Press, Lausanne.*

[22] Hauswirth, D. (2015), **„A study of the novel approaches to soil displacement monitoring using distributed fiber optic strain sensing"**, *PhD thesis No. 22282, ETH Zürich.*

[23] Thévenaz, L. & Niklès, M. (2007), **„Recent progress in Brillouin distributed fiber sensing"**, *The 2nd International Workshop on Opto-electronic Sensor-based Monitoring in Geoengineering, Nanjing, China, pp. 12-19.*

[24] Cotter, D. (1983), **„Stimulated Brillouin scattering in monomode optical fiber",** *J. Opt. Commun. Vol. 4, No. 1, pp. 10-19.*

[25] Horiguchi, T., Kurashima, T., & Tateda, M. (1989), **„Tensile strain dependence of Brillouin frequency shift in silica optical fibers",** *IEEE Photonics Technology Letters, Vol. 1, No. 5, pp. 107-108.*

[26] Niklès, M. (2007), **„Fibre optic distributed scattering sensing system: Perspectives and challenges for high performance applications",** *3rd European Workshop on Optical Fibre Sensors (EWOFS)*, Proc. of SPIE, Vol. 6619, pp. 0D-1-0D8.

[27] Horiguchi, T., Shimizu, K., Kurashima, T., Tateda, M. & Koyamada, Y. (1995), **„Development of a distributed sensing technique using Brillouin scattering",** *Journal of Lightwave Technology*, Vol. 13, No. 7, pp. 1296-1302.

[28] Niklès, M., Thévenaz, L. & Robert, P.A. (1997), **„Brillouin gain spectrum characterization in single-mode optical fibers",** *Journal of Lightwave Technology*, Vol. 15, No. 10, pp. 1842-1851.

[29] Omnisens SA (2012), **„Datasheet DITEST STA-R Series",** www.omnisens.com.

[30] Samiec, D. (2011), **„Verteilte faseroptische Temperatur- und Dehnungsmessung mit sehr hoher Ortsauflösung",** *Photonik, No. 6, pp. 34-37.*

[31] Zhang, H. & Wu, Z. (2008), **„Performance evaluation of BOTDR-based distributed fiber optic sensors for crack monitoring",** *Structural Health Monitoring*, Vol. 7, pp. 143-156.

[32] Niklès, M. (2009), **„Long-distance fiber optic sensing solutions for pipeline leakage, intrusion and ground movement detection",** *Fiber Optics Sensors and Applications VI, Udd, E., Du, H.H. & Wang, A. (eds.)*, Proc. of SPIE, Vol. 7316, pp. 02-1-02-13.

[33] Luna Inc. (2013), **„Datasheet Optical Backscatter Reflectometer, Model OBR 4600",** lunainc.com.

[34] Luna Inc. (2014), **„Datasheet Optical Distributed Sensor Interrogator, Model ODISI-B",** lunainc.com.

[35] Luna Inc. (2012), **„Optical backscatter reflectometer 4600",** user guide. Luna technologies, Blacksburg.

[36] Iten, M. (2011), **„Novel applications of distributed fiber-optic sensing in geotechnical engineering",** *PhD thesis No. 19632*, ETH Zürich.

[37] Iten, M., Hauswirth, D., Fischli, F. & Puzrin, A.M. (2012), **„Distributed Fibre-optic Sensors in Geotechnical Engineering Monitoring",** *ISSMGE Bulletin*.

[38] Brugg Kabel AG (2011), **„Datasheet BRUsens strain V3",** www.bruggcables.com/sensing.

[39] Brugg Kabel AG (2011), **„Datasheet BRUsens strain V9",** www.bruggcables.com/sensing.

[40] Brugg Kabel AG (2013), **„Datasheet BRUsens strain V1",** www.bruggcables.com/sensing.

[41] Brugg Kabel AG (2011), **„BRUsens Temperature 85°C",** www.bruggcables.com/sensing.

[42] Schweizerischer Verband der Strassen- und Verkehrsfachleute VSS (2013), **„Walzasphalt – Konzeption, Ausführung und Anforderungen an die eingebauten Schichten",** *Norm SN 640 430.*

[43] Méndez, A. & Diatzikis, E. (2006), **„Fiber optic distributed pressure sensor based on Brillouin scattering",** *Optical Fiber Sensors 2006*, OSA Technical Digest, paper ThE46.

[44] Iten, M. (2011), **"Novel applications of distributed fiber-optic sensing in geotechnical engineering",** *PhD thesis No. 19632*, ETH Zürich.

[45] Rabaiotti, C. (2008), **„Inverse analysis in road geotechnics",** *PhD thesis No. 18135*, ETH Zürich.

[46] Rabaiotti, C., Hauswirth, D., Fischli, F., Facchini, M. & Puzrin, A.M. (2017), **„Structural health monitoring of airfield pavements using distributed fiber-optics sensing",** *SMAR 2017, Zurich.*

[47] Airbus (2017), **„A340-200/300 – Aircraft characteristics - Airport and maintenance planning",** *AIRBUS S:A:S Customer Services, Technical Data Support Service, Blagnac Cedex, France.*

[48] Airbus (2017), **„A330 – Aircraft characteristics - Airport and maintenance planning",** *AIRBUS S:A:S Customer Services, Technical Data Support Service, Blagnac Cedex, France.*

[49] A.M. Puzrin and C. Rabaiotti (2010), **„A thermomechanical framework for non-linear hyperviscoelastic materials",** *Journal of Rheology, Vol 54, pp 619-642*

[50] Pedro Yap (1988), „**A comparative Study of the Effect of Truck Tire Types on Road Contact Pressures**", *SAE Technical Paper Series Nr. 881846*

[51] M. De Beer, C. Fisher and Jooste F. J. (1997), „**Determination of pneumatic tire/pavement interface contact stresses under moving loads and some effects on pavements with thin asphalt surfacing layers**", *8th International Conference on Asphalt Pavements (8th ICAP '97), August 10-14,1997, Seattle, Washington, USA. Vol. 1, pp 179-227.*

[52] Zhong Qi Yue and Otto J. Svec (1995), „**Effects of tire-pavement contact pressure distributions on the response of asphalt concrete pavemetns**", *Canadian Journal for civil Engineering, Vol 22, 849-860*

[53] Joh T. Tielking and Freddy L. Roberts (1987) „**Tire Contact Pressure and its effect on pavement strain**", *Journal of Transport Engineering, Vol 113, No. 1 , 56-71*

[54] Rex William Hansen, Carl Bertrand, K. M. Marshek, and W.R. Hudson (1989), „**Truck tire pavement contact pressure distribution characteristics for super single 18-22.5 and smooth 11R24.5 tires**", *Research report 1190-1, Center for transportation research, The University of Texas at Austin*

[55] Hao Wang , Imad L. Al-Qadi and Ilinca Stanciulescu (2012) „**Simulation of tyre–pavement interaction for predicting contact stresses at static and various rolling conditions**"*, International Journal of Pavement Engineering, 13:4, 310-321*

[56] R. L. Lytton, J. U., E.G. Fernando, R. Roque, D. Hiltunen, S.M. Stoffels (1993), **„Development and validation of performance prediction models and specifications for asphalt binders and paving mixes"**, *Strategic highway research program (SHRP-A-357)*

[57] Y. Richard Kim and Dallas N. Little (1990), **„One-dimensional constitutive modeling of asphalt concrete"**, *Journal of Engineering Mechanics, Vol. 116, No. 4, 751-772*

[58] R.A. Schapery (1984), **„Correspondence Principles and a generalized J Integral for Large Deformation and Fracture Analysis of Viscoelastic Media "**, *International Journal of Fracture, Vol 25, 195-223*

[59] Yong-Rak Kim, D. H. Allen, D.N. Little (2007), **„Computational Constitutive Model for predicting nonlinear viscoelastic damage and fracture failure of asphalt concrete mixtures"**, I*nternational Journal of Geomechanics, Vol. 7, No. 2, 102-110*

[60] M. Arraigada, M.N. Partl (2016), **„Test Report No 5214011902",** *EMPA, Swiss Federal Laboratories for Materials Science and Technology*

[61] SIMULIA (2014), **Abaqus 6.14 Analysis User's guide.**

Project Closure

Schweizerische Eidgenossenschaft
Confédération suisse
Confederazione Svizzera
Confederaziun svizra

Eidgenössisches Departement für
Umwelt, Verkehr, Energie und Kommunikation UVEK
Bundesamt für Strassen ASTRA

FORSCHUNG IM STRASSENWESEN DES UVEK

Version vom 09.10.2013

Formular Nr. 3: Projektabschluss

erstellt / geändert am: 10.12.2018

Grunddaten

Projekt-Nr.:   VSS2014-501

Projekttitel: Distributed fiber optic strain sensing in pavements

Enddatum: 31.3.2018

Texte

Zusammenfassung der Projektresultate:

Das Ziel dieses Projektes war die Untersuchung des messtechnischen Potentials von in Asphaltschichten eingebauten Glasfaserkabeln zur verteilten Messung der Dehnungen in Verkehrsflächen. Dies mit dem Zweck, das Tragverhalten der Schichten unter Verkehr mit dieser neuartigen Sensortechnologie zu messen und zu beurteilen können. Dazu wurden in einem ersten Schritt die vom Projektpartner "Brugg Kabel AG" zur Verfügung gestellten robusten Glasfaserkabel im Labor hinsichtlich eines möglichen nachteiligen Effekts der hohen Belagseinbautemperaturen untersucht. Daneben wurden verschiedene Einbaumethoden dieser Glasfaserkabel direkt an den Versuchstandorten evaluiert. Der in diesem Forschungsprojekt vorgesehene Verwendungszweck der Glasfaserkabel erlaubte es, zusammen mit den verwendeten Einbauverfahren, die Glasfaserkabel als Sensoren an zwei Versuchstandorten in unterschiedlicher Tiefe in die Asphaltschichten einzubauen.

In der Folge wurden an den Standorten Flughafen Zürich und Hohlstrasse in Zürich Dehnungen mit räumlich sehr hoher Auflösung von rund 10mm in den Asphaltschichten unter Verkehrslast gemessen. Die Messungen wurden unter verschiedenen Randbedingungen durchgeführt. Einerseits wurden die Dehnungen unter kurzzeitig stehenden Fahrzeugen sowie unter mit verschiedenen Geschwindigkeiten darüberfahrenden Fahrzeugen durchgeführt. Bei Letzterem wurden die Dehnungen zusätzlich mit hoher zeitlicher Auflösung von 100Hz während der Überfahrt gemessen. Andererseits wurden die Messungen mit verschiedenen Lasten und in verschiedenen Jahreszeiten durchgeführt, um den Einfluss der Lastgrösse wie auch der Asphalttemperatur abzubilden.

Die entlang des Glasfaserkabels zeitlich wie räumlich hochaufgelösten Dehnungen geben eine einzigartige detaillierte Einsicht in das Tragverhalten der Asphaltschichten und erlauben auf der anderen Seite auch eine zumindest teilweise Charakterisierung des den Sensor überfahrenden Fahrzeuges. Weiter wurde abschliessend versucht, mittels numerischer Modellierung die gemessenen Dehnungen nachzubilden, um Rückschlüsse über die Materialparameter sowie über das Tragverhalten der involvierten Schichten zu gewinnen.

Schweizerische Eidgenossenschaft
Confédération suisse
Confederazione Svizzera
Confederaziun svizra

Eidgenössisches Departement für
Umwelt, Verkehr, Energie und Kommunikation UVEK
Bundesamt für Strassen ASTRA

Zielerreichung:

Die Zielsetzungen dieses Forschungsprojektes wurden erreicht. Die kontinuierlich messenden Glasfasersensoren konnten unter realen Baustellenbedingungen in üblichen Bauprojekten im Asphalt eingebaut und es konnten an zwei Versuchsstandorte Dehnungen gemessen werden. Die im Asphalt eingebauten Sensoren erwiesen sich als robust und lieferten im Zeitraum dieses Forschungsprojektes verlässlich zeitlich wie räumlich hochaufgelöste Dehnungsdaten unter Verkehrslast, welche zur numerischen Modellierung der Problemstellung verwendet werden konnten.
Das vorliegende Forschungsprojekt zeigt, dass die Verwendung von Glasfasersensoren auch in der eher rauen Umgebung von Asphaltschichten machbar ist und das diese Sensorklasse wertvolle Messresultate zur Beurteilung des Tragverhaltns von Asphaltschichten liefern kann.

Folgerungen und Empfehlungen:

Verteilt messende Glasfasersensoren erlauben eine zeitlich wie räumlich hochaufgelöste kontinuierliche Dehnungsmessung in Asphaltschichten. In Kombination mit anderen Messtechniken, könnten Sie benutzt werden, um das Tragverhalten von neuen Materialien oder die Angemessenheit neuer Dimensionierungsmethoden zu überprüfen. Zudem erlauben die Messungen mit dynamischer Belastung Rückschlüsse über einige Charakteristiken des überfahrenden Fahrzeuges. Es erscheint zum jetzigen Zeitpunkt sinnvoll, die Möglichkeiten dieser Technologie in diesem Bereich weiter auszuloten. Zudem wird empfohlen, im Sinne einer weiteren Verbesserung der Anwendung dieser Technologie, Messresultate von unterschiedlichen Glasfaserkabeltypen und Sensoreinbauverfahren miteinander zu vergleichen, um ein möglichst optimiertes Sensorverhalten in den Asphaltschichten zu erreichen. Zudem bietet sich die Möglichkeit, die einzigartige Messdatenbasis dieses Projekts mit einer verfeinerten numerischen Analyse abzubilden, um das Tragverhalten detaillierter zu studieren.

Publikationen:

Rabaiotti, C., Hauswirth, D., Fischli, F., Facchini, M. & Puzrin, A.M. (2017), „Structural health monitoring of airfield pavements using distributed fiber-optics sensing", SMAR 2017, Zurich.

Der Projektleiter/die Projektleiterin:

Name: Puzrin   Vorname: Alexander M.

Amt, Firma, Institut: Institut für Geotechnik, ETH Zürich

Unterschrift des Projektleiters/der Projektleiterin:

Schweizerische Eidgenossenschaft
Confédération suisse
Confederazione Svizzera
Confederaziun svizra

Eidgenössisches Departement für
Umwelt, Verkehr, Energie und Kommunikation UVEK
Bundesamt für Strassen ASTRA

FORSCHUNG IM STRASSENWESEN DES UVEK

Formular Nr. 3: Projektabschluss

Beurteilung der Begleitkommission:

Beurteilung:

Das Projekt zeigt im Bereich des Monitorings von Dehnungen in Asphaltschichten unter Verkehrslast neue Möglichkeiten auf. Die Glasfasersensorik erlaubt heutzutage die Messung von engmaschigen Dehnungsverteilungen im Asphalt unter stehender und fahrender Belastung entlang der eingebauten Glasfaser. Die Messresultate zeigen interessante Einblicke in die Lastabtragung von Asphaltschichten und erlauben gegebenenfalls neue Interpretationen hinsichtlich der Interaktion Rad - Strasse. Dies insbesondere dann, wenn diese Resultate mit einer treffenden numerischen Modellierung der Problemstellung gekoppelt werden.

Umsetzung:

Die untersuchte Messtechnik erwies sich an den Versuchsstandorten als praxistauglich und könnte prinzipiell angewendet werden. Einige weitere Untersuchungen bezüglich eines optimierten Zusammenwirkens von Sensor und Asphalt (Kabel, Einbauverfahren) wären noch durchzuführen. Als umsetzungshemmend wirken sich die nach wie vor relativ hohen Beschaffungskosten der benötigten faseroptischen Messgräte aus.

weitergehender Forschungsbedarf:

Das Forschungsprojekt ortet im Bereich der numerischen Modellierung der Versuche, dem optimieren des Sensorverhaltens sowie der Auslotung der Grenzen bezüglich der Charakterisierung von Fahrzeugüberfahrten Potential und weiteren Forschungsbedarf.

Einfluss auf Normenwerk:

vorerst keiner, da es sich um ein Entwicklungsprojekt in der Messmethodik handelt

Der Präsident/die Präsidentin der Begleitkommission:

Name: Stolz   Vorname: Martin

Amt, Firma, Institut: Berner Fachhochschule, Institut für Siedlungsentwicklung und Infrastruktur

Unterschrift des Präsidenten/der Präsidentin der Begleitkommission:

Forschung im Strassenwesen des UVEK: Formular 3   Seite 3 / 3

Register of reports in road research

The register of the recently publiced closing reports can be downloaded under www.astra.admin.ch (*Forschung im Strassenwesen --> Downloads --> Formulare*).

Register of reports in road research